A Study of Flow Patterns and Surface Wetting in Gas-Oil-Water Flow

A dissertation presented to

the faculty of

the Russ College of Engineering and Technology of Ohio University

In partial fulfillment

of the requirements for the degree

Doctor of Philosophy

Kok Eng Kee

August 2014

This dissertation titled

A Study of Flow Patterns and Surface Wetting in Gas-Oil-Water Flow

by

KOK ENG KEE

has been approved for

the Department of Mechanical and Systems Engineering

and the Russ College of Engineering and Technology by

Srdjan Nešić

Russ Professor of Chemical and Biomolecular Engineering

Dennis Irwin

Dean, Russ College of Engineering and Technology

ABSTRACT

KEE, KOK ENG, Ph.D., August 2014, Mechanical Engineering

A Study of Flow Patterns and Surface Wetting in Gas-Oil-Water Flow

Director of Dissertation: Srdjan Nešić

Three-phase gas-oil-water flow is a common occurrence in the oil and gas industry. The presence of water in the pipeline can lead to internal corrosion if the free water, dissolved with corrosive species, comes into contact with the wall surface, a scenario known as 'water wetting.' With the introduction of a gas phase, the flow dynamics become much more complicated due to the varying degree of spatial distribution of the immiscible fluids. The present work addresses how the addition of a gas phase to the oil-water flow can change the flow dynamics and surface wetting behavior. The work mainly focuses on the hydrodynamic aspects of the flow and how they may affect the surface wetting in pipe flow.

Experimental work was first carried out on oil-water systems to investigate flow patterns and surface wetting behavior in order to establish a baseline for the subsequent measurement of three-phase flow into which CO_2 gas was introduced. The experiments were conducted in a large scale 0.1 m ID flow loop. Test fluids used were light model oil LVT200 and 1 wt.% aqueous NaCl. Flow pattern images were visually captured with a high speed video camera and surface wetting behavior was measured using conductivity pins.

In oil-water flow, flow patterns can be divided into two broad categories dependent on whether the two immiscible liquids are dispersed or separated. Under those flow conditions, the surface wetting behavior can be categorized into four types of wetting regimes based on the intermittency of the wetting behavior as measured by the conductivity pins.

In the three-phase gas-oil-water flow, the effects of gas added to the oil-water system were investigated. Flow patterns and surface wetting were quantified at various liquid velocities, gas velocities and water cuts. At low water cut, the wetting results showed that adding the gas phase can help to keep water off the pipe wall, leading to oil wetting. At high water cut, water wetting prevailed and adding gas did not lessen the intensity of wetting.

Tomographic techniques were employed to study the cross sectional distribution of the fluid phases in multiphase flow pipes. Knowing the strength and limitations, the techniques can be used for meaningful interpretation of flow patterns. They were not suited, however, for detecting water distribution at low water cut.

A mechanistic three-phase water wetting model has been proposed and implemented. The model was built from the framework of the gas-liquid flow model and the oil-water wetting model. The model has been validated with the laboratory data for three different types of flow patterns.

DEDICATION

To

My loving parents, Kee Yaw Heng and Kong Koi Yin

My beloved sisters Siew Yen, Siew Mun

My esteemed mentor, Daisuku Ikeda

and all other friends and family members

For their

Love and faith

ACKNOWLEDGMENTS

First and foremost, I would like to express my heartfelt appreciation to my advisor Dr. Srdjan Nešić. Through his superior academic guidance, I learned tremendously on how to critically analyze and present results as well as handle questions whenever I was academically challenged.

I am deeply indebted to my previous Water Wetting Joint Industry Project (WWJIP) leader Dr. Sonja Richter and the current project leader Dr. Luciano Paolinelli for the technical directions given in the research. Their professional expertise has been an inspiring example for me.

I would like extend my sincere gratitude to Dr. David Young, Dr. Bruce Brown and Dr. Marc Singer, Dr. Dusan Sormaz for their unwavering academic assistance during my PhD journey. I gratefully thank Mr. Al Schubert, Cody Shafer, Alexis Barxias, Steve Upton, Phil Bullington and Daniel Cain for their excellent technical support in the laboratory work. Special thanks to Becky Gill for her administrative support as well as Garret Brown and Branka Sormaz for the IT support. My great appreciation goes to Dr. Bert Pots for his helpful guidance and discussions related to my research.

Sincere gratitude to my friends and fellow graduate students: Marijan Babic, Wei Li, Peng Jin, Zheng You Gui, Ning Jing, Thu Tran, Guo Shaoqiang, Gao Xin, Najmiddin Yaakob, Nor Roslina and other colleagues for their camaraderie and support. They have contributed to an enjoyable working environment at the Institute. I am forever indebted to Marijan Babic for his immense help in the experimental work and our insightful discussions about science and life in general.

Finally, I would like to express my heartfelt gratitude to my beloved my family members for their unconditional love, patience and understanding during the journey working towards my academic goal.

TABLE OF CONTENTS

LIST OF TABLES

LIST OF FIGURES

CHAPTER 1: INTRODUCTION

1.1 Background

Multiphase flow is a complex flow phenomenon that involves the simultaneous flow of two or more physically immiscible fluids within conduits. The term *multiphase* typically refers to the flowing mixture of substances of different states, such as in gas-liquid flow, but can also broaden to encompass the mixture of different components of the same physical state, such as oil-water flow where the components are immiscible (Wallis, 1969). Multiphase flow environments are routinely encountered in a wide spectrum of industrial applications, ranging from hydrocarbon transportation, power generation, mining, food production and petrochemical processing.

The particular manner in which the respective phases spatially distribute themselves in a pipe can result in a broad variety of complicated flow patterns (Hewitt, 2005). The presence of distinctive and deformable boundaries between different fluid phases are the characteristic features of multiphase flow systems. The occurrence of particular flow pattern types depends on a multitude of influencing factors, such as the pipe diameter, pipe inclination, physical properties of the fluids, presence of surface active compounds, surface wettability, as well as operational parameters such as flow rate and water cut. There has been extensive research work in industry and academia to understand the effects of the various aspects of the complex multiphase flow phenomenon such as flow hydrodynamics, thermodynamics, fluid composition, flow assurance and flow-induced corrosion.

1.2 Motivation

In oil and gas industry, the multiphase flow environment can be encountered both during the production and transportation of hydrocarbon products *via* pipelines. Most oil production wells

naturally contain some fraction of formation water (brine) and gases, which are often transported simultaneously in the flowlines to the processing facilities prior to separation. However, the presence of water and dissolvable acid gases such as CO_2 and H_2S can pose an interior corrosion risk to the steel pipe. Since the corrosive species are soluble in the aqueous phase, the likelihood of internal corrosion increases if the water drops out from the oil phase and comes into contact with the pipe wall, a scenario known as 'water wetting' (Cai *et al*., 2004). On the other hand, the corrosion risk can be reduced if 'oil wetting' occurs, a scenario when the water phase is entrained by the flowing oil and the wall is wetted by the oil or gas. Hence, the issue of water wetting and entrainment in the transportation of hydrocarbon products is of paramount importance. Practicing engineers need to understand the flow dynamics, fluids characteristics and the surface wettability as those factors can influence how the water drops out or becomes entrained by the bulk oil flow, subsequently affecting the corrosion risk.

Much of the research work on water wetting has been directed to understanding the wetting behavior in two-phase oil-water flow. Cai and co-workers (2005, 2012) at Ohio University employed multi-array conductance probes to study the water wetting behavior of oil-water flow in a large-scale flow loop setting. There is an extensive body of research on the hydrodynamics and flow characteristics in two-phase flow (gas-liquid, oil-water) and three-phase flow (gas-oil-water) systems. These studies mostly focus on the flow patterns, pressure gradient, liquid holdup, and other flow pattern-specific hydrodynamic parameters. However, the study of water wetting in the three-phase gas-oil-water flow has received little attention. Little emphasis has been placed on water entrainment and surface wetting experiments in the work relating to three-phase flow.

1.3 Objectives and hypotheses

The main goal of the research has been the study of surface wetting behavior in a three-phase flow environment. In order to achieve the goal, the flow patterns and surface wetting behaviors for two-phase oil-water flow were first investigated in the large-scale flow loop in order to establish baselines for subsequent three-phase flow measurements.

The specific objectives of the present study have been:

- Investigation of the flow patterns in two-phase oil-water and three-phase gas-oil-water flow using a large scale multiphase flow loop.

- Investigation of the surface wetting behavior and oil-water distribution in two-phase oil-water and three-phase gas-oil-water flows.

- Implementation of a one-dimensional mechanistic model for predicting flow patterns and water wetting in three-phase flow system.

The following hypotheses were used to examine the behavior of surface wetting in a three-phase flow environment:

- The surface wetting is determined by the access of water to the pipe wall surface, and whether the water is in the form of continuous phase or dispersed phase.

- The surface wetting is determined by the global gas-liquid flow patterns, and if the gas influences the distribution of water.

- The surface wetting is determined by the distribution of water phase in local oil-water flow structure, and is dependent on whether the water is separated or dispersed.

1.4 Structure of dissertation

The dissertation is organized as follows:

Chapter 2 is a concise literature review on the flow patterns, wetting phenomenon, droplet breakup mechanism and wetting models. Chapter 3 describes the experimental details and the measurement techniques used in the small-scale laboratory tests and large-scale flow loop experiments. Chapters 4 and 5 discuss the flow pattern visualization and surface wetting results from the flow loop study of the oil-water system and gas-oil-water system, respectively. In Chapter 6, the imaging results of the cross-sectional flow patterns and phase distribution of multiphase flow systems using the tomographic equipment are presented. Chapter 7 outlines the water wetting model for the oil-water system and presents a three-phase water wetting model for the gas-oil-water system. The dissertation finishes with the conclusions and recommendation for future work in Chapter 8.

Part of the work described in the thesis has been submitted as a proceedings paper at an international conference, as listed in the references.

CHAPTER 2: LITERATURE REVIEW

2.1 Flow patterns

Multiphase flow is defined as the concurrent flow of materials with two or more *phases* within a conduit (a channel or pipe). A *phase* refers to a state of matter, such as gas, liquid or solid. The term *multiphase* also refers to the flow of materials with different *components*, namely phases having dissimilar chemical substances. For example, steam-water flow is a two-phase, while air-water flow is a two-component system. Oil-water flow is a two-component liquid-liquid system. The above examples are considered to be two-phase flows in which the phases are either noted as continuous or dispersed components (Wallis, 1969).

For a conduit carrying multiphase fluids, a variety of flow patterns may arise from the way the fluid phases physically distribute themselves within the conduit (Shoham, 2006). Flow patterns, also termed flow regimes, refer to the existence of deformable interfaces between the immiscible phases. The observed flow pattern can be a function of a variety of parameters including the fluid hydrodynamics, fluid properties, phase volume fraction and pipe geometry. These flow patterns can be represented as bounded areas in a two-dimensional graph, termed as flow pattern map or flow regime map. A flow pattern map is typically plotted with two independent mapping parameters, such as the superficial phase velocities, in abscissa and ordinate axes. An example of a flow pattern map is given in Figure 2-1. The boundaries on the map are the flow transition lines located by the experimental data; hence, the map is valid within the range of test conditions (Taitel *et al*., 1978).

Flow patterns are primarily classified based on experimental observations which could be somewhat subjective. The same physical flow pattern can be reported with different names among researchers. To keep the designations manageable, Wallis (1969) postulated a multi-level

classification for the flow patterns. The primary level describes the morphological flow patterns which are spatially distinctive with respect to each other; for example, separated or dispersed flow in a liquid-liquid flow, slug or annular flow in a gas-liquid flow. In the secondary level, a further subdivision is made within each of these distinctive flow patterns to describe the nature of the local interaction between the phases. For example, separated flow with mixing at the interface in a liquid-liquid system. The Wallis methodology can be well applied for two-phase flow systems.
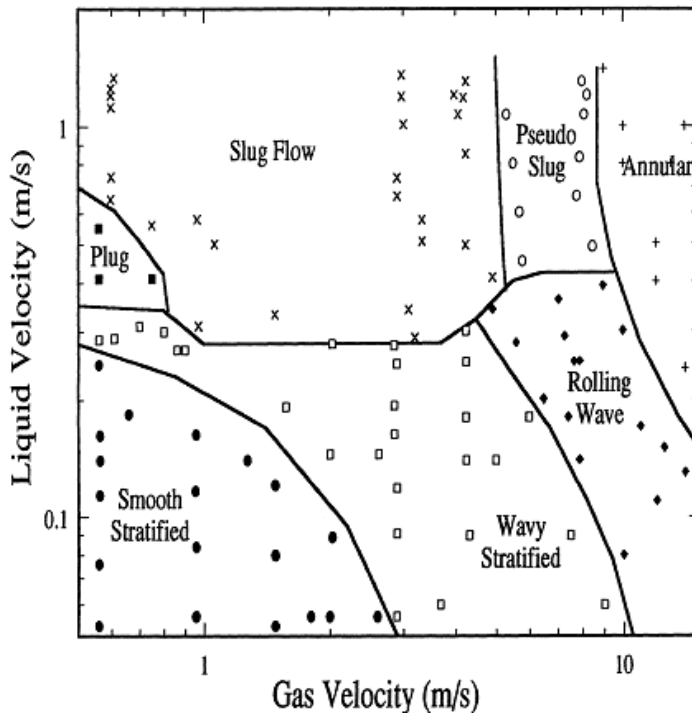
Figure 2-1: Gas-liquid flow pattern map produced by Lee (1993) showing transition boundaries for CO_2-water flow system in a 0.1 m ID horizontal pipe.

2.1.1   Flow pattern identification techniques

A variety of techniques have been used by researchers to identify flow patterns. The most common techniques are described below:

2.1.1.1 Visual observation

This is a straightforward and common technique which employ photography or video recording to capture the flow patterns of clear fluids through a transparent pipe section (Brown *&* Govier, 1961; Hesketh *et al.*, 1991; Vielma *et al.*, 2008). The technique is suited for fast motion fluid flow since the flow patterns can be recorded and analyzed later by video playback at a slower rate. The method is not suited for opaque fluids where visualization is limited to near-wall flow structures. Other drawbacks are that the visual assessments can be somewhat subjective and the curvature of the pipe may cause optical distortion. Trallero *et al*. (1997) used a fluid filled jacket of a square box surrounding the view pipe to compensate for the optical distortion. Hasson *et al.* (1970) discussed the use of view-box liquid with similar refractive index to wall material in order to minimize the optical distortion.

2.1.1.2 Conductance probes

Electrically-based probes have been used to determine the local void fraction and phase continuity in multiphase flow environment. The technique is based on local instantaneous measurement of electrical property (conductivity, impedance or capacitance) of different flowing phases that may fluctuate in time and space (Cartellier & Achard, 1991). Despite variations in the design of conductance probes, they shared some common features having an exposed metal tip as the electrode, surrounded by an outer conductive casing as the ground, and sheathed by insulation material filled in between, as shown in Figure 2-2. The probes can be excited by either a direct current or alternating current source depending on the measurement types. The sensor probe forms part of the electric circuit such that the strength of the output signal relies on the local phase covering the exposed sensor tip and grounded terminal. Because of the contrast in the dielectric constants, the probes can display a contrasting signal that can distinguish the phases.

A number of researchers have used conductance probe technique to characterize the flow patterns. The technique has the benefit of minimizing the risk of subjective assessment associated with visual observation. Russell & Lamb (1965) used a simple conductivity probe to detect the salt tracer as a means to characterize the film hydrodynamics in annular flow. Trallero (1995) used an array of eight conductance probes to identify the local phase continuity in a horizontal oil-water flow system. Flores (1997) employed dual-electrode conductance probes that were installed at different radial distances to characterize the vertical and inclined oil-water flow patterns. Angeli & Hewitt (2000) used a high frequency (1 GHz) impedance probe to detect the local phase continuity and a conductivity needle probe to determine the continuous phase in oil-water system. Cai *et al*., (2005, 2012) and the co-workers (Li *et al*., 2006; Ayello *et al*., 2008) at Ohio University engineered a large number of non-intrusive conductivity probes flush mounted onto the inner pipe wall to detect the water wetting behavior in oil-water flow system.
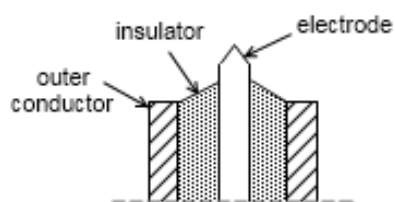
Figure 2-2: Schematics of a typical conductance probe.

2.1.1.3 Tomographic techniques

Process tomography has been widely used as an imaging tool in industry to provide dynamic process information of multiphase fluids moving in a vessel. The output is a two-dimensional slice image, or tomogram, showing the spatial distribution of the process parameter. There has been development of various tomographic modalities based on physical phenomena namely electromagnetic waves (X-ray, γ-ray and microwave), ultrasound, and electrical impedance

(capacitance, resistivity). Comprehensive reviews on this subject area can be found in papers (Chaouki *et.al*, 1997; George *et al*., 1998) and books (Williams & Beck, 1995; Grangeat, 2009). The following is a brief explanation on the electrically based tomography system which was used in this work. The experimental details and results are described in Chapter 6.

There are two core modalities in electrical tomography based on either capacitance or conductivity measurement of the flowing media. They are electrical capacitance tomography (ECT) for the permittivity measurement and electrical resistance tomography (ERT) for the resistivity measurement.

ECT can be used to differentiate phases in gas-liquid systems because of the large difference in dielectric constant between the gas and liquid phases. ECT is non-intrusive and fast sensing technique. A number of researchers have reported on the use of ECT in multiphase flow metering (Yang *et al*., 1995; Ismail *et al*., 2005), gas-liquid flow system (Gamio et al., 2005; Jeanmeure *et al*., 2002), oil-water flow system (Bolton *et al*., 1999; Hasan & Azzopardi, 2007), three-phase flow system (Corlett, 1999) and image reconstruction algorithms (Isaksen, 1996).

ERT works well if one of the components in the flowing media is slightly more conductive than the other. It exploits the differences in electrical conductivity between the phases and can be applied to oil-water systems. Sharifi & Young (2013) presented an extensive review on the ERT applications in various process industries. Dickin & Wang (1996) described the ERT design and process application. Several researchers reported the use of ERT to characterize the flow patterns (Ma *et al*., 2001; Dong *et al.*, 2003).

2.1.2   *Horizontal oil-water flow patterns*

In horizontal oil-water flow, the flow patterns can be classified into two broad categories dependent on whether the immiscible liquids are in separation or dispersion. When oil and water

move slowly together in a pipe, gravity is the dominant force causing the immiscible liquids of different density to flow in stratified layers. Under sufficiently turbulent flow motion, the stratification is disrupted and dispersion takes place causing one of the phases loses its continuity and becomes entrained as droplets.

Compared to gas-liquid flow, the differences in properties between oil-water phases are relatively smaller, resulting in less distinctive flow patterns. The oil-water flow structure seems to be dictated more by the differential properties between the liquids such as the density, viscosity and interfacial tension. The interplay of these properties can result in a varying degree of local spatial distribution of the phases at the interface.

The oil-water experiments can be traced back to the 1950s. In one of the early work, Russell *et al.* (1959) collected experimental data for a horizontal oil-water system using a small diameter 25.4 mm ID pipe. The oil phase fluid used was refined mineral oil (μ_o = 18 cP). Three types of flow patterns were reported: *oil bubbles in wate*r, *stratified* and *mixed* flow.

Oglesby (1979) carried out extensive flow experiments to characterize oil-water flow patterns. By using a 38 mm ID horizontal pipe, he classified up to 14 different flow patterns, ranging from *segregated flow* at the lowest velocity to *homogenous dispersed* flow at the highest velocity.

Arirachakaran (1983) acquired experimental data for a horizontal oil-water system in a 1.5-inch ID pipe using oils with a broad range of viscosities (μ_o = 4.7 to 115 cP). He reported five types of flow patterns: *stratified, mixed, intermittent, dispersed and annular. Annular* flow was noted to exist for the case of high viscosity oil.

Trallero (1995) performed flow pattern characterization experiments using a 50 mm ID horizontal pipe. The oil phase fluid used was naphthenic white oil (μ_o = 29 cP). By employing photography, video and conductance probes, he classified six types of flow patterns using standardized nomenclature, as illustrated and explained in Figure 2-3. His flow pattern

designations and abbreviations were adopted by other subsequent researchers, although additional new flow patterns were also defined (Simmons & Azzopardi, 2001; Vielma *et al.*, 2008; Amundsen, 2011).

Figure 2-3: Classification of horizontal oil-water flow patterns in 50 mm ID pipe (reproduced and adapted from Trallero, 1995).

Malhotra (1995) used a large diameter pipe of 102 mm ID to investigate two- and three-phase horizontal flows at Institute for Corrosion and Multiphase Technology (ICMT), Ohio University. Two types of test fluids were used for the oil phase: LVT200 (μ_o = 2 cP) and Britol 50T (μ_o = 100 cP). He described three observed flow patterns: *bubble*, *semi-segregated* and *semi-mixed* flows.

Vedapuri *et al.* (1997) expanded the work using the same flow loop facility and described five types of flow patterns: s*tratified, semi-stratified, semi-mixed, semi-dispersed* and *dispersed flow*.

Nädler & Mewes (1997) experimentally studied the flow patterns and emulsion phenomena of an oil-water system in a 59 mm ID horizontal pipe. The oil phase fluid used was white mineral oil. Different reduced values of oil viscosity (from 35 cP to 28 cP) were attained by increasing the test temperatures (18 °C to 35 °C). They presented seven types of flow pattern (Figure 2-4), which shared a similar designation to Trallero's work (1995), and reported that different types of dispersion in flow can be distinguished according to the observed flow pattern and measured pressure gradients.

Figure 2-4: Classification of horizontal oil-water flow patterns in 59 mm ID pipe (reproduced and adapted from Nädler & Mewes, 1997).

Elseth (2001) identified three types of stratified and six types of dispersed flow patterns from his experimental work using a kerosene-water system in a horizontal 2-inch ID stainless steel pipe.

By using visual observations and a gamma densitometer instrument, the fine details of the local phase distribution were captured, hence providing additional flow patterns to describe the flow structure. Amundsen (2011) expanded on the work of Elseth (2001) at the same facility using similar techniques. The complete list of flow patterns proposed by them is given in Table 2-1.

Table 2-1: Oil-water flow pattern classification (Elseth , 2001; Amundsen, 2011)

Flow pattern	Abbrevation
Stratified flow	ST
Stratified flow with mixing at the interface	ST & MI
Stratified wavy	SW
Dispersion of water in oil and oil	Dw/o & o
Dispersion of oil in water and water	Do/w &w
Dispersion of water in oil and water	Dw/o & w
Dispersion of oil in water and oil	Do/w & o
Dispersion of water in oil and dispersion of oil in water	Dw/o & Do/w
Plug flow	PG
Water in oil emulsion	w/o
Oil in water emulsion	o/w

In the experimental work by Cai *et al*., (2005, 2012) and his co-workers (Li, 2009; Tang, 2010), a large diameter 0.1 m ID horizontal pipe was used to investigate the oil-dominated liquid-liquid flow. The working fluids were 1 wt.% NaCl brine and light oil LVT200 ($\mu_o = 2$ cP). Five types of flow patterns were reported, namely, *smooth stratified, stratified with water globules*, *stratified with mixing layer, semi-dispersed* and *fully dispersed* flows. The produced flow pattern map is given in Figure 2-5. By reexamining their flow patterns with the designations proposed by Trallero (1995): *smooth stratified* is equivalent to *ST, stratified with mixing layer* is *ST & MI*, *semi-dispersed* is *Dw/o & o*, *fully dispersed* is *w/o*, whereas stratified with water globules is not

accounted. By using conductivity pins, the surface wetting behavior at the pipe wall under different flow conditions was measured.
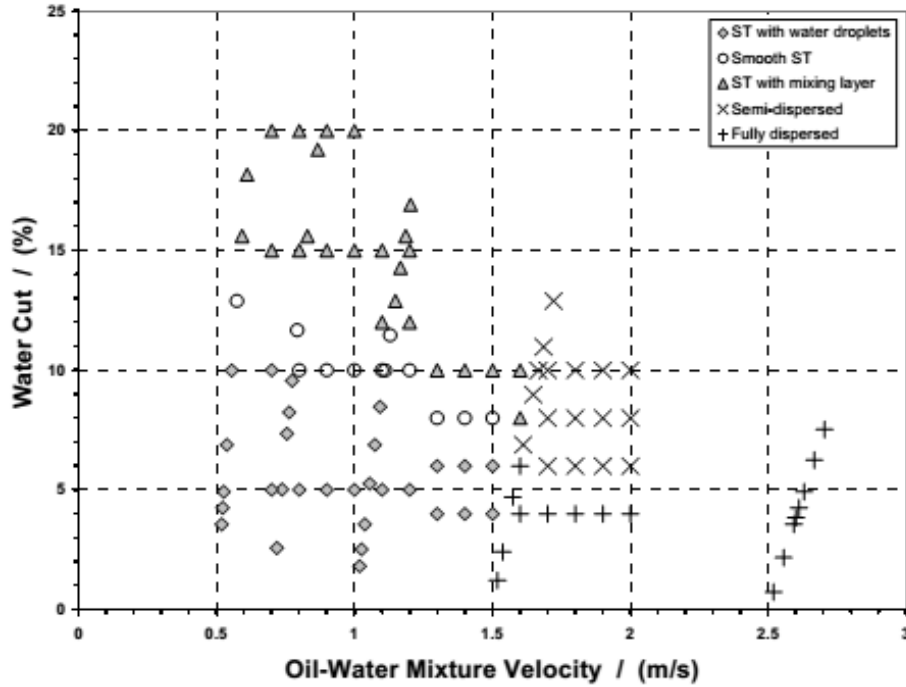
Figure 2-5: Flow pattern map for LVT200-water flow in 0.1 m ID horizontal pipe (reproduced with permission from Li, 2009).

2.1.3 *Vertical oil-water flow patterns*

The available literature data on a vertical two-phase oil-water system suggested that the observed flow patterns generally fall into either water-continuous flow or oil-continuous flow. Unlike the horizontal oil-water system, complete separation of water and oil phases is not seen in the vertical flow. The discontinuous phase tends to be dispersed in various sizes and shapes of droplets within the continuous carrier fluid.

Govier *et al*., (1961) carried out vertical flow experiments in a small diameter 1-inch ID vertical pipe using three types of oil with different viscosities (μ_o = 0.9 cP to 150 cP). By adopting

nomenclature used in gas-liquid flow, they designated five types of flow patterns (Figure 2-6) into two broad categories as follows:

Water dominated: *oil bubbles in water, oil bubbles/slugs in water, oil froth.*

Oil dominated: *oil froth with water drops, water drops in oil.*
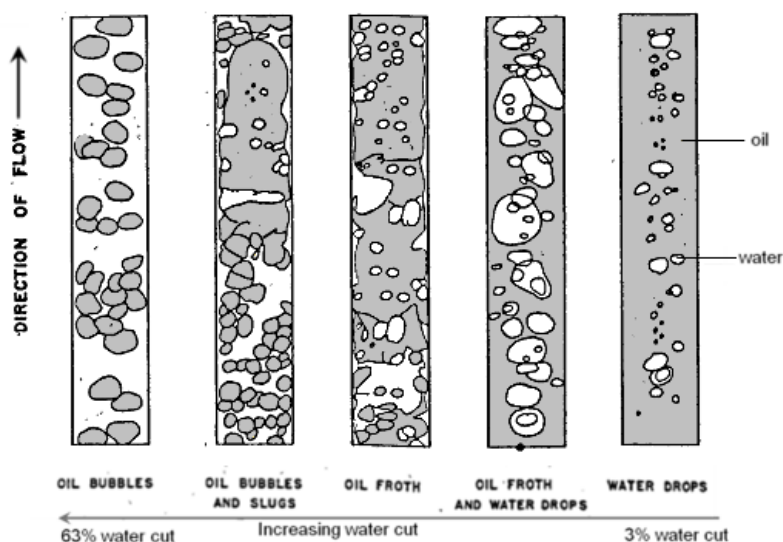
Figure 2-6: Classification of vertical oil-water flow (reproduced and adapted from Govier *et al.*, 1961).

Their flow pattern designation was somewhat arbitrary, as some terms were used interchangeably. Here, *bubble* denotes a small sphere of liquid, rather than the conventional meaning of a gas bubble. The term *slug* refers to a distorted pocket of liquid, without the characteristic bullet-shaped gas bubble typically present in gas-liquid flow. Their nomenclature did not adequately reflect the true flow structure in the vertical oil-water flow.

Using a large diameter pipe of 7.25 inch ID, Zavareh *et al.* (1988) studied the vertical oil-water flow using light refined oil ($\mu_o = 2.5$ cP) and water. The flow pattern results were limited to low liquid flow rates due to large pipe size. They reported *bubble, dispersed bubble, inverted*

bubble and *inverted dispersed bubble* flow patterns. The term *inverted* refers to the inversion of water-continuous to oil-continuous flow.

Flores (1997) conducted the oil-water flow experiments in a 2-inch ID vertical and inclined pipe using refined oil (μ_o = 20 cP) and water. Visual observations and conductance probes were employed to identify the flow patterns. The latter technique was used to minimize the subjective assessment associated with the visual observation. The flow patterns were classified into two major categories: water-dominant and oil-dominant flows, each consisting of three distinctive flow patterns as shown in Figure 2-7:

Dispersion: Oil-in-water dispersion or water-in-oil dispersion.

Very fine dispersion: Seen at higher flow rate in which the discontinuous phase is further dispersed into finely distributed droplets.

Churn: Occurs when large droplets (or globules) agglomerate and coalesce into highly irregular pockets of liquids.
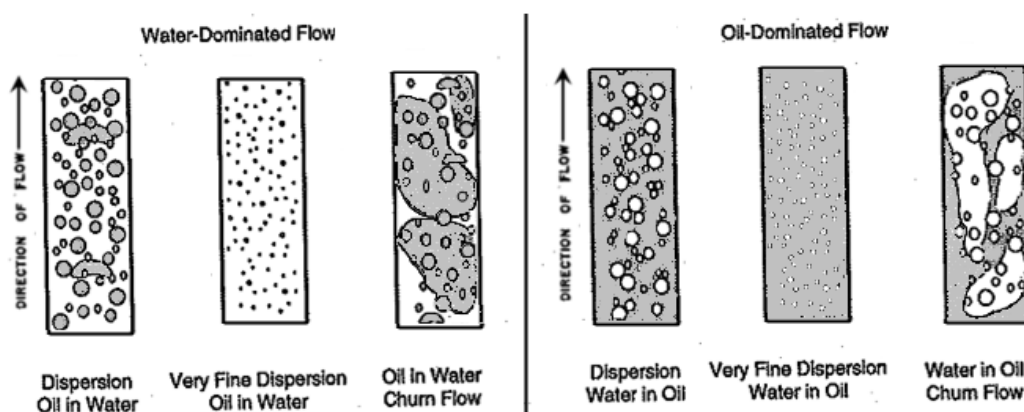
Figure 2-7: Classification of vertical oil-water flow patterns (reproduced and adapted from Flores, 1997).

Du *et al.* (2012) used a small diameter 20 mm ID pipe to study the vertical oil-water flow pattern. The test fluids used were white oil (μ_o = 12 cP) and tap water. Similar to Flores's work,

mini-conductance array probes were employed to identify the flow patterns. They identified similar flow patterns and transitions from oil-dominated to water-dominated flows, namely *water drops in oil, transition (oil froth)*, *oil drops in water, dispersed oil in water*, and *oils in water slug*.

2.1.4   Horizontal gas-oil-water flow patterns

The concurrent flow of three immiscible phases in the pipes can result in a multitude of complex flow patterns due to the interplay of various parameters such as pipe geometry, fluid properties, flow rate, phase fraction, and interfacial interaction. The available literature reveals very few experimental work have been carried out on the field of three-phase flow. There is also no generalized three-phase flow pattern map, all the available maps are purely empirical data applicable to specific test environments.

In a pioneering work, Sobocinski (1955) carried out three-phase oil-water-air flow experiments using a 3-inch ID plastic pipe. The oil phase used was diesel oil (μ_o = 3.8 cP). He classified nine different flow patterns based on gas-liquid flow and oil-water flow configurations, as listed in Table 2-2.

Table 2-2: Three-phase flow pattern classification (Sobocinski, 1955)

No.	Three-phase flow pattern
1	No liquid mixing Stratified
2	No liquid mixing Ripple
3	Inception of oil & water mixing surface waves
4	Incipient emulsion light waves
5	Incipient emulsion w/ waves
6	Partial emulsion w/ waves
7	Partial emulsion w/ heavy waves
8	Partial emulsion w/ light crests
9	Emulsified / semi annular

Açikgöz *et al*. (1992) collected extensive experimental data for a horizontal three-phase flow system covering both oil-dominated and water-dominated flows. The tested oil fluid used was viscous (μ_o = 116 cP) in a relatively small diameter 19 mm ID pipe. They systematically classified 10 different types of flow patterns (see Table 2-3) in a three-part classification scheme according to the status of the continuous liquid phase (oil-base or water-base), discontinuous liquid phase (dispersed or separated) and gas-liquid flow configuration.

Table 2-3: Three-phase flow pattern classification (Açikgöz *et al*., 1992)

No.	Three-phase flow pattern (three-part designation)		
1	Oil-based	/dispersed	/plug flow
2	Oil-based	/dispersed	/slug flow
3	Oil-based	/dispersed	/stratified/wavy flow
4	Oil-based	/separated	/stratified/wavy flow
5	Oil-based	/separated	/stratifying/annular flow
6	Oil-based	/separated/dispersed	/stratifying/annular flow
7	Water-based	/dispersed	/slug flow
8	Water-based	/dispersed	/stratified/wavy flow
9	Water-based	/separated/dispersed	/ incipient stratifying/annular flow
10	Water-based	/dispersed	/stratifying-annular flow

Lee (1993) published work for seven observed horizontal flow patterns using an oil-water-gas CO_2 system in a 75 mm ID flow loop. The fluids used were LVT200 (μ_o = 2 cP) as the oil phase, tap water and CO_2 gas. The three-phase flow patterns were found to differ from those observed in gas-liquid and oil-water two-phase flow systems, as depicted in Figure 2-8. The three-phase flow patterns classified by the author were based on the designations typically found in gas-liquid flow. Upon comparison, the three-phase slug flow was observed to occur at lower liquid velocities and three-phase annular flow at lower gas velocities than its two-phase gas-oil flow counterpart.
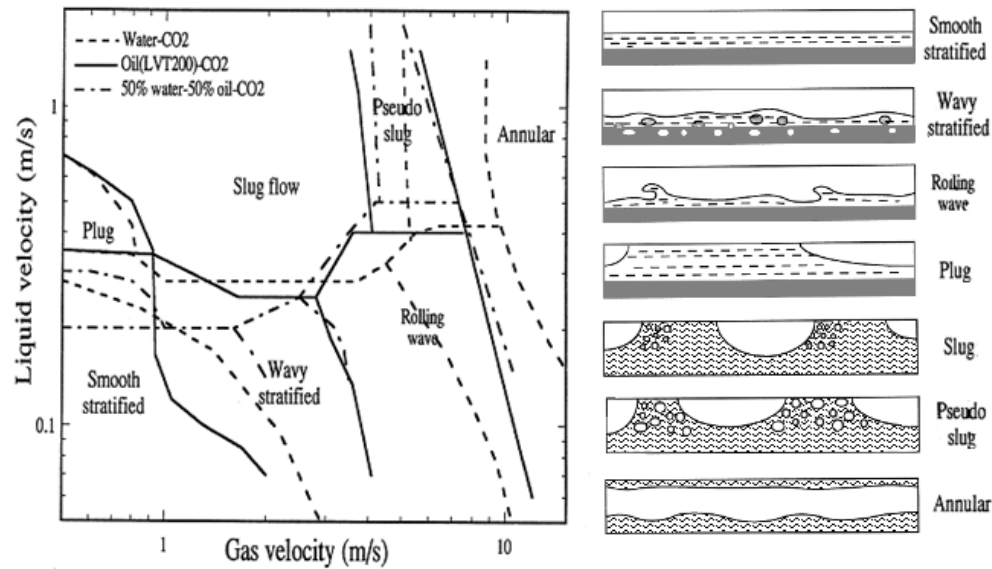
Figure 2-8: Three-phase flow patterns and flow pattern map. Flow transitions for two-phase were included in the map for comparisons (reproduced and adapted from Lee, 1993).

Pan (1996) focused on horizontal three-phase flow experiments at elevated pressures (6 bar) using a 78 mm ID flow loop. He devised another multi-part flow patterns classification scheme and proposed 15 types of three-phase flow patterns, but only eight of them were observed in the actual tests. By comparing the experimental data with available literature data, considerable flow pattern variations were found between the two-phase and three-phase systems.

Table 2-4: Horizontal three-phase flow pattern classification identified by Pan (1996)

No.	Three-phase flow pattern (three-part designation)		
1	Dispersed	/oil-continuous	/slug flow
2	Dispersed	/oil-continuous	/stratified flow
3	Dispersed	/oil-continuous	/annular flow
4	Dispersed	/water-continuous	/slug flow
5	Dispersed	/water-continuous	/stratified flow
6	Dispersed	/water-continuous	/annular flow
7	Separated		/slug flow
8	Separated		/stratified flow

Keskin *et al.*(2007) studied the horizontal three-phase air-water-oil system in a 51 mm ID pipe. As shown in Table 2-5, they proposed a two-part flow pattern classification scheme with 12 individual flow patterns. The scheme consists of two parts: the first part denotes the gas-liquid flow pattern and the second part denotes the liquid-wall relation. Distinctions were found in the flow pattern transitions between two-phase and three-phase flows. Their work demonstrated that the two-phase gas-liquid flow model was ineffective in predicting the three-phase flow patterns.

Table 2-5: Horizontal three-phase flow patterns identified by Keskin *et al.*(2007)

No.	Horizontal three-phase flow pattern (two-part designation)		
	Gas-liquid relation	**/ liquid-wall relation**	**abbreviation**
1	Stratified	/ Stratified	ST-ST
2	Stratified	/ Dual continuous	ST-DC
3	Stratified	/ Oil continuous	ST-OC
4	Stratified	/ Water continuous	ST-WC
5	Intermittent	/ Stratified	IN-ST
6	Intermittent	/ Dual continuous	IN-DC
7	Intermittent	/ Oil continuous	IN-OC
8	Intermittent	/ Water continuous	IN-WC
9	Annular	/ Oil continuous	AN-OC
10	Annular	/ Water continuous	AN-WC
11	Dispersed Bubble	/ Oil continuous	DB-OC
12	Dispersed Bubble	/ Water continuous	DB-WC

2.1.5   *Vertical gas-oil-water flow patterns*

Only a limited number of publications are available on the experimental work of vertical three-phase flow. Most of the work focused on identifying the three-phase flow patterns.

In Shean's (1976) work, three-phase flow experiments were conducted primarily to study the bubble and slug flow patterns in a 19 mm ID vertical pipe. He presented the three-phase flow pattern transitions based on a two-phase oil-water flow regime map.

Pleshko (1990) conducted three-phase flow experiments in a 51 mm ID vertical pipe. The test fluids used were Isopar V (μ_o = 10 cP), water and air. By comparing the flow pattern data with the gas-liquid predictive flow model by Taitel *et al*. (1980), the author found some mismatch of predictions in the flow transitions of three-phase flow.

Woods *et al.* (1998) used a smaller diameter 1-inch ID Perspex pipe and identified eight types of vertical upward oil-water flow patterns that can be broadly divided into oil-continuous and water-continuous flows, as shown in Figure 2-9. Mineral oils with viscosity, μ_o = 20 cP and 150 cP were used. Their flow conditions were limited to fairly low mixture liquid velocity (< 0.4 m/s). The influences of flow patterns on holdups and pressure drops were reported.
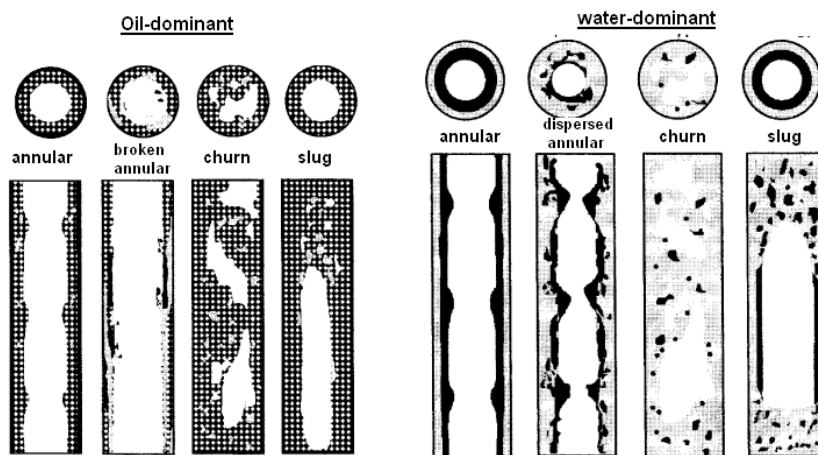
Figure 2-9: Classification of vertical flow patterns in 1-inch ID pipe (reproduced and adapted from Woods *et al*. 1998).

Gao & Jin (2011) employed an array of conductance probes to identify the flow patterns of a vertical three-phase system by statistically analyzing the nonlinear time-series flow signal outputs. They focused on water-dominant flow and identified four types of flow patterns, namely: *bubble, transitional bubble-slug, slug* and *emulsion type slug* flows.

2.2 Wetting in fluid flow

The steel pipelines used in the upstream hydrocarbon production often have concurrent flowing phases of oil, water and gas. The assessment for corrosion typically looks into the presence of free water and the concentration of corrosive species such as CO_2, H_2S, and organic acids. Without the presence of free water in the pipe, there is no corrosion. If water is present, the corrosive species can be dissolved in the aqueous phase, leading to corrosion if the water 'wets' the steel pipe wall. Wetting refers to the propensity of a liquid to adhere to a surface of a solid. For wetting phenomena in multiphase pipe flow environment, there are a number of direct and indirect parameters that interact with flow and impact the water wetting behavior. They are described as follows:

2.2.1   Fluid properties

Oil density: The greater the contrast between the oil and water densities, the more likely it is that the heavier water separates, due to gravity, and accumulates at the pipe bottom. If the oil and water densities are similarly matched in an oil-water dispersion system, the dispersed phase does not separate as easily by natural coalescence and settling at rest.

Oil viscosity: Viscosity refers to the stickiness of the fluid phase. More viscous oil can better entrain the water droplets in dispersion. Water droplet tends to sink more slowly in a more viscous oil as given by Stokes' law: $U_\infty = gd_p^2\Delta\rho/18\mu$, where U_∞ is the terminal velocity, μ the viscosity, d_p the droplet diameter and $\Delta\rho$ the differential density. In oil-water emulsions, the apparent viscosity concept is considered. The apparent viscosity of the mixture can be considerably higher than the viscosity of the respective phase alone if the emulsion is tight. This is explained by droplet crowding in the emulsion, leading to a non-Newtonian behavior (Kokal, 2005).

Oil-water interfacial tension: Interfacial tension refers to the surface tension at the interface of oil and water phase. It is a property that causes the oil-water interface to behave like a stretched membrane (Ben Amar et al, 2011). A larger interfacial tension value corresponds to a higher cohesive force, which requires a larger magnitude of turbulent breaking force to act against the interfacial tension force. On the other hand, a smaller value of interfacial tension promotes droplets generation and dispersion as less turbulent breaking force is required. In oil-water systems, a decrease in interfacial tension can be caused by a temperature rise or the presence of corrosion inhibitors, impurities or surface active compounds soluble in the oil and/or water phase.

Contact angle: Contact angle θ is a quantitative measure of the liquid/solid surface wettability. Consider a liquid droplet resting on a solid surface, it may spread as a film or remain as a droplet. The contact angle is measured in the liquid phase at the three phase boundary where the liquid, solid and gas contact lines intersect as shown in Figure 2-10. The relationship is described by Young's equation (Young, 1805) which relates the balance of horizontal components of the surface tensions at equilibrium:

$$cos\theta = \frac{\gamma_{SG} - \gamma_{SL}}{\gamma_{LG}} \tag{2.1}$$

where γ_{SG}, γ_{LG}, and γ_{SL} are the surface tensions of the solid-gas, solid-liquid and liquid-solid interface, respectively.
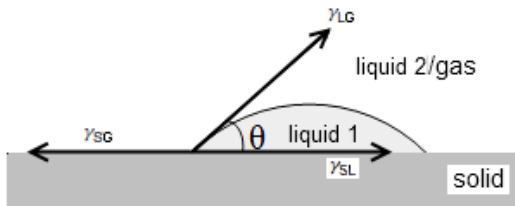
Figure 2-10: Measurement of contact angle θ.

The spreading of a liquid droplet on a surface is controlled by the competition of cohesion and adhesion forces. If the liquid molecules experience stronger cohesive force to each other than the adhesive force between the liquid and solid molecules, the liquid droplet will bead up and remain a spherical droplet that is less likely to spread on the solid surface, showing a contact angle $\theta > 90°$. On the other hand, if the cohesive force is stronger than the adhesive force, then the liquid droplet will spread on a surface, leading to a contact angle $\theta < 90°$. As shown in Figure 2-11, a hydrophobic surface is non-wettable with the liquid droplet, resulting in a contact angle θ close to 180°. A hydrophilic surface is wettable with the liquid that spontaneously coats the surface with a contact angle θ close to zero.

The presence of surface active compounds or corrosion inhibitors in the aqueous phase can alter the surface wettability by decreasing the surface tension and increasing the contact angle. Tang (2010) reported that adding 5 ppm of quat corrosion inhibitor can reverse the steel surface wettability form hydrophilic to hydrophobic in his oil-in-water contact angle measurement.
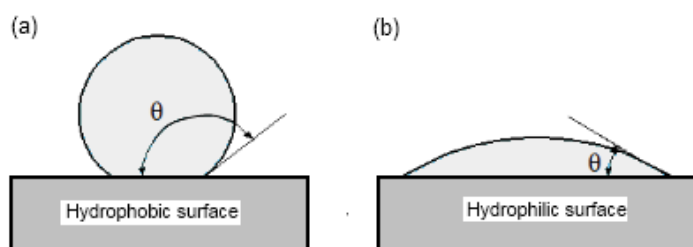
Figure 2-11: (a) Liquid droplet beads up on a hydrophobic surface, (b) Liquid spreads on a hydrophilic surface.

Emulsion: An emulsion is a dispersion system consisting of two immiscible liquids, one of which is dispersed as droplets in the other continuous phase. Water-in-oil (W/O) emulsions are commonly encountered in upstream production pipelines. The emulsion tendency varies considerably between crude oils. Some form unstable emulsions that separate quickly. Others

form fairly stable emulsions due to the presence of surface active compounds naturally occurring in the crude oils such as asphaltenes, resins, and waxes (Kokal, 2005) . The amount of water that emulsifies with crudes varies considerably, from <1% up to 60% (Becher, 1966). The rheological behaviors of the W/O emulsions depend on a number of factors such as the temperature, fluids viscosities, emulsion tightness, phase fraction ratio, and solid impurities (Kokal, 2005).

Water pH: A change in water pH can influence the ionization of polar groups, such as the molecules with acidic or basic functional groups that may adsorb on the oil-water interface. For example, if the pH is changed from neutral to more acidic values, the interfacial tension shifts upwards. For crude oil containing natural surface active substance, the ionization process of polar groups of surface active components can occur in the liquid phases as well as at the liquid/liquid and liquid/solid interface; hence, changing the adsorption, emulsion tendency, emulsion stability and liquid/solid wetting properties of the system (McLean & Kilpatrick, 1997).

2.2.2 *Piping properties*

Pipe diameter: Systems with large diameter pipes are gravity dominated while small diameter pipes are surface tension dominated (Brauner *et al*., 1998). The flow dynamics can be different between pipe sizes due to the different relative magnitudes of these competitive forces. Given the same flow rate, larger pipes lead to slower velocity and lower level of fluid turbulence, causing denser water droplets to drop out due to gravity. Gas-liquid flow in a small diameter tube, known as a capillary tube, has a prominent surface tension effect that could result in flow patterns different from those in large diameter tubes (Mishima & Hibiki, 1996).

Pipe inclination: In liquid-liquid flow, any change in the pipe inclination may affect the phase distribution. Flores *et al*. (1999) experimentally demonstrated that the oil-water flow patterns in inclined pipes differed significantly from vertical and horizontal flows. The interplay

of turbulent dynamic pressure, viscous drag and gravitational force components normal and parallel to the pipe wall can generate flow patterns of unique hydrodynamic features. Horizontal pipes are subjected to dominant gravity force that favors fluid separation. In upward inclined pipes, water tends to flow more slowly because of the gravity component pulling parallel down an inclined wall, causing *in situ* water holdup to increase. Changes in the pipe topographic and inclination profiles may lead to low points for water accumulation. In gas-liquid system, the stratified-wavy flow region expands considerably at the expense of the intermittent flow region as the pipe inclination increases (Barnea *et al.*, 1982). This implies increased likelihood of liquid separation and water wetting for inclined pipes in three-phase flow.

Pipe material: Different pipe materials exhibit different affinities for the water phase depending on the surface wetting properties. A clean steel surface is typically hydrophilic which means it is preferentially wetted by water. However, the interacting parameters such as surface roughness, prior wetting history and chemical heterogeneity (oxidation or contamination) can potentially affect the contact angle and wetting properties of the substrate (Chau *et al.*, 2009). Hasson *et al*., (1970) pointed out the wall wetting effect in shifting the transition of flow patterns. By intentionally enhancing the hydrophobicity of a glass tube, the core annular flow was reported to prevail. Angeli & Hewitt (1998) used two different pipe materials: steel and acrylic in the liquid-liquid flow experiments. The surface wettability of the steel appeared to depend on the prior wetting history (oil wet or water wet), while the acrylic pipe was hydrophobic. Angeli & Hewitt (2000a) extended their earlier work by using stainless steel and acrylic pipes. Considerable differences in flow patterns were observed between these two pipes. The tendency for dispersion was greater in the stainless steel as opposed to the acrylic tube.

Surface roughness: Surface roughness may affect the flow pattern. As suggested by Angeli & Hewitt (2000b), rougher wall surface may lead to more disturbed flow due to a higher degree of fluid turbulence and wall shear stress. Surface roughness can influence the contact angle and

surface wettability. According to Wenzel (1936), surface roughness can further magnify the wetting properties of the solid. If the surface is preferentially hydrophilic, it will become even more hydrophilic after the surface roughness is added.

Flow disturbance: Water wetting and corrosion attack can be found at the locally downstream of an obstacle. A sudden change in the flow geometry such as obstruction or protrusion can generate strong flow disturbance that results in flow separation accompanied by recirculation and secondary flow (Nesic & Postlethwaite, 1990). This can lead to local water entrainment at the turbulent jet zone and water wetting at the recirculation zone depending on the disturbed flow structure.

Pipe bend: As the liquids flow around a curved conduit, the centripetal acceleration and a skewed pressure distribution generated from the bend give rise to a secondary flow motion as a pair of counter-rotating *Dean* vortices (Dean, 1928). The *Dean* vortices superimposed on the primary flow can cause the liquid particles to coil transversely in circular streamlines. For highly turbulent flow, flow separation may occur on the inner wall of the curvature, causing liquid (water) to be trapped within the recirculation zone along the inner wall.

2.2.3   Operational parameters

Flow rate: The turbulence kinetic energy is directly related to the input flow rate. Both droplet breakage and coalescence processes occur in the turbulent dispersions (Tsouris & Tavlarides, 2004). At low flow rate, the level of turbulence is low, leading to water drop out (water wetting) as the droplet coalescence process and gravity become more dominant. The turbulent breaking forces increase with the flow rate, resulting in more droplet breakup and dispersed flow (oil wetting). Cai *et al.* (2012) showed that there exists a critical velocity that can fully entrain the water phase, effecting the transition from water wetting to oil wetting.

Water cut: In a system with low water cut, the turbulent breaking forces can fragment and entrain the water droplets as dispersion, leading to oil wetting. With an increase in the water cut, the likelihood for water wetting increases as the droplet coalescence process and gravity become more dominant than the droplet breakup process.

Phase inversion: If the water cut in an oil-water dispersion system is increased beyond a critical level, phase inversion occurs in which the water-in-oil (W/O) dispersion inverts to oil-in-water (O/W) dispersion. The phase inversion is a complex phenomenon which varies considerably and depends on a number of factors such as the fluid properties, phase fraction ratio, emulsion 'tightness' related to droplet size (Woelflin, 1942), droplet distribution, or energy input. Arirachakaran *et al*. (1989) reported that the effective viscosity and pressure loss in oil-water dispersion showed an abrupt peak close to the phase inversion point. The magnitude of the peak was higher in low viscosity oils than those of high viscosity oils.

Flow patterns: The oil-water distribution differs from one flow pattern to another. In oil-water pipelines, the flow patterns are mostly either separated or dispersed, corresponding to the pipe wall being water wet or oil wet. A special case of core-annular flow can occur in oil-water flow under certain conditions. By having high viscosity and low density differences between oil and water phases, the viscous oil may form the core phase, surrounded by the low viscosity water as the annular film (Charles *et al.*, 1961). In three-phase flow pipelines, the annular flow displaces the liquid phase close to the wall, increasing the likelihood for water contacting the wall.

Upstream shear rate history: The droplet size distribution in the downstream is influenced by the upstream shear rate history (Pots *et al*., 2006). If the oil-water mixture is forced to flow through a constricted area such as a choke valve, the fluids accelerate and the turbulent intensity rises. The pressure drop across the choke can be very large; thus the droplets can break up in the turbulent jet zone resulting in a dispersion flow in the downstream (van der Zande *et al*., 1999).

Wetting history: According to the results by Tang (2010), pre-wetting the steel surface with crude oil can significantly alter the water-in-oil contact angle by rendering the surface more hydrophobic. Valle (2000b) found that the propensity for water wetting increased if the steel was water wetted initially, and *vice versa*. It appeared that the initial wetting history of the steel pipe dictated the subsequent wetting behavior, recognized as the wetting hysteresis. Among the possible causes for wetting hysteresis are the surface roughness and the chemical heterogeneity of the solid surface (Shanahan, 1995).

2.2.4   Surfactants and additives

Crude oil components: Adsorption of crude oil components can alter the surface wettability. Because of the complexity of the crude components, there could be multiple interacting mechanisms that contribute to the alteration of surface wettability (Buckley *et al*., 1998). Asphaltenes are a heavy polar fraction of crude oils that show strong surface activity. As an aggregated state in crudes, they accumulate at the interfacial films surrounding the water droplets and stabilize the emulsions (McLean & Kilpatrick, 1997). If precipitated from the crude oil, asphaltenes form a protective barrier on the pipe wall. Ajmera *et al*. (2010) found that the precipitated asphaltenes provided corrosion inhibition and altered the wettability of the steel surface. Waxes are the high molecular-weight paraffin (C20+) that typically precipitate when the crude oil is cooled below its wax appearance temperature. However, Yang *et al*. (2012) found that the wax film was not as protective and can be removed by shear, resulting in localized attack on the steel surface.

Surfactants: The addition of surfactants can influence emulsion behavior as they impede the coalescence of the dispersed phase and stabilize the emulsion. Surfactants are molecules with dual characteristics. Part of the molecule is a long hydrocarbon chain which is hydrophobic. The

other molecular part is a generally charged head which is hydrophilic, as shown in Figure 2-12. As a result, surfactants exhibit dual affinity for both polar phase (water) and non-polar phase (oil), this leads to preferential adsorption at the interface. The addition of surfactants causes the surface tension to fall until the critical micelle concentration (CMC) is reached, above which there is no further reduction in surface tension (Rosen, 2004). Li (2009) reported that an addition of 20 ppm "quat" corrosion inhibitor was able to decrease the oil-water interfacial tension and alter the wettability of steel surface from hydrophilic to hydrophobic. It made the water entrainment by the oil easier at a lower velocity.

non-polar tail
(hydrophobic)

polar head
(hydrophilic)
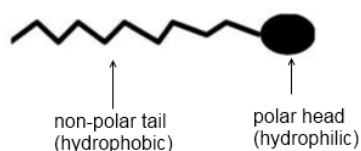
Figure 2-12: Schematic surfactant molecule.

2.3 Droplet breakup and water wetting mechanisms

Liquid-liquid dispersion flow occurs if one of the phases is dispersed in the form of droplets entrained within the bulk continuous flow. The dispersed phase exists as a population of drops that is continuously created and destroyed by the droplet breakage and coalescence processes under turbulent flow. The distribution of the droplet size can influence the hydrodynamic characteristics and wetting behavior of the system. There are several factors that affect the simultaneous occurrence of breakup/coalescence processes. Generally, the droplet breakage process generally prevails at regions of high turbulent energy dissipation rate, while the coalescence process dominates at regions of low turbulent energy dissipation rate (Tsouris & Tavlarides, 2004).

In general, there are four main categories of droplet breakup mechanisms. The breakup can be due to: (a) turbulent fluctuation and collision, (b) high viscous shear stress, (c) shearing-off process, and (d) interfacial instability. Readers can refer to an extensive review article by Liao & Lucas (2009) describing all these mechanisms. In this work, the focus is on the fluid droplet breakup mechanism caused by the turbulent fluctuation as it is more applicable for turbulent dispersion having low viscosity water as the dispersed phase in turbulent pipe flow.

2.3.1   Droplet breakup mechanism

The fundamental theoretical analysis on the droplet breakup model in turbulent flow was carried out independently by Kolmogorov (1949) and Hinze (1955). They postulated that the breakup of a droplet in a flowing stream is a result of interactions with the dynamic pressure forces, viscous forces and surface tensions. By assuming a homogeneous and isotropic turbulent flow field, the dynamic pressure forces exerted by the turbulent eddies control the maximum stable droplet size. As shown schematically in Figure 2-13, the turbulent eddies bombard the droplet surface causing oscillations until they overcome the surface tension force. Only the surrounding eddies with length scales of similar order to the droplet size will have sufficient breaking force to act against the droplet surface tension force under the fluctuations in the hydrodynamic pressure. Under such conditions, the energy spectrum of Kolmogorov's turbulence theory can be applied to estimate the strength of turbulent eddies having a length scale equal to a droplet diameter in the inertial subrange (Kolmogorov 1949).
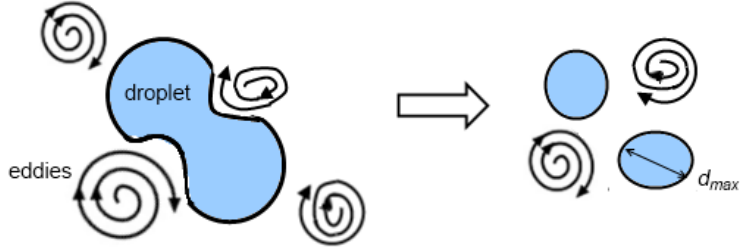
Figure 2-13: Schematic of large droplet being broken up by the turbulent eddies.

Hinze (1955) pointed out that the viscous force within the droplet can be neglected if the dispersed phase viscosity is sufficiently small. He postulated that the droplet breakup occurs when a critical Weber number is exceeded. A Weber number is a dimensionless parameter that is governed by the surface tension σ and dynamic pressure forces from the fluid inertia, defined as:

$$We_{crit} = \frac{\rho_c u'^2 d_{max}}{\sigma} \tag{2.2}$$

where ρ_c is the density of the continuous phase, d_{max} is the maximal droplet diameter, u' is the mean value of the fluctuation velocity across the droplet between a characteristic length equal to d_{max}. For an isotropic and homogenous turbulent flow, u' can be related to d_{max} and the mean rate of energy dissipation $\bar{e}$ is given as:

$$u'^2 = 2(\bar{e}\, d_{max})^{2/3} \tag{2.3}$$

For flow in a circular pipe with diameter D, $\bar{e}$ is the mean rate of energy dissipation (unit: m^2/s^3), related to the frictional pressure gradient and continuous phase velocity U_c as follows:

$$\bar{e} = \left|\frac{dP}{dl}\right|_{fric} \frac{U_c}{\rho_c} = \frac{2U_c^3 f_c}{D} \tag{2.4}$$

where subscript 'c' denotes the continuous phase, f is the Fanning friction factor calculated from the Blasius-type equation as follows:

$$f_c = C \operatorname{Re}_c^{-n} \qquad \begin{cases} C = 16, \ n = 1 & \text{Laminar flow} \\ C = 0.046, \ n = 0.2 & \text{Turbulent flow} \end{cases} \tag{2.5}$$

and the Reynolds number of the continuous layer is given as $\operatorname{Re}_c = \rho_c U_c D / \mu_c$.

By fitting Clay's (1940) experimental dispersed droplet size data to his model, Hinze estimated the critical Weber number for droplet breakup as $We_{crit} = 1.18$. By using Eq. (2.2) to (2.4), Hinze formulated Eq. (2.6) as the criterion for determining the maximal stable droplet diameter d_{max} that can be sustained before breakup:

$$d_{max} = 0.725 \left(\frac{\sigma}{\rho_c} \right)^{0.6} \left(\frac{2 f U_c^3}{D} \right)^{-0.4} \tag{2.6}$$

The above equation is valid for interaction of a single droplet with the surrounding continuous phase, hence dilute dispersion. Furthermore, the largest droplet size is assumed to be in the inertial subrange length scale between the Kolmogorov micro scale L_k and the length scale of energy containing eddies in a pipe diameter D, yielding the following relation:

$$L_k = \left(\frac{v_c^3}{\varepsilon} \right)^{0.25} \leq d_{max} \leq 0.1D \tag{2.7}$$

where is v_c the kinematic viscosity of the continuous phase.

Sleicher (1962) argued that most droplet breakup took place close to the wall where the turbulence was least isotropic and homogenous. Based on dimensional nalysis, he proposed a maximum droplet size model that relates the influencing variables in Eq. (2.8). The model includes a viscosity group that accounts for the effect of high dispersed phase viscosity.

$$\left(\frac{d_{max} \rho_c U_c^2}{\sigma} \right) \left(\frac{\mu_c U_c}{\sigma} \right)^{0.5} = 38 \left(1 + 0.7 \left(\frac{\mu_d U_c}{\sigma} \right)^{0.7} \right) \tag{2.8}$$

where μ_c and μ_d are the dynamic viscosity for the continuous and dispersed phase, respectively. The effect of pipe diameter on droplet size was not considered in the model. Subsequent work by

Paul & Sleicher (1965) found that the maximum droplet size was slightly influenced by the pipe diameter.

For the case of a droplet size larger than the length scale of energy containing eddies (d_{max}>0.1D) in turbulent pipe flow, Kubie & Gardner (1977) equated the mean velocity fluctuations u' in Eq.(2.3) to be $u' = 1.3u*$, where $u*$ is the friction velocity:

$$u* = \sqrt{\frac{\tau}{\rho_c}} = U_c \sqrt{\frac{f}{2}} \qquad (2.9)$$

Using the relations in Eq.(2.2) and Eq.(2.9), they derived the following correlation for predicting the maximal droplet size larger than the length scale of energy containing eddies (d_{max} >0.1D):

$$d_{max} = 1.385 \frac{\sigma}{f\rho_c U_c^2} \qquad \text{for } d_{max} > 0.1D \qquad (2.10)$$

Hesketh et al. (1987) incorporated the Weber number derived by Levich (1962) in Hinze's model and modified the criterion for maximal stable droplet size as:

$$d_{max} = \left(\frac{We'_{crit}}{2}\right)^{0.6} \left(\frac{\sigma^{0.6}}{\rho_c^{0.4}\rho_d^{0.2}}\right) \left(\frac{2fU_c^3}{D}\right)^{-0.4} \qquad (2.11)$$

where We'_{crit} is the modified critical Weber number that includes the dependence of density of dispersed phase on the bubble size, yielding We'_{crit} as:

$$We'_{crit} = \frac{\rho_c u'^2}{\sigma / d_{max}} \left(\frac{\rho_d}{\rho_c}\right)^{1/3} \qquad (2.12)$$

Brauner (2001) extended Hinze equation to predict the maximum stable droplet/bubble size for dense dispersion system. Under such condition, the droplet coalescence process and the interaction of densely populated droplets become important, leading to an increase in droplet size.

The model is based on the energy balance (in power term) between the turbulent kinetic energy and the surface tension energy, as follows:

$$\frac{\rho_c u'^2}{2} Q_c = C_H \frac{6\sigma}{d_{max}} Q_d \qquad (2.13)$$

where Q is the volumetric flow rate for respective phases and C_H is a tunable constants, set as 1. The final expression of the maximum stable droplet diameter d_{max} is derived as:

$$d_{max} = 2.22 C_H^{0.6} \left(\frac{\rho_c}{\sigma}\right)^{-0.6} \left(\frac{1-\varepsilon_d}{\varepsilon_d}\right)^{-0.6} \left(\frac{fU_c^3}{D}\right)^{-0.4} \left[\frac{\rho_m}{\rho_c(1-\varepsilon_d)}\right]^{-0.4} \qquad (2.14)$$

2.3.2 Droplet size distribution

The analysis of droplet size distribution is an essential step in characterizing the droplet or bubble dispersion system. The droplet size measurement techniques can be broadly based on two principles: photographic technique and probe technique. The photographic/video recording technique is a direct non-intrusive measurement method by observing the dispersion through a transparent pipe wall. The limitations of the technique include the use of only non-opaque liquids, the illumination of the dispersion, and the likelihood of capturing only dispersion close to the transparent wall. On the other hand, the probe method is an intrusive method utilizing various measurement principles such as an optical probe (Simmons & Azzopardi, 2001; Boxall *et al.*, 2010), conductivity mesh (Lucas *et al.*, 2001) and dual impedance probe (Zenit *et al.*, 2001). The probe measures locally and can be placed around the test vessel for sampling purposes.

Only limited experimental work had been done on droplet size distribution generated by a flowing stream in pipe flow. Early work was performed by Karabelas (1978), who systematically measured the water droplet size formed in oil-water pipe flow using photographic and droplet encapsulation techniques. He concluded that Hinze's model was generally in agreement with his

droplet size data. The measured droplet size spectra were found to adequately fit to the upper limit log-normal and Rosin-Rammler distribution functions. Hesketh *et al*., (1987) examined the Sauter mean diameter d_{32} and maximum droplet diameter d_{99} for gas-liquid dispersion systems. He fitted the droplet size distribution to Log-normal function and found the maximal droplet size d_{max} correlated closely with the estimated d_{99} values. Angeli & Hewitt, (2000a) conducted horizontal oil-water flow loop experiments to study the droplet size distribution. They reported that the Log-normal and Rosin-Ramler distribution functions were adequate to represent their droplet size distribution. Vielma *et al.*, (2008) analyzed the droplet size data for various dispersion scenarios in oil-water pipe flow. They demonstrated that the Log-normal distribution was the best fitted probabilistic function for the droplet size spectra.

The droplet size data of dispersion system can be described by Log-normal distribution. The probability density function $f(x)$ is given as (Hesketh *et al.*,1987):

$$f(x) = \frac{1}{x\sigma\sqrt{2\pi}} \exp\left[-\frac{(\ln x - \mu)^2}{2\sigma^2} \right]$$
(2.15)

where μ and σ are the distribution parameters obtained from the geometric mean of ln x and standard deviation of ln x, respectively.

The Sauter mean diameter (SMD) or d_{32} refers to the surface area mean diameter, which is often used to characterize the droplet size distribution. SMD is given as:

$$SMD = \sum_{i=1}^{N} d_i^3 \left/ \sum_{i=1}^{N} d_i^2 \right.$$
(2.16)

where N is the number of droplets and d_i is the diameter of the ith droplet in the distribution.

The maximal stable droplet/bubble size d_{max} is the largest stable droplet/bubble that can exist in a given turbulent flow field according to Hinze droplet breakup model (Hinze, 1955). In a droplet size distribution spectrum, the statistical parameter d_{95} which is the 95 percentile size of

the droplet distribution, representing the maximal droplet size, can be statistically estimated from the cumulative size probabilistic distribution (Karabelas, 1978).

2.3.3 Forces analysis for droplet in dispersion

There are various potential forces that can contribute to the motion of dispersed droplets in a flowing stream. The text books by Clift *et al.* (2005) and Crowe *et al.* (1997) provide further details on the subject. Some of the relevant forces are briefly described below:

- *Viscous drag* arises from the viscous resistance exerted by the surrounding fluid on the individual droplet/particle. The force acts opposite to the relative motion of the droplet and tends to guide it along the streamlines. The force can be expressed as:

$$F_D = \frac{C_D}{2} \rho_c U_{drop}^2 \left(\frac{\pi d_{drop}^2}{4} \right) \tag{2.17}$$

where C_D is the drag coefficient, ρ_c is the continuous phase density, d_{drop} is the droplet diameter, U_{drop} is the droplet velocity. Subscript 'c' denotes the continuous phase.

- *Body forces* arises from the gravity or buoyancy acting on the displaced mass, expressed as:

$$F_B = \frac{\pi}{6} d_{drop}^3 \Delta \rho g \tag{2.18}$$

- *Virtual mass force* arises from the positive acceleration of a droplet that requires the acceleration of the fluid surrounding the droplet (Clift *et al.*, 2005). It is assumed to be the product of acceleration and half of the displaced mass. It is also called as *added mass force*.

$$F_V = \frac{1}{2} \frac{\pi \rho_{drop} d_{drop}^3}{6} \frac{dU_{drop}}{d\tau} \tag{2.19}$$

- *Saffman lift force* arises due to the non-uniform velocity profile around a droplet particle that is near to the wall as the extra drag exerted by the wall causes the droplet to lag behind

(Saffman, 1965). Because of the velocity difference, the flow past a droplet results in a pressure difference on different transverse sides that will cause the droplet to lift sideways to lower pressure in regions perpendicular to the flow direction. The expression for Saffman force has the form (Varaksin, 2007):

$$F_S = 1.61 \rho_{drop} d_{drop}^2 \gamma^{1/2} \left(\frac{\mu_c}{\rho_c} \right)^{1/2} \left(U_c - U_{drop} \right)$$

(2.20)

where γ is the shear rate and μ_c is the dynamic viscosity of the continuous phase

- *Turbophoresis force* can be found in annular flow in which the motion of entrained fluid droplets in a turbulent gas stream tend to show a transverse shift from high in the pipe core to low turbulent intensity of fluctuation in the wall region, leading to enhanced deposition of fluids in the pipe annulus. The turbophoresis force can be expressed as (Varaksin, 2007):

$$F_T = \frac{1}{2} \frac{\pi \rho_{drop} d_{drop}^3}{6} \left(\frac{\partial \overline{u}_r'^2}{\partial r} \right)$$

(2.21)

- *Lubrication force* is experienced when a particle/droplet approaches close to the wall due to the viscous dampening as it squeezes the film out between the droplet and the wall (Vigolo *et al*., 2013).

2.3.4   Water wetting modeling

Crude oil by itself is typically not corrosive and can serve as a natural barrier for water from accessing the steel wall. If the oil stream carrying traces of water is sufficiently turbulent, the water phase can be dispersed in the form of droplets entrained within the flowing oil, leading to dispersion flow and oil wetting. However if the dispersion is destabilized, water droplets starts to settle and accumulates onto the pipe wall, leading to water wetting and internal corrosion. Hence, it is of great interest for the oil and gas producers to manage the corrosion threats by preventing

the occurrence of water wetting. The issue becomes more complex if the pipelines carry concurrent flow of gas, oil and water. A variety of multiphase flow patterns can take place and these flow patterns will influence the wetting preference on the pipe surface in different ways (Vera & Hernandez, 2006). The available literature indicates limited quantitative research has been done on the subject of water separation and entrainment, particularly on the mechanism of water wetting. Some of the pertinent work is described below:

2.3.4.1 Wicks and Fraser model

Wicks & Fraser (1975) proposed the first functional model to predict water wetting. In the model, they assumed that water droplets behave like solid particles, and the sand transport correlation was derived from the experimental data using sand in various liquids. The model calculates the minimum oil velocity required to sweep out the settled water. Their model calculations involved the use of graphs and dimensionless parameters that are restricted within the calibrated experimental data range.

2.3.4.2 de Waard model

de Waard & Lotz (1993) presented a simplistic empirical multiplier F_{oil} as the wetting factor multiplier used in the corrosion analysis. The on/off wetting multiplier solely relied on the threshold of water cut WC and the liquid velocity U as follows:

$$\begin{aligned} F_{oil} &= 1 & WC \geq 30\% \text{ or } U \leq 1 \text{ m/s} \\ F_{oil} &= 0 & WC < 30\% \text{ and } U > 1 \text{ m/s} \end{aligned} \tag{2.22}$$

As a rule of thumb, the model simply called for a minimal liquid velocity of 1 m/s and water cut of 30% for operation under oil wetting condition. It is noted that the model was based on empirical criteria that neglects other contributing factors of crude oil properties and hydrodynamics characteristics.

de Waard *et al.* (2003) later revisited and updated the original empirical model by proposing an equation based on the relationship between the °API gravity and the emulsion stability breakpoint.

$$WC_{break} = -0.0166°API + 0.83 \qquad 50 > °API > 20 \tag{2.23}$$

In this model, W_{break} changes inversely with crude oil density (low°API has high density). W_{break} refers to the critical water cut that can be entrained by the oil before the emulsion stability is disrupted and separated into individual phases. The emulsion stability breakpoint is linked to the API gravity. The semi-mechanistic model was a leap forward from the original model but still lacked other pertinent parameters such as pipe diameter and inclination that can contribute to the likelihood of water wetting.

2.3.4.3 Diffusion-convection model

As the density difference between the oil and water phase is relatively small, it creates a scenario where the flux of settling droplets due to gravity is balanced by the upward flux due to the turbulent diffusion. Hence, several researchers proposed the use of a diffusion-convection model for liquid-liquid dispersion flow. Karabelas (1977) developed a closed-form diffusion-convection model for predicting the droplet concentration distribution in pipe flow. His approach inspired Segev (1984), Mols & Oliemans (1998), Valle (2000a), Pots *et al*. (2006), and Amundsen (2011) to further expand and improve the model using more advanced formulations..

The model presented here was based on the work of Karabelas (1977) and Segev (1984). The distribution of water droplets across a pipe section was developed using the diffusion-convection equation. For a full developed steady-state flow in a turbulent flow field, the flux *j* of

the dispersed droplets, is described by the diffusive transport (a function of concentration gradient dC/dz) and the convective transport (product of concentration and velocity) as:

$$j = -\Gamma \frac{dC}{dz} + U_s C \qquad (2.24)$$

where U_s the terminal settling velocity, and Γ the droplet eddy diffusivity (unit: m²/s). From empirical data, they modeled Γ as:

$$\Gamma = 0.128 DU \sqrt{f/2} \qquad (2.25)$$

where D is the pipe diameter, U the liquid velocity, f the Fanning friction factor.

The terminal settling velocity U_s for the droplet can be estimated from Stokes' law:

$$U_S = g d_p^2 \Delta\rho / 18\mu \qquad (2.26)$$

where d_p is the maximal droplet diameter calculated using Hinze's model given in Eq.(2.6).

As the flux going in and coming out of the control volume must be equal, the net flux across the vertical transverse plane is set as zero. Eq. (2.24) becomes a one-dimensional parabolic partial differential equation that can be solved for the droplet concentration profile C as:

$$C(r,\theta) = C_{avg} exp\left(-\alpha cos\theta \frac{r}{0.5D}\right) \qquad (2.27)$$

where $r,\ \theta$ are polar coordinates, C_{avg} the average *in situ* water concentration, α is a dimensionless parameter given as $\alpha = DU_s / 2\Gamma$.

Pots *et al*. (2006) used a power law function to best-fit the droplet concentration profile in Eq.(2.27) to solve for the water concentration at the pipe bottom as:

$$C_{bottom} = C_{avg}(1 + a\alpha)^b \qquad (2.28)$$

where the constants *a* and *b* are empirically calibrated as *a* = 1.5, *b* = 1.3. They proposed a critical water concentration value of C_{bottom} = 0.6, below which water wetting is anticipated to take place. The critical velocity for water entrainment can be iteratively calculated.

2.3.4.4 Water wetting model

Cai *et al*. (2004, 2012) formulated a mechanistic model to predict the critical entrainment velocity required to disperse the water phase on the basis of the liquid-liquid flow pattern transition work by Brauner (2001). The premise of the model was that the turbulent kinetic energy from the oil phase was solely expended to act against the oil-water surface energy and fragment the water phase into discrete droplets. If all the free water was entrained by the flowing oil, then water will be kept off from the wall leading to oil wetting behavior. Originating from the theoretical droplet breakup mechanism, the water wetting model considers a number of parameters which include the physical properties of the fluids, pipe diameter, pipe inclination, superficial velocities and water cut.

Based on the framework of Cai model, Tang (2010) developed a water wetting that included the effect of surface wettability (change in contact angle). He argued that additional interactions between the water-steel and oil-steel surfaces in the presence of surface active compounds from the crude oils can influence the droplet breakup process and the water entrainment by the flowing oil. The new model accounted for the extra turbulent kinetic energy required to create news surfaces resulting from the solid/fluid surface interactions. He calibrated and compared the model with laboratory data using different types of crude oils.

The detailed formulations for both water wetting models will be presented in Chapter 7.

CHAPTER 3: EXPERIMENTAL SETUP

In this chapter, the experimental details and the measurement techniques employed in this work will be discussed. The overall experimental work can be divided into small scale laboratory tests and large scale flow loop experiments.

3.1 Small scale laboratory tests

The small scale laboratory tests were mainly performed to measure fluid properties using the equipment available in the laboratory, namely:

- Falling ball viscometer, for viscosity measurement.

- DuNuoy ring tensiometer, for surface/interfacial tension measurement.

3.1.1 Falling ball viscometer

Viscosity is a measure of a fluid's internal friction when the relative movement of fluid layers takes place. A falling ball viscometer (make Haake GmbH), as shown in Figure 3-1, is used in this work to measure dynamic viscosity, μ, in mPa·s or equivalently cP. The principle is based on Stokes' law for the case of a solid sphere falling under gravity in a vertical vessel filled with a viscous fluid. The test procedure is performed as per ASTM D445 standard (2006). The technique involves dropping a sphere into a glass vessel filled with the test liquid, recording the time t required for the sphere to pass through a known distance (s = 100 mm) between two specified markers in the vessel. Once the downward gravity force is balanced by the opposite viscous drag, the ball falls through the liquid at a terminal velocity V_T which can be calculated if the time and distance of the fall are known ($V_T = s/t$). The force balance leads to the following expression:

$$\frac{\pi}{6} d_{ball}^3 \Delta \rho g = 3\pi \mu d_{ball} V_T \quad \text{or} \quad \mu = \frac{d_{ball}^3}{18} \frac{\Delta \rho g}{V_T} \tag{3.1}$$

where d is the diameter of the ball and $\Delta \rho$ is the density difference between the ball and test fluid. The measured dynamic viscosity μ is given as follows:

$$\mu = t \Delta \rho K \tag{3.2}$$

where t is the ball's falling time, and K is a constant depending on the ball's size and marked distance.

For the case of a viscous and incompressible fluid flowing around a falling sphere, Stokes' law is applicable providing that the flow is laminar with low Reynolds Numbers. However, this rheological technique is unsuitable for non-Newtonian liquids in which the viscosity is dependent on the shear rate. For elevated temperature conditions, the jacket enveloping the glass tube can be surrounded with a water-filled jacket bath to maintain the test liquid at the desired temperature.
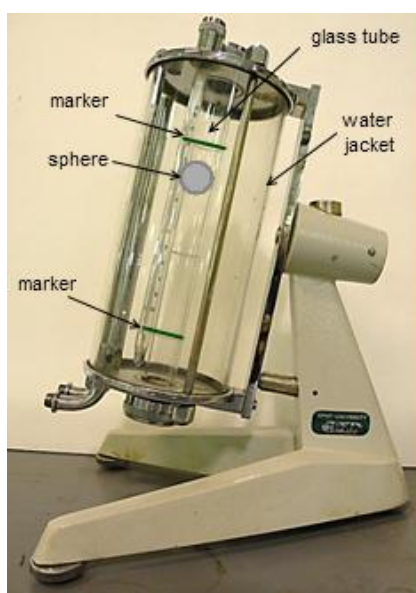
Figure 3-1: Falling-ball viscometer (Haake GmbH).

3.1.2   DuNouy tensiometer

Surface tension and interfacial tension can be measured by a ring method using a DuNouy Tensiometer (make CSC Scientific Co. Inc.) as shown in Figure 3-2. The test procedure is performed as per ASTM D971 standard (1999). The technique involves slowly lifting a ring out of a test liquid and measuring the pull force required to rupture the liquid film from the liquid interface. The interface acts as an energy barrier preventing one liquid from being mixed into the other. If the interface is between the air and liquid, the surface tension is measured. If the interface is between two immiscible fluids such as oil and water, then the interfacial tension is measured. As shown in Figure 3-3, a platinum-iridium ring is immersed in the test fluid and slowly drawn upward through the liquid interface until the liquid film formed in the ring undergoes rupture. At the film breaking point, the tensiometer measures the surface or interfacial tension expressed in units of dyne per centimeter (dyne/cm), or equivalently milliNewtons per meter (mN/m). The surface tension σ is given by the following equation:

$$\sigma = \beta \frac{F}{4\pi R} \tag{3.3}$$

where F = apparent pull force (N), R = ring radius (cm). A correction factor, β, is considered to take account of the extra volume effect and shape of the liquid hanging from the ring at the film rupture point. By following the correlation proposed by Zuidema & Waters (1941), the correction factor β for interfacial tension can be simplified as:

$$\beta = 0.725 + \sqrt{\frac{1.452P}{C^2(\rho_D - \rho_d)} + 0.04534 - \frac{1.679}{R/r}} \tag{3.4}$$

where C is ring circumference (= $2\pi R$), R/r is the ratio of ring radius to wire radius, ρ_D is density of the heavier phase, ρ_d is the density of lighter phase.

Figure 3-2: DuNouy ring tensiometer.
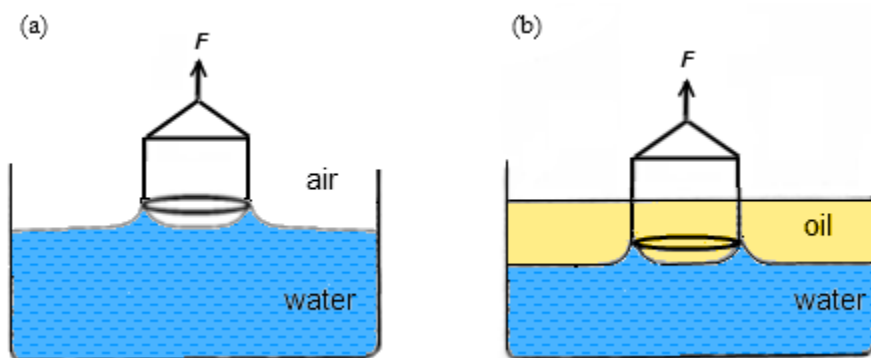
Figure 3-3: Schematics of DuNouy ring method for measuring (a) surface tension, (b) interfacial tension.

3.1.3 Working fluids

The working fluids used in flow loop experiments were LVT200 as the oil phase, 1 wt.% NaCl aqueous solution as the water phase and CO_2 as the gas phase. The LVT200 (manufacturer: Calumet Penreco) is a hydrotreated light paraffinic oil (C9-C16) with 40 °API at 60 °F. The oil is

typically used as an intermediate ingredient, solvent or lubricant in the chemical industries. It has a clear light yellowish color. It forms an unstable dispersion with water that quickly separates at rest. The water phase was prepared by adding reagent grade sodium chloride (NaCl) salt in deionized water. The properties of the fluids are listed in Table 3-1.

Table 3-1: Properties of test fluids used in the flow loop experiments

Liquid phase	Value @ 25 °C
Oil Phase	LVT200
Density (kg/m^3)	823
Dynamic viscosity (cP)	2.7
Surface tension (mN/m)	28.5
Oil-water interfacial tension (mN/m)	40.5
Water-in-oil contact angle	73
Water phase	1wt.% NaCl (aq)
Density (kg/m^3)	1000
Dynamic viscosity (cP)	1
Surface tension (mN/m)	72.2
Conductivity (mS/cm)	18.5
Gas phase	CO_2
Density (kg/m^3)	1.8
Dynamic viscosity (cP)	0.015

3.2 Large-scale multiphase flow loop

The flow experiments were conducted in an inclinable large-scale multiphase flow loop system that can be used to study two-phase oil-water and three-phase gas-oil-water flow environments. The schematic layout for oil-water system and gas-oil-water system are shown in Figure 3-4 and Figure 3-5, respectively. The system consists of the following main components:

- Main multiphase flow line and test sections
- Multiphase separation facilities
- Liquid storage and pumping facilities

3.2.1   Main line and test sections

The main part of the multiphase flow loop consists of a 30 m long line, with an internal diameter (ID) of 0.1 m (4 inch), on a rig structure made of rectangular steel columns of a 40 cm × 76 cm cross-section. This section of the flow line is fully inclinable from 0° (horizontal) to a 90° (vertical) position driven by a pair of high pressure, variable piston displacement hydraulic systems. The oil flow is fed directly into the main line while the water is pumped from the water storage tank through a 2-inch ID PVC pipe and connected to the main line *via* a tee-section. The gas stream is circulated by a gas blower and connected into the main line *via* a 45-degree elbow. The mixing of the fluid streams is carried out in the upstream section, as shown in Figure 3-6. The mixture flows through a 3.6 m long flexible hose, which allows for further mixing and rig inclination, before entering the first upstream leg of the main line. The main line (Figure 3-7) consists of two parallel legs with an approximate length of 13 m each, connected by a 180-degree bend. The mainline is made up of PVC material except for the test sections. Figure 3-8 shows the flow loop in vertical orientation, which has approximate height of 15 m.

In the upstream leg of the flow loop, three test sections: tomography test section, conductivity pins test section and visualization section are installed for flow experiment measurements as detailed in Table 3-2. The schematics in Figure 3-9 show the upstream leg of the flow loop consisting of a tomogaphy test section, a conductivity pins test section and a visualization section, located approximately at $L = 7.5$ m ($L/D = 75$), 11.5 m ($L/D = 115$), and 12.5 m ($L/D = 125$) from the entrance nozzle, respectively. A photo of the test sections is shown in Figure 3-10. The tomography test section is mounted with a test spool fitted with electrical capacitance tomography (ECT) and electrical resistance tomography (ERT) equipment, used for cross-sectional imaging of the flowing fluid media. The conductivity pins section is installed with a circular array of custom-made pin electrodes on the interior pipe wall, used for surface wetting

measurement. The visualization section is made of a transparent PVC pipe, used for viewing the flow patterns.

Subsequently, the fluids flow through a 180-degree bend, into the second leg of the main line. The second leg has a 1.8 m long transparent pipe for flow visualization located 9.5 m downstream from the U-bend. The mixture fluids exit the main line through a 3.6 m long flexible pipe before returning to the separation station in order to be separated out into individual phases.

Table 3-2: Details of test sections in the flow loop

Test Section	Material	Distance from entrance nozzle over diameter *(L/D)*	Measurement
Tomography	stainless steel	75	Cross-sectional imaging
Conductivity pins	carbon steel	115	Surface wetting
Visualization	transparent PVC	125	Flow patterns
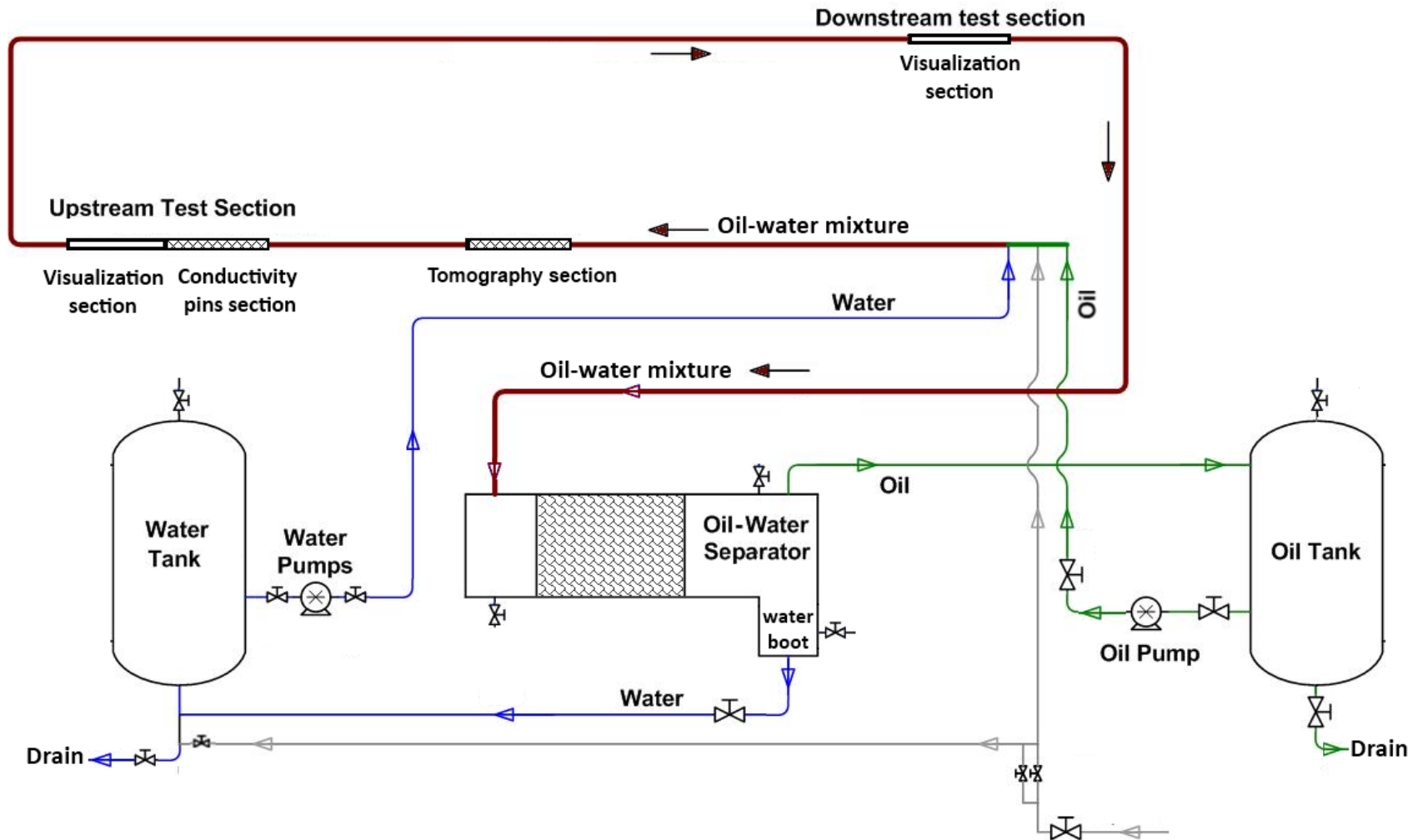
Figure 3-4: Schematics of large-scale flow loop used in oil-water flow experiments.
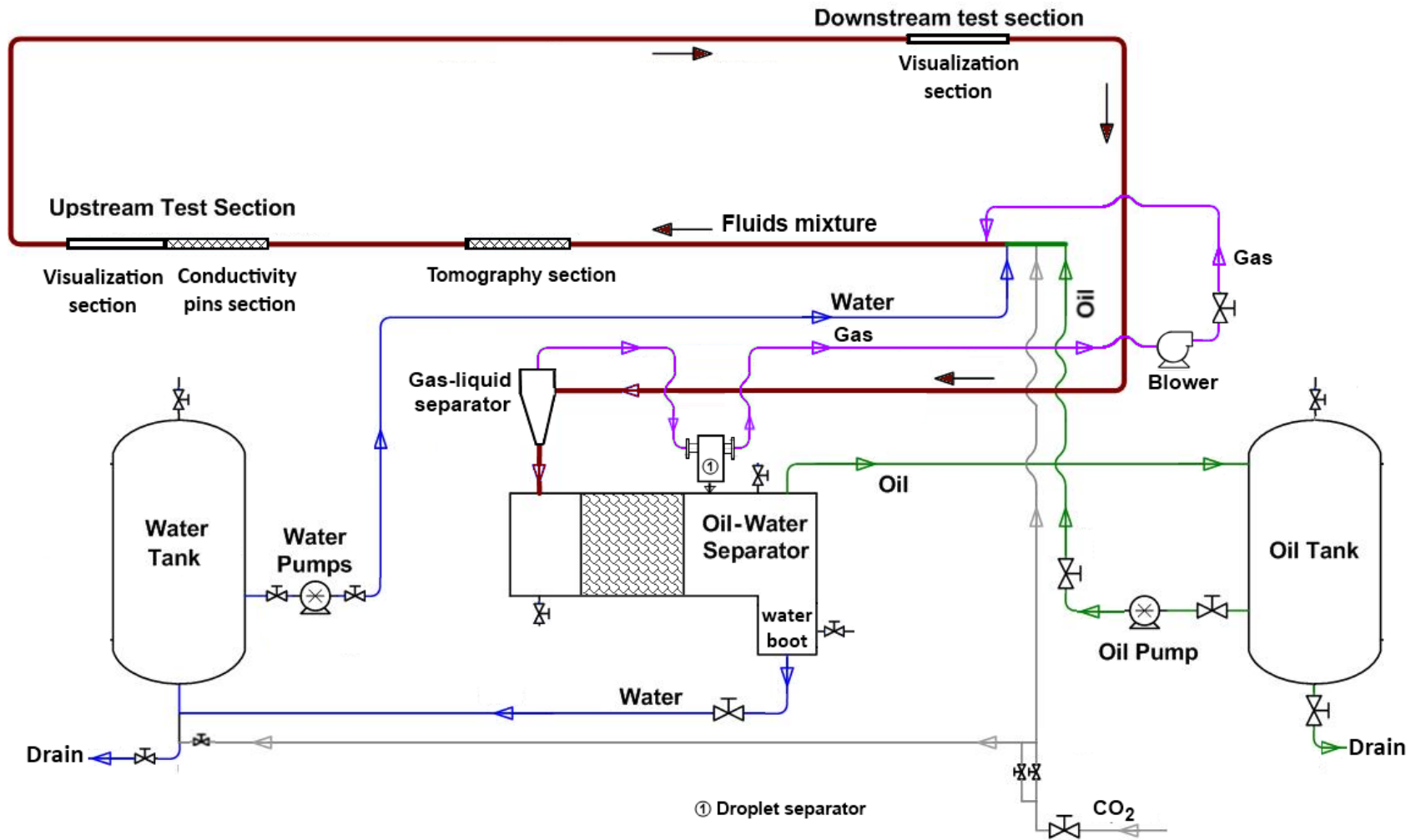
Figure 3-5: Schematics of large-scale flow loop used in gas-oil-water flow experiments.
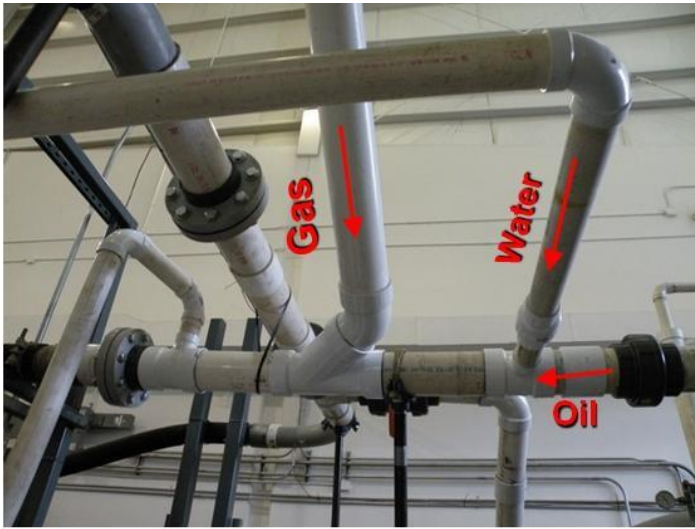
Figure 3-6: Mixing section for gas, oil and water phases at the main line entrance.
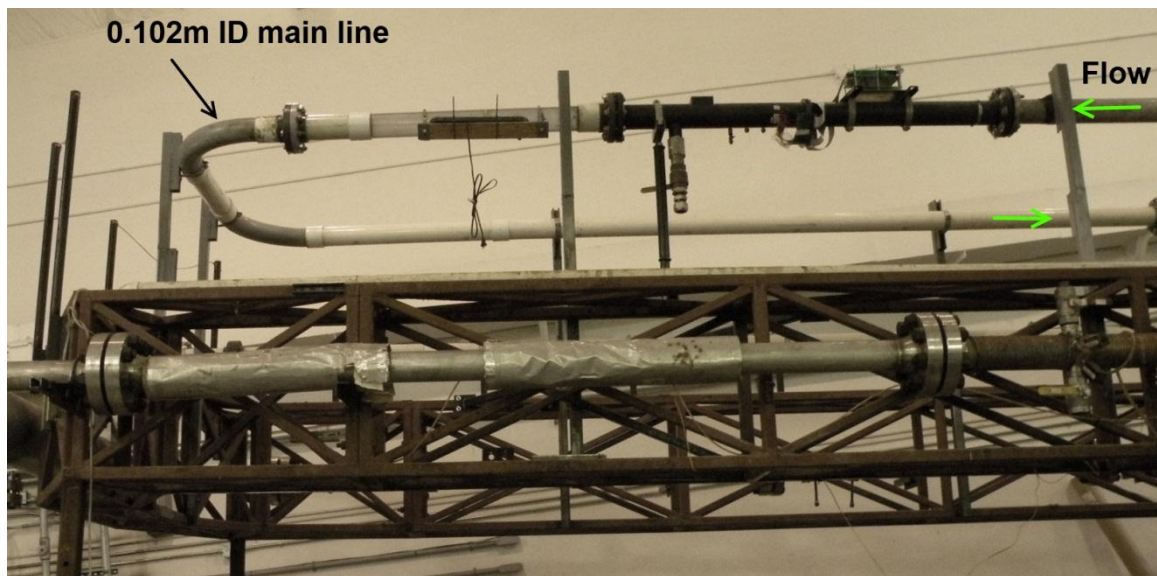
Figure 3-7: A section of main line near the U-bend, showing transparent pipe and conductivity pin section.
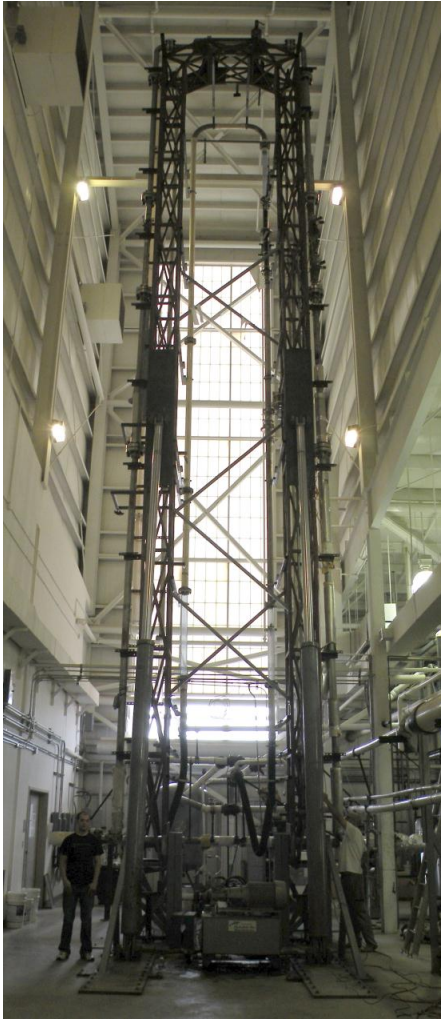
Figure 3-8: Large-scale multiphase flow loop in vertical orientation.
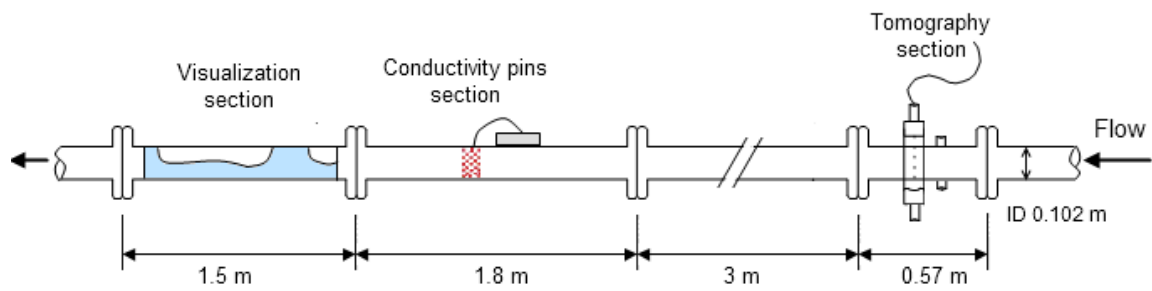
Figure 3-9: Schematics of test sections installed on the first leg of the main line.
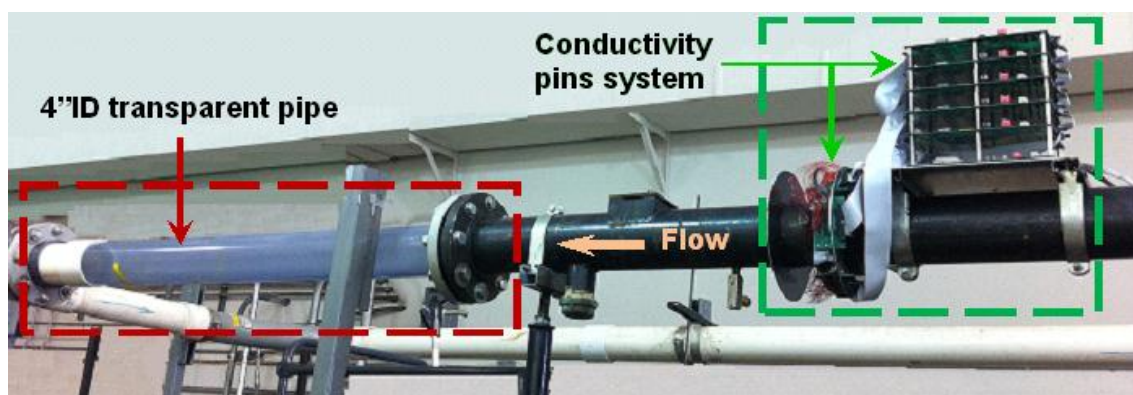
Figure 3-10: Conductivity pin section and visualization section.

3.2.2 Liquid storage and pumping facilities

Two vertical standing stainless steel vessels, each with a storage capacity of 1.2 m³ (300 gallons) hold the oil and water. Liquid is pumped into the main flow line by progressive cavity pumps, each equipped with a variable speed induction motor. The motor is controlled by a frequency control panel that allows users to regulate the flow rate. The progressive cavity pump consists of a helically shaped rotor eccentrically rotating in a nitrile rubber stator that delivers a fixed amount of liquid with each revolution regardless of the system head pressure. The quantity of fluid delivered, expressed in gallon per minute (GPM), directly depends upon the rotor's revolutions per minute (RPM). For the oil line, the pump (model 2J175, Moyno) has a rated 45 HP (horse power) motor that delivers approximately 300 GPM at every 100 RPM. For the water line, the pump (model 35651, Moyno) has a rated 1.5 HP motor that delivers approximately 1.4 GPM at every 100 RPM. A photo of the oil storage and pumping facility is shown in Figure 3-11.

The carbon dioxide (CO_2) gas stream is circulated to the main line in a closed loop by a heavy duty industrial blower (model 3200, Tuthill Pneumatics). The blower is a positive displacement type blower. It consists of a pair of three-lobe profiled rotors rotating inside an oval

shape casing that displaces a fixed volume of gas at constant speed regardless of the discharge pressure. Hence, the flow rate is dependent on the operating speed. The blower is suited for gas service requiring high volumes but low pressure, not exceeding 1 bar between the blower inlet and discharge. The gas velocity were measured using a thermal mass flow meter, Omega FMA-906-V, whose principle is based on measuring the heating or cooling effect of the gas flow on an heated element held at constant temperature. The gas velocity is given by the proportional relation of the flow dependent cooling and the power required for maintaining the heated element at constant temperature.

In this work, approximately 600 gallons of LVT200 and 350 gallons of water are used in running the flow loop experiments. The operating range is controlled within the superficial velocity of 0.25 m/s to 2.0 m/s for the oil phase, 0.005 m/s to 0.15 m/s for the water phase, and 0.5 m/s to 50 m/s for the gas phase.

Figure 3-11: Oil pump and oil storage tank.

3.2.3 Separation facility

Upon exiting the main line, the mixture fluids are directed to the separation facilities (Figure 3-11 and Figure 3-12) to separate them into individual streams. The mixture fluids first flow through a horizontal gas-liquid separator made of a 6 m long, 30 cm ID PVC pipe section connected to a 30 cm ID PVC tee-section at the end. The heavier liquids flow down from a tee pipe section into the liquid-liquid separator, while the lighter wet gas stream flows upward into a droplet separator that further removes the entrained liquid droplets before connecting back to the dry gas line leading to the gas blower.

Oil-water separator is a 2 m^3 (550 gallon) capacity horizontal liquid-liquid separator vessel, designed for the separation of oil-water emulsions using a coalescer and a series of parallel separator plates. The coalescer is fitted with a wire wool-like medium that enhances the total surface area for trapping the droplets. It holds the droplets long enough for the individual drops to merge into larger droplets. The droplets then flow through a series of plate separators made of corrugated sheets that further intercept the larger droplets and enhance the separation of the oil/water phase by buoyancy/gravity. The water, being the denser phase, settles to the bottom at the water boot and is drained back to the water storage tank by gravity for further circulation. The oil, being the lighter phase, flows up through the top outlet and back to the oil storage tank by head pressure difference. The interior and exterior wall surfaces of the separator are coated with corrosion resistant epoxy paint to prevent rusting (Figure 3-13).

Figure 3-12: Multiphase separation facility.
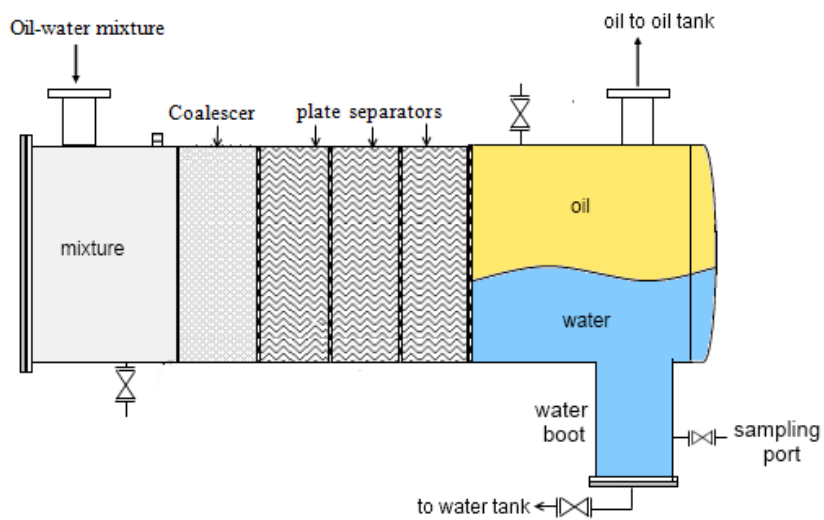
Figure 3-13: Schematics of an oil-water separator.

Droplet separator is a vertical standing inline vane-type separator is used to remove entrained droplets and mists from the wet gas stream. As shown schematically in Figure 3-14, the vessel has an inline vane configuration with the inlet and outlet ports on opposite sides but at the same elevation. The separation takes place within the internal vane bundles, which consists of parallel angled baffle plates assembling a zigzagged flow channel. When the liquid-laden wet gas passes through the vane bundle, the mixture is forced to change directions several times. The heavier liquid droplets tend to impinge on the vane wall due to their inertia and are collected as a film of liquid draining down to an internal liquid sump below the vane bundle. This feature ensures that the recovered liquids are isolated from the gas stream without further re-entrainment.
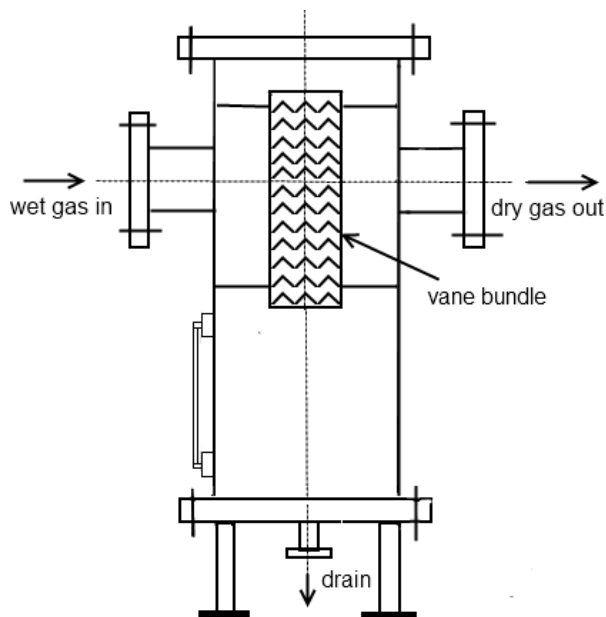
Figure 3-14: Schematics of an inline vane-type droplet separator.

3.3 Instrumentation

The instrument and the associated measurement techniques employed in the large-scale multiphase flow loop are listed as follows:

- High speed camera, for flow pattern visualization

- Conductivity pins, for surface wetting measurement

- Electrical tomography, for cross-sectional flow imaging

3.3.1   High speed video camera

The high speed video camera used in this work was a Phantom model V12.1. The video camera has a 1280 × 800 pixels CMOS sensor, capable of 6,000 frame per second (fps) at full resolution. It is set up with the following settings: framing rate of 6,000 fps and exposure duration of 90 μs to 120 μs, Nikon 50 mm lens for wide angle images and 105 mm lens for close-up images. During filming, the rather heavy unit was supported by a heavy duty Manfrotto tripod facing the vertical frontal plane of a transparent PVC pipe as depicted in Figure 3-15. Proper illumination was required to provide adequate lighting for filming the flow patterns. The light source was a Pallite VII light fixture which used eight tungsten-halogen bulbs (2.4 kW), emitting a high intensity light. The light source was positioned behind the transparent pipe such that the illumination through the pipe would be directly opposite the camera lens on the other side of pipe. A white sheet of translucent paper was placed in between the light source and the pipe to evenly diffuse the light. The overall filming operation is shown schematically in Figure 3-16.
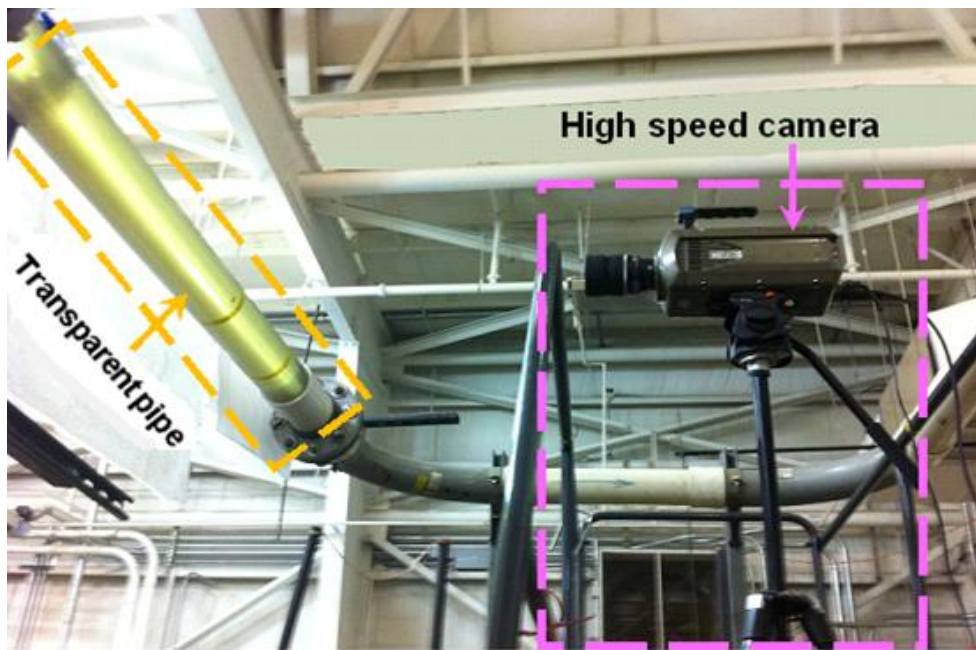
Figure 3-15: Setup of a high speed camera filming the flow pattern.
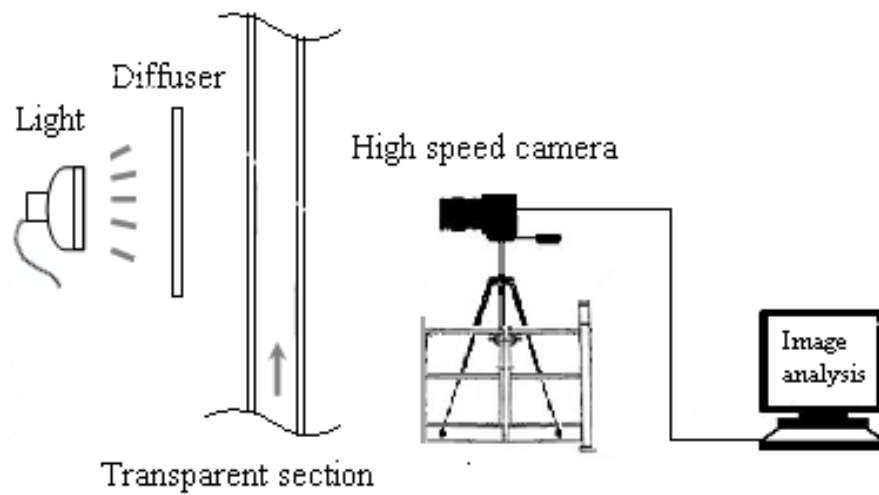
Figure 3-16: Schematic diagram of the filming operation.

3.3.2   Conductivity pins

The surface wettability is determined by use of conductivity pins which are flush mounted on the interior wall of a 0.1 m ID carbon steel test section. In this work, two types of test sections were used throughout the flow loop experimental campaign, 180° and 360° pin sections, with identical pin design and working principle. The difference is the former section comprises pins covering one half of the pipe circumference; hence it is named the 180° pin section while the latter comprises pins covering the entire pipe circumference, named the 360° pin section. It should be noted that the 180° pin section was used in the first three years of the project, before it was replaced by the 360° pins section in the latter stage of the project. The details for both test sections are explained below.

3.3.2.1 180° pin section

Figure 3-17 shows a 0.1 m ID mild steel test section flushed mounted with a total of 93 custom-made conductivity pins covering the lower half 180° of the section. The section is suited for testing two-phase oil-water in horizontal flow since the water phase, being heavier, is most likely in contact with the wall surface in the lower pipe section. In the 180° pin section, the pins were spatially arranged in a staggered row pattern, from 3 to 9 o'clock pipe position, as shown schematically in Figure 3-18(a). The pins were arranged in such fashion so as to minimize the risk of water 'snaking' around the pins (Li, 2009). The use of large number of pins is beneficial in capturing the unstable or intermitting wetting behavior while also providing for outliers. During operation, each pin emits a two-level signal that indicates either oil wet or water wet. The wetting data is then processed by an in-house conductivity pin program and collectively presented as a wetting snapshot as presented in Figure 3-18(b). The snapshot consists of array of circles that represent the exact pin arrangement from 3 to 9 o'clock. The circles are either filled with red

color representing oil wet or blue color representing water wet (but converted to white for oil wet and black for water wet in the printed document). If certain pins are non-responsive or faulty, they can be taken off by the program and appear as blank spaces in the wetting snapshot.

3.3.2.2 360° pin section

In 360° pin section, the interior wall of the 0.1 m ID carbon steel pipe section is fitted with a total of 160 conductivity pins around the entire pipe circumference. The 360° test section provides additional detection area to study the water distribution and surface wetting behavior over the entire pipe periphery, which is particularly useful for vertical pipe flow. This section was commissioned in the latter stage of the experiment campaign and was used in repeats of some of the flow experiments. Similar to 180° pin section, the 360° pin section shares identical pin construction, grid configuration, and working principle. The produced wetting snapshot is shown in Figure 3-19. The array of pins is presented such that the top and bottom rows are the 12 o'clock position while the middle row is the 6 o'clock position if the section is tested in horizontal orientation. The oil wetted pins are represented by white hollow circles whereas water wetted pins are black solid circles.
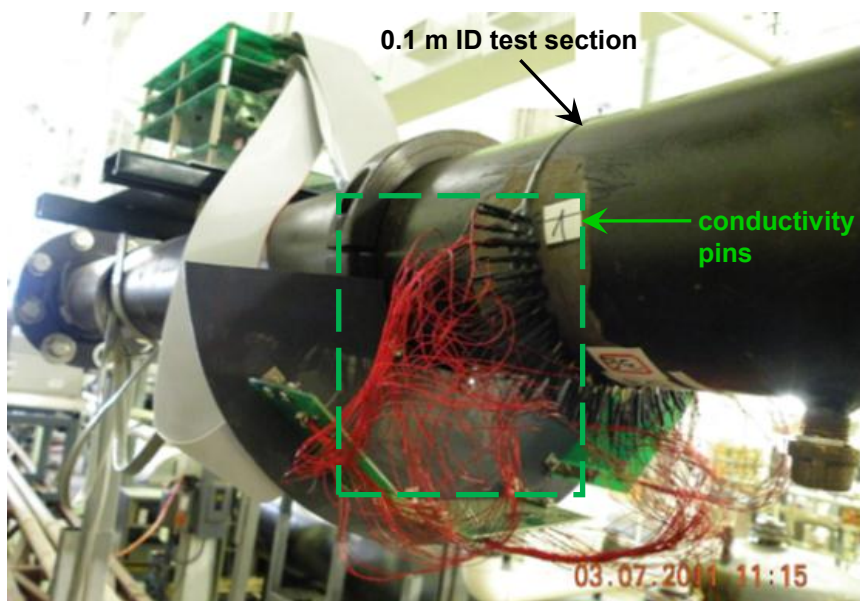
Figure 3-17: 0.1 m ID steel test section, showing the 180° pin section.
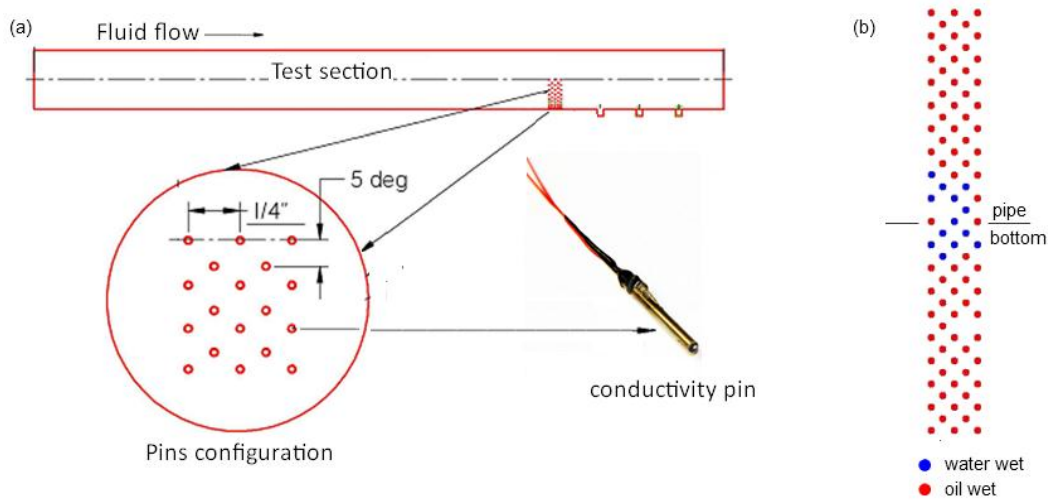
Figure 3-18: a) Schematic grid layout of the conductivity pins flushed mounted on the lower half of the wall in 180° pin section, (b) A typical wetting snapshot produced by 180° pin section.
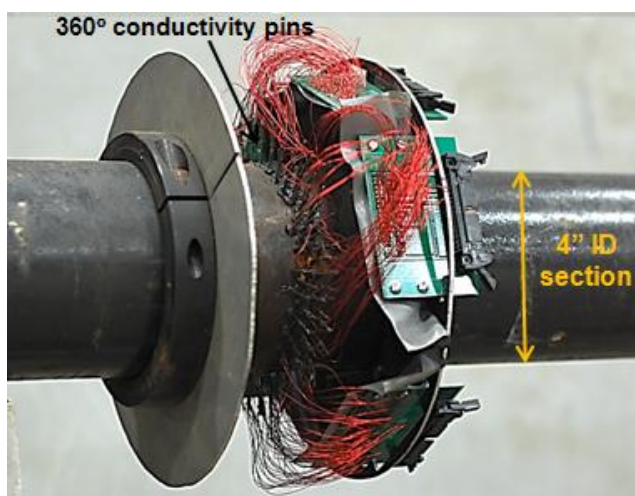
Figure 3-19: 0.1 m ID steel test section, showing the 360° conductivity pins flush mounted around the pipe.
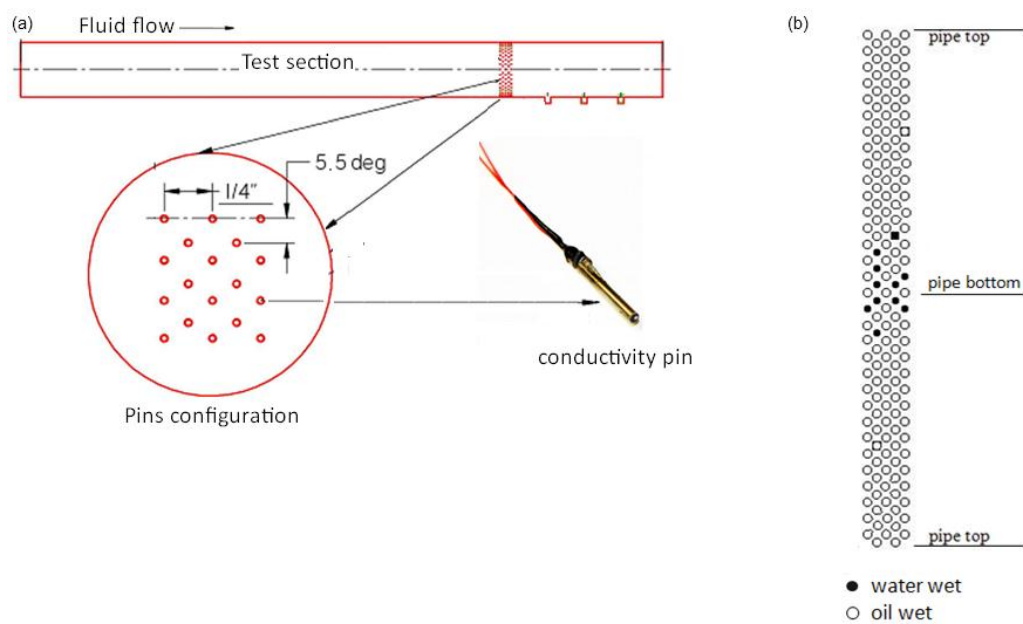
Figure 3-20: a) Schematic grid layout of the conductivity pins flushed mounted on the wall in 360° pin section, (b) A typical wetting snapshot produced by 360° pin section.

3.3.2.3 Pin design and circuitry

Figure 3-21 is an image of a conductivity pin flush mounted in the interior pipe wall. Figure 3-22 is the sectional view of the pin assembly. Each pin was custom-built using 0.8 mm (0.032") diameter stainless steel wire. Each pin was inserted into a 1.5 mm diameter stainless steel casing as ground, with epoxy in between the gap to hold and insulate the contact. The pin assembly was then epoxy-coated and fit in to a 1.6 mm (1/16") hole opening such that only the exposed pin tip is flush to the interior wall of the carbon steel pipe section.

Figure 3-21: Conductivity pin as seen from pipe inside (courtesy Al Schubert).
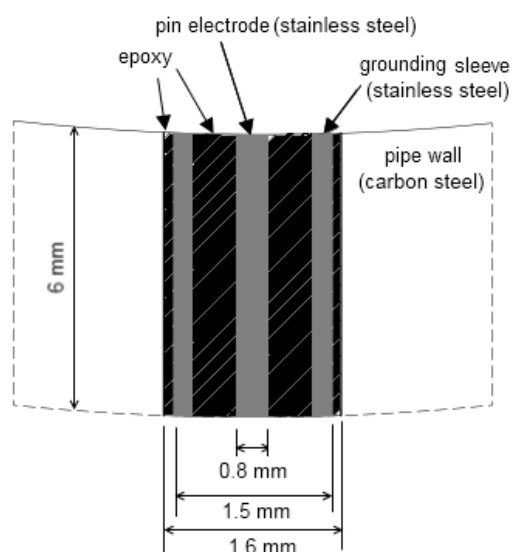
Figure 3-22: Cross sectional view of a conductivity pin flush mounted in a pipe wall.

The circuitry used for each pin sensor is shown in Figure 3-23, which consists of a simple network of voltage divider and voltage comparator. The voltage divider circuit measures the voltage drop across the pin, which depends on the conductivity of the fluid phase covering the exposed pin tip and grounded terminal. Since oil and water are vastly different in conductivity, the circuit displays a contrasting voltage drop signal that can distinguish the phases. During operation, a square wave source voltage V_1 oscillating from 0 V to +4.5 V at 100 Hz is supplied. At this relatively low frequency, only the resistive element is measured. If the exposed pin tip is bridged by conductive water, a low resistive circuit loop is formed between the exposed pin tip and the grounded casing that results in a low voltage drop in the pin circuit. If the exposed pin is covered by oil, a high resistive circuit loop is formed and a high voltage drop is detected in the circuit. The voltage response, V_{in}, can then be compared with a reference threshold voltage V_{ref} in a voltage comparator circuit to produce a two-level signal. The V_{ref} value is calibrated against the salinity of the water used in the flow loop. Slightly saline water is preferred to strengthen the electrolyte and improve the response signal quality (Cartellier & Achard, 1991). The two-level signal logic for the surface wetting condition is as follows:

If $V_{in} \leq V_{ref} \Rightarrow$ water wet

If $V_{in} > V_{ref} \Rightarrow$ oil wet

The signals are processed by a data acquisition system in a microprocessor circuit. The local instantaneous signals of all pins are displayed by a conductivity pin program in a host computer as a pictorial wetting snapshot with time stamp, as shown in Figure 3-24. The snapshots can be saved as either single frame or multiple frames at a user-defined interval.
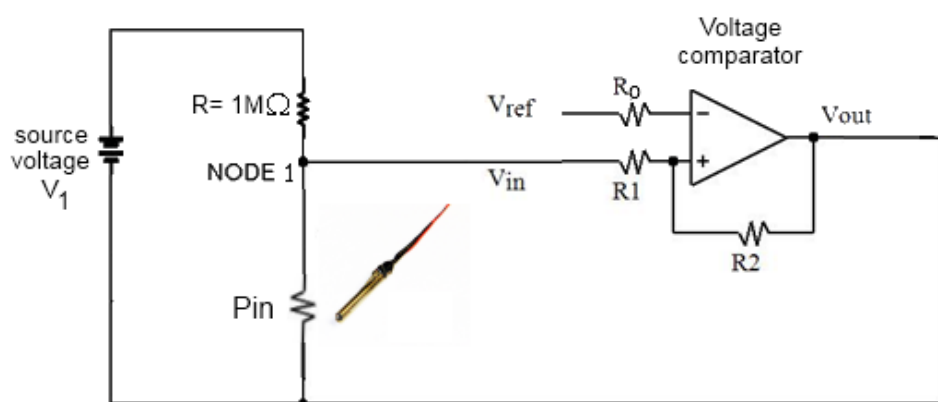
Figure 3-23: The simplified circuitry used in conductivity pin system.
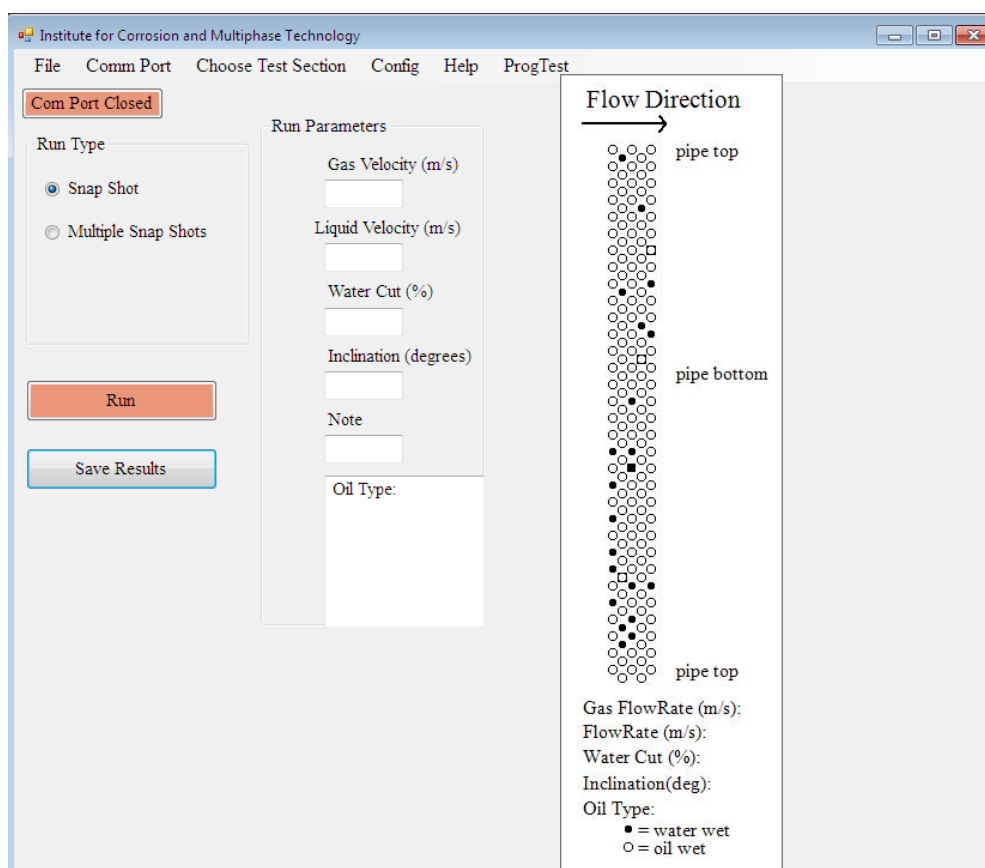
Figure 3-24: Graphical user interface of the conductivity pin program.

3.3.3   Tomographic equipment

The tomographic equipment is a non-invasive imaging technique to investigate the internal flowing content and cross-sectional phase distribution inside the pipeline. The output is a tomographic image that is a two-dimensional slicing view across the transverse section of the pipeline showing the spatial distribution of the measured parameter. Two types of tomography systems fitted into a stainless steel section are located approximately at $L = 7.5$ m ($L/D =75$) from the entrance nozzle. A photo of the tomographic equipment is shown in Figure 3-25. They are electrically-based with the following modalities:

- Electrical Resistance Tomography (ERT**),** based on resistivity measurement

- Electrical Capacitance Tomography (ECT), based on capacitance measurement

Further explanation on the tomographic equipment can be found in Chapter 6.
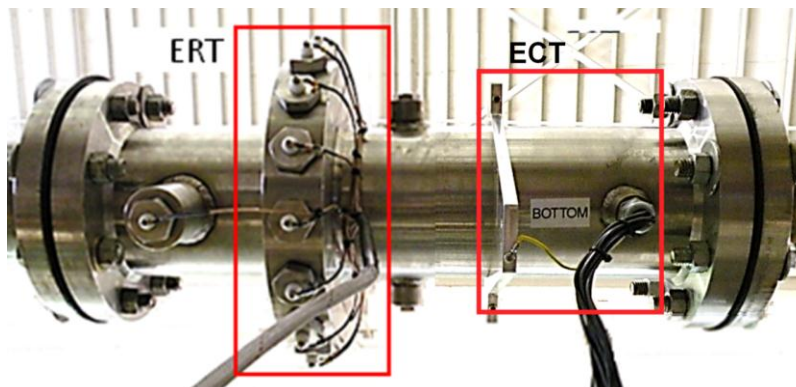
Figure 3-25: Tomography system with ERT and ECT sensors in a 0.1 m ID test section.

3.4 Experimental procedures

The conductivity measurements can be affected if there is contamination on the pin surface, *i.e.*, the pins become less sensitive. Therefore, it is important that the conductivity pins test section is properly cleaned and polished according to the following procedures:

i.   Wipe off the oil slime in the test section interior with rags soaked with isopropanol.

ii.   Polish the test section using a rotating honing tool (silicon carbide tips of 120 grit) and water as the lubricant.

iii.   Wipe the interior of the polished test section with rags soaked with isopropanol until the interior surface is not stained and is free of abrasive particles.

iv.   Use a slightly moist rag to wipe the test section, followed by a dry rag for the final wipe.

v.   Circulate the large-scale flow loop with a continuous run of CO_2 gas-oil slugs for approximately 30 minutes to remove any water or residues and to recondition the pins.

vi.   Run the conductivity pins program. At this state, all pins should display negative response (oil wet) except for those non-responsive pins which will be discarded from the program.

For each experimental series of two-phase oil-water flow pattern and surface wetting experiments carried out in the large-scale flow loop, the following procedures are performed:

i.   Before starting the experiments, the fluids are conditioned as follows:

    a.   Deoxygenate the water tank with CO_2 gas.

    b.   Deoxygenate the oil with CO_2 gas by circulating them in the flow loop.

ii.   Start the experiment by first circulating the flow loop with the oil phase.

iii.   At a desired mixture liquid velocity, introduce the water at the lowest water cut.

iv.   Observe for fully developed flow after 10 minutes. Record the flow pattern and/or run the conductivity pin program for the surface wetting.

v.   Gradually increase the water cut (up to 20%) and adjust the oil velocity so as to maintain the desired mixture liquid velocity. Repeat step iv until the range of water cut has been tested.

vi. Stop the water flow and introduce the gas-oil slug flow to 'rinse' the flow loop. This is an effective way to displace water from the main line and return the test section to the oil wet state. If needed, the rinsing step is sometimes performed between tests in step v.

vii. Repeat step iii to step vi for the next mixture liquid velocity in the test series.

For each experimental series of three-phase gas-oil-water flow experiments carried out in the large-scale flow loop, the general procedures are:

i. Before the experiment, deoxygenate and condition the fluids.

ii. Start the experiment by first circulating the flow loop with the oil phase.

iii. At a desired mixture liquid velocity, introduce the desired water cut.

iv. Start the gas blower to circulate the gas phase from the lowest velocity.

viii. Observe for fully developed flow. Record the flow pattern and/or run the conductivity pin program for the surface wetting.

v. Gradually increase the gas velocity while maintain the same mixture liquid velocity and water cut. Repeat step viii until the range of gas velocity has been tested.

vi. Stop the water flow and introduce the gas-oil slug flow as the rinsing step to return the test section to oil wet state.

vii. Repeat step iii to step vi for the next mixture liquid velocity and water cut in the test series.

CHAPTER 4: RESULTS FOR OIL-WATER FLOW

4.1 Introduction

Flow loop experiments were carried out to characterize the flow patterns. The use of high speed video recording equipment greatly enhanced the visualization of the flow patterns, succinctly capturing the details of flow features which were unattainable in conventional camcorder recording. It should be noted that the changes of some flow patterns were gradual, showing no sharp transition. Hence the identifcation of a flow pattern should contain some key flow structures sufficiently distinctive for observers to recognize with a nomenclature reflective of the flow structure occurring in the pipe. The present work focused on studying the flow patterns and water wetting in oil-dominated flow where the oil is the continuous phase and the water is the secondary phase with water cut up to 20%, as can be commonly found in oil production field conditions. Part of the work in this chapter was presented by the author at a recent international conference (Kee *et al.*, 2014).

4.1.1   Horizontal oil-water flow patterns

The horizontal oil-water flow patterns can be classified into two broad categories: separated and dispersed flows, according to the distribution of the phases. At low flow rate, the oil phase and water phase flow separately. Some degree of fluid mixing and entrainment may be present at the oil-water interface. Separated flow is typically observed in horizontal or near horizontal flow. As the oil flow rate increases, the flow has sufficient turbulence to break up the water phase into droplets of varying size. The observed oil-dominated flow patterns for water cut ranging from 0–20% are described below and illustrated in Figure 4-1.

Stratified smooth (ST-S) is a flow with continuous oil and water phases separated with a smooth interface. Entrainment of water was not observed.

Stratified with globules (ST-G) occurs at a low water cut where swarms of densely packed water droplets/globules are seen moving at the lower half of the pipe. The mobility of the droplets is somewhat restricted as they agglomerate to move as a single unit.

Stratified with mixing layer (ST-M) has a mixing layer flowing in the intermediate between the continuous oil and water phases. The oil-in-water and water-in-oil dispersions can be present in the mixing layer.

Semi-dispersed (S/D) is a form of dispersion where droplets are entrained as an inhomogeneous water-in-oil dispersion with an increased concentration towards the lower half of the pipe due to gravity.

Fully-dispersed (D) occurs when water droplets are homogenously distributed across the pipe. The droplets are smaller and they appear to move as fast as the bulk oil flow.
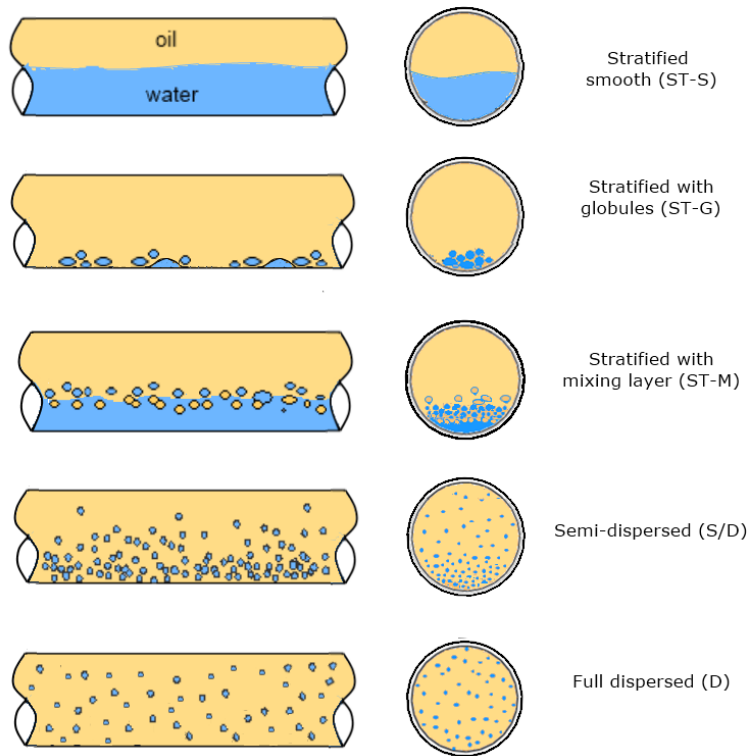
Figure 4-1: Schematics of observed horizontal oil-water flow patterns (oil-continuous flow).

By comparing to the nomenclature established by Trallero (1995), the flow patterns can be equivalently classified as follows: *stratified smooth* is equivalent to *ST*, *stratified with mixing layer* is *ST & MI*, *semi-dispersed* is *Dw/o & o*, *fully dispersed* is *w/o*, whereas stratified with water globules is not accounted.

4.1.2   Vertical oil-water flow patterns

While separated flow can be observed in horizontal or near-horizontal pipes, it does not exist in vertical flow. Flores (1997) reported that segregated flows in a 2-inch ID pipe persisted to an inclination angle of 33°. This work focused on oil-dominated flow with water cut up to 20%, two subgroups of water-in-oil dispersion flow patterns: *dispersed droplets* and *dispersed globules* were observable in the experiments. Other types of flow patterns such as churn or pseudo-slug

flow, as reported by Flores (1997), were not captured since they occurred at higher ranges of water cut. The flow features of the water-in-oil dispersion are described below along with the schematic sketch of the flow patterns shown in Figure 4-2.

Dispersed globules flow is seen at low liquid velocity where large clusters of irregularly shaped blobs of water globules are intermixed with small spherical water droplets in the continuous oil flow. The droplets are fairly rounded, as governed by the surface tension. The larger globules are either in a flat oval or irregularly deformed shape. The large globules flowed with significant slippage with respect to the bulk oil flow.

Dispersed droplets flow occurs at higher flow rate where fine round water droplets are dispersed uniformly across the pipe. The droplets move in a relatively straight flow path. The fine droplets appeared to flow as fast as the continuous oil flow with negligible slippage.
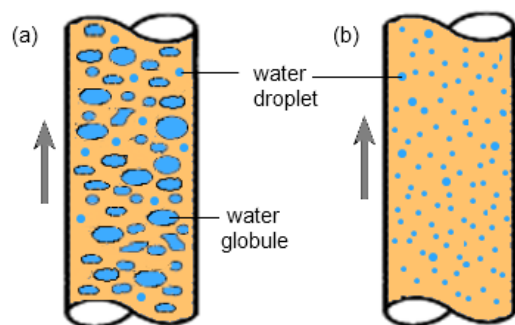
Figure 4-2: Schematics of (a) dispersed globules flow pattern, (b) dispersed droplets flow pattern.

4.2 Experimental details

The large-scale inclinable 0.1 m ID flow loop was setup to study the oil-dominant flow in horizontal and vertical pipe with water cuts ranging from 1% up to 20%. Schematic of the two-phase flow loop is given in Figure 3-4. A total of 117 test points have been collected for the oil-water flow test conditions as shown in Table 4-1. Some of the test points were repeated during the

experimental campaign. The flow loop experiments were conducted by increasing water cuts at fixed mixture liquid velocities. The mixture liquid velocity is the sum of superficial oil and superficial water velocities. Due to the capacity limit of the water pump, the highest testable water cut range was lowered with increased mixture liquid velocity, as listed in Table 4-2. The oil phase used in the experiments was refined paraffinic oil, a commercial LVT200. The water phase used was 1 wt.% NaCl solution, prepared from deionized water and analytical grade NaCl. The density ratio between the oil and water is about 0.823, while the dynamic viscosity difference is a factor of 2.7. The emulsion is unstable and tends to separate quickly (less than a minute). Approximately 150 ppm of red food dye (red 44) was added to the water phase to provide a better contrast for visual examination. Interfacial tension measurement was performed for water added with the food dye and no appreciable change in interfacial tension value was noticed. The properties of the test liquid are given in Table 3-1.

Prior to actual experiments, the conductivity pins test section was thoroughly polished and cleaned according to the following procedures as outlined in Section 3.4. Two types of measurements were taken during the tests, corresponding to flow pattern and surface wetting measurements. Since a clear model oil was used in the flow loop tests, the flow patterns can be visually observed. Once the flow was fully developed, the flow pattern was captured by the high speed video camera through the transparent viewing pipe section located side-by-side with the conductivity pins section downstream of the first leg of the flow loop (approximately $L/D = 100$). The wetting data were measured by the conductivity pins after achieving consistent wetting.

Table 4-1: Test matrix for horizontal and vertical oil-water flow

Parameter	Value	
System conditions	1 atm. @ 25 °C	
Oil phase	LVT200	
Water phase	1 wt.% aqueous NaCl	
Pipe ID (m)	0.1	
Inclination (°)	0° (horizontal)	90° (vertical)
Mixture liquid velocity V_m (m/s)	0.2 –2.0	0.5 – 1.5
Water cut (%)	1 - 20	1 - 20
Number of test points	76	41

Table 4-2: Ranges of water cuts testable in the flow loop

Mixture liquid velocity V_m (m/s)	Test range of water cuts (%)
0.5	1 - 20
0.7	1 - 20
1.0	1 - 18
1.3	1 - 14
1.5	1 - 12
1.7	1 - 10
2.0	1 - 8

4.3 Horizontal oil-water flow

4.3.1   Flow patterns at high water cut

The use of high speed video camera (model Phantom v12.1) in this work greatly enhanced the visualization of the flow patterns and understanding of the flow features. The tool can succinctly capture the hydrodynamic behaviors of the water film or dispersed droplets, which were unobtainable by conventional camcorder. The images of the horizontal flow patterns taken from the high speed video camera will be presented and discussed in four groups of mixture liquid velocities, each group tested with varying water cuts up to 20%. In general at low mixture liquid velocity, separated flow was observed even at low water cut. With increasing mixture

liquid velocity, dispersion of water phase occurred at low water cut but gradual phase separation was observed as the water cut increased. It should be noted that the change of flow pattern was gradual, showing no sharp transition. Primary attention was given to the distribution of water that was seen in contact with the wall. The water phase can be in the form of a continous layer or dispersed droplets.

4.3.1.1 Mixture liquid velocities V_m of 0.5 m/s and 0.7 m/s

At these velocities, the flow pattern results obtained from the high speed video camera are presented in Figure 4-3 and Figure 4-4. The calculated Reynolds number (Re) was 2×10^4 to 3×10^4, which corresponded to the turbulent flow region (Re > 2,300) in pipe flow. Two different types of flow patterns can be observed: *Stratified with globules (ST-S)* flow at < 5% water cut, and *Stratified with mixing layer (ST-M)* flow at 5 % to 20% water cut.

At the lowest 1% water cut, the flow moves in the forms of loosely packed droplets flowing at the pipe bottom, with a size range of between 2.0 mm to 5.5 mm. The droplets generally maintained their quasi-spherical shape approximately until 5.5 mm. Any droplet above the size lost its sphericity and became stretched along the horizontal plane, forming a flat elongated globule (Reyssat *et. al*, 2007). The criteria for sphericity can be explained by the concept of capillary length, $L_C = (\sigma/\Delta\rho g)^{1/2}$ governed by the oil-water interfacial tension and gravity. As the water cut increased above 1% water cut, larger globules were observed to flow alongside with swarms of densely packed droplets in the lower pipe section. Some of the elongated globules coalesced to form a semi-continuous stream of water snaking unstably at the bottom wall. At water cut $\geq$ 10%, stratified flow with a mixing layer (*ST-M*) flow pattern can be observed. A relatively thick continuous water layer flowed at the pipe bottom, continuous oil phase flowed on

top, and a dispersion layer flowed at the intermediate oil-water interface. The dispersion layer was similar to an emulsion consisting of water-in-oil droplets and oil-in-water droplets.

4.3.1.2 Mixture liquid velocity V_m of 1 m/s

The flow pattern images are presented in Figure 4-5. Three types of flow patterns can be identified: *semi-dispersed* (*S/D*) flow at 1% water cut, s*tratified with globules (ST-S)* flow at 2% to 5% water cuts, and s*tratified with mixing layer* (*ST-M*) flow at 10% water cut and above.

At this intermediate liquid velocity with 1% to 5% water cuts, the low amount of water can be entrained as water-in-oil dispersion by the continuous oil flow. The effect of gravity caused an inhomogeneous dispersion of the droplets, resulting in a *semi-dispersed* (*S/D*) flow pattern in which water was sparsely dispersed in the upper pipe section, but more populated in the lower pipe section due to gravitational pull. As the water cut further increased above 10% water cut, a continuous water layer can be seen along with a dispersion layer at the interface. The flow pattern was characterized as *stratified with mixing layer* (*ST-M*).

4.3.1.3 Mixture liquid velocities V_m of 1.3 m/s and 1.5 m/s

Figure 4-6 and Figure 4-7 show the flow pattern results at these ranges of velocities with varying water cuts. Three types of flow patterns can be observed: *full dispersed flow (D) flow* at 1% water cut, *semi-dispersed* (*S/D*) flow at 2% to 8% water cuts, and s*tratified with mixing layer* (*ST-M*) flow at > 10% water cut.

At the lowest water cut (1% water cut), a full dispersed flow pattern can be observed where the water phase was dispersed and suspended evenly across the pipe section by the continuous oil flow. With a slight rise of water cut above 1%, the flow pattern transitioned to semi-dispersed flow in which water droplets increasingly concentrated in the lower pipe section due to gravitational pull, resulting in an inhomogeneous dispersion. Some of the partially lifted droplets

were seen to deviate from the flow path and momentarily 'touch' the pipe wall. At 10% water cut and above, an intermediate flow pattern gradually transitioning from dispersed flow to a separated flow pattern can be seen. Macroscopically, the latter case displayed a somewhat separated flow structure due to the marked difference in droplet populations between the upper and lower regions. A closer look at the local flow pattern in the lower pipe section revealed that these droplets flowed closely and collided with each other. Traces of an unstable water stream started to appear.

4.3.1.4 Mixture liquid velocities V_m of 1.7 m/s and 2 m/s

At this flow condition with high Reynolds number ($Re > 7 \times 10^4$), a *full dispersed* (*D*) flow pattern was observed and the images are presented in Figure 4-8 and Figure 4-9. At 1% water cut, break up of water occurred in the turbulent oil stream in which the water droplets were dispersed and suspended homogeneously across the pipe section; no continuous water film can be seen. At 5% water cut, a high population density of water droplets were observed to pack more closely; no continuous water layer was noticeable at the bottom wall.

The flow data pattern results are plotted in a flow pattern map shown in Figure 4-10 with mixture liquid velocity on the *x*-axis and water cut on the *y*-axis. Each data point in the map represents the flow pattern at the given flow condition. The empirical transition lines, delineating the transitions of each flow pattern, are included in the map.
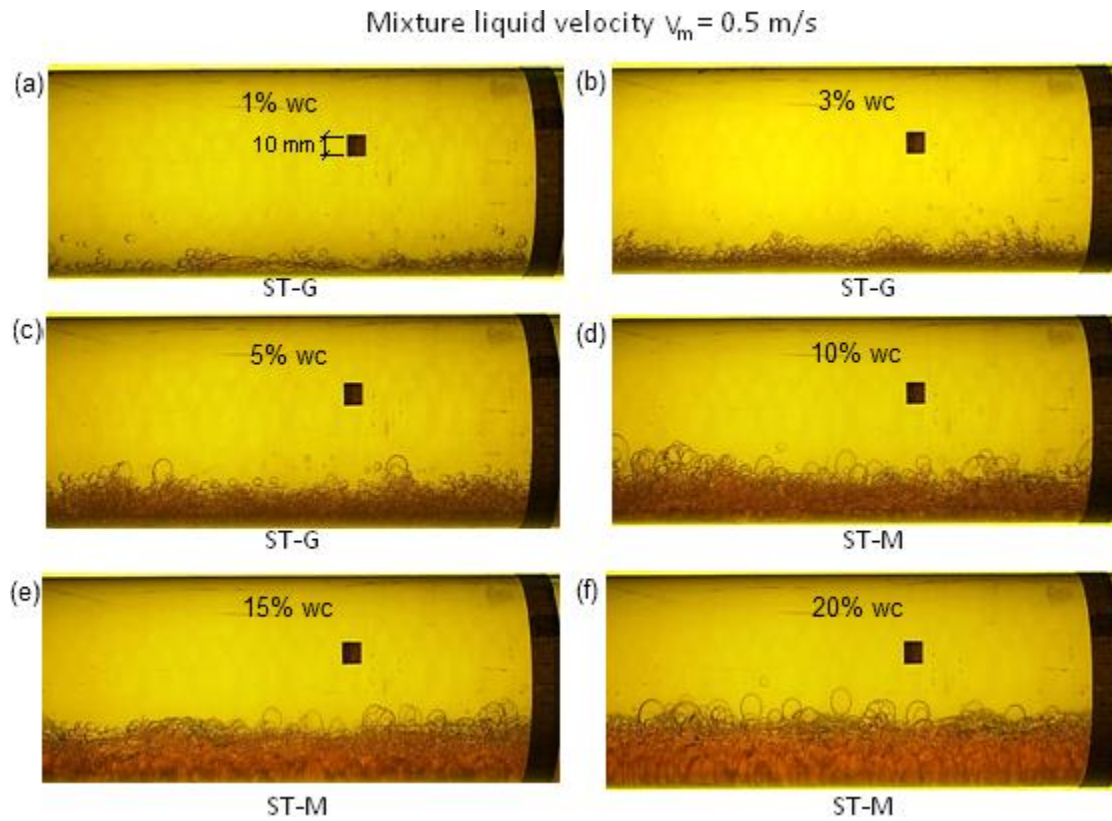
Figure 4-3: Images of horizontal flow patterns of LVT200-water system at liquid velocity V_m = 0.5 m/s from 1% to 20% water cuts.
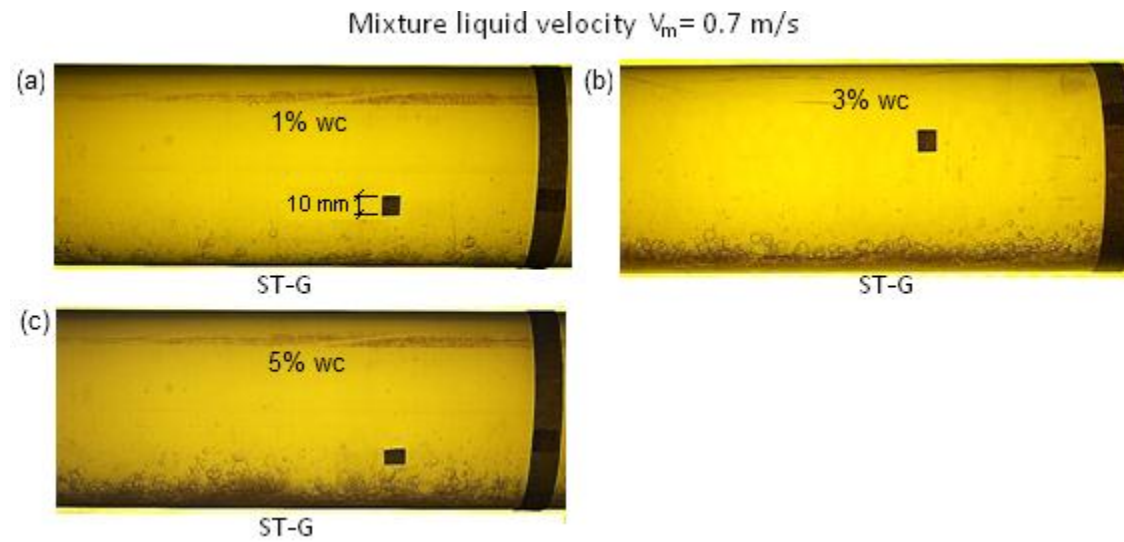
Figure 4-4: Images of horizontal flow patterns of LVT200-water system at liquid velocity V_m = 0.7 m/s from 1% to 20% water cuts.

Mixture liquid velocity V_m = 1.0 m/s
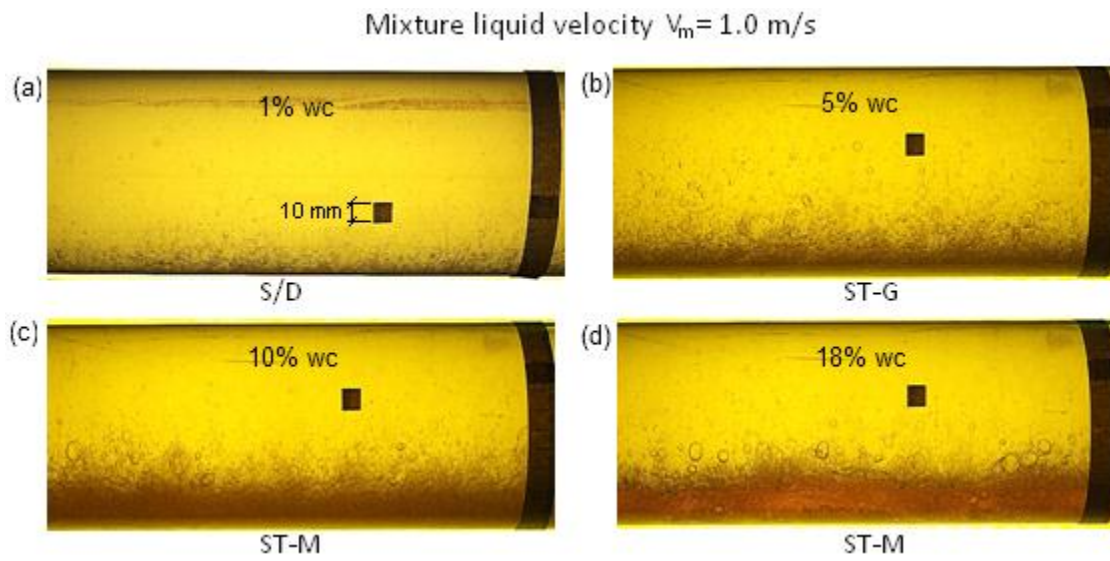
Figure 4-5: Images of horizontal flow patterns of LVT200-water system at liquid velocity V_m = 1.0 m/s from 1% to 18% water cuts.

Mixture liquid velocity V_m = 1.3 m/s
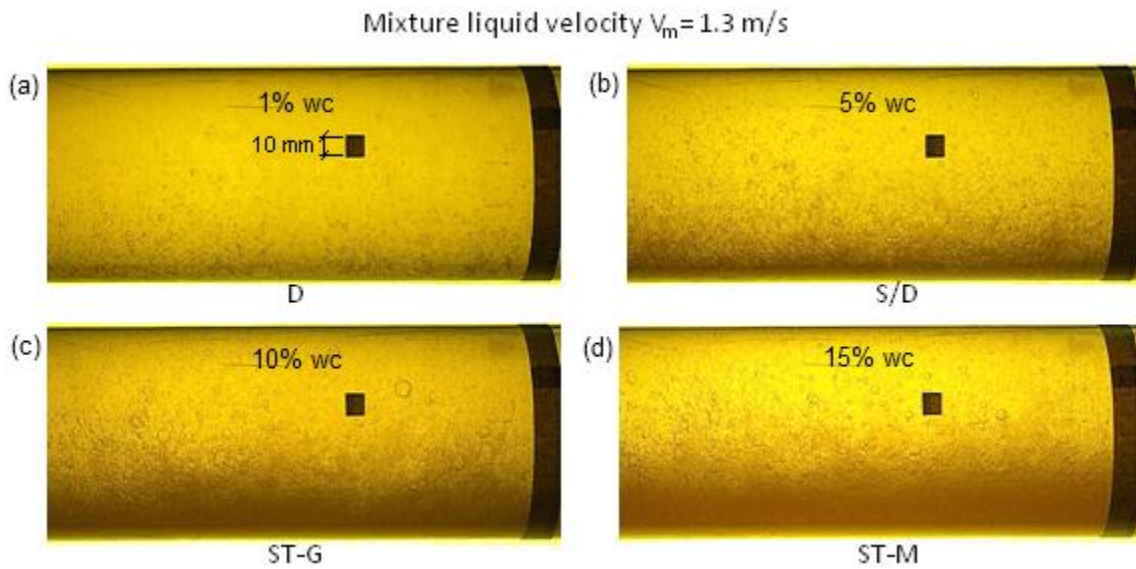
Figure 4-6: Images of horizontal flow patterns of LVT200-water system at liquid velocity V_m = 1.3 m/s from 1% to 15% water cuts.

Mixture liquid velocity $V_m = 1.5$ m/s
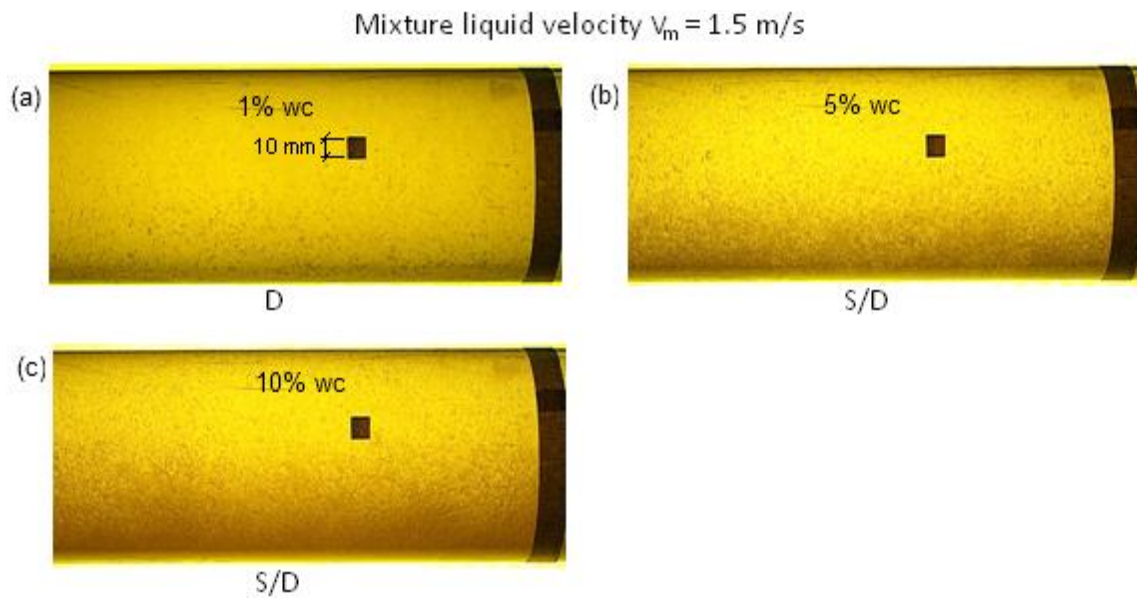
Figure 4-7: Images of horizontal flow patterns of LVT200-water system at liquid velocity $V_m =$ 1.5 m/s from 1% to 15% water cuts.

Liquid mixture velocity $V_m = 1.7$ m/s
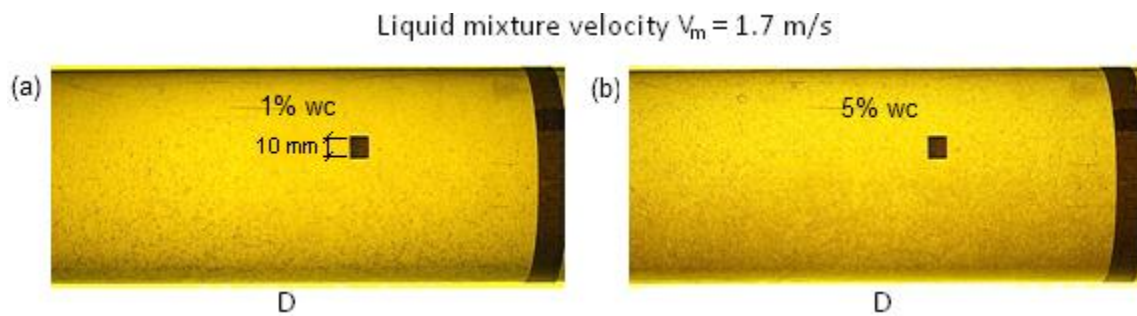
Figure 4-8: Images of horizontal flow patterns of LVT200-water system at liquid velocity $V_m =$ 1.7 m/s for 1% and 5% water cuts.

Liquid mixture velocity $V_m = 2$ m/s
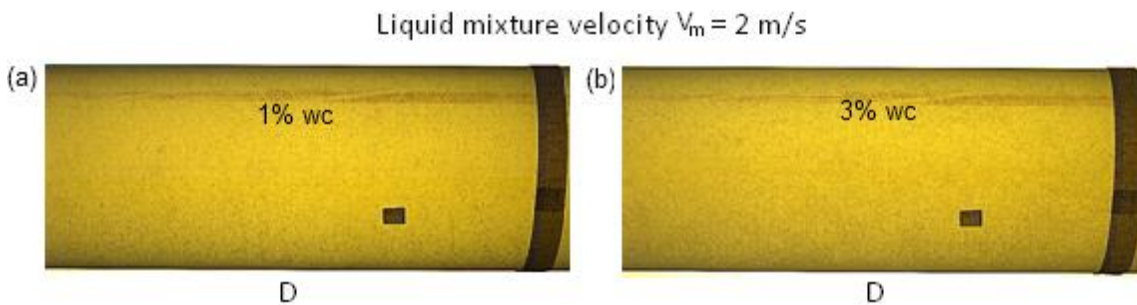
Figure 4-9: Images of horizontal flow patterns of LVT200-water system at liquid velocity $V_m =$ 2.0 m/s for 1% to 3% water cuts.
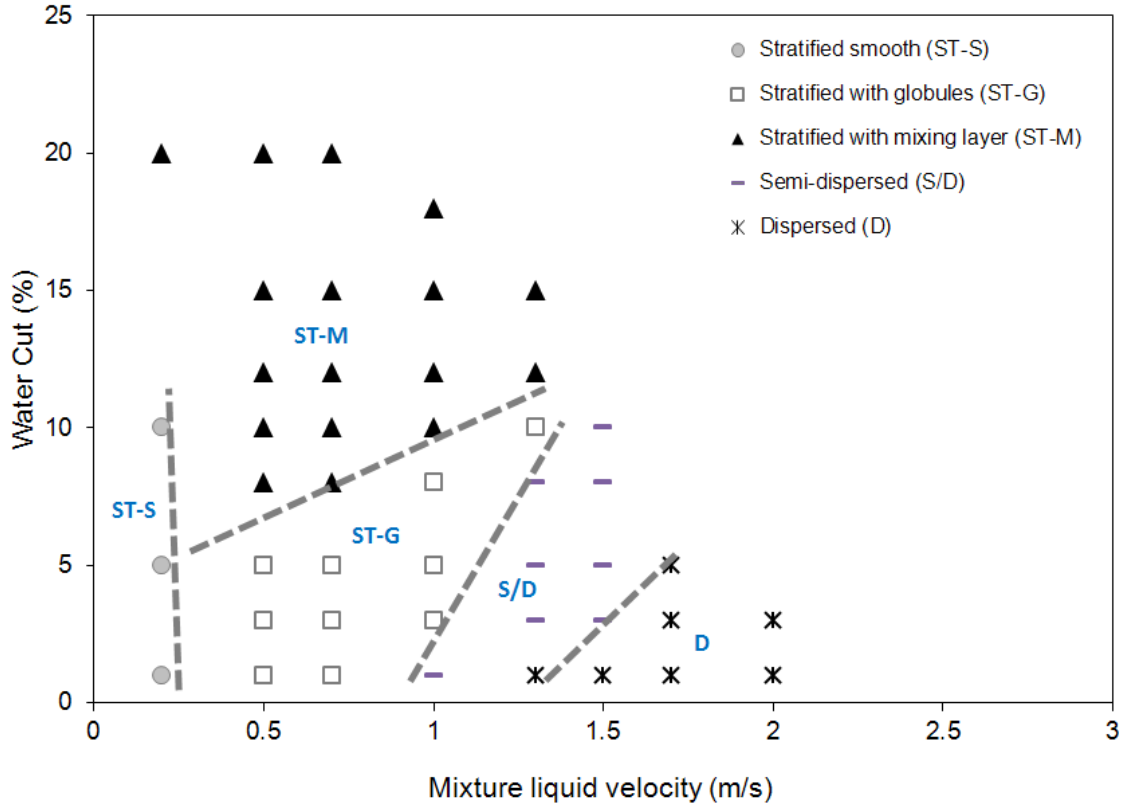
Figure 4-10: Flow pattern map for horizontal LVT200-water flow in a 0.1 m ID pipe.

4.3.2   Flow patterns at low water cut

Water concentration data collected from an Omani field case showed that "pure" hydrocarbon transportation pipelines have the potential to still contain traces of water of between 0.35 – 0.5% at the pipe bottom (Pots *et al*.,2006). Hence, it is pertinent to study the flow patterns and water wetting at these very low water cut conditions. In this work, the experiments were performed at 0.5% water cut and compared with results at 1% water cut under varying mixture liquid velocities.

4.3.2.1 Mixture liquid velocities V_m of 0.5 m/s and 0.7 m/s

At 0.5% and 1% water cut, water droplet out occurred and moved as swarms of dispersed droplets/globules at the bottom of the pipe, characterized as the stratified-globules (ST-G) flow

pattern as shown in Figure 4-11. The size of water droplets/globules ranged from 2-5.5 mm, with larger globules sheared into an elongated oval shape. Underneath these droplets, segmented rivulets of water were seen to 'snake' around at the bottom wall. The discrete droplets/globules did not appear to coalesce for the observed duration (less than 1 sec) of droplets traveling through the transparent pipe.

4.3.2.2 Mixture liquid velocities V_m of 1 m/s and 1.3 m/s

At 0.5% and 1% water cut, semi-dispersed flow patterns were observed at these velocities as shown in Figure 4-12. The water phase was in dispersion but distributed with a gradient of increased concentration towards the lower half of the pipe due to gravity. The crowding of water droplets adjacent to the pipe bottom causes the droplets to momentarily touch the wall. The droplets showed an approximate size distribution of 1-3 mm. The observed semi-dispersed flow patterns did not appear to differ significantly except the water droplets distributed at the lower pipe section were denser and larger at the lower liquid velocity of 1 m/s compared to 1.3 m/s.

4.3.2.3 Mixture liquid velocities V_m of 1.5 m/s and 1.7 m/s

The flow has sufficient turbulent force to break up and fully disperse the water phase. As shown in Figure 4-13, the water was in dispersion with finely distributed droplets. The droplet size was approximately less than 2 mm. The droplets were rather evenly distributed across the pipe section, more noticeably at higher liquid velocity and low water cut. A slight increase of water cut appeared to gently skew toward denser water distribution at the lower pipe section.

(a) Liquid velocity Vm = 0.5 m/s   (b) Liquid velocity Vm = 0.7 m/s
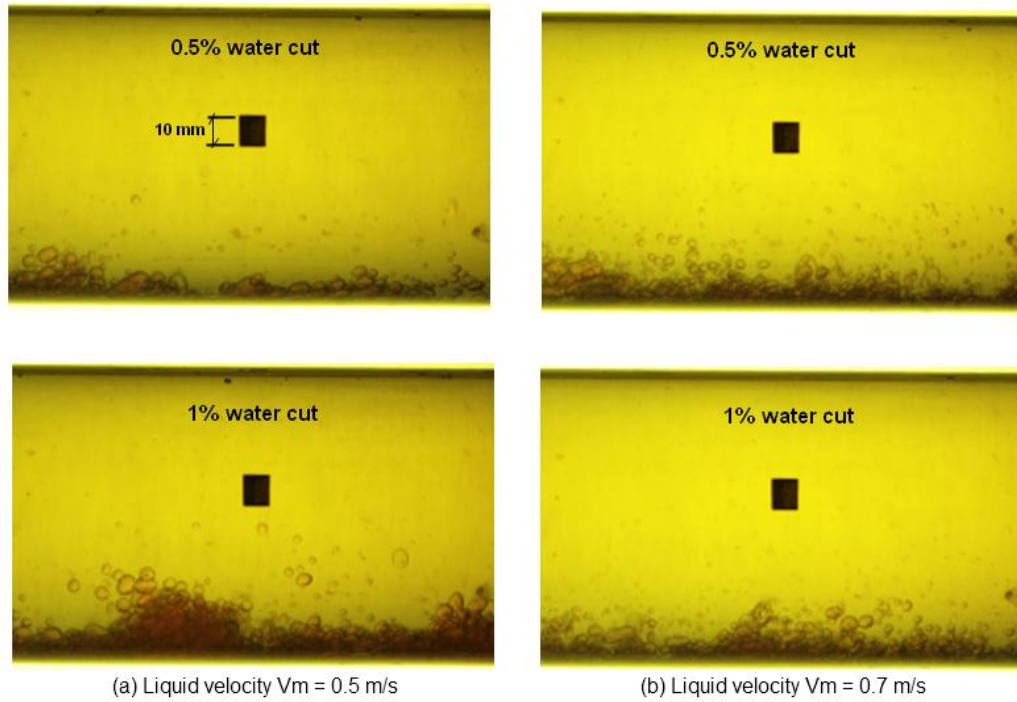
Figure 4-11: Stratified with globules flow patterns of LVT200-water system at 0.5%-1% water cut for liquid velocity: (a) V_m= 0.5 m/s, (b) V_m= 0.7 m/s.

(a) Liquid velocity Vm = 1.0 m/s   (b) Liquid veloctiy = 1.3 m/s
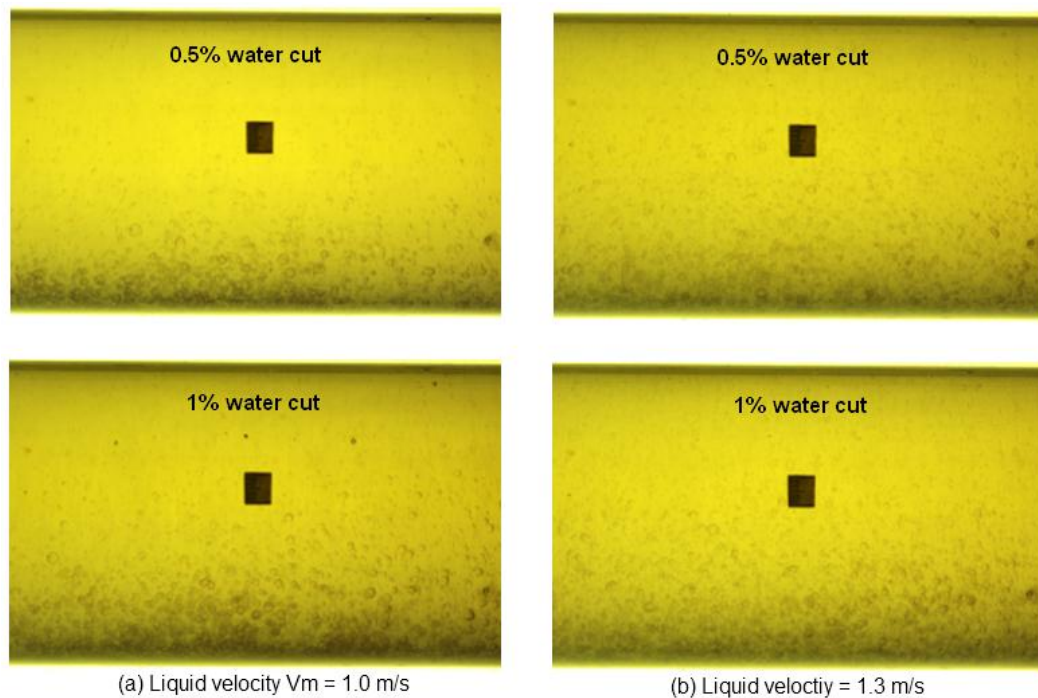
Figure 4-12: Semi-dispersed flow patterns of LVT200-water system at 0.5%-1% water cut for liquid velocity: (a) V_m= 1.0 m/s, (b) V_m= 1.3 m/s.
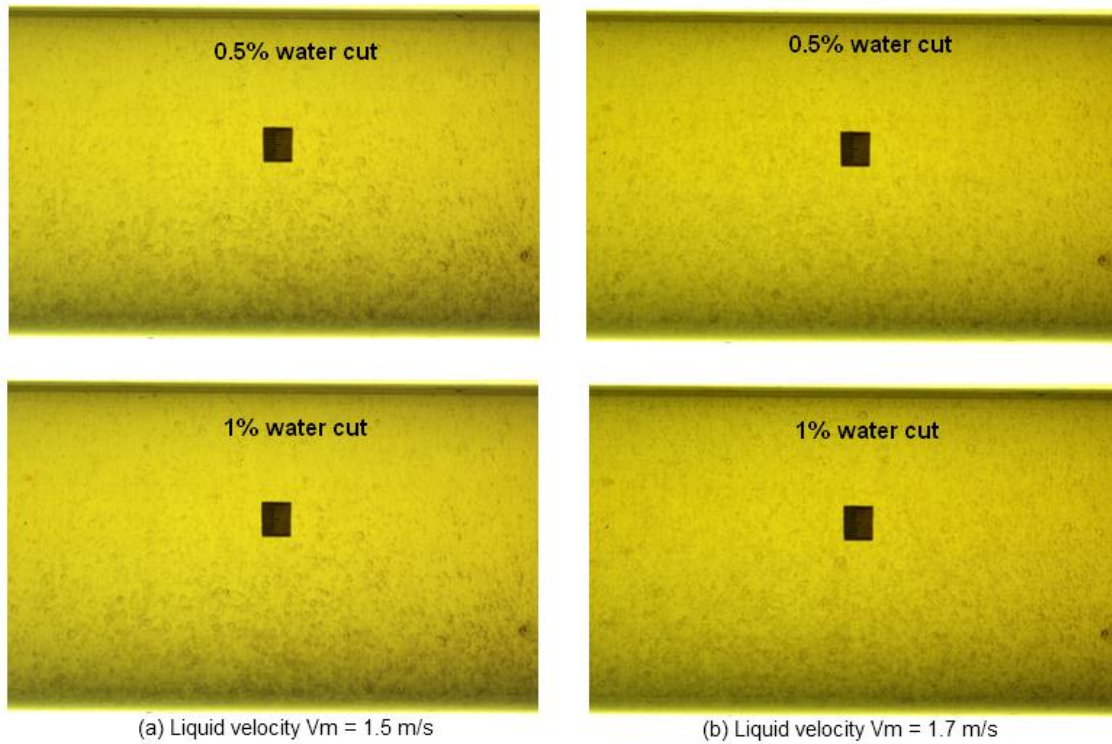
Figure 4-13: Dispersed flow patterns of LVT200-water system at 0.5%-1% water cut for liquid velocity: (a) V_m = 1.5 m/s, (b) V_m = 1.7 m/s.

4.3.2.4 View from pipe bottom

Photographs were also taken from the pipe bottom (6 o'clock position) using a Nikon D40 digital camera. Images taken from this perspective could provide additional information regarding the behavior of the water phase at the bottom pipe wall, whose details might be obscured when viewed horizontally.

At mixture liquid velocities V_m of 0.5 m/s and 0.7 m/s, the stratified globules (ST-G) flow patterns were seen at these conditions (Figure 4-14). The water dropped out and moved as swarms of droplets/globules at the pipe bottom. These swarms of droplets flowed in a somewhat wavy fashion along the pipe. Occasionally some segmented, semi-broken rivulets of water were seen 'snaking' around the pipe bottom.

At mixture liquid velocities V_m of 1.0 m/s and 1.3 m/s, the semi-dispersed flow patterns were reported at these flow conditions (Figure 4-15). The water phase was dispersed as droplets and no continuous water layer could be seen. Most water droplets were suspended in the flow, where some droplets appeared to be distributed closer to the lower half of the pipe.

At mixture liquid velocities V_m of 1.5 m/s and 1.7 m/s, the dispersed flow patterns were reported at these flow conditions as depicted (Figure 4-16). The water phase was dispersed into finely distributed droplets that were suspended in the flow.
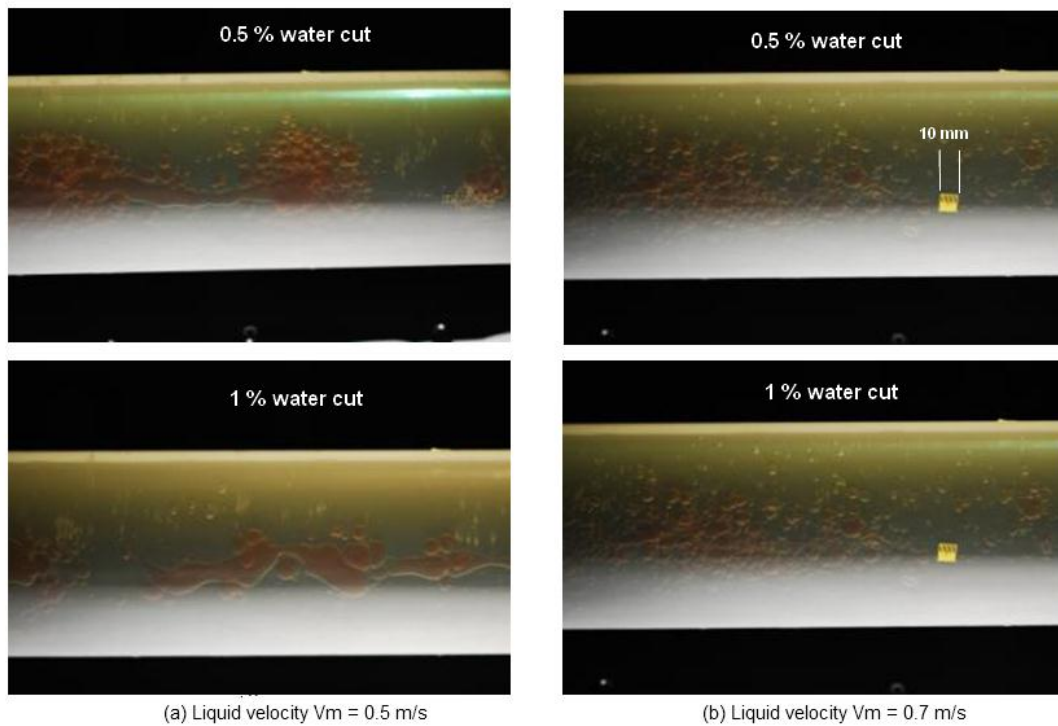
Figure 4-14: Images of horizontal LVT200-water flow patterns viewed from pipe bottom at 0.5%-1% water cut, (a) V_m = 0.5 m/s, (b) V_m = 0.7 m/s.

(a) Liquid velocity Vm = 1 m/s

(b) Liquid velocity Vm = 1.3 m/s
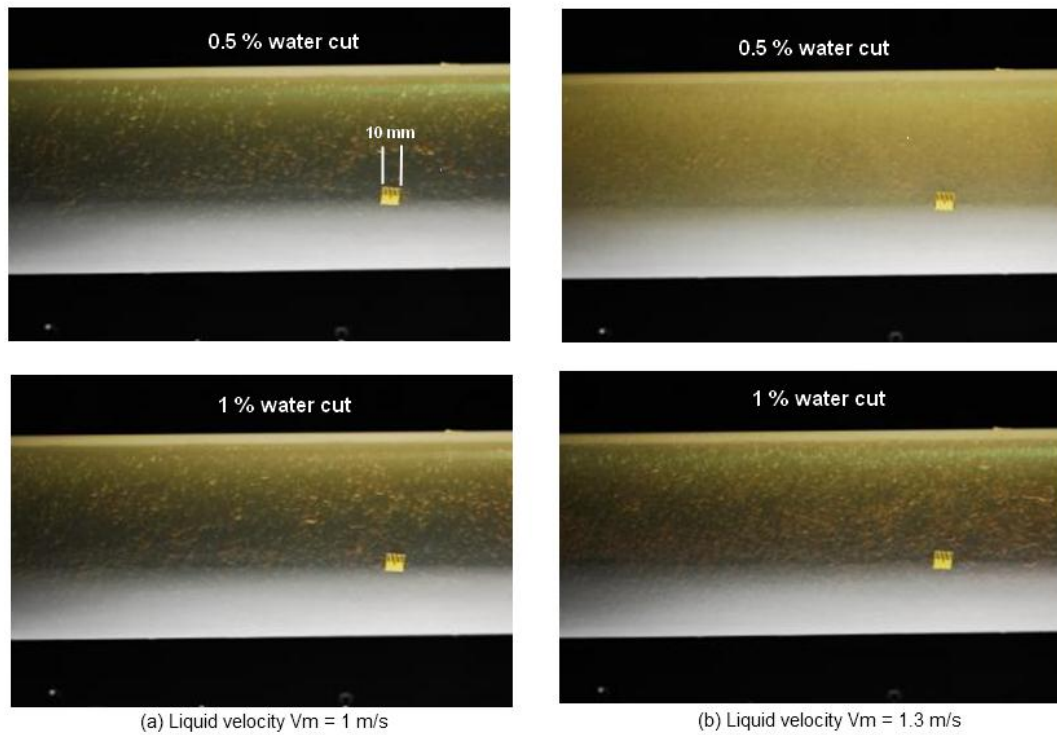
Figure 4-15: Images of horizontal LVT200-water flow patterns viewed from pipe bottom at 0.5%-1% water cut, (a) V_m = 1 m/s, (b) V_m = 1.3 m/s.

(a) Liquid velocity Vm = 1.5 m/s

(b) Liquid velocity Vm = 1.7 m/s
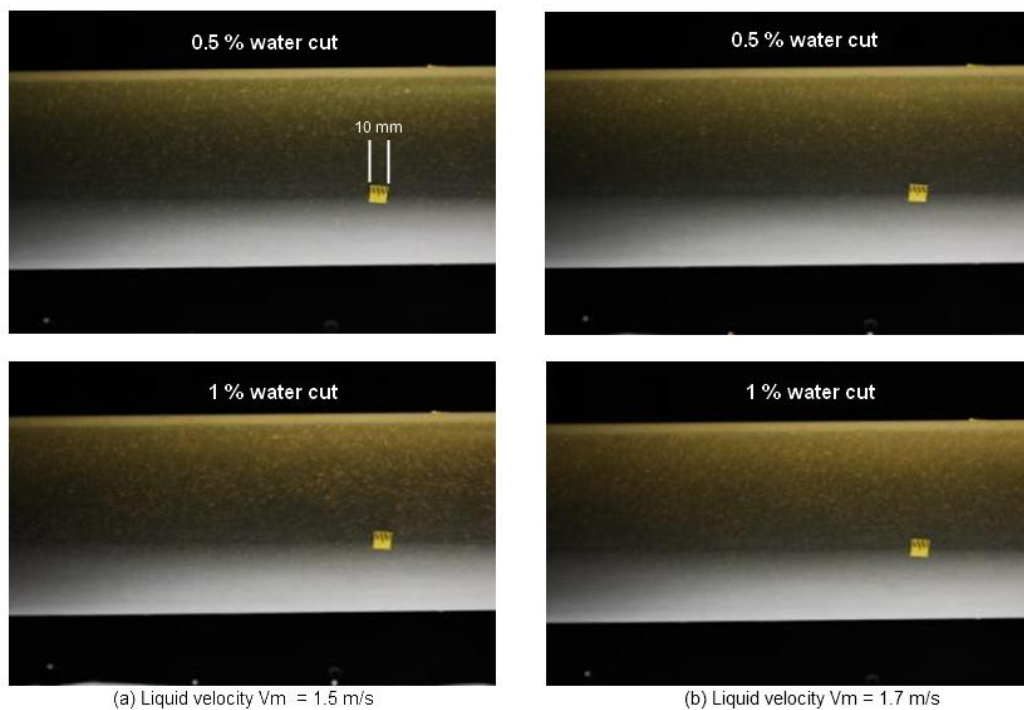
Figure 4-16: Images of horizontal LVT200-water flow patterns viewed from pipe bottom at 0.5%-1% water cut, (a) V_m = 1.5 m/s, (b) V_m = 1.7 m/s.

4.3.3 *Surface wetting at high water cut*

The surface wetting study was performed in the flow loop using a steel test section mounted with a spool of conductivity pins. The surface wetting results were generated using a model oil LVT200-water system without additives or surfactants, and tested at a clean steel surface condition. By analyzing the surface wetting behavior as measured by the conductivity pins at various flow conditions, four categories of surface wetting regimes can be identified as given in Table 4-3, with the corresponding wetting snapshot examples illustrated in Figure 4-17.

Table 4-3: Classification of surface wetting regimes

	Wetting Regime	**Description**
1	Stable water wet	Some pins are water wet and stay water wet.
2	Unstable water wet	more than 3% of the pins stay water wet, some pins change intermittently between oil wet and water wet.
3	Unstable oil wet	not more than 3% of the pins stay water wet, some pins change intermittently between oil wet and water wet.
4	Stable oil wet	all pins are wetted by oil.

For the *stable water wet* regime, the pins displayed positive response (indicated by black solid circles, • in the snapshot) corresponding to a steady flow of continuous water layer in contact with the wall surface. The location of the water wetted pins was closely related to the presence of water observed through the viewing section. For example, water wetted pins can be found clustering around the 6 'o clock orientation if separated flow takes place in a horizontal pipe. For the *stable oil wet* regime, the pins displayed negative response (open circles, o in the snapshot) around the pipe periphery corresponding to water fully entrained by the bulk flow and only the oil phase in contact with the wall. For the mixed positive and negative responses, they were either categorized as *unstable oil wet* or *unstable water wet*. Both cases displayed

intermittent wetting behavior but with different degrees of wetting intermittency. For *unstable oil wet*, most of the pins were oil wetted with a few pins showing intermittent wetting; while for *unstable water wet*, > 3% of pins stayed permanently water wet and some pins changed intermittently between oil wet and water wet. In previous work (Li, 2009; Tang, 2010), these two wetting behaviors were collectively grouped as *intermittent wetting*. However, it was recognized that a case where pins showing mostly oil wet was quite different from another case where pins were mostly water wet with some intermittent wetting. From the corrosion standpoint, the latter case would have greater propensity for corrosion than the former case since the probability of free water interacting with the steel surface is higher, hence enhancing the replenishment of dissolved corrosive species at the surface. It should be noted that the system is built with redundancy by mounting a large number of conductivity pins on the wall. For the LVT200-water system used in this work, it is established that over 3% of the positive pin response can be considered as *water wetting* behavior to eliminate the possibility of non-responsive pins or outliers.
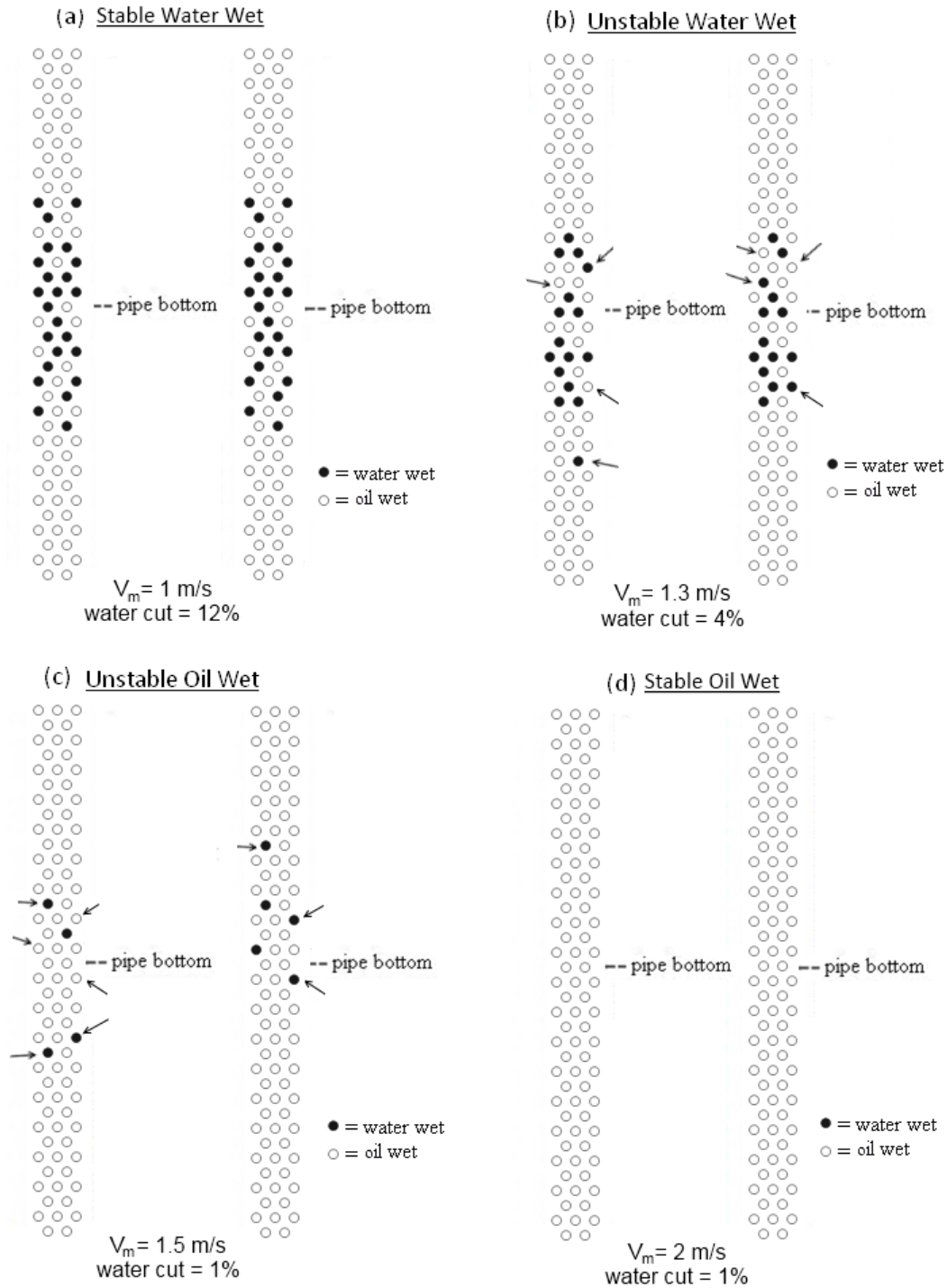
Figure 4-17: Four categories of wetting regimes: (a) stable water wet, (b) unstable water wet, (c) unstable oil wet, and (d) stable oil wet. Arrows indicate intermittent pins switching between oil wet and water wet.

Using the proposed surface wetting regimes, the wetting data in horizontal flow using the LVT oil-water system can be plotted in a surface wetting map as shown in Figure 4-18. The map shows four types of surface wetting regimes that could exist in a horizontal oil-water flow system. An experimental boundary line between oil wetting and water wetting is included to delineate the transition. The wetting results were cross-checked with the flow pattern map in Figure 4-10.
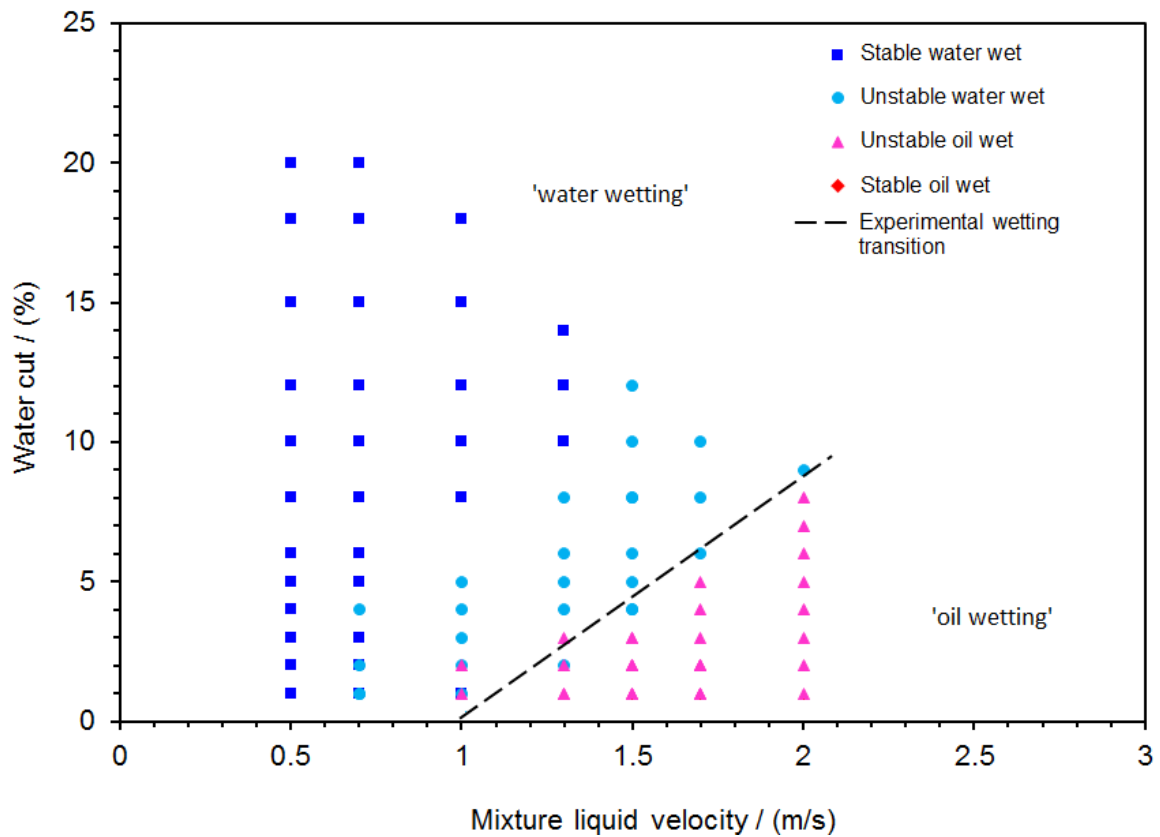
Figure 4-18: Surface wetting map for horizontal LVT-water flow in the present study.

4.3.3.1 Mixture liquid velocities V_m of 0.5 m/s and 0.7 m/s

Stratified globules (ST-G) flow observed at low water cut and stratified with mixing layer (ST-M) observed at water cut >7% were reported at these flow conditions. The wetting snapshots indicated that *stable water wet* behavior persisted for all water cuts at $V_m = 0.5$ m/s. The water

wetting location was located around the 6 o'clock position and corresponded to the observed continuous flow of the water phase. The area of water wetting location grew as the water cut increased. By slightly increasing the liquid velocity to $V_m = 0.7$ m/s, u*nstable water wet* was seen at low water cut <5% and changed to *stable water wet* when the water cut was further increased. The *unstable water wet* behavior at low water cut corresponded to the presence of swarms of closely dispersed water droplets intermittently 'touching' along the pipe. The behavior can also be observed at the oil-water interface where a layer of dispersion may exist and water droplets intermittently touch the tube wall.

It is noted that the responses of the conductivity pins can vary with time and space since the surface wetting closely corresponds to the local water distribution that is influenced by hydrodynamics and flow patterns. For example, the *stable water wet* condition will show a cluster of pins constantly wetted by water that are unchanged with time and space. However, the *unstable water wet* condition will have additional pins that change intermittently with time and space. In order to quantitatively describe the different wetting behaviors, a wetting intensity snapshot and bar chart averaged over time duration of 0.5–2 minutes as shown in Figure 4-19 were produced. The pin snapshot taken at one second each is an intensity map showing the averaged wetting frequency for each individual pin ranging from 0% to 100% water wet, denoted by a grayscale color bar. The bar chart contains the averaged wetting intensity and the occurrence probability of each range of wetting intensities. In Figure 4-19, the wetting intensity at mixture liquid velocities V_m of 0.5 m/s and 0.7 m/s are compared at low and high water cut. In this case, the intermittent/unstable wetting behavior, indicated by the midrange intensity, is more noticeable at low water cut. The intensity of water wetting increased with water cut.
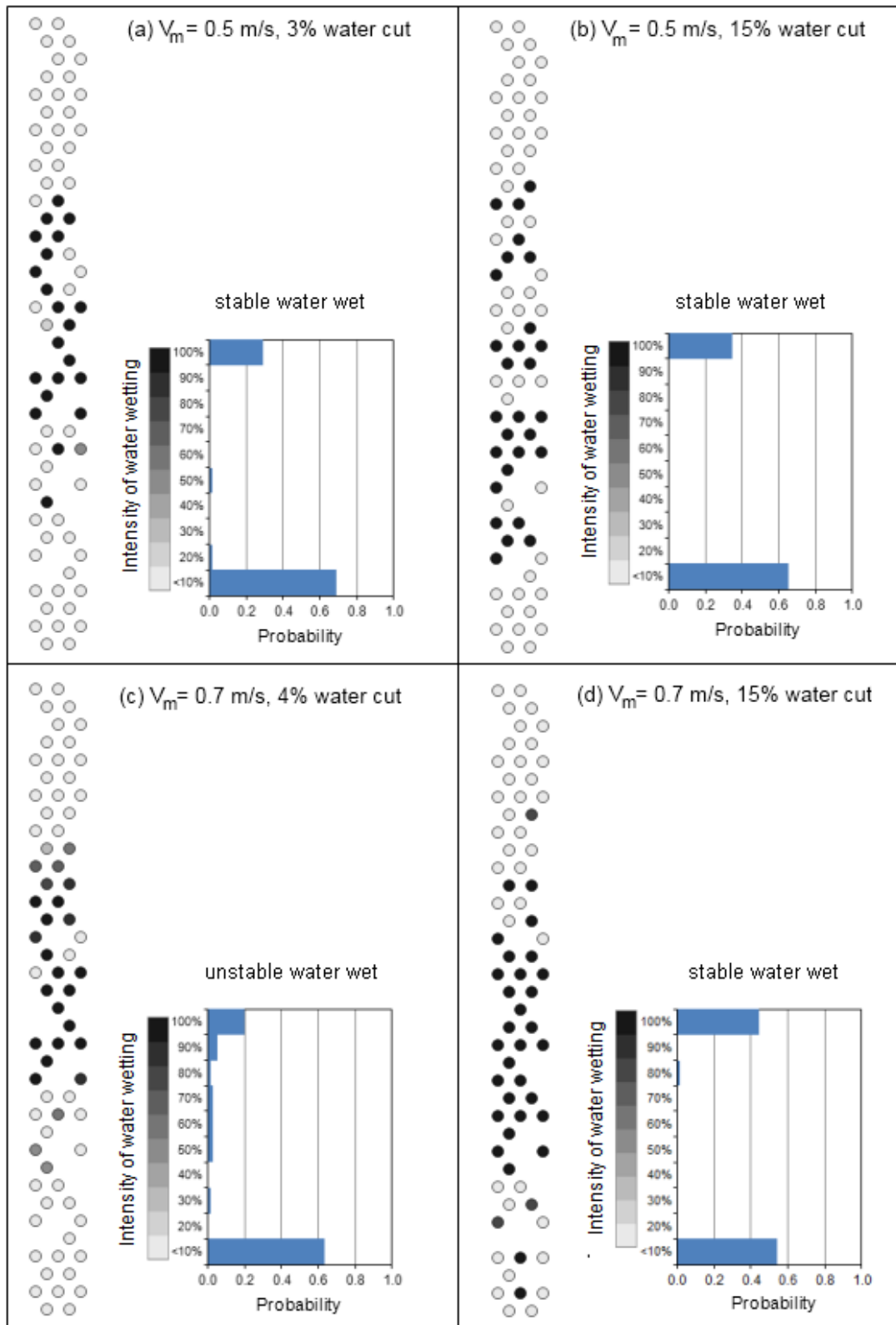
Figure 4-19: Examples of wetting intensity analysis for liquid velocities V_m of 0.5 m/s and 0.7 m/s.

4.3.3.2 Mixture liquid velocities V_m of 1 m/s and 1.3 m/s

By cross-checking the experimental flow pattern map in Figure 4-10, the flow patterns were observed to change gradually from semi-dispersed (S/D) to ST-G and ST-M as the water cut increased. As shown in Figure 4-20, the wetting intensity snapshots at V_m = 1 m/s showed *unstable water wet* at low water cut < 5% and *stable water wet* at higher water cut. It was noted that the lower the water cut, the lower the degree of water wetting that could be observed. The wetted location was observed around the pipe bottom, indicating the presence of water droplets 'touching' the pipe wall. By increasing the liquid velocity to V_m = 1.3 m/s, the degree of water wetting intermittency lessened as the oil flow exerted greater turbulent forces to disperse the water phase. However complete *stable oil wet* was not achieved, instead the surface wetting became *unstable oil wet* at low water cut < 4%, *unstable water wet* at intermediate water cut 4-8% and stable water wet at higher water cut of 10% (Figure 4-20). The unstable wetting behavior can be explained by the water droplet distribution of the semi-dispersed flow pattern, in which the water droplets were sparsely dispersed in the upper pipe section but became concentrated in the lower half section due to gravity. If the droplets are relatively large and heavy, they tend to deviate from the streamlines and momentarily wet the wall before they are lifted away.
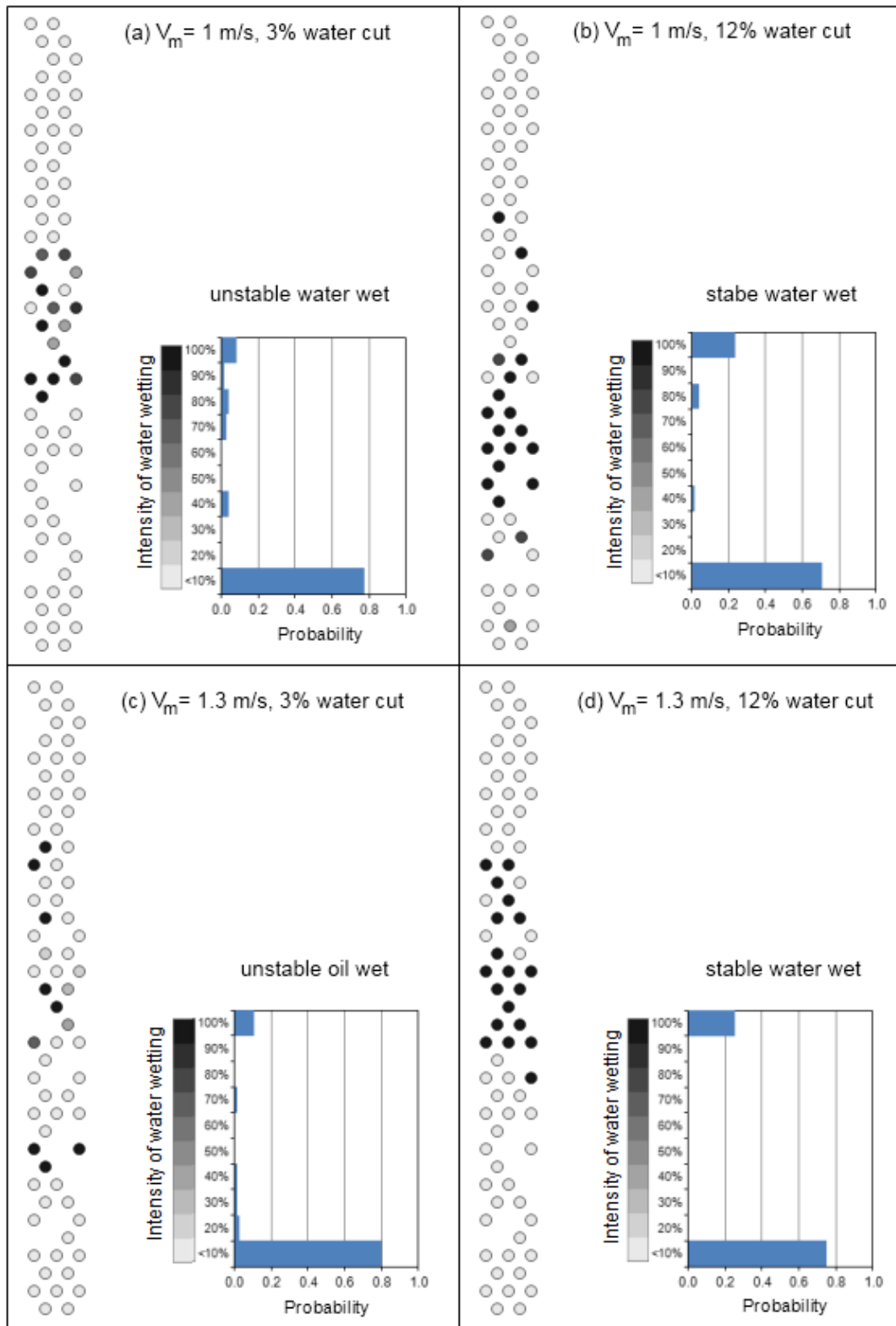
Figure 4-20: Examples of wetting intensity analysis for liquid velocities V_m of 1 m/s and 1.3 m/s.

4.3.3.3 Mixture liquid velocities V_m of 1.5 m/s, 1.7 m/s and 2 m/s

The dispersed flow patterns were reported at low water cuts, while the semi-dispersed flow patterns were seen at higher water cuts, more noticeable at slower liquid velocity. At the lowest 0.5% water cut, the surface wetting showed *stable oil wet* behavior which indicated that the entire interior wall was wetted by the oil phase. However a slight rise of water cut to 1% resulted in *unstable oil wet* in these range of velocities as shown in the wetting intensity map in Figure 4-21. The *unstable oil wet* behavior became more prevalent at higher mixture liquid velocity, showing less intensity for wetting intermittency. *Unstable water wet* behavior was observed at higher water cut > 5% when the intermittency of water wetted pins became more frequent as the flow patterns transitioned to semi-dispersed flow (Figure 4-21). The surface wetting results showed gradual transition from *unstable oil wet* to *unstable water wet* behavior. Some repeated test points in the semi-dispersed flow pattern were found to exhibit an indefinite case between *unstable oil wet* and *unstable water wet*. The unstable behavior can be explained by the possibility of water droplets settling down and momentarily 'touching' the wall before they were lifted away. The findings indicated local water distribution on the wall that was intermittent and unstable in nature. The wetting behavior at mixture liquid velocity of 2 m/s showed a similar response to 1.7 m/s, with wetting intermittency occurring at much lower frequency. *Stable oil wet* was observed at the lowest 0.5% water cut. The wetting behavior gradually changed to *unstable oil wet* and *unstable water wet* condition as the water cut increased. The wetting intensity map is shown in Figure 4-22.
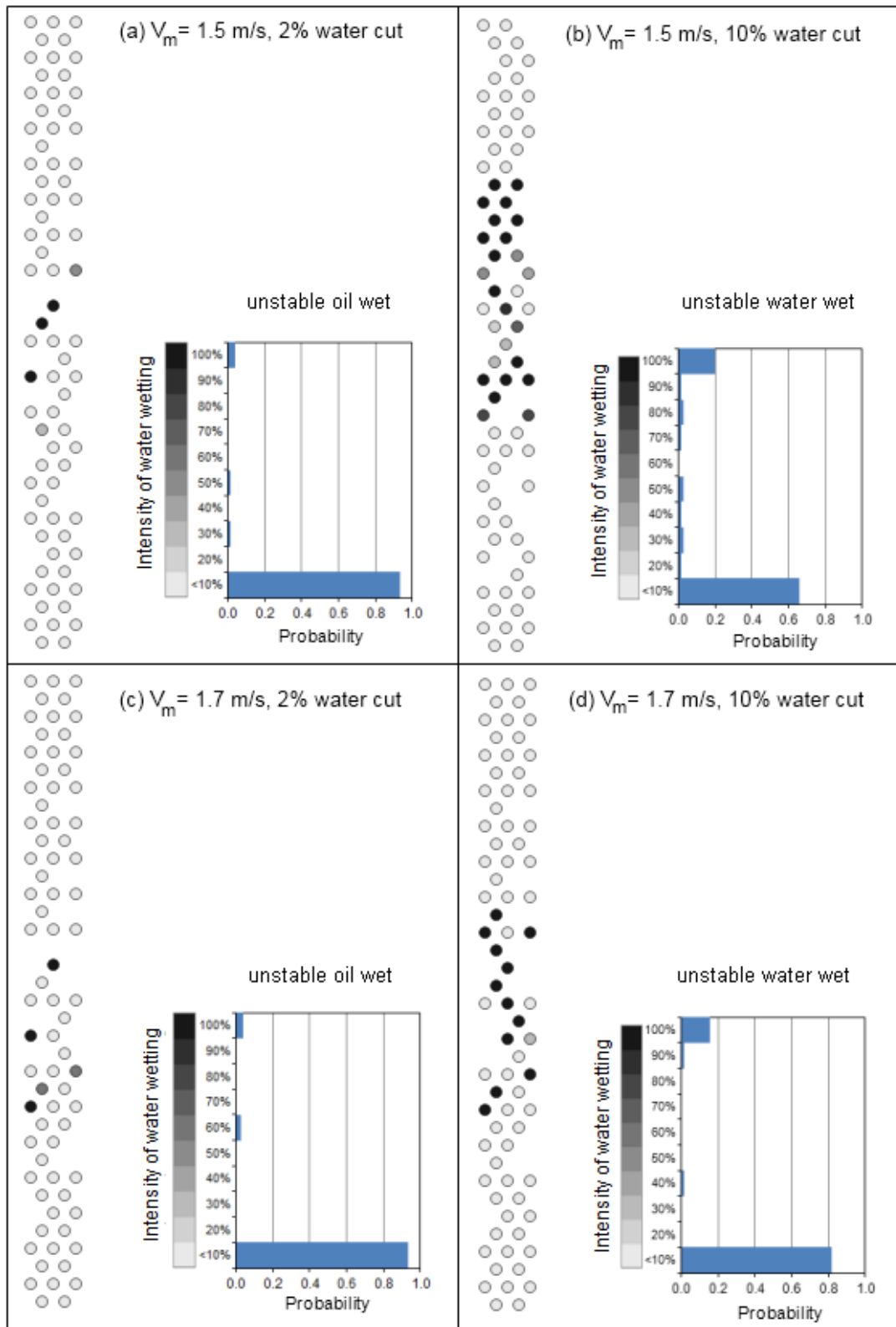
Figure 4-21: Examples of wetting intensity analysis for liquid velocities V_m of 1.5 m/s and 1.7 m/s.
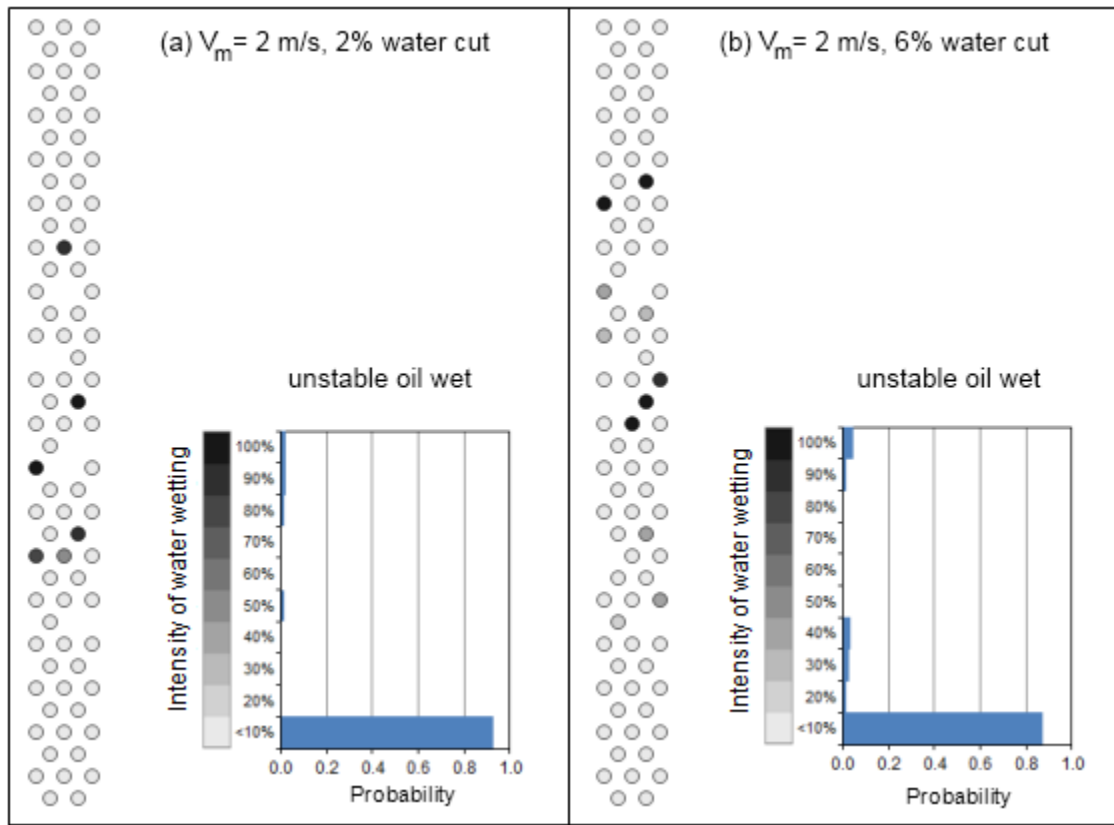
Figure 4-22: Examples of wetting intensity analysis for liquid velocities V_m of 2 m/s.

The surface wetting results showed that water wetting persisted in separated flow when a continuous water layer was present in the horizontal pipe flow. The water wetting locations were found predominantly around the 6 o'clock position in the horizontal pipe. While transitioning to semi-dispersed and dispersed flow patterns at higher velocities, the pipe wall was not completely kept from wetting even though the water phase was mostly dispersed as droplets. The water droplets can still drop out and intermittently wet the pipe wall. The degree of wetting intermittency depended on the liquid velocity and water cut. The division of intermittent wetting into *unstable oil wet* and *unstable water wet* carried a practical implication for the likelihood of internal corrosion occurrence in the pipe. From the standpoint of corrosion, the *water wet* and *unstable water wet* behaviors can be collectively be grouped as 'water wetting' condition in

which corrosion is very likely to occur; while *stable oil wet* and *unstable oil wet* were collectively grouped as 'oil wetting' in which the corrosion is less likely to occur. The presence of unstable localized drops of water on the pipe wall is not as corrosive as the continuous flowing water film since the transport of corrosive species is limited if the water is not replenished continuously.

The current wetting results were compared to previous wetting results using the old pin system (see Cai, *et al*., 2012). As shown in Figure 4-23, the previous wetting results displayed greater oil wetting behavior at lower water cuts (<3% water cut) and high mixture liquid velocities (>1.7 m/s) compared to the present results. The differences can be attributed to:

- Increased sensitivity of the improved pin system that could detect traces of water on the pipe wall.

- Improved pin surface preparation at the start of experiments by polishing and rinsing with continuous running of gas-oil slugs to remove grimes/impurities that may deposit on the pins.
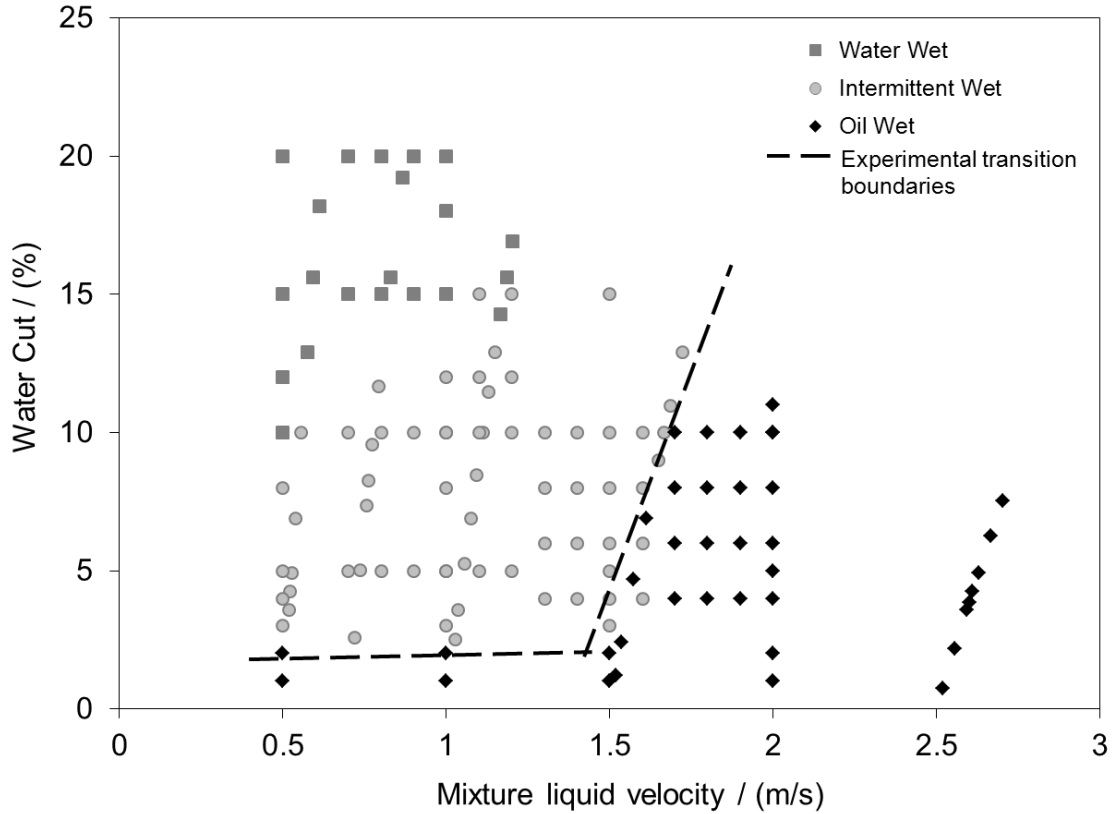
Figure 4-23: Surface wetting map of horizontal LVT200-water flow using previous conductivity pin design (Cai *et al.*, 2012).

4.3.4   Surface wetting at low water cut

The results in this section focus on the surface wetting data at low water cuts of 0.5% and 1%.

4.3.4.1 Mixture liquid velocity V_m of 0.5 m/s and 0.7 m/s

The stratified globules (ST-G) flow patterns were reported at these flow conditions. The wetting intensity snapshots at 0.5% and 1% water cut (Figure 4-24) indicated that *stable water wet* and *unstable water wet* persisted at these conditions. The results implied that water wetting was possible at this low level of water if the liquid velocity is low. The water wet areas indicated

by the solid black circles in the snapshot were located at the pipe bottom which corresponded with the observed swarms of water globules 'touching' the pipe bottom.

4.3.4.2 Mixture liquid velocities V_m of 1 m/s and 1.3 m/s

The semi-dispersed flow patterns were reported at these flow conditions. The wetting snapshots at V_m = 1 m/s (Figure 4-24) indicated *unstable oil wet* at 0.5% water cut and *stable water wet* at 1% water cut. The wetted location was observed around the pipe bottom, which indicated the presence of free water. By increasing the liquid velocity to V_m = 1.3 m/s, the degree of water wetting decreased as the surface wetting became *unstable oil wet* at 0.5% and 1% water cut (Figure 4-25). The *unstable oil wet* behavior can be explained by the droplet distribution of the semi-dispersed flow pattern, in which droplets were seen to distribute with increased concentration toward the lower half of the pipe section. The lower liquid velocity and/or higher water cut posed a higher probability for larger water droplets to drop and momentarily wet the wall before they were lifted.

4.3.4.3 Mixture liquid velocities V_m of 1.5 m/s and 1.7 m/s

The dispersed flow patterns were reported at these conditions. At 0.5% water cut, the wetting snapshot (Figure 4-25) showed *stable oil wet* condition which indicated that the entire interior wall was wetted by oil phase. However a slight rise of water cut to 1% resulted in *unstable oil wet* for both velocities, indicating the possibility of dispersed water droplets settling down and momentarily contacting the pipe wall. Compared to semi-dispersed flow, the intermittency of pin wetting occurred at much lower frequency.

The overall summary of the surface wetting for horizontal oil-water flow at 0.5% to 1% water cuts is shown in Table 4-4. The surface wetting results showed that dispersed or semi-dispersed flow pattern did not guarantee the pipe wall to be free from water wetting even though the water

phase had been dispersed as droplets. The water droplets still can drop out and intermittently wet the pipe wall depending on the liquid velocity and water cut. The wetting results also showed that the instances of intermittent wetting was sensitive to water cut, where it changed from stable oil wet to unstable oil wet with a mere increase of 0.5% water cut. The entrainment velocity corresponds to the liquid velocity required to entrain the water and sustain the oil wetting condition. It was established that light or low viscosity oils generally separate fairly easy and require higher entrainment velocity compared to heavy or viscous oil (Cai et al., 2012). For the LVT200-water system which has fairly light and low viscosity oil, the wetting results showed that the entrainment velocity was about 1 m/s to 1.3 m/s at 0.5% to 1% water cut. This means that water can drop out and, consequently, wetting can occur if the mixture liquid velocity is less than 1.3 m/s at such low water cut. The wetting results at low water cuts were added to the horizontal oil-water wetting map and plotted in Figure 4-26.

Table 4-4: Summary of surface wetting results at low water cut

Liquid velocity (m/s)	Water cut (%)	Experimental wetting results
0.5	0.5	Stable water wet
	1.0	Stable water wet
0.7	0.5	Unstable water wet
	1.0	Stable water wet
1.0	0.5	Unstable oil wet
	1.0	Stable water wet
1.3	0.5	Unstable oil wet
	1	Unstable oil wet
1.5	0.5	Stable oil wet
	1.0	Unstable oil wet
1.7	0.5	Stable oil wet
	1.0	Unstable oil wet
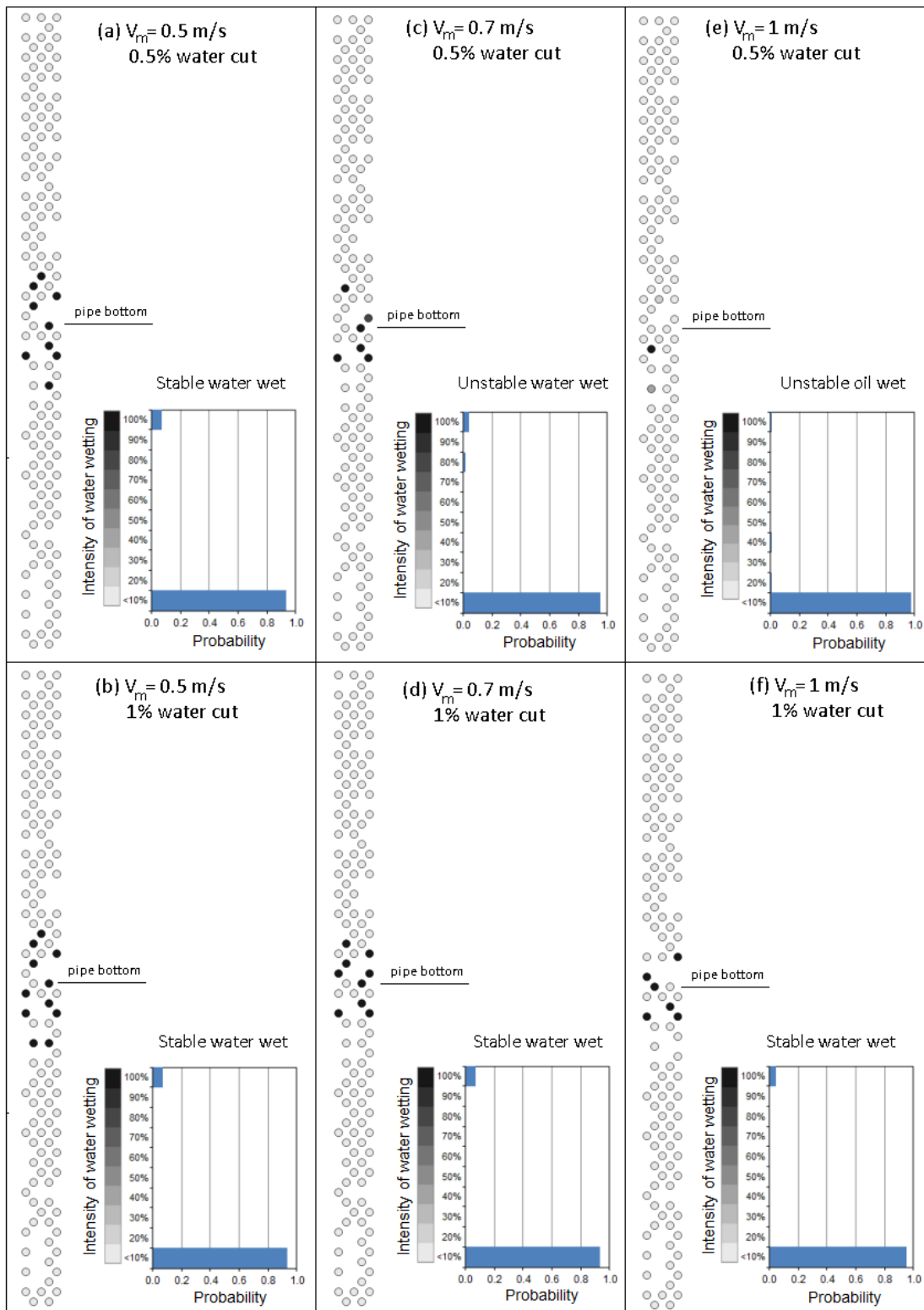
Figure 4-24: Wetting intensity analysis for liquid velocity V_m = 0.5-1 m/s, water cut = 0.5-1%.
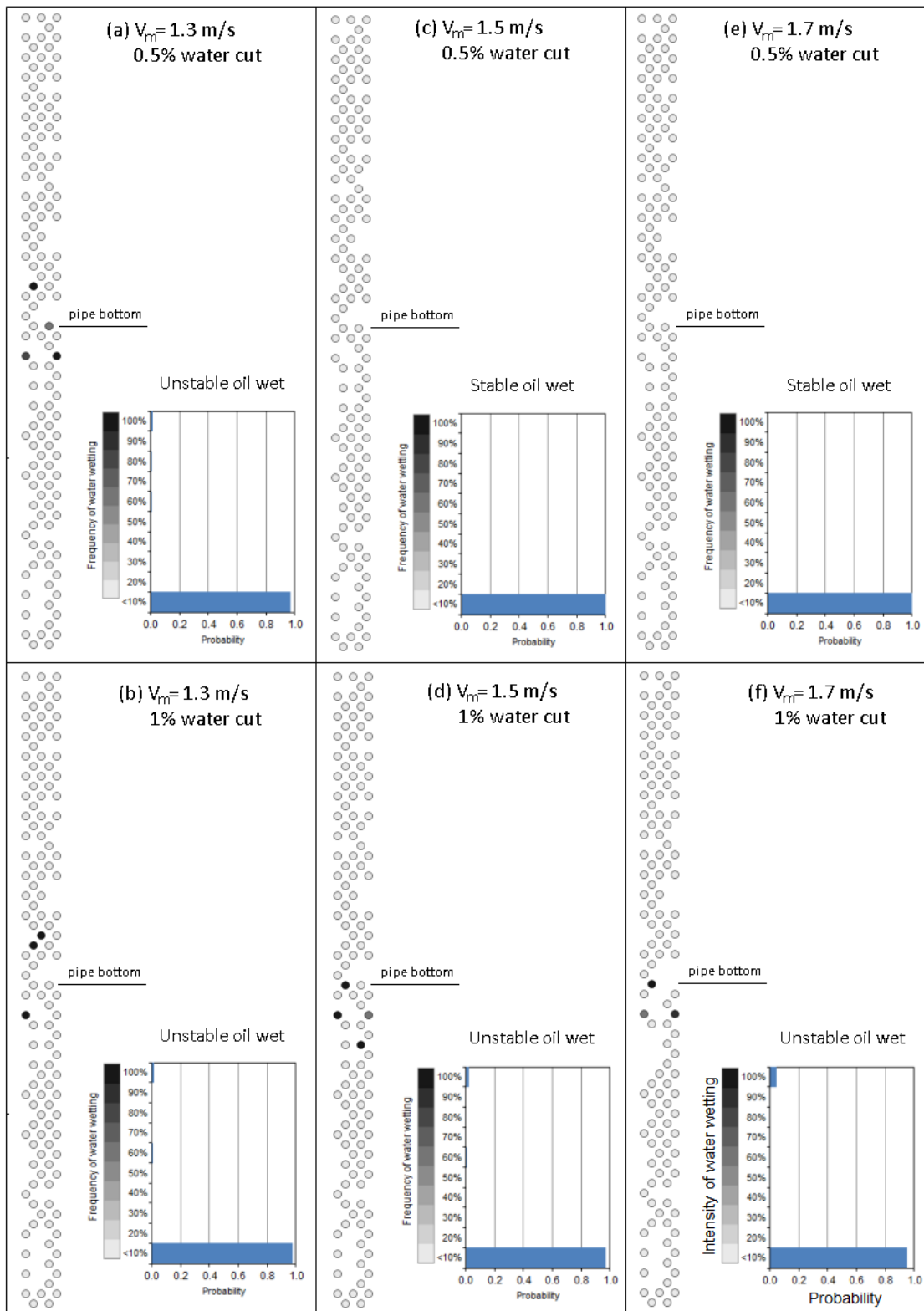
Figure 4-25: Wetting intensity analysis for liquid velocity V_m = 1.3-1.7 m/s, water cut = 0.5-1%.
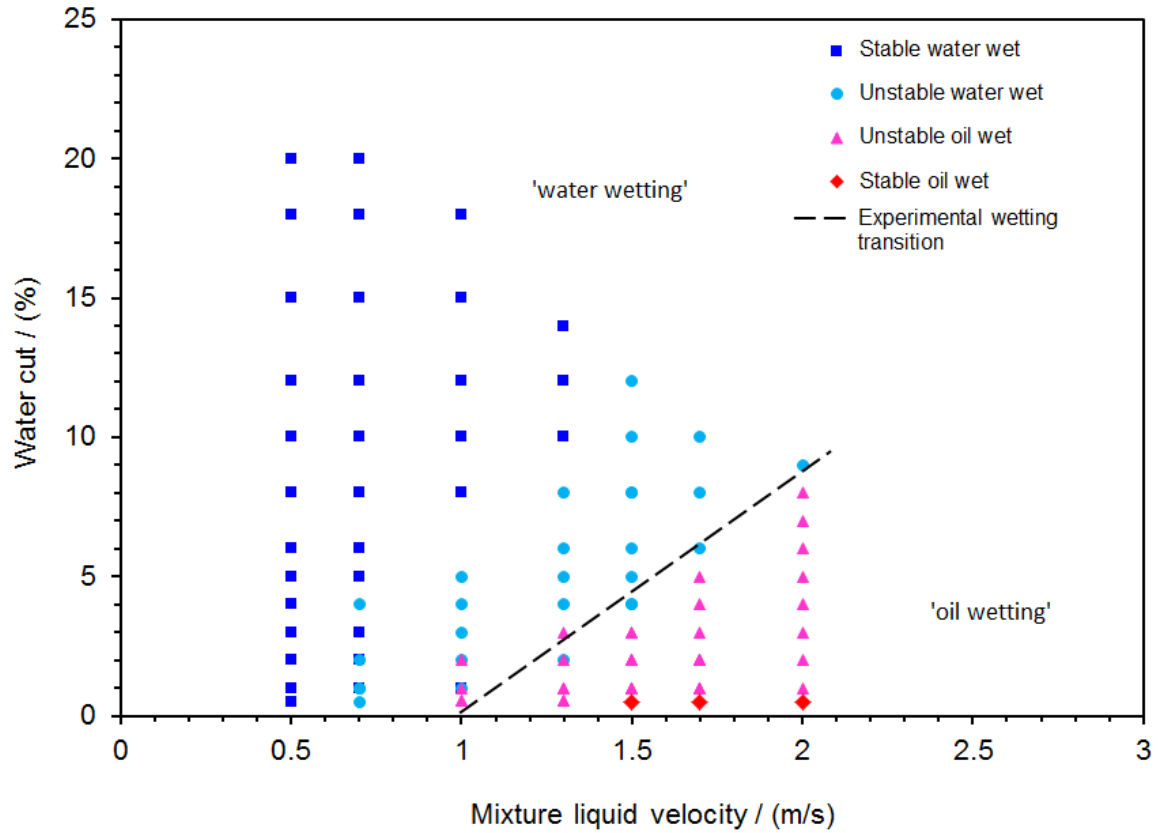
Figure 4-26: Low water cut wetting data added on the wetting map for horizontal LVT200-water flow.

4.4 Vertical oil-water flow

4.4.1 Flow patterns

The flow pattern results for upward vertical flow of LVT200-water systems are presented in this section. For the given flow conditions, oil-in-water dispersed flow patterns were observed. They were further identified as *dispersed globules* and *dispersed droplets* flow patterns, based on the geometry and slip velocity of the dispersed phase. The flow pattern images from the high speed video will be discussed in three groups of mixture liquid velocities, each group tested with varying water cuts.

4.4.1.1 Mixture liquid velocity V_m of 0.5 m/s

The images taken from the high speed camera are presented in Figure 4-27, showing dispersed globules flow pattern at liquid velocity of 0.5 m/s from 3% to 20% water cut. At a low water cut of 3%, the water was dispersed in the form of globules/droplets that were sparsely distributed within the continuous bulk oil flow. The droplets/globules were rounded and relatively small. At 5% water cut, clusters of large water globules can be seen to flow along with the dispersed droplets. The water globules were in flat ovals similar to a '*hamburger*' shape. They flowed in an upward path with very little sideways swerving. As the water cut increased to 10%, the water globules grew into a larger irregular shape that deformed unsteadily as they flowed upwards. The water globules were observed to move much slower than the droplets, showing noticeable slippage. Forces slowing the individual droplet motion are viscous drag and gravity forces.

At the highest tested water cut of 20%, the water globules appeared to cease to grow in size. The droplets became rounded, more closely packed and became harder to observe as discrete droplets. The *in situ* volume fraction of the dispersed phase exceeded the input water cut, resulting in a densely packed dispersion. It was believed that the densely packed droplets bounded by the finite pipe diameter restricted the droplet mobility and growth. These droplets, being closely packed, were likely to 'touch' and wet the pipe when they are flowing in close proximity to the bounded wall. No water slug/churn was observed at all tested water cuts.

4.4.1.2 Mixture liquid velocity V_m of 1 m/s

The flow pattern results at liquid velocity of 1 m/s are shown in Figure 4-28. The observed flow patterns showed a gradual transition from dispersed globules to dispersed droplets flow pattern as evidenced by the diminishing occurrence of larger globules. Because of higher liquid velocity, the increased turbulence resulted in dispersion of water droplets to a finer size that

distributed uniformly across the pipe. At 3% water cut, the water droplets were sparsely distributed across the pipe. Small water droplets and some irregularly shaped globules flowed upward. As water cut was increased to 10%, the dispersed water droplets grew larger and became densely packed. At high water cut of 18%, the droplets were similar in size to that observed for 10% water cut but became more closely packed. The droplets did not seem to coalesce into a larger droplet size.

4.4.1.3 Mixture liquid velocity V_m of 1.5 m/s

At this high liquid velocity, the water phase was broken up into very fine droplets due to the intense turbulence, which is characterized as a dispersed droplet flow pattern as shown in Figure 4-29. The water phase was fully mixed in the oil flow and became difficult to be discretely identified from the images. In addition, the flow pattern visibility was compromised by the unwanted entrainment of air (exists as a dark feature in the image) into the bulk flow from the oil tank. A low level of oil in the tank at high oil velocity unwittingly resulted in gas from the gas cap mixing with the oil leaving the oil tank and circulating in the flow loop.

The flow pattern map results for vertical oil-water flow are plotted in a flow pattern map shown in Figure 4-30, showing *dispersed globules* at lower liquid velocity and *dispersed droplets* at higher liquid velocity.
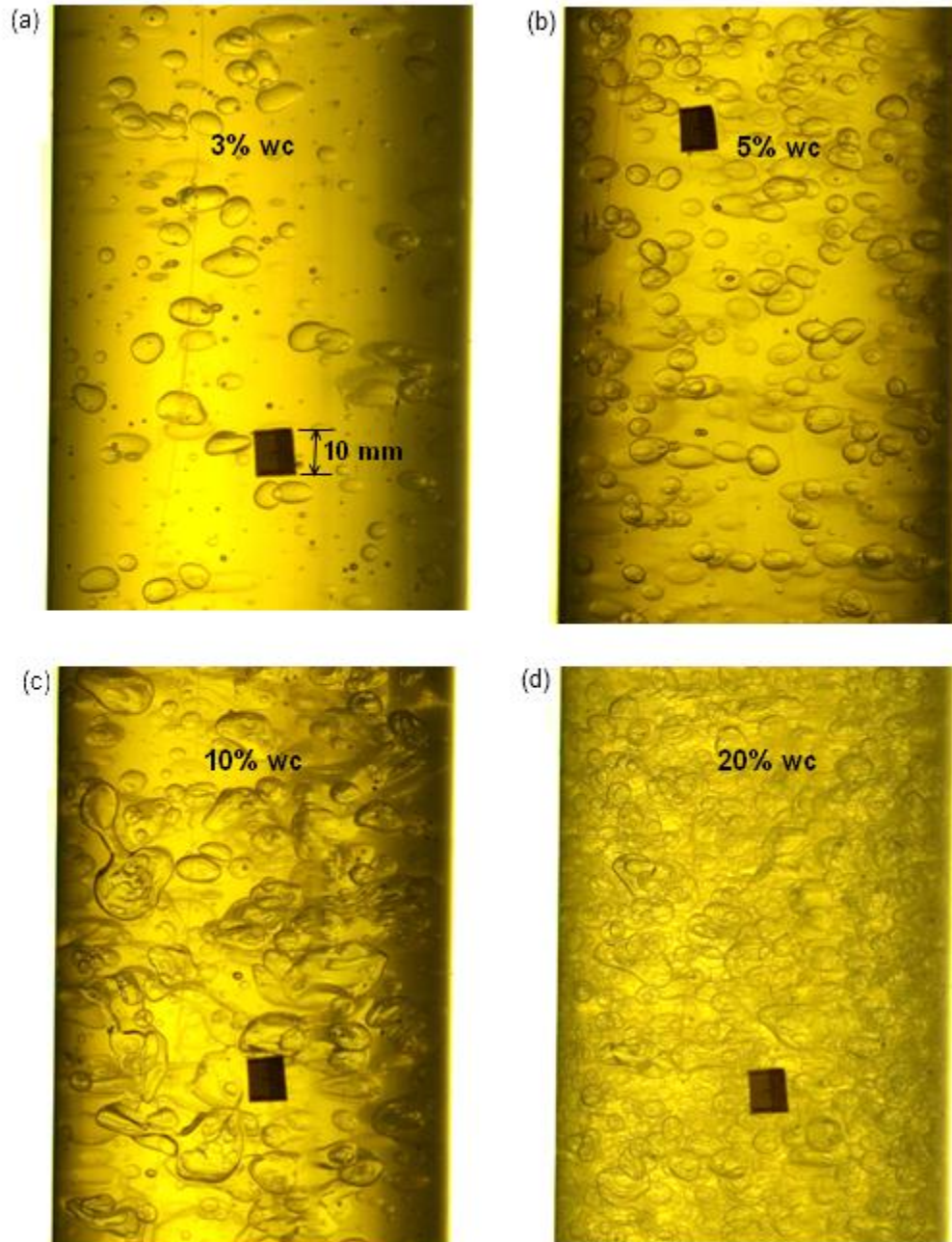
Figure 4-27: Images of vertical oil-water flow patterns at liquid velocity $V_m = 0.5$ m/s for 3% to 20% water cuts.
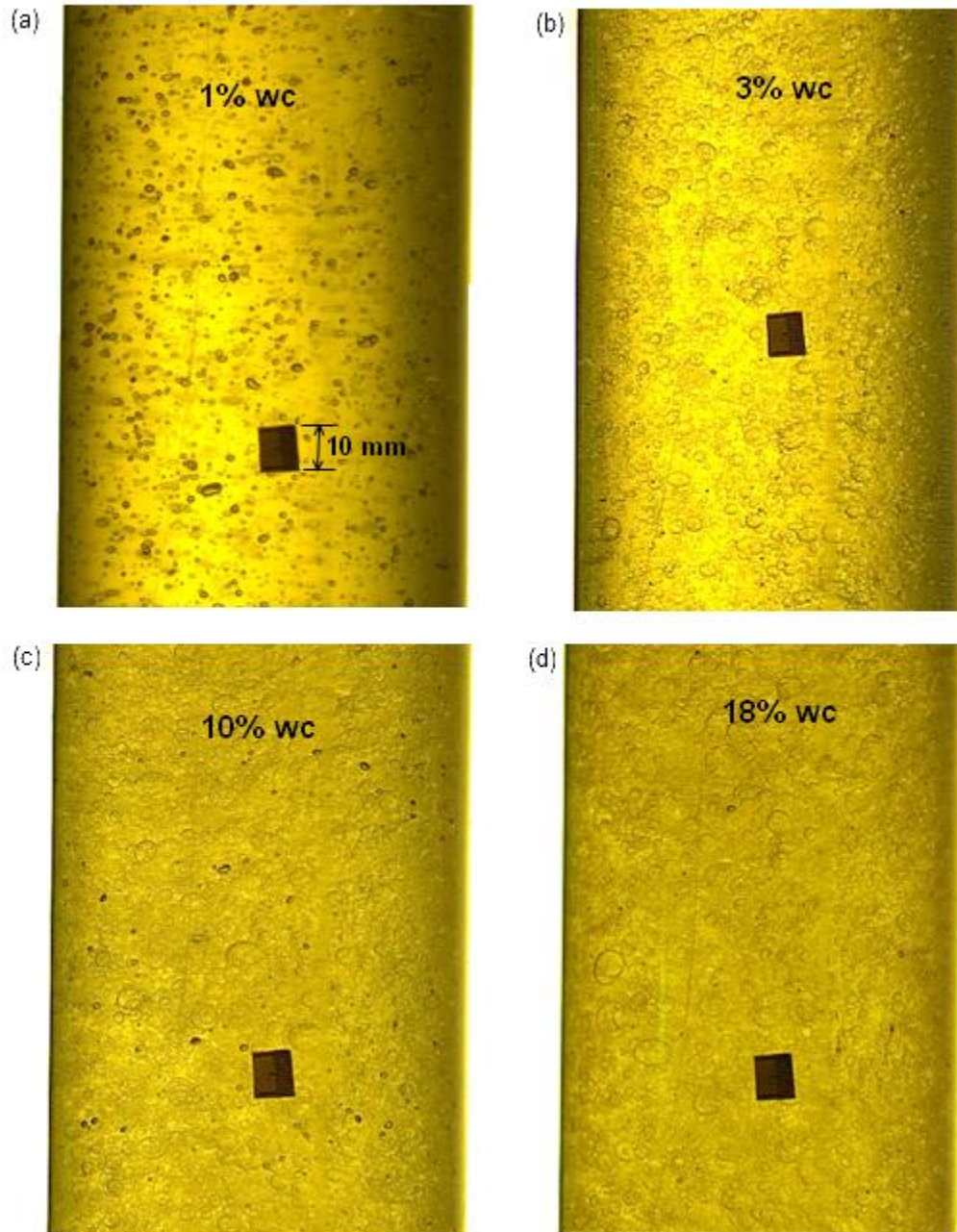
Figure 4-28: Images of vertical oil-water flow patterns at liquid velocity V_m = 1 m/s for 1% to 18% water cuts.
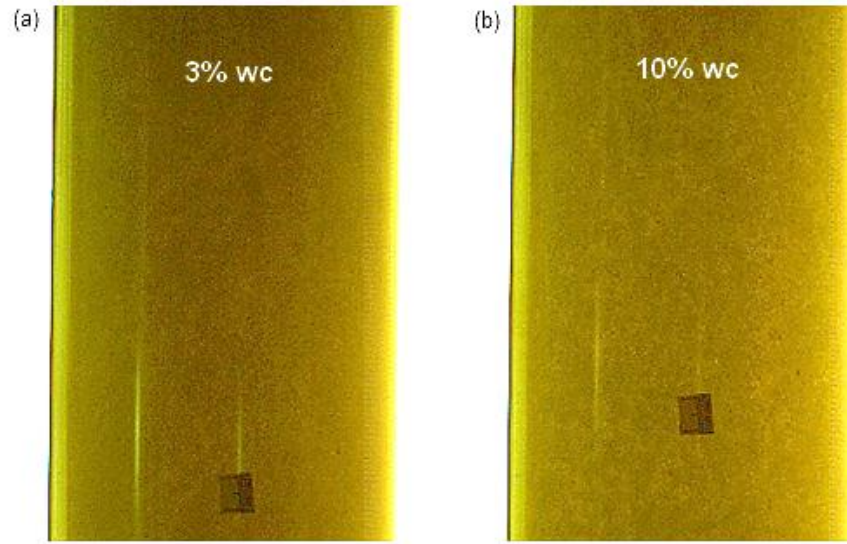
Figure 4-29: Images of vertical oil-water flow patterns at liquid velocity V_m = 1.5 m/s for 3% and 10% water cuts.
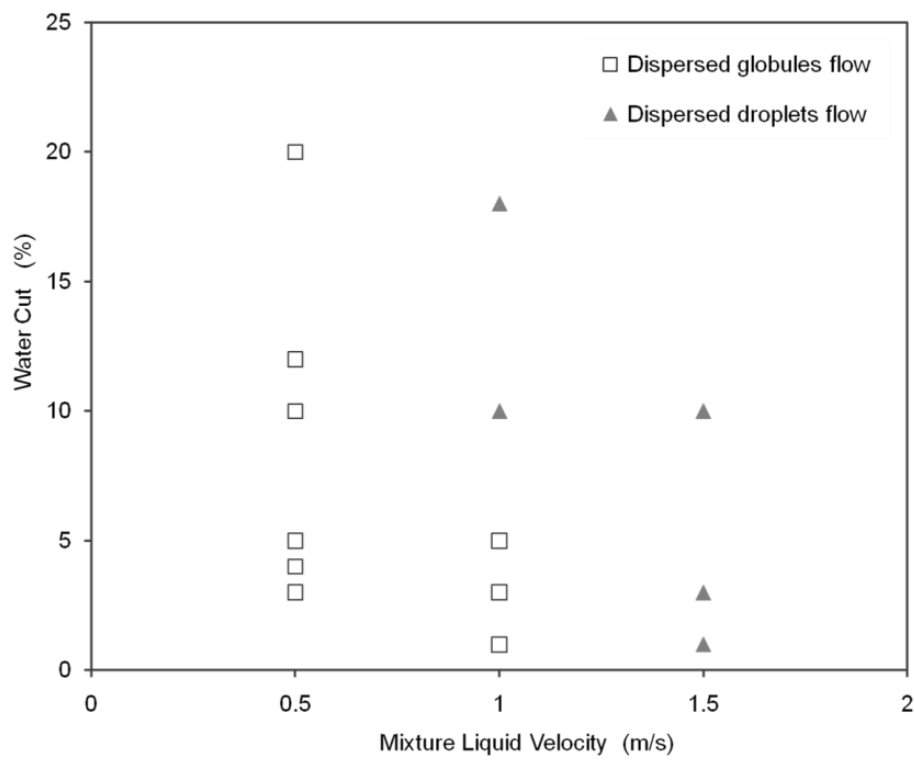
Figure 4-30: Flow pattern map for vertical LVT200-water flow in a 0.1 m ID pipe.

4.4.2   Surface wetting

The surface wetting experiments were performed in the vertical flow loop using a steel test section mounted with 360-degree conductivity pins. Similar to the horizontal oil-water flow, the surface wetting results were obtained using model oil LVT200-water system, and tested on a clean steel surface condition. Prior to actual tests, the vertical pipe was circulated with continuous run of gas-oil slugs for half hour which proved to be helpful in removing any water film that might backflow and stick on the test section while inclining the flow loop to vertical orientation. The surface wetting data were analyzed according to four categories of wetting regimes: *stable water wet, unstable water wet, unstable oil wet and stable oil wet* (see Section 4.3.3).

The wetting results obtained from the conductivity pins are plotted on a wetting map in Figure 4-32 with the water cut as the *y*-axis and total mixture liquid velocity as the *x*-axis. Each data point on the map indicates the surface wetting regime at the tested conditions. The surface wetting results show that *stable oil wet* generally prevails for vertical oil-water flow, which means water is kept from wetting the pipe wall by the continuous oil phase. One example of stable oil wet condition is given in the wetting intensity analysis in Figure 4-31. The surface wetting changed to *unstable oil wet* when the water cut increased beyond 14% at liquid velocities of 0.5 m/s to 1 m/s, see the example of unstable oil wet condition in Figure 4-31. At those flow conditions, the wetting results indicated that most of the pipe wall area was oil wet with few locales (indicated by pins) changing intermittently and randomly. The numbers of water wetted locales were limited; indicating the *unstable oil wet* condition was as good as the *oil wet* condition
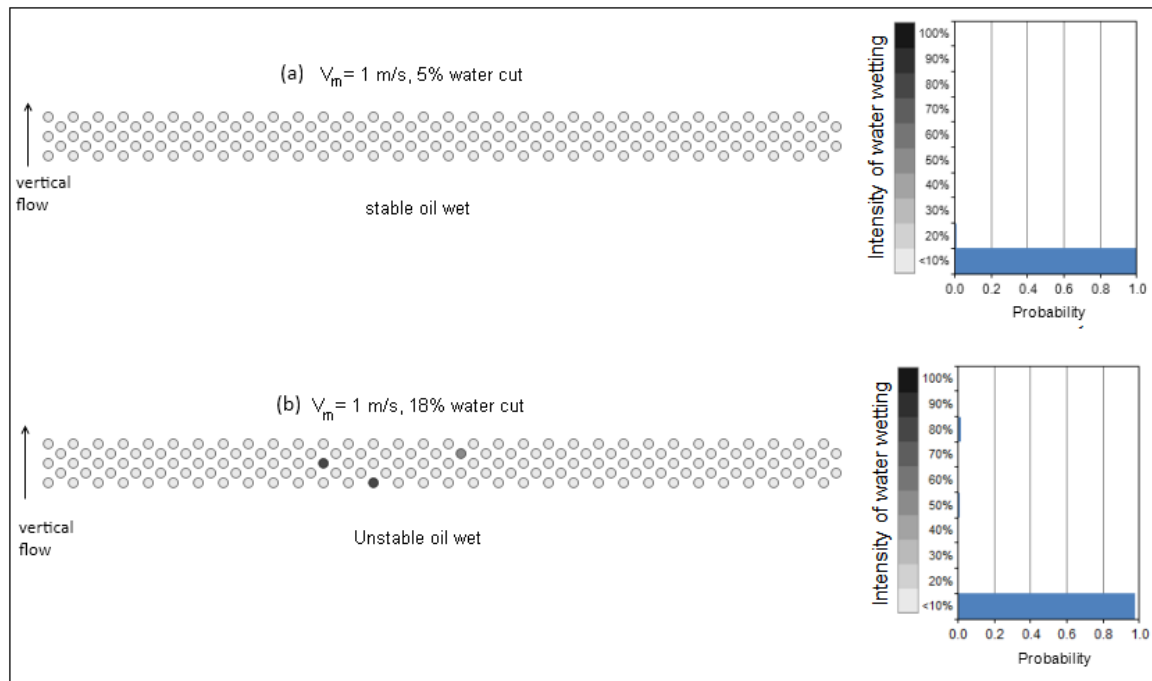
Figure 4-31: Example of wetting intensity analysis at V_m = 1 m/s, 5% water cut, showing stable oil wet.

With an increase in liquid velocity, the droplet size was reduced due to the higher turbulent breaking force to act against the droplet surface tension. However the velocity did not have a remarkable influence on the surface wetting. The water phase was mostly kept from the pipe wall regardless of the input velocity, indicating the flowing water droplets seldom deviated from the streamline of a straight flow path. Upon examining the high speed camera recordings, the oil wetting behavior at low water cut can be explained by the sparse distribution of water droplets/globules that moves in a relatively straight upward path, with little likelihood of impinging sideways onto the wall since the gravity is not acting to pull the water to the wall and the viscous drag tends to guide the fluid particle along the streamlines of bulk flow. Increasing the water cut beyond 14% caused the dispersed droplets to coalesce to larger size and pack more closely to each other. These crowded globules near the wall were likely to contact and wet the pipe wall when they are flowing in close proximity to the wall, resulting in *unstable oil wetting*.

However, the wetting is minimal as the Saffman lift and lubrication force may exist to prevent the droplets from approaching too close to the solid wall (Hubbe *et al.*, 2009). In addition, the *unstable oil wet* behavior appeared to be slightly more prevalent at lower liquid velocity compared to higher liquid velocity. If the droplets are relatively large in lower liquid velocity, one needs to consider the effect of gravity and momentum as they are likely to deviate from the streamlines of flow. On the other hand, the smaller droplets entrained in fast flowing oil stream may be thought to have less likelihood of collision to the wall due to their smaller inertia and more rounded geometry to flow in a straight path.

In the current study, the prevailing oil wetting occurred for a freshly polished test section in vertical flow. However, the truly vertical pipes seldom exist in the oil fields. It was observed that when the test section was slightly inclined off the true vertical axis (90°), the gravity pulled down the water droplets to wet the inclined wall, resulting in *water wetting*. Once the water adhered to the pipe wall which is naturally more hydrophilic (water-loving), the wetting persisted and was not easily displaced by the continuous oil flow alone. The
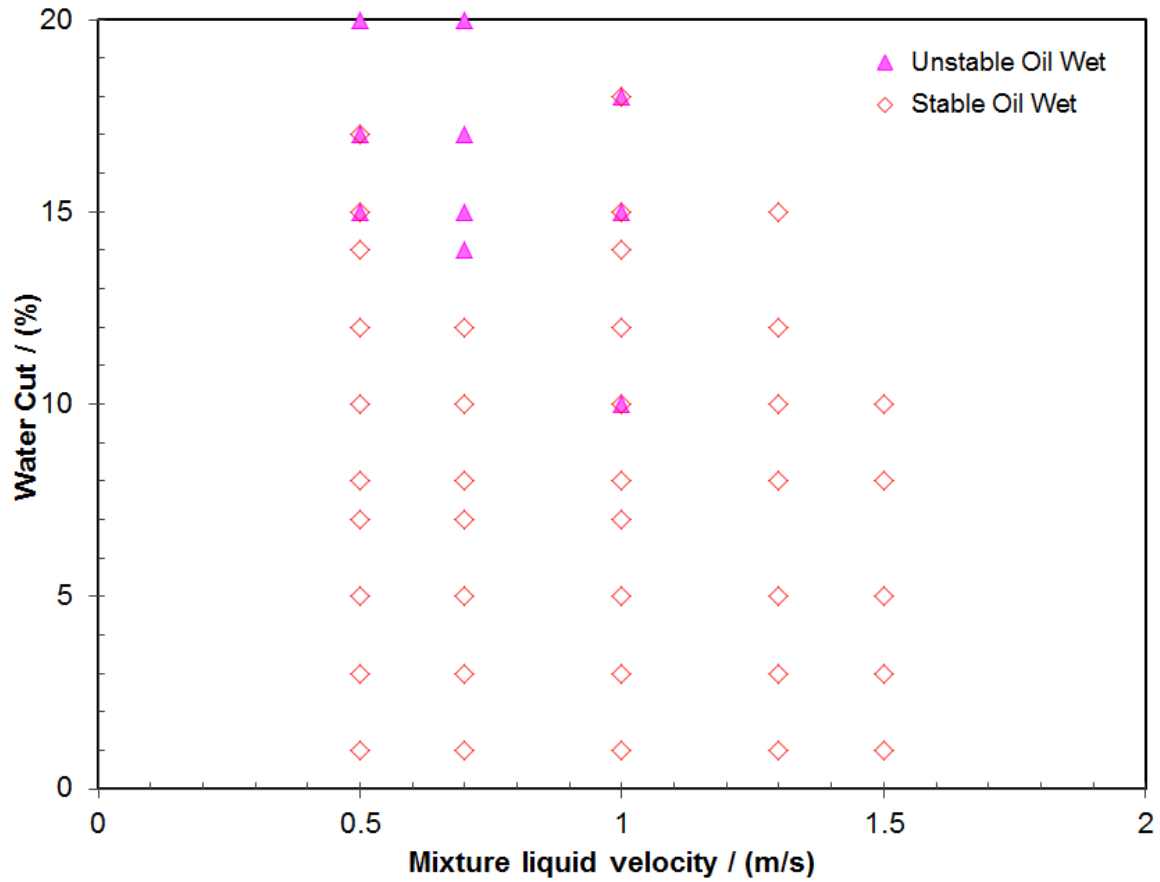
Figure 4-32: Surface wetting map for vertical LVT200-water in the present study.

4.5 Droplet size distribution

The water-in-oil dispersion experiments were carried out in a 0.1 m ID horizontal flow loop using LVT 200 model oil as the continuous phase and 1 wt.% NaCl aqueous solution as the dispersed water phase. The test series was designed to study the influences of flow rate and concentration fraction of the dispersed phase by varying the total mixture liquid velocities from 1 m/s to 1.7 m/s at two fixed water cuts: 1% and 5%. The water cut of 5% was chosen as the upper limit with the current device set up. Beyond 5% water cut, the dispersion formed was found to be too dense to be discretely distinguished. The image analysis was carried out for water-in-oil

dispersion flow pattern for the case of semi-dispersed and fully dispersed flow patterns in horizontal oil-water flow.

The photographic technique is a simple and direct way of measuring the droplet size based on the image obtained. This method has some limitations related to the focus and illumination issues as it may only capture images of droplets closest to the wall. The experimental procedure and image analysis are described below. Droplet motions were recorded with a high speed camera (model Phantom v12.1) with the image data logged continuously to a host computer. The droplet images were analyzed using image processing software, Phantom Cine Viewer™ v2.0, that allowed digital image enhancement and measurement. The image scale was obtained by calibrating the measurement with a 10 mm length ruler placed on the transparent wall of the viewing pipe section. For better recognition of individual droplets, the images were manually adjusted to attain optimal brightness, contrast, sharpness and color. The images were converted into gray scale and imported to Excel for pixel counting. The individual droplet size was estimated by measuring the largest chord length. A sampling of at least 50 discrete droplets with spherical or near spherical shape was measured for each test case. Following the work of Hesketh, et al. (1987) and Vielma, et al. (2008), the droplet size distribution can be statistically described by a log-normal distribution function. The droplet size spectra were statistically analyzed and fitted to log-normal function. SMD (Sauter mean diameter) and d_{95} (95 percentile size in the droplet distribution, representing maximum droplet size) were determined for each case.

4.5.1   Droplet size in horizontal flow

By analyzing the high speed video files, the water droplets at various dispersion conditions of horizontal oil-water flow can be extracted. In pipe flow, the breakup of a single droplet occurs when the surface tension force holding a droplet together is overcome by the local fluid inertial

force generated by the turbulent fluctuations as described by Hinze theory (Hinze, 1955). Figure 4-33 shows the snippets of water droplets at varying mixture liquid velocities for the case of 1% and 5% water cuts. It was observed that at low velocity, the water-in-oil dispersion was sparse and large size. As the velocity increased, the dispersion became smaller size and packed more densely. This was attributed to an increase in turbulent energy with higher oil velocity which could fragment the water into smaller droplets. The effects of changing flow velocity and concentration fraction of dispersed phase are examined. From the collection of measured droplet size, the statistical parameters μ and σ were determined for each case as listed in Table 4-5.

In the log-normal distribution, the geometric mean is calculated by taking the average of the logarithmic values of a data set and converted back to a base 10 number, expressed as e^{μ}. The geometric mean characterizes the central tendency of a data set that is unbiased by few very high or low values, as compared to arithmetic mean which is biased upward by data points of high values (Dittmann & Maug, 2008). The expression for geometric mean is written in Eq. (4.1):

$$\text{Geometric mean: } e^{\mu} = \exp\left\{\frac{1}{n}\sum_{i=1}^{n}\ln(x_i)\right\} \tag{4.1}$$

Table 4-5: Log-normal distribution parameters for droplet size spectra in oil-in-water dispersion

Test run	Superficial velocity (m/s)		Log-normal distribution parameters		Geometric mean e^{μ} (mm)
	V_{so}	V_{sw}	σ	μ	
1.0 m/s, 1% water cut	0.99	0.01	0.27	0.77	2.15
1.3 m/s, 1% water cut	1.287	0.013	0.24	0.66	1.93
1.5 m/s, 1% water cut	1.485	0.015	0.24	0.57	1.77
1.7 m/s, 1% water cut	1.683	0.017	0.27	0.44	1.56
1.0 m/s, 5% water cut	0.95	0.05	0.31	0.90	2.45
1.3 m/s, 5% water cut	1.235	0.065	0.32	0.78	2.19
1.5 m/s, 5% water cut	1.426	0.075	0.24	0.70	2.01
1.7 m/s, 5% water cut	1.615	0.085	0.36	0.34	1.40
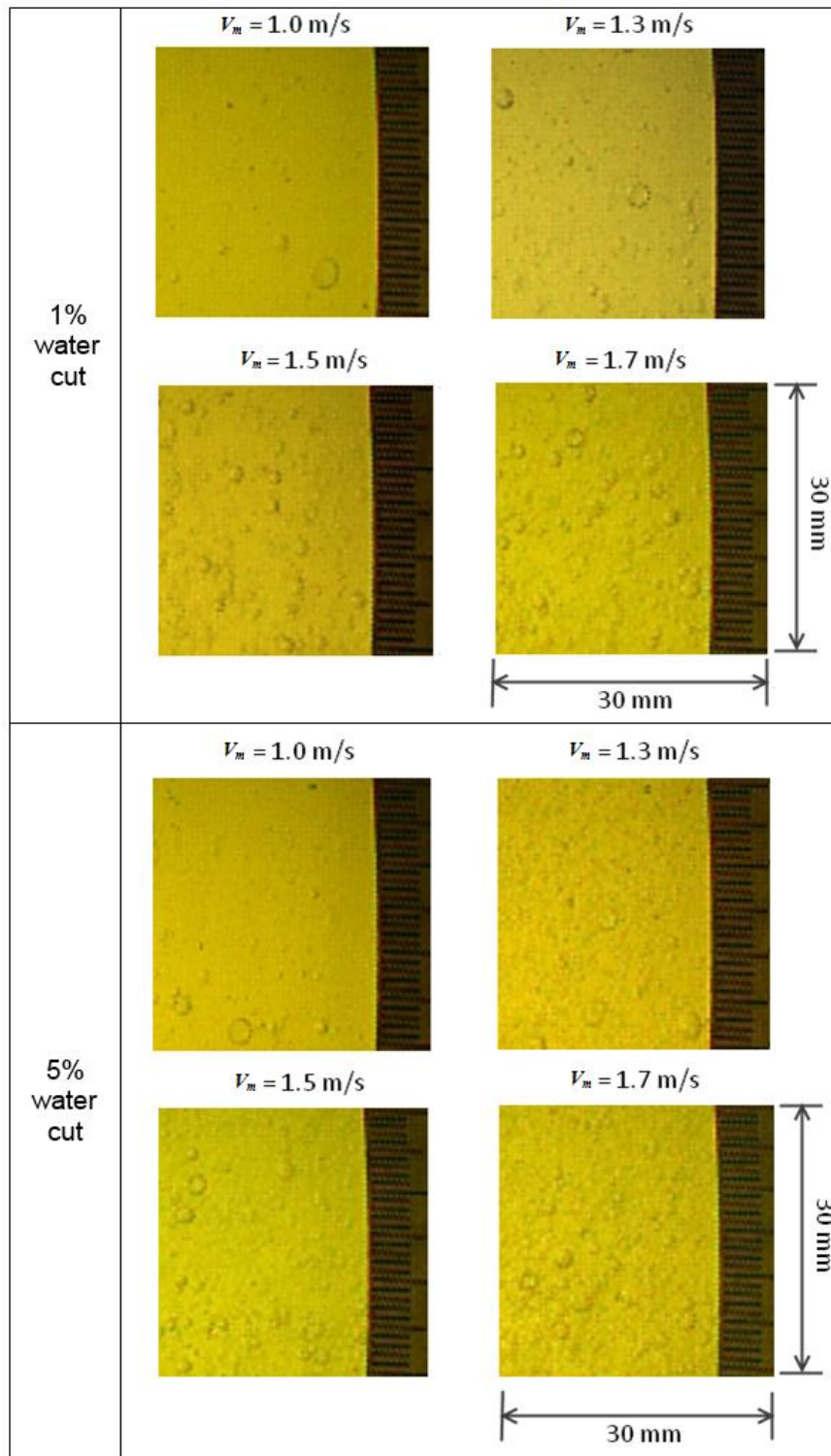
Figure 4-33: Snippet images of water-in-oil dispersion at liquid velocities V_m = 1 m/s to 1.7 m/s for 1% for 1% and 5% water cuts.

The evolution of the geometric mean diameter of the droplet size distribution has been plotted in Figure 4-34. The plot shows a linear reduction trend with an increase of mixture liquid velocity for the case of 1% and 5% water cuts.
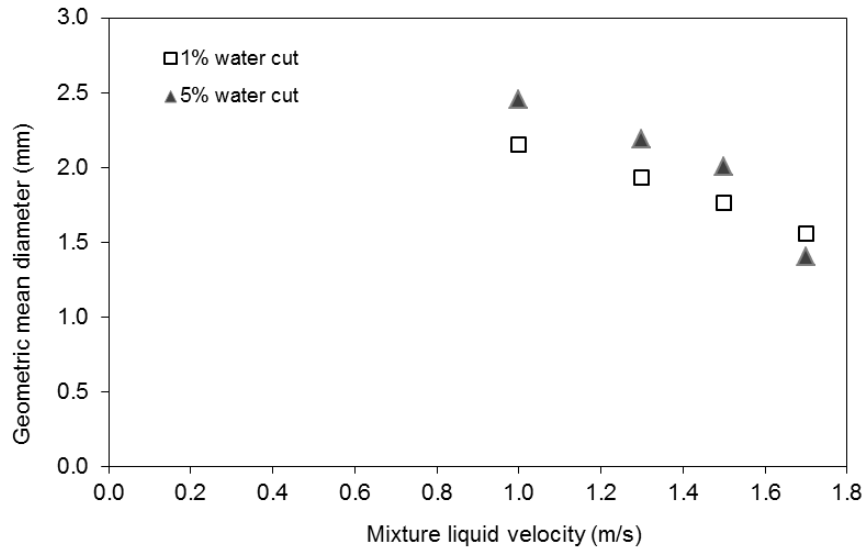
Figure 4-34: Variation of geometric mean diameter with liquid velocity at 1% and 5% water cut.

The log-normalized distribution and cumulative distribution for the droplet size spectra at different liquid velocities are plotted in Figure 4-35 for 1% water cut and Figure 4-36 for 5% water cut, respectively. The distribution profiles are shifted leftward and became narrower to smaller size scale as the liquid velocity increases. This can be attributed to the increased fragmentations tendency of larger droplets into smaller ones as the turbulence breaking force increases at high liquid velocity.
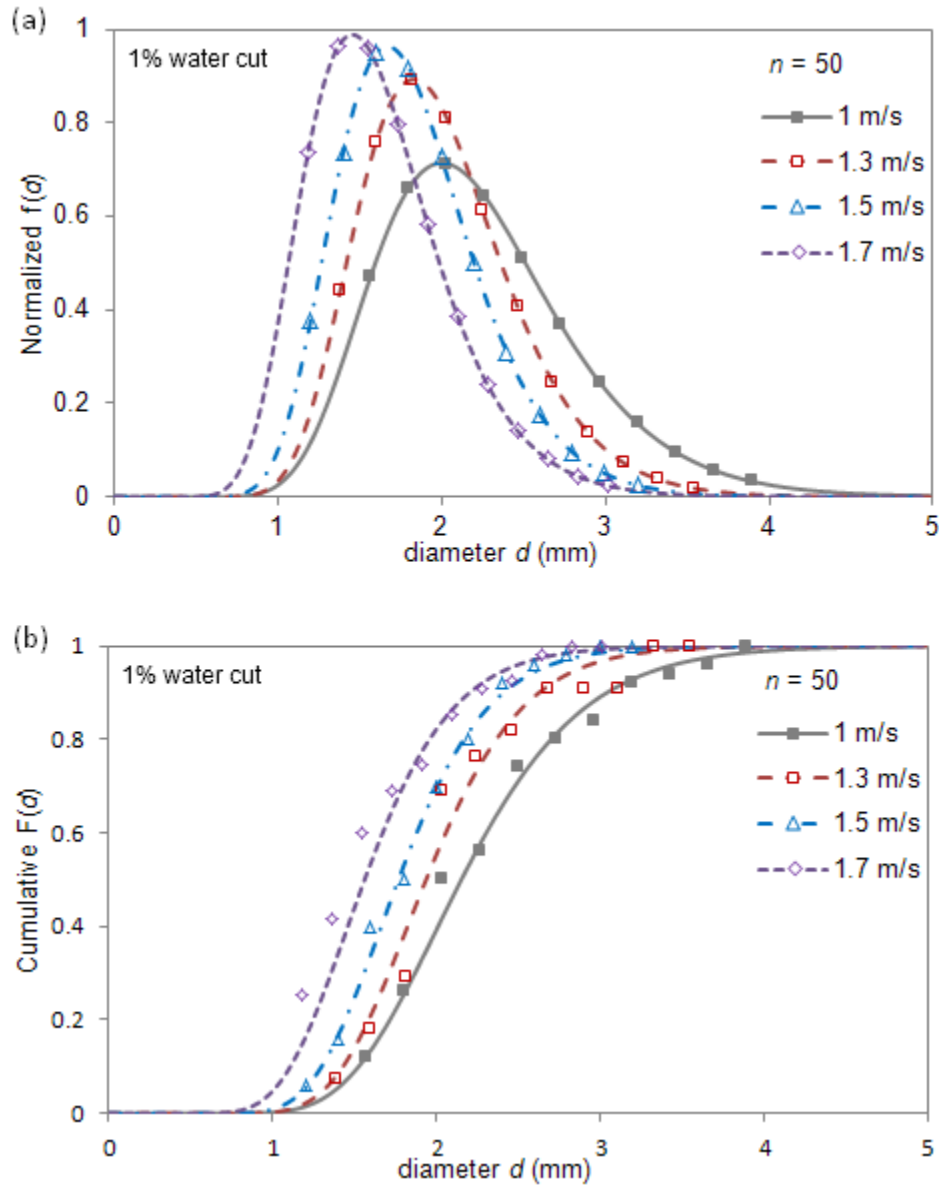
Figure 4-35: Profiles of droplet size spectra with different liquid velocities at 1% water cut and best fit with (a) normalized and (b) cumulative, log-normal distribution.
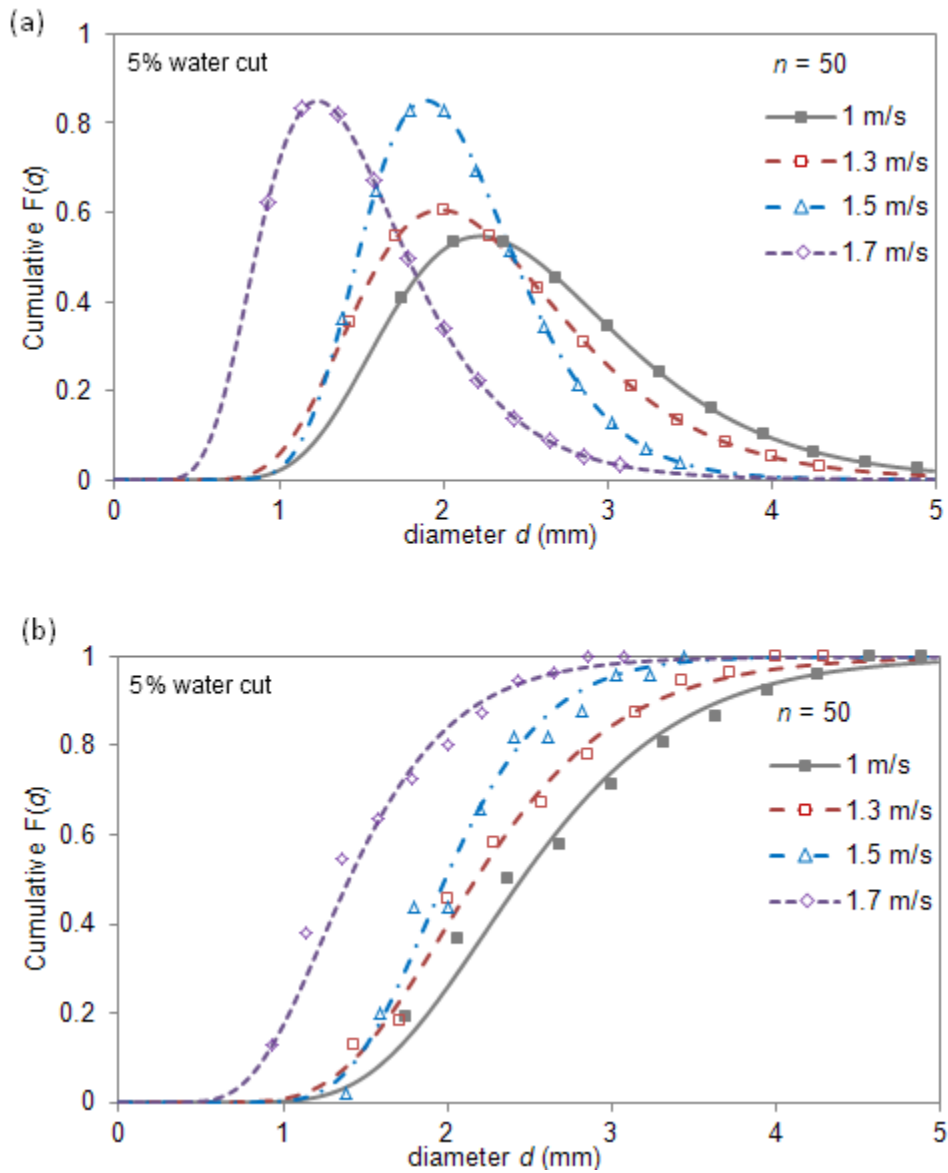
Figure 4-36: Effect of change in mixture liquid velocity on experimental droplet size data at 5% water cut and best fit with (a) normalized and (b) cumulative Log-normal.

By fitting the measured droplet size spectra to a log-normal distribution function, the 95th percentile d_{95} of the droplet distribution can be estimated for each test case. The SMD can be computed according to Eq.(2.16) and the results are shown in Table 4-6. The values for largest measured droplet diameter d_{max} are also included.

Table 4-6: Droplet size results in water-in-oil dispersion

Test run	diameter (mm)		
	$d_{max}{}^+$	d_{95}	d_{32} (SMD)
1 m/s 1% water cut	3.7	3.3	2.6
1.3 m/s 1% water cut	3.2	2.9	2.3
1.5 m/s 1% water cut	2.8	2.6	2.0
1.7 m/s 1% water cut	2.6	2.4	1.9
1 m/s 5% water cut	4.6	4.1	3.1
1.3 m/s 5% water cut	4.0	3.7	2.8
1.5 m/s 5% water cut	3.2	3.0	2.3
1.7 m/s 5% water cut	2.9	2.8	1.9

+ diameter of largest measured drop

Figure 4-37(a) shows the variation of the SMD with total mixture liquid velocities for water cut of 1% and 5% respectively. The maximum and minimum variations (with 95% confidence interval) for the data set are included in the plot. The variations were the inferential error incurred through the manual measurements of droplet size. As the total mixture liquid velocity increases, the SMD tends to reduce due to higher turbulence intensities provide stronger breaking force to break up the droplets. Similar behavior was reported by Vielma, et al. (2008). If one compares the data the same liquid velocity with similar level of turbulence, the SMD for 1% water cut is smaller than that at 5% water cut. It is noted that the size difference diminishes as the liquid velocity increases.

Figure 4-37(b) depicts the change of the d_{95}, a statistical parameter representing the maximal droplet size in the droplet distribution with varying mixture liquid velocities at fixed 1% and 5% water cut, respectively. The d_{95} was found to decrease with rising liquid velocities, showing similar trend as the SMD data. An increase in the mixture liquid velocity provides larger turbulent forces to break up the water into smaller droplets while an increase in water cut increases the

coalescence tendency to form larger water droplets, more noticeably when the turbulence level decreases.

Results in Table 4-6 show the three listed diameters: d_{max}, d_{95} and SMD correspond very closely to each other. The comparisons are plotted in Figure 4-38 and linear correlations can be found between the SMD, d_{95}, and d_{max} as follows:

$$SMD = 0.76 d_{95} \qquad d_{max} = 1.1 d_{95} \tag{4.2}$$

The fixed constants of proportionality suggest that these diameters can be equivalently interchanged for droplet size correlation calculations. In comparison with other droplet size studies for liquid-liquid dispersion in pipe flow, the SMD/d_{95} ratio derived from Karabelas (1978) was approximately 0.49. Hesketh, *et al.* (1987) reported an average SMD/d_{99} ratio of 0.62. Using two different types of pipe material, Angeli & Hewitt (2000) derived significantly different SMD/d_{95} ratios which was 0.92 for acrylic pipe and 0.50 for stainless steel pipe. It appeared that the droplets were affected by the properties of the fluids, pipe diameter and pipe wall material.
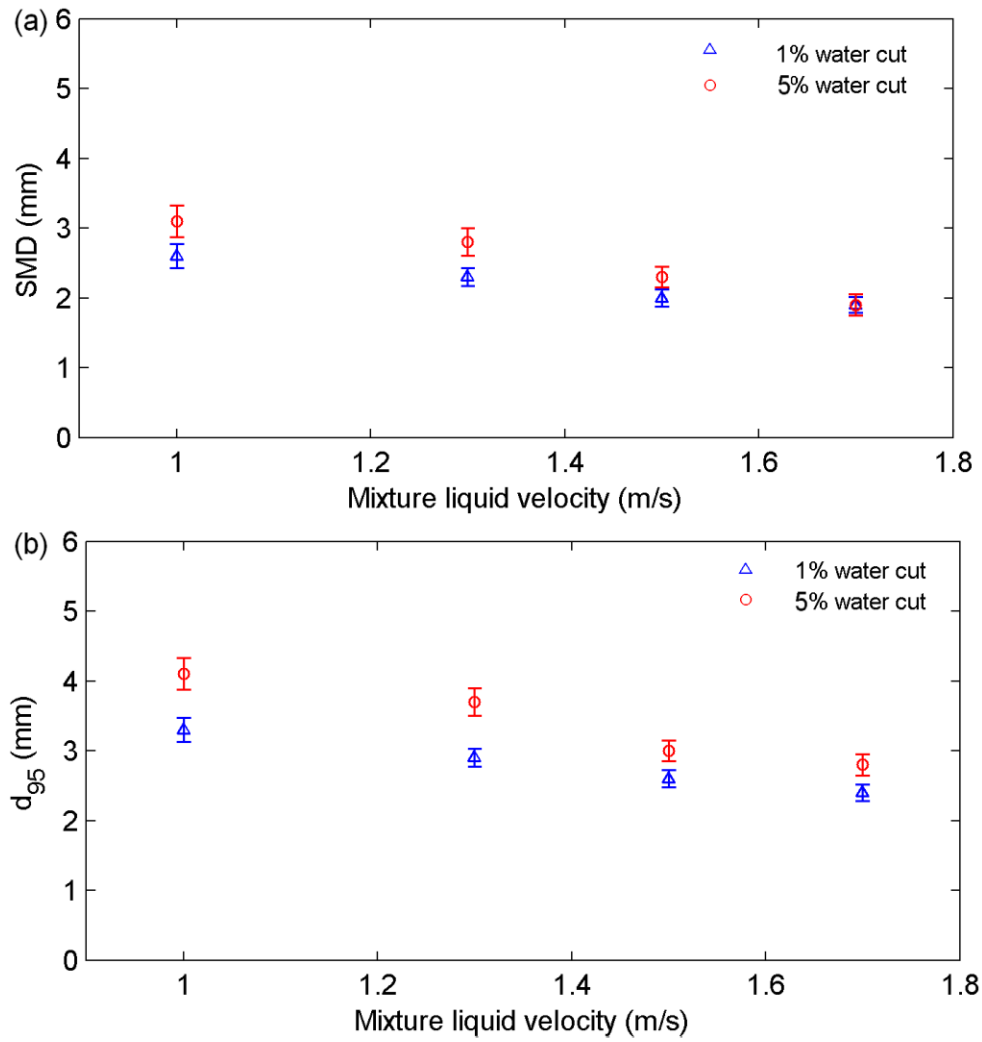
Figure 4-37: Variation of (a) SMD, and (b) diameter d_{95} with mixture liquid velocity at 1% and 5% water cuts in water-in-oil dispersion.
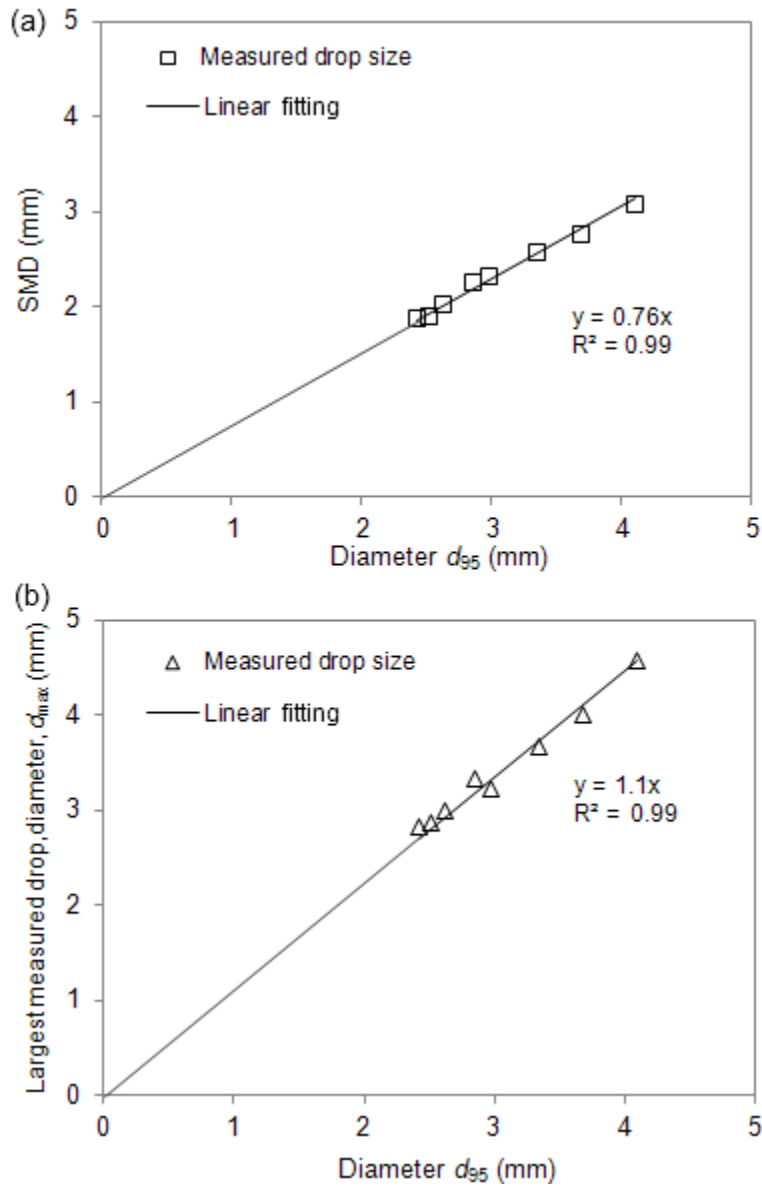
Figure 4-38: (a) Linear correlation between SMD and diameter d_{95}. (b) Linear correlation between d_{max} and diameter d_{95}.

4.5.2 Droplet size in vertical flow

The maximum droplet size d_{max} was measured by inspecting for the largest chord length of spherical droplets from the images taken by high speed video camera. Figure 4-39 shows the images of dispersed water droplets from 3% to 20% water cut at mixture liquid velocities of 0.5

and 1.0 m/s. The measured d_{max} values (averaged from 20 droplets) were then compared with the calculated values obtained from the water wetting model in Eq.(7.14) and plotted in Figure 4-40. It can be observed that the measured d_{max} values increased with water cut until they reached a maximum at 10% water cut. At higher water cut, the interactions of densely packed droplets bounded by the finite pipe diameter could have restricted further droplet growth. At mixture liquid velocity of 0.5 m/s, the model agreed well with experimental data up to 10% water cut, however, it over predicts at 20% water cut. At mixture liquid velocity of 1 m/s, the model predicts fairly well compared with the data at mixture liquid velocity of 0.5 m/s.
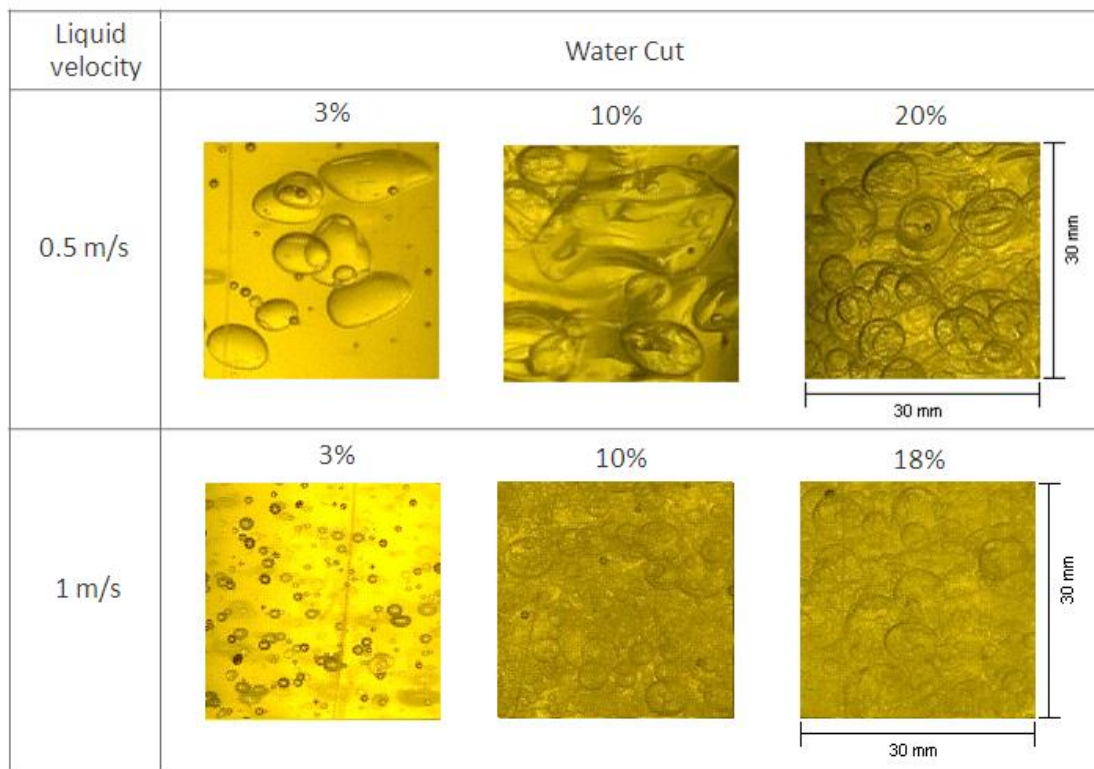
Figure 4-39: Images of water-in-oil droplets at mixture liquid velocities of 0.5 m/s and 1 m/s at water cuts from 3% to 10% in vertical pipe flow.
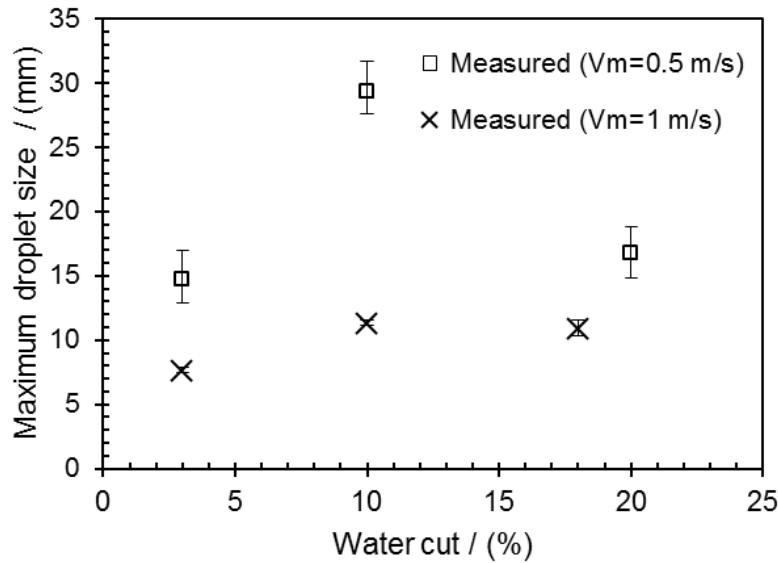
Figure 4-40: Comparison of the measured and model predicted maximum droplet size at 0.5 m/s and 1.0 m/s in vertical oil-water flow.

4.6 Ferrous ion concentration measurements

The surface wetting behavior in a carbon steel pipeline can be indirectly linked to the likelihood of corrosion. In a CO_2-saturated oil-water mixture environment, corrosion is expected to take place once the water and corrosive species, such as dissolved acid gas like CO_2, comes into contact with the bare steel wall. Corrosion is initiated according to:

$$Fe_{(s)} + CO_{2(aq)} + H_2O_{(l)} \leftrightarrow Fe^{2+} + CO_3^{2-} + H_{2(g)} \tag{4.3}$$
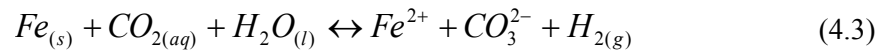
The iron oxidation leads to a rise in dissolved ferrous iron (Fe^{2+}) concentration in the water phase, which can be correlated to the corrosion rate. On the other hand, no corrosion is expected if the water is kept away from the pipe wall.

One way to study the relationship between surface wetting and corrosion rate in a large scale flow loop is by measuring the change of soluble Fe^{2+} concentration originating from the oxidation

of carbon steel test section in CO2-saturated oil-water mixture environment. Before running the flow experiments, the internal wall of the steel test section was polished thoroughly to remove scales and the 1 wt.% NaCl aqueous solution in the flow loop was continuously deoxygenated with CO_2 gas for 8 hours. The final measured water pH was 4.4 and the dissolved O_2 concentration was measured to be 0.5 ppm using the CHEMets colorimetric test kit.

Four cases (a) to (d) of different horizontal oil-water flow conditions were considered as given in the test matrix in Table 4-7, along with the observed flow patterns and the corresponding surface wetting. The flow conditions were so chosen in order to study the influence of different flow patterns and surface wetting on the concentration of dissolved Fe^{2+}. At each condition, three independent water samples were taken from the water boot of the oil-water separator at every two-hour interval up to 10 hours. Each sample was diluted to 1:1 and reacted with FerroVer reagent. Spectrophotometry (Genesys 10vis) was then used to measure the total soluble iron (Fe^{2+}, Fe^{3+}) concentration, and five measurement repetitions were performed for each sample.

Table 4-7: Test matrix for ferrous iron measurement

Mixture liquid velocity V_m (m/s)	Water cut (%)	Flow pattern	Surface wetting
(a) 0.5 m/s	10	Stratified with mixing layer	Stable water wet
(b) 1.0 m/s	10	Stratified with mixing layer	Stable water wet
(c) 1.0 m/s	1	Semi-dispersed	Unstable water wet
(d) 1.5 m/s	1	Dispersed	Unstable oil wet

The changes of Fe^{2+} concentration measurements for cases (a) to (d) were plotted in Figure 4-41 to Figure 4-44. Linear regression lines were included to best-fit the data. The slope of the best-fit line represents the rate of change of Fe^{2+} concentration in ppm per hour (ppm/hr).

- Case (a) $V_m = 0.5$ m/s, 10% water cut

The flow pattern was observed as stratified flow with mixing layer, having *stable water wet* behavior at the pipe bottom. As shown in Figure 4-41, the measured Fe^{2+} concentration increases linearly with time which corresponds to continuous oxidation of bare steel in the presence of continuous water layer at pipe bottom. The total change of Fe^{2+} was 0.61 ppm over 10 hours and the rate obtained from the best-fit slope was 0.06 ppm/hr.

- Case (b) $V_m = 1$ m/s, 10% water cut

The observed flow pattern was stratified flow with mixing layer, having *stable water wet* regime. The data set in Figure 4-42 display the highest rise in Fe^{2+} concentration with time which indicated higher mass transfer rate in the presence of continuous water layer and higher liquid velocity. The total Fe^{2+} change was 1.46 ppm and the rate of Fe^{2+} change is 0.15 ppm/hr, which was almost twice the rate higher than that in case (a).

- Case (c) $V_m = 1$ m/s, 1% water cut

The observed flow was semi-dispersed flow pattern with *unstable water wet* regime. The unstable water wet was attributed by the water droplets momentarily wetting the pipe bottom. The Fe^{2+} concentration results in Figure 4-43 increases linearly with time, with total Fe^{2+} change as 0.73 ppm and the rate of change of 0.07 ppm/hr. The rate of Fe^{2+} change was similar to the case (a). It appeared that the unstable water wetting behavior still can cause considerable iron oxidation.

- Case (d) $V_m = 1.5$ m/s, 1% water cut

The observed flow pattern was dispersed flow with *unstable oil wet* regime at the bottom of the tubular. The data set in Figure 4-44 displays the lowest total change of Fe^{2+} with time, in a near flatline trend since the interior wall was wetted by the oil phase most of the time. The total rate of Fe^{2+} change was taken as 0.017 ppm/hr. The results indicated that the iron oxidation was negligible in the case of unstable oil wet condition which was as good as oil wet condition.

From the flow loop results, the rate of Fe^{2+} change can be ranked in a descending order as follows: case (b) > case (c) > case (a) > case (d). The results implied that high liquid velocity coupled with high water cut gave rise to higher Fe^{2+} concentration. It appeared that iron oxidation took place whether the pipe wall was in stable water wet or unstable water wet condition. The iron oxidation was negligible if the water was kept away from the pipe wall.
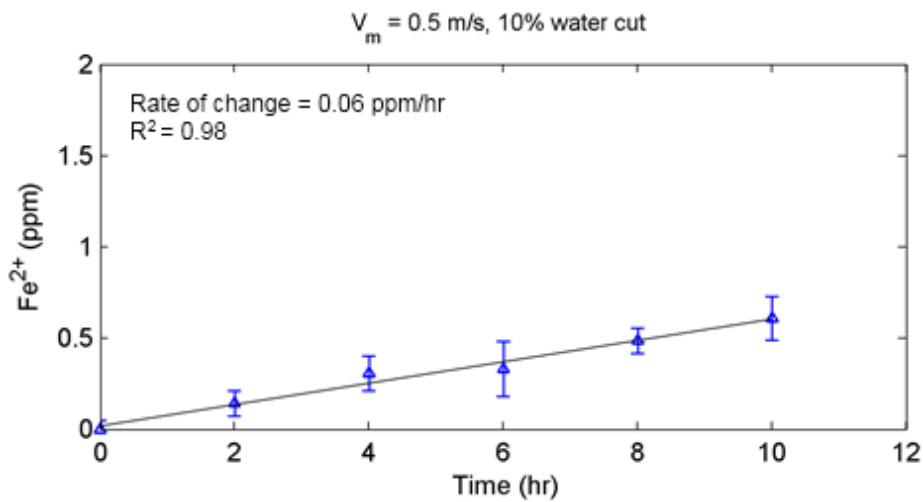
Figure 4-41: Variation of Fe^{2+} concentration for case (a) liquid velocity of 0.5 m/s, 10% water cut.
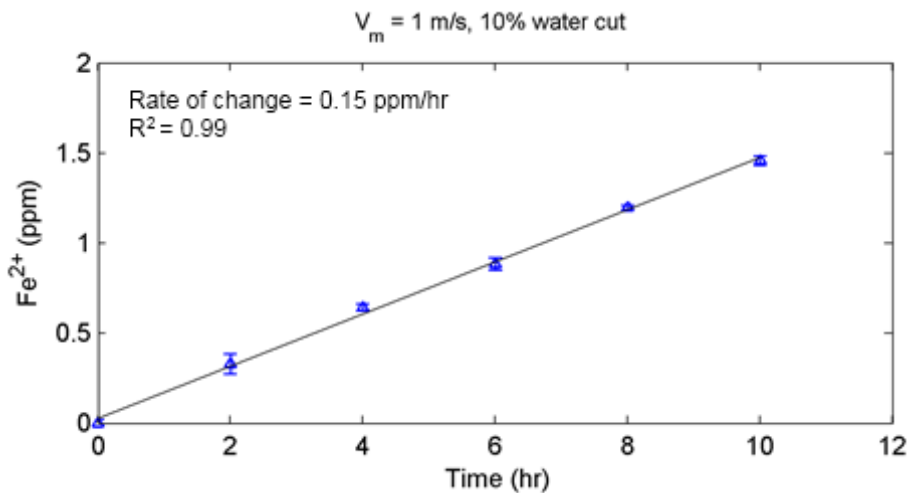
Figure 4-42: Variation of Fe^{2+} concentration for case (b) liquid velocity of 1 m/s, 10% water cut.
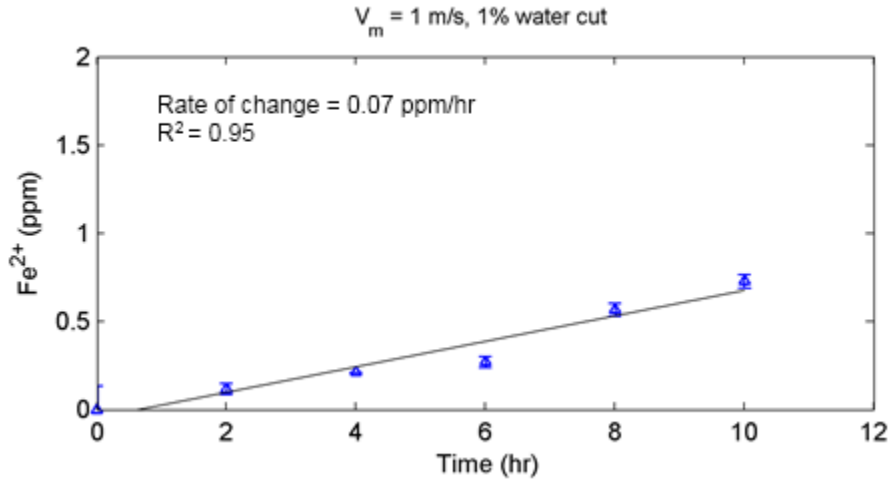
Figure 4-43: Variation of Fe^{2+} concentration for case (c) liquid velocity of 1 m/s, 1% water cut.
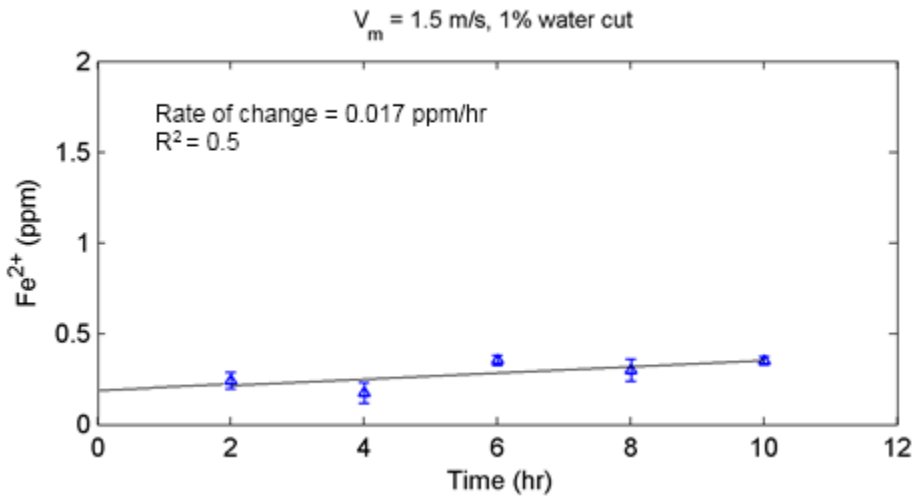
Figure 4-44: Variation of Fe^{2+} concentration for case (d) liquid velocity of 1.5 m/s, 1% water cut.

By assuming uniform CO_2 corrosion under film-free environments, the corrosion rate can be estimated from the Fe^{2+} concentration by considering the water wetted area of the test section, the volume of water, and the test duration at the given flow conditions. Eq.(4.4) is used to estimate the corrosion rate as follows:

$$CR = \frac{\Delta W}{\rho_{st} \cdot A_w \cdot t} = \frac{slope \cdot V}{\rho_{st} \cdot A_w} \qquad (4.4)$$

where slope is rate of change of Fe^{2+} concentration, V the volume of water ($V = 1.323$ m^3), A_w the water wetted area, ρ_{st} the density of steel material.

The water wetted area A_w can be estimated from the conductivity pins wetting snapshots by multiplying the wetted perimeter with the total length of the test section as shown in Figure 4-45. The averaged water wetted perimeters are depicted in Figure 4-46 at each flow condition except for case (d) in which the corrosion rate was assumed negligible in accordance to unstable oil wet. The results showed that the estimated water wetted perimeters were almost similar for case (a) and (b) at 10% water cut while 2.5 times smaller for case (c) at 1% water cut. By estimating the corrosion rates from the flow loop tests, the results showed that the corrosion rate for case (b) and (c) were fairly close within the error margin, while lower for case (a). The estimated CO_2 corrosion rates are displayed in Table 4-8 and Figure 4-47. The results implied that the presence of water wetting at high turbulent flow could lead to a rise in the corrosion rate. This can be explained by an increased rate of mass transport process.

It is noted that this method is a crude estimate considering the wide margin of uncertainties associated in large-scale flow loop. The flow loop test is not as carefully controlled as a glass cell test, which the environment is tightly sealed and purged to prevent oxygen ingress. The uncertainties related to the flow loop tests were identified as follows: Fe^{2+} concentration (slope), wetted area from the pins snapshot and volume of water in the flow loop. The error analysis was performed using Eq. (4.5). The uncertainties are also included in the reported values.

$$\frac{\Delta CR}{CR} = \frac{\Delta slope}{slope} + \frac{\Delta Vol}{Vol} + \frac{\Delta Area}{Area} \qquad (4.5)$$

The corrosion rates estimated based on Fe^{2+} concentration measurements were compared with the predicted corrosion rates using MULTICORP 5, a corrosion software package developed by the Institute for Corrosion and Multiphase Technology (Nesic *et al.*, 2005, You, 2013). Further details on the software package can be referred from the online URL address: http://www.corrosioncenter.ohiou.edu/software/multicorp. The predicted values were in the range of 1.4 to 1.6 millimeter per year (mm/y), which was in good agreement with the estimated values from the flow loop experiments, considering the wide margin of uncertainties from this type of test.

Table 4-8: Comparisons of corrosion rates

Liquid velocity V_m (m/s)	Water cut (%)	Water wetted perimeter (mm)	Estimated corrosion rate (mm/y)	Predicted corrosion rate by MULTICORP 5 (mm/y)
(a) 0.5 m/s	10	62	0.8 ± 0.3	1.4
(b) 1.0 m/s	10	67	1.8 ± 0.3	1.5
(c) 1.0 m/s	1	26	2.2 ±0.7	1.6
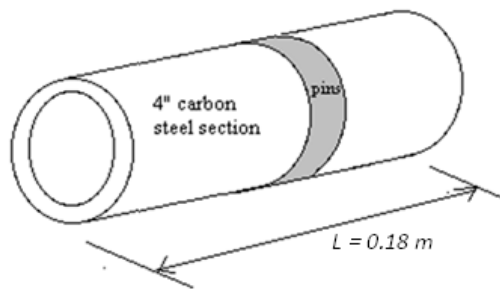
Figure 4-45: 0.1 m ID steel test section showing the conductivity pins mounted spool. The water wetted area A_w is calculated by multiplying the wetted perimeter w and the total length L.

(a) 0.5 m/s 10% water cut

mean water wetted perimeter, $w = 62$ mm

(b) 1 m/s 10% water cut

$w = 67$ mm

(c) 1 m/s 1% water cut

$w = 26$ mm
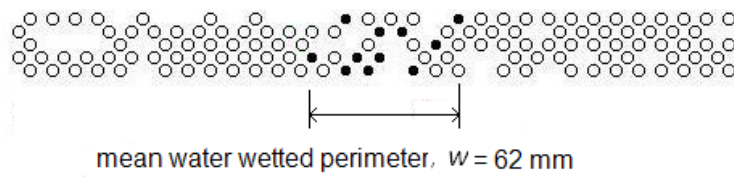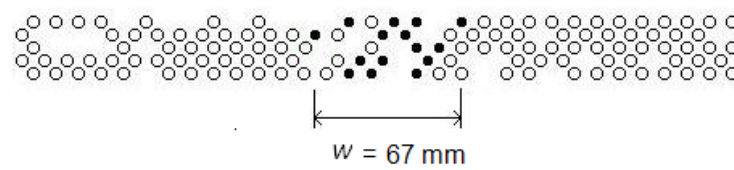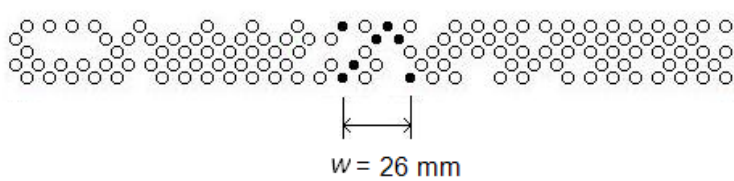
Figure 4-46: Water wetted perimeter estimated from the conductivity pins snapshots at the flow conditions: (a) $V_m = 0.5$ m/s, 10% water cut, (b) $V_m = 1$ m/s, 10% water cut, (c) $V_m = 1$ m/s, 1% water cut.
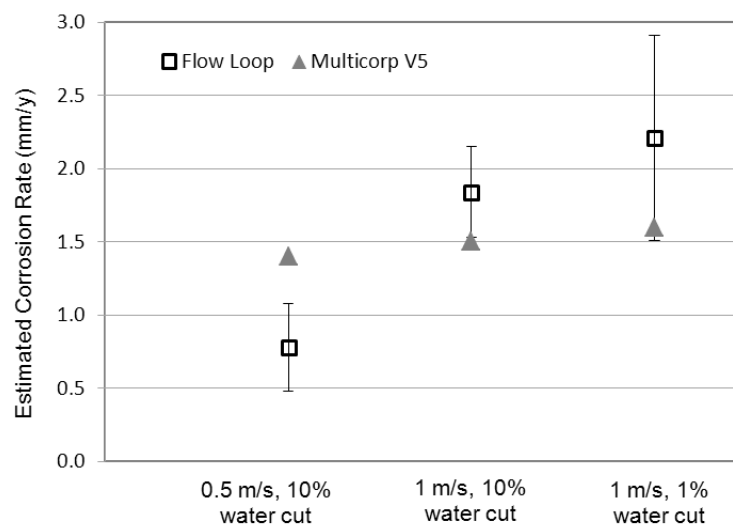
Figure 4-47: Comparison of estimated corrosion rates from the flow loop tests and predicted corrosion rate using MULTICORP 5.

4.7 Summary

- In horizontal oil-water flow with the oil phase as the dominant phase, five types of flow patterns can be observed. They are stratified smooth, stratified with globules, stratified with mixing layer, semi-dispersed and dispersed flows.

- In vertical oil-water flow, dispersed bubble and dispersed globule flows were observed.

- With the use of high speed video camera and conductivity pins, it was possible to observe how the water was distributed locally in the flow and related to the water wetting phenomena. The wetting behavior can be interpreted with the aid of visualization and conductivity pins.

- Conductivity pins was an instrumental tool to detect the water wetting behavior around the pipe circumference. Four types of wetting regimes: water wetting, unstable water wetting, unstable oil wetting, and oil wetting were proposed to describe the wetting behaviors as measured by the conductivity pins.

- In horizontal flow, water wetting prevailed at the pipe bottom when the flow was stratified at low mixture liquid velocity and/or high water cut.

- For semi-dispersed flow that occurs at high liquid velocity, the wetting became unstable water wet or oil wet. The lower the water cut or the higher the liquid velocity, the lesser the extent of intermittent wetting. The intermittent wetting was largely caused by the water droplets momentarily 'settling and 'touching' the pipe wall.

- Stable oil wet was observed in dispersed flow at the lowest tested water cut, namely 0.5%.

- In vertical flow, the dispersed water droplets/globules were observed to flow upward in a relatively straight path. The wetting was predominantly oil wet across the tested velocities. The rise of liquid velocity did not seem to greatly affect the surface wetting. For water cuts above 15% at low mixture liquid velocity, unstable water wetting was observed caused by the crowding of water droplets close to the wall.

- The Log-normal distribution function is adequate in representing the droplet size distribution in the water-in-oil dispersion system. As the mixture liquid velocity increased, the distributions became narrower and shifted leftward to smaller size scales.

- Sauter mean diameter (SMD) of the water droplet was found to decrease with increasing mixture liquid velocity due to the higher turbulent breakage forces. The SMD at 1%water cut was smaller than that at 5% water cut. The size difference diminished as the liquid velocity increased.

- In flow loop tests, the presence of water wetting coupled with high flow velocity could lead to a rise in the corrosion rate, caused by an increased mass transport rate.

CHAPTER 5: RESULTS FOR GAS-OIL-WATER FLOW

5.1 Introduction

Three-phase gas-oil-water flow environment is a common occurrence in the oil and gas industry. The crude oil from offshore hydrocarbon production is often transported as a mixture of gas-oil-water *via* pipeline transmission. Since multiple immiscible phases present in the pipes, a wide variety of complicated flow patterns can arise. Therefore, it is of paramount importance to understand the distribution of water under various three-phase flow conditions and how they affect surface wetting in the pipelines.

The main emphasis of this section is on three-phase flow patterns and surface wetting. The three-phase flow and wetting experiments were performed in a large diameter (0.1 m ID) flow loop using model paraffinic oil LVT 200, 1 wt.% aqueous NaCl and CO_2 gas. The three-phase flow loop experimental work includes the flow pattern visualization and surface wetting measurement in both horizontal and vertical pipes.

5.1.1   Horizontal gas-oil-water flow patterns

In the horizontal gas-oil-water flow, five types of oil-continuous flow patterns can be identified in this flow loop work. They are described and illustrated in Figure 5-1:

Stratified flow (ST) is characterized by the concurrent flow of liquid streams at the base and a gas stream at the top of the pipe. The liquid phases may be separated or slightly dispersed at their interface. The gas-liquid interface may be smooth or show some waviness caused by the drag of the gas passing over the liquid.

Elongated bubble (EB) is a form of intermittent flow that occurs at low gas velocity; the flow is also called plug flow. It has the characteristic feature of long gas pockets (plugs) trapped at the

pipe top, moving alternately in between the continuous sections of liquid that fully occupy the pipe. No entrained gas bubbles can be seen in the liquid section.

Slug (SL) occurs when the liquid waves rise to bridge the entire pipe section forming a liquid slug, whilst the gas flows alternately as a large bubble in between the train of liquid slugs (Dukler & Hubbard, 1975). The large gas bubble passes on top of a slower moving stratified liquid layer characterized as the gas bubble-liquid film zone. The liquid slug moves more energetically that overruns the slow moving liquid film ahead. The slug front is a highly turbulent mixing region in the form of vortices with aerated gas bubbles. The upper wall is wetted at each passage of the liquid slug. The liquid-rich slugs cause large pressure fluctuation.

Wavy annular (WA) occurs at the transition between slug and annular flow. The flow lacks the characteristic pressure fluctuation found in slug flow. Increasing the gas flow rate causes the periodic slug to disappear and the wavy interface becomes greatly disturbed. High amplitude waves are aperiodically generated that momentarily sweep around the pipe periphery but do not quite touch the pipe top. The upper pipe wall is occasionally wetted by the frothy waves and covered by an unstable liquid film that keeps falling diagonally downward (Shoham, 2006). The breakup of the unstable waves becomes a source for droplet entrainment in the gas phase.

Annular-mist (AM) occurs at very high gas velocity where gas flows at the pipe core and liquid moves as a thin annular film enveloping the pipe wall. The turbulent gas core contributes to a rough gas-liquid interface containing interfacial waves of varying amplitudes (Russell & Lamb, 1965). Some of the liquid droplets are entrained as mist in the pipe core. The liquid film is distributed asymmetrically with a thicker film at the base than the top due to the influence of gravity.

The elongated bubble and slug flow patterns can be viewed as an intermittent flow, characterized by alternating flow of liquid and gas phases. The wavy annular flow which borders on the transition to annular flow can be considered as a form of unstable annular flow.
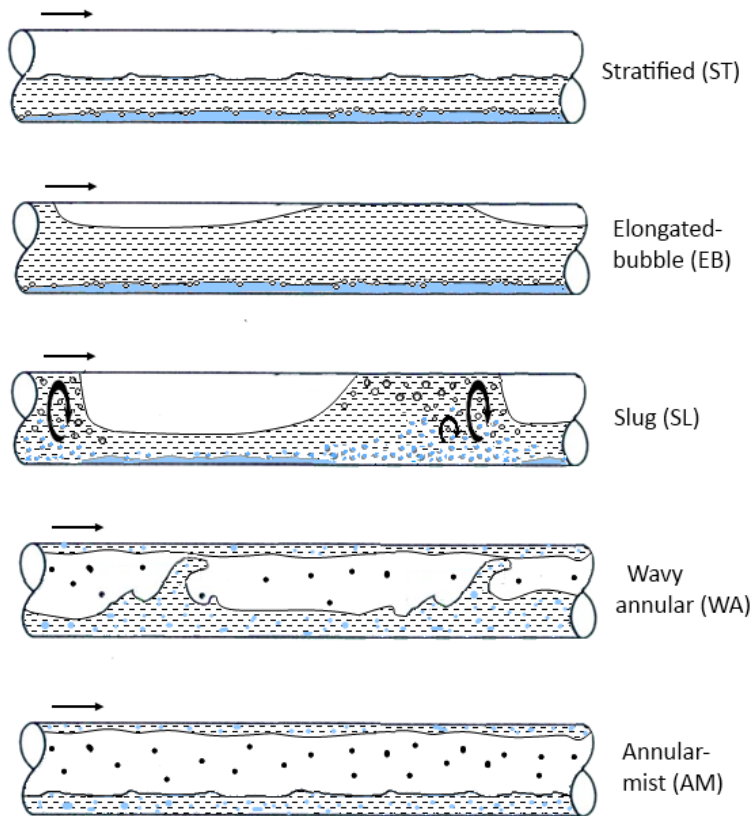
Figure 5-1: Schematics of oil-continuous horizontal three-phase flow patterns showing stratified, elongated bubble, slug, wavy annular and annular-mist flows.

5.1.2   *Vertical gas-oil-water flow patterns*

In the vertical gas-oil-water flow, two types of flow patterns can be observed under the test conditions using a 0.1 m ID vertical pipe. They are described and illustrated in Figure 5-2:

Churn is a form of intermittent flow which exists between slug and annular flow. The flow has a characteristic flooding wave phenomenon with periodic flow reversals of liquid film (Hewitt & Jayanti, 1993), which can be observed as an oscillatory up-and-down motion of the liquid. Flooding is a phenomenon related to the limit of stable countercurrent of gas-liquid flow

(Jayanti & Hewitt, 1992), above which large interfacial waves will form and surge up the pipe, disrupting the liquid into discontinuous chunks in a chaotic fashion.

Annular–mist occurs at very high gas velocities with gas flows in the pipe core and thin liquid film flows upward as an annulus around the pipe periphery. Disturbance waves may present on the interface that can occasionally break up as small entrained droplets in the central gaseous core.
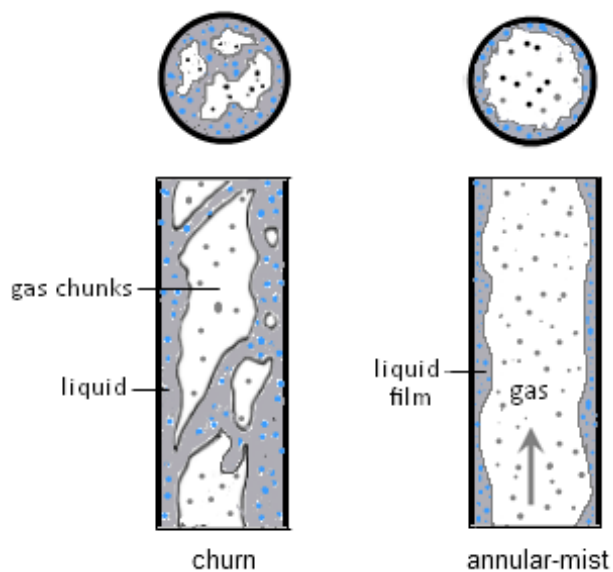
Figure 5-2: Schematics of vertical three-phase churn and annular-mist flow patterns.

5.2 Experimental details

Three-phase gas-oil-water flow experiments were carried out in the large-scale inclinable flow loop to study the flow patterns and surface wetting in horizontal and vertical 0.1 m ID pipe. Figure 3-5 shows the schematics of the three-phase flow loop. The flow and wetting experiments were conducted at fixed water cuts by varying the total mixture liquid velocities and superficial gas velocities. The mixture liquid velocity is the sum of superficial oil and water velocities. The test matrices for horizontal and vertical gas-oil-water flow are shown in Table 5-1. For each

mixture liquid velocities, the gas blower was operated according to the testable ranges of gas velocities as listed in Table 5-2. The useful range of gas velocities becomes limited as the liquid velocity increases due to the capacity limit of the current flow loop setup. The test fluids used were light model oil LVT200 as the oil phase, 1 wt.% aqueous NaCl as the water phase and CO_2 as the gas phase. 250 ppm of red food dye (red 44) was added to the water phase to provide better contrast for visual examination. The properties of the test fluids are listed in Table 3-1.

Flow patterns and surface wetting measurements were taken once the flow was fully developed. A high speed video camera was used to capture the flow patterns in the transparent pipe section located downstream of the first leg of the flow loop (approximately $L/D = 115$). The surface wetting data were taken from the spool of conductivity pins mounted onto the test section located side by side with the transparent pipe section. Before running the actual flow and wetting tests, the conductivity pins on the test section were thoroughly polished. The test section was then rinsed with a continuous run of gas-oil slug flow for 30 minutes in order to displace residue water, wash away impurities and recondition the pins back to an oil wetting condition.

Table 5-1: Test matrices for horizontal and vertical three-phase flow experiments

Parameter	Value	
Oil phase	LVT200	
Water phase	1 wt.% aqueous NaCl	
Gas phase	CO_2	
Pipe ID (m)	0.1	
Inclination (°)	0° (horizontal)	90° (vertical)
Mixture liquid velocity V_m (m/s)	0.2 – 1.5	0.5 – 1.5
Superficial gas velocity, V_{sg} (m/s)	1 – 45	5 – 45
Water cut (%)	1 – 20	1 – 10

Table 5-2: Testable range of superficial gas velocities in the flow loop.

Mixture liquid velocity, V_m (m/s)	Water cut (%)	Test range of superficial gas velocity, V_{sg} (m/s)	
		Horizontal flow	Vertical flow
0.2	1 - 20	1 - 45	5 - 45
0.5	1 - 20	1 - 45	5 - 45
0.7	1 - 20	1 - 25	6 - 25
1.0	1 - 18	1 - 15	6 - 12
1.3	1 - 14	1 - 8	6 - 8
1.5	1 - 12	1 - 7	6 - 8

5.3 Horizontal gas-oil-water flow

The three-phase flow patterns are highly dynamic and complex due to the presence of the energetic gas phase. In this work, the use of a high speed video camera (model Phantom v12.1) greatly augments the interpretation of the flow structures with respect to the space and time scale. By using a high framing rate of 6,000 fps, the flow video recording can be played back in slow motion with the Phantom Cine Viewer^{TM} software. As an attempt to capture the dynamic nature of the flow patterns, the sequential evolutions of the flow structures and their characteristic features are first described in this section. The resultant flow patterns can then be grouped by different water cuts, with each group tested at varying liquid and gas velocities. This was followed by classification of surface wetting results by different water cuts. The wetting data, as measured by the conductivity pins and the interpretation was greatly aided by the visualization results in explaining the surface wetting behavior in three-phase flow settings.

5.3.1   Images of sequential evolution of flow patterns

In this section, the sequential evolution of the three-phase flow structures will be described in detail for four major types of flow patterns: *elongated bubble (DB), slug (SL), wavy-annular (WA) and annular-mist (AM)* flows. Time series images of the flow patterns are included to illustrate

visually the evolution of the flow as some flow features may be present in one image, but not in all images. The first two flow patterns are collectively known as intermittent flow regimes, which are highly dynamic or chaotic as characterized by the alternate succession of liquid and gas phases in time and space. *EB* flow occurs at low gas velocity at high liquid fraction, while the *WA* flow prevails at high gas velocity at low liquid fraction. In general, the global structures of these major types of flow patterns shared similarities to those flow conditions occurring at different water cuts. The differences incurred in the local spatial distribution of the water phase depend on the amount of water present in the flow system. Hence, primary attention is directed to the distribution of the water phase; whether it comes in contact or kept from the pipe wall, and how this could impact the surface wetting behavior. It should be noted that for the LVT200-water system, dispersed bubble or stratified flow was unobserved in the given test range as the stratified flow was dominant at low liquid velocity, below 0.2 m/s, while dispersed flow only appeared at high liquid velocity, beyond 8.0 m/s, for the current flow loop. Valle (2000) reported distinctly different flow pattern transitions using crude oil in three-phase flow experiments, in which the dispersed/bubbly flow was dominant for most tested velocity ranges instead of slug flow.

5.3.1.1 EB flow

Figure 5-3 is a sequence of images at an interval of 0.2 s obtained from the high speed camera for EB flow observed at a mixture liquid velocity V_m of 0.2 m/s, 5% water cut and superficial gas velocity V_{sg} of 0.7 m/s. *EB* flow can be viewed as a weaker form or limiting case of slug flow. *EB* flow can be observed at a low gas velocity < 1 m/s before it transitioned to slug flow. The first image at time $t = 0$ s shows a long gas bubble at the top with a stratified oil-dominant liquid layer at the bottom that flows relatively slowly. The water drops down mostly as densely packed droplets (3 mm to 6 mm) with some coalescence as a continuous water layer underneath the layer of droplets. In the following images, one can view the passage of a long plug of liquid containing

some entrained gas bubbles. The length can be 20 to 40 pipe diameters. The image at $t = 0.2$ s shows the front of the long plug of liquid entrained with gas bubbles. The image at $t = 0.4$ s shows the plug front has passed and the shear of the faster moving liquid is transmitted to the slower moving liquid layer underneath, leaving behind a local wake region of disturbed flow filled with entrained gas bubbles in recirculatory motion, caused by the swirling vortices (Maxworthy, 1967). At $t = 0.6$ s, as the recirculating flow extends downstream to the bottom wall, some water droplets are sheared into elongated form and partially lifted off the wall. The lift can be explained by the non-uniform velocity profile at different depths. The upper liquid layer moves faster than the lower liquid layer, creating a pressure difference and sucking up the water. At $t = 0.8$ s, some water droplets are lifted partially and get churned by the faster moving fluid. At $t = 1.2$ s, the liquid plug starts to decelerate as it reaches the tail. The liquid accumulates in the lower half of the pipe and the gas moves in the form of an elongated gas pocket in the upper pipe wall. A layer of slowly moving water droplets can be seen at the pipe bottom.
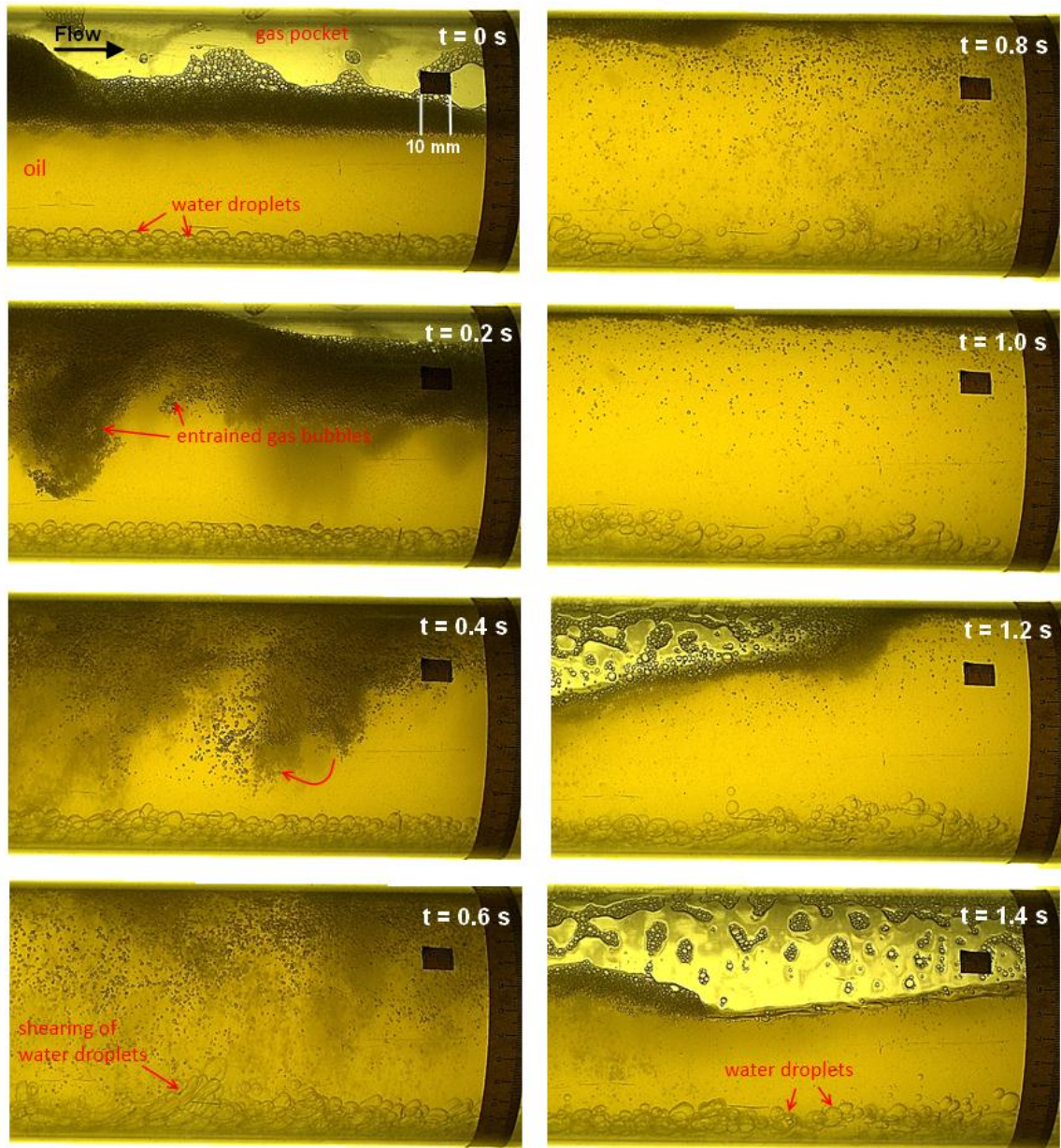
Figure 5-3: Sequential images (top left to bottom right) of elongated bubble (EB) flow at 0.20 s interval at $V_m = 0.2$ m/s, 5% water cut, $V_{sg} = 0.7$ m/s.

5.3.1.2 SL flow

Figure 5-4 is a sequence of images at an interval of 0.05 s obtained from the high speed camera for *SL* flow observed at the mixture liquid velocity V_m of 0.2 m/s, 5% water cut and

superficial gas velocity V_{sg} of 1.6 m/s. *SL* flow was dominant for most of the tested gas velocity range where a distinct alternate structure of liquid slug and gas bubble-liquid film zone can be seen. The first image at time $t = 0$ s shows a stratified gas bubble-liquid film zone with a large gas pocket passing on top and oil-dominant liquid flowing at the base. The water phase moves rather slowly and drops down as closely packed droplets (3 mm to 6 mm), again with a degree of coalescence as a continuous water layer underneath the layer of droplets. In the following images, one can view the evolution of the liquid slug as a large amplitude wave rises on the interface and blocks the entire pipe section. The image at $t = 0.05$ s shows the leading edge of the slug front which is a turbulent froth zone entrained with gas bubbles. Since the slug front moves faster than the liquid film ahead, it entraps a multitude of gas bubbles as it plunges across the free liquid surface ahead, analogous to that of a plunging jet in hydraulic jumps (Chanson, 1996). The image at $t = 0.1$ s shows a dense plume of finely entrained gas bubbles being formed as the plunging jet penetrates the free surface at the impact zone. Because of the velocity difference, the intrusion of the slower moving liquid film with the faster moving liquid slug induces intense rolling vortex motions in the turbulent wake field that circulate the swarms of entrained gas bubbles and spiral them downstream (Bonizzi & Issa, 2003; Maxworthy, 1967). The distance of the film intrusion constitutes the length of the mixing vortex (Dukler & Hubbard, 1975). The image at $t = 0.2$ s shows that as the swarms of entrained gas bubbles reach the bottom wall, they are deflected transversely downstream, shearing and partially lifting the water droplets along the way. It appeared that the swirling vortices under the action of turbulence are responsible to churn up the water droplets. At $t = 0.25$s onwards, the gas bubbles gradually migrate upwards by buoyancy to coalesce, while the water droplets settle down by gravity as the turbulence is dissipated along the slug length. At the trailing edge of the slug body, liquid shedding occurs in which the aerated liquid phase decelerates and stratifies into a gas bubble–liquid film zone. Gas bubbles continue to coalesce in the upper pipe region, while water droplets drop out and accumulate in the pipe

bottom. For some slug flow conditions with slow flowing gas, the liquid film may momentarily stop and back flow until the next train of slug approaches. In those cases, the water phase completely separates out from the oil phase.
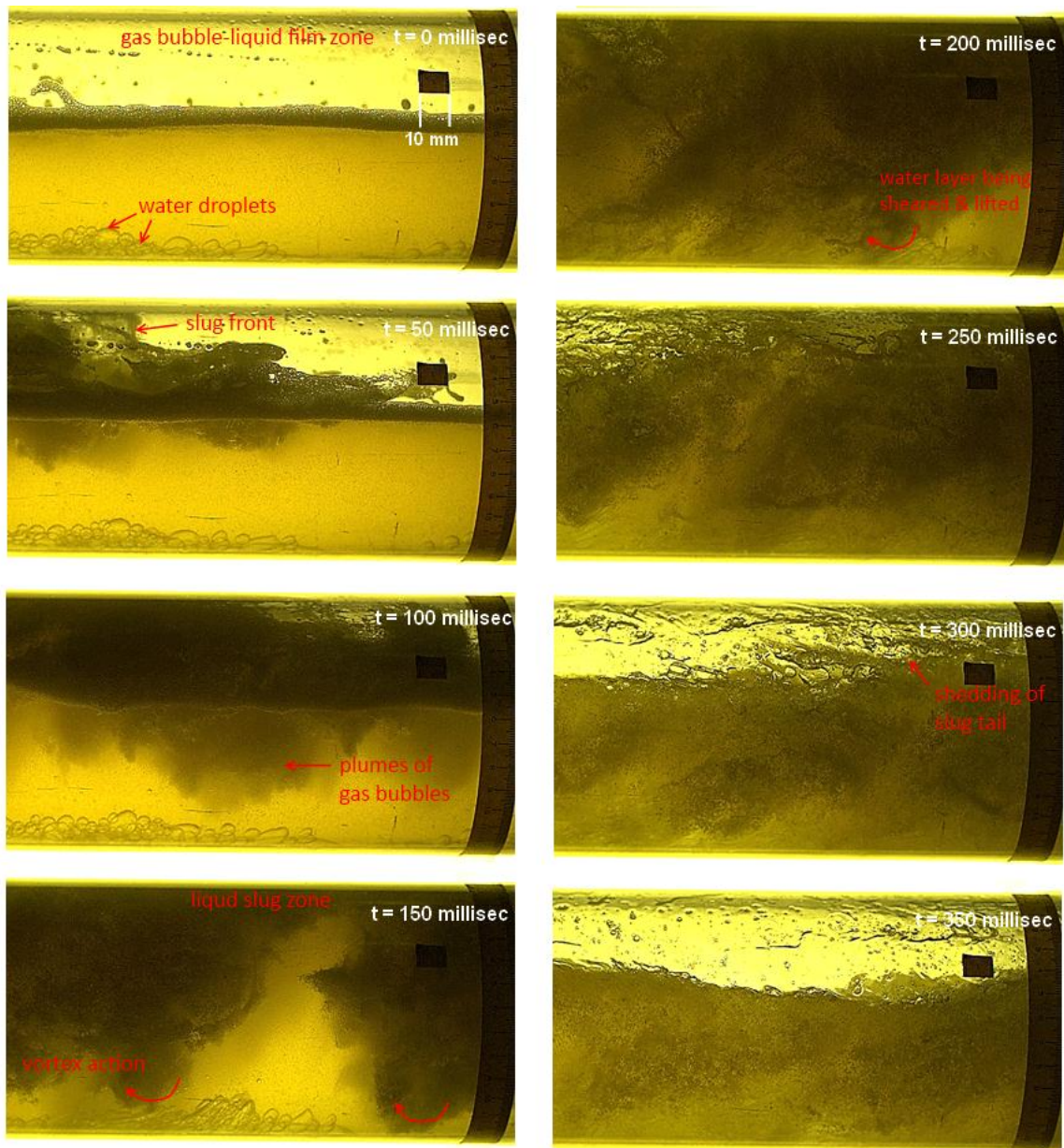
Figure 5-4: Sequential images of slug (SL) flow at 0.05 s interval at V_m = 0.2 m/s, 5% water cut, V_{sg} = 1.6 m/s.

5.3.1.3 WA flow

The flow pattern can be observed transitioning between slug and annular flow as the gas flow rate is further increased. The sequence of images taken 0.05 seconds apart is shown in Figure 5-5 for *WA* flow observed at mixture liquid velocity V_m of 0.2 m/s, 5% water cut and superficial gas velocity V_{sg} of 18.9 m/s. The flow has a somewhat stratified wavy fashion with intermittent upsurge of unstable wave; the upper gas layer is continuously atomized by liquid droplets while the lower liquid layer is highly disturbed and entrained with gas bubbles. At $t = 0$ s, the interface is greatly disturbed by the fast flowing gas which has a tendency to drag the liquid near the interface and lead to its acceleration. This results in unstable disturbance waves that surge intermittently across the interface. These large amplitude waves momentarily sweep around the pipe periphery but do not quite bridge the pipe top (Shoham, 2006). These waves are a primary source for droplet entrainment and replenishment of the liquid film (Cohen & Hanratty, 1965). As seen in the image at $t = 0.1$ s, as these unstable waves surge, their wavy interfaces are torn off and carried away by the gas stream as atomized droplets. The leading edge of the unstable waves is often laden with swarms of entrained droplets. Images from $t = 0.15$ s and onward show the upsurge motion of the disturbance waves that momentarily roll up and wet the upper side wall (2 to 10'o clock), leaving behind a liquid film as the waves plunge back to the interface, entrapping gas bubbles along with it. At $t = 0.35$ s, some of these entrained liquid droplets can be seen to collide and deposit downstream in the upper circumferential wall. An unstable liquid film on the pipe wall can be seen to keep draining down the wall diagonally, as evidenced by the sheen of liquid rippling across the wall surface. The water phase cannot be discerned from the images, as it has been highly mixed in the turbulent flow.
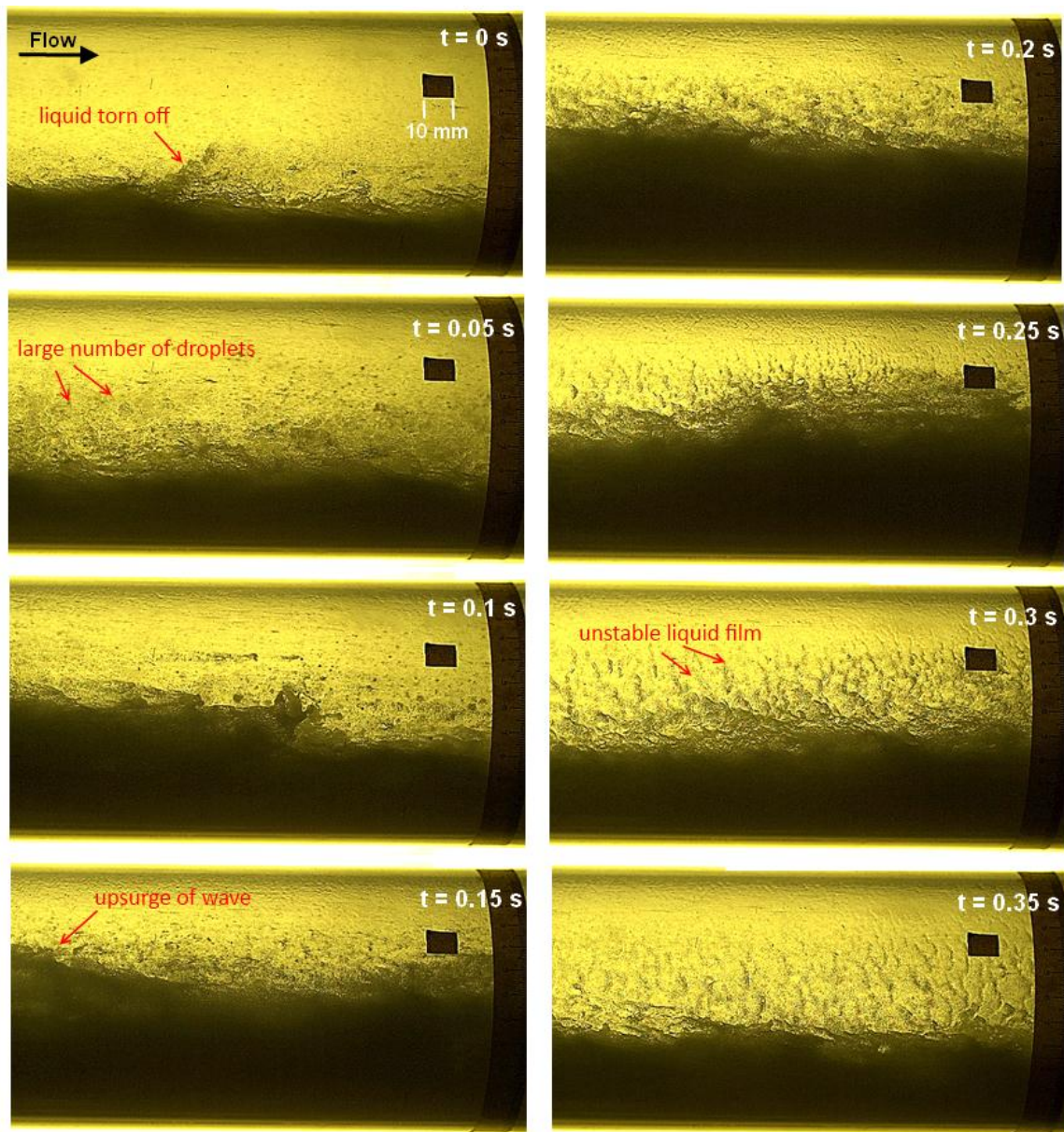
Figure 5-5: Sequential images of wavy annular (WA) flow at 0.05 s interval at V_m = 0.2 m/s, 5% water cut, V_{sg} = 18.9 m/s.

5.3.1.4 AM flow

Figure 5-6 shows the sequence of images taken 0.05 seconds apart for *AM* flow observed at V_m = 0.2 m/s, 5% water cut and V_{sg} = 37.1 m/s. The four images show that the gas flows at the central pipe core are laden with entrained liquid droplets, whilst a layer of annular liquid film

moves along the wall. Because of gravity, the liquid film is asymmetrically distributed with a thicker film at the pipe bottom. Similarly, the entrained liquid droplets are asymmetrically distributed with increased concentration towards the lower pipe section. At the liquid film interface, two types of waves can be generated. Ripple waves are small perturbation waves that give rise to interfacial roughness, while the disturbance waves are large amplitude roll waves that are randomly generated and torn off as entrained liquid droplets in the gas core as a result of the gas shear (Rodriguez, 2009). From the video analysis, the annular liquid film appears to be replenished by two mechanisms. Firstly, the upper wall was observed to be wetted aperiodically by instantaneous upsurge of the disturbance waves (Hanratty & Hershman, 1961; Russell & Lamb, 1965). Secondly, the circumferential wall was observed to be randomly impinged by the liquid droplets entrained in the gas core (Russell & Lamb, 1965). The former case was observed to be more the dominant wetting mechanism. These mechanisms contribute to a thin annular liquid film that traverses with surface ripples along the direction of the gas stream. The occurrence of droplet entrainment from the disturbance wave and droplet deposition at the circumferential wall occur continuously, contributing to misty flow in the gas core, annular liquid film on the periphery and rough wavy interface at the base (Paras & Karabelas, 1991). No visible traces of water can be discernible due to the opaque nature of the fluid mixture. It is unclear how the water is distributed in the near wall region, as the thin film is probably turbulent due to the presence of large disturbance waves on top. The reported critical Reynolds number (Re) for the onset of turbulence lies in the range of Re = 250 – 800 (Fulford, 1964). Sotto Mayor (2007) argued that the turbulence transition in the liquid film is a gradual and complex process, which may be influenced by small film interface oscillation or surface irregularities.
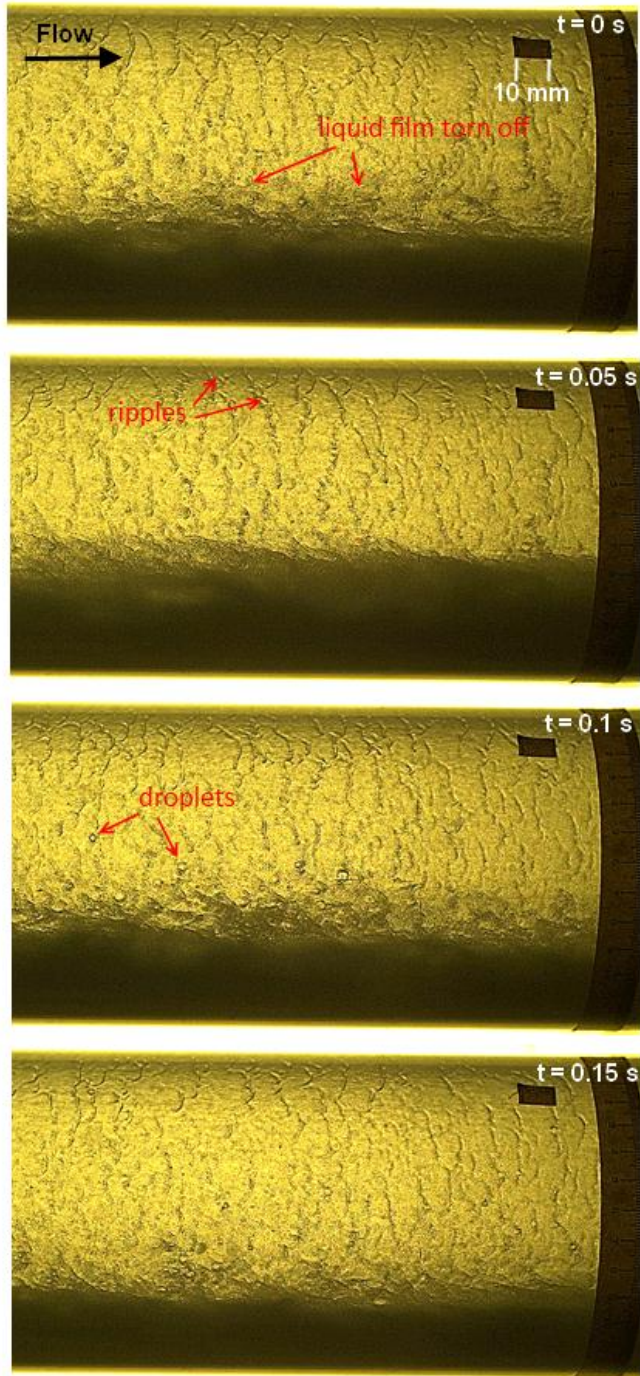
Figure 5-6: Sequential images of annular-mist (AM) flow patterns at 0.05 s interval at V_m = 0.5 m/s, 5% water cut, V_{sg} = 37.1 m/s.

5.3.2   Flow patterns

The visualization results from the high speed camera for different flow conditions are presented in the order of low to high water cuts. The data points were then plotted in a series of flow pattern maps at different water cuts, namely 1%, 5% and 18%-20% water cuts for mixture liquid velocities ranging from 0.2 to 1.3 m/s. For each series of results, the flow patterns are shown in the order of increasing superficial gas velocity which typically starts from elongated bubble (*EA*), then slug (*SL*), wavy annular (*WA*), and finally annular-mist (*AM*) flows. The global structures for each flow patterns have been described in the previous sections. The results here will focus on the distribution of water in the flow structure. The water distribution can be dynamically varied according to different locations and instances in the flow structure. There are two possible types of local interfacial structure within the liquid-liquid flow: *Dispersion* where the water phase is dispersed as droplets in the continuous oil phase. The water droplets may or may not contact the pipe wall intermittently, depending on the degree of dispersion. *Separation* where the water and oil flow as separated phases in the pipe. Here, water is always in contact with the pipe wall.

It is noted that the flow field tends to become more opaque and water is hardly discernible with increasing gas velocity due to the gas entrainment within the fluid mixture, particularly in wavy annular and annular-mist flow patterns. In this case, the whereabouts of water in the fluid mixture can only depend on the use of conductivity pins, which would detect what phase comes into contact with the wall surface.

5.3.2.1 1% water cut

High speed images were taken for horizontal gas-oil-water flow conditions at 1% water cut by varying mixture liquid velocity V_m from 0.2 m/s to 1.3 m/s. For all tested gas velocities ranging from 0.8 m/s to 2.6 m/s, *EA* and *SL* flow patterns were observed as depicted in Figure 5-7. Both

flow patterns were intermittent flow, characterized by alternating flow of liquid slug and stratified gas bubble-liquid film section. The flow data points are plotted in a flow pattern map in Figure 5-8. The map is plotted with superficial gas velocity V_{sg} as x-axis and mixture liquid velocity V_m as y-axis. The map shows the transition between different flow patterns, *i.e.*, *EB, SL, WA* and *AM* with increasing superficial gas velocity. Empirical transition lines distinguishing between *EB/SL, SL/WA* and *WA/AM* were included in the flow pattern map.

- Water distribution in *EB* flow

At low mixture liquid velocity V_m = 1.3 m/s, it was observed that the water droplets (colored by red dye) accumulated in the bottom wall. Some large water droplets (approximate 5 mm) were slightly perturbed and stirred up with the passage of liquid slug, then dropped down after the tail of the slug. At higher mixture liquid velocity V_m = 1.3 m/s, the water droplets were smaller (approximate 1.5 mm) and more dispersed, with a gradient of concentration towards the pipe bottom.

- Water distribution in *SL* flow

By moderately increasing the gas velocity, the flow imparted more turbulent mixing in the liquid slug, resulting in increased dispersion of water droplets. With low water fraction of 1%, the water in the form of fine droplets (approximately 1.5 mm to 2 mm) can be entrained and suspended in the liquid slug region, a more likely occurrence as velocity increases.
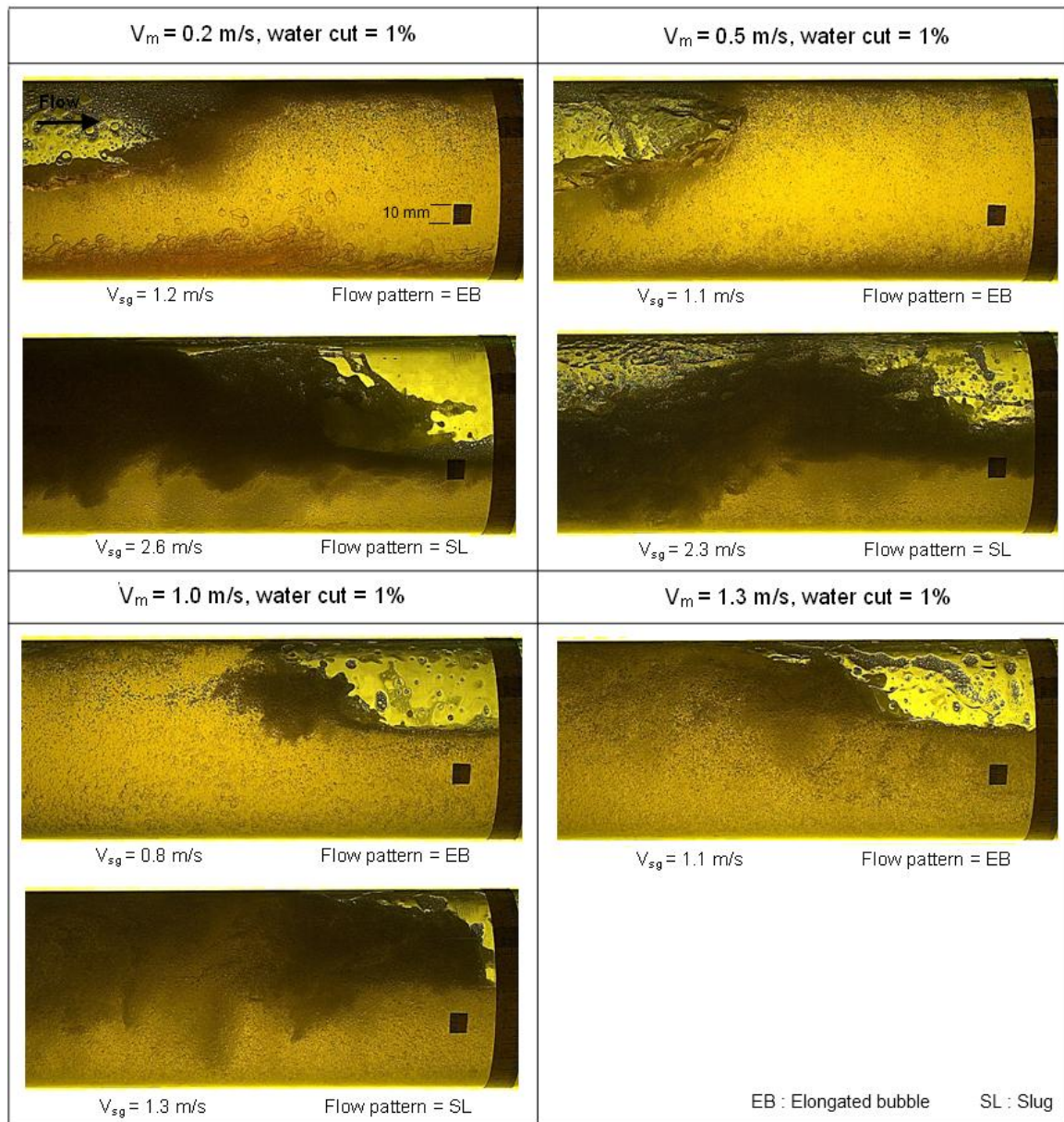
Figure 5-7: Images of flow patterns at V_m = 0.2 m/s to1.3 m/s, 1% water cut showing elongated bubble (EL), slug (SL) flows for CO_2-LVT200-water system.
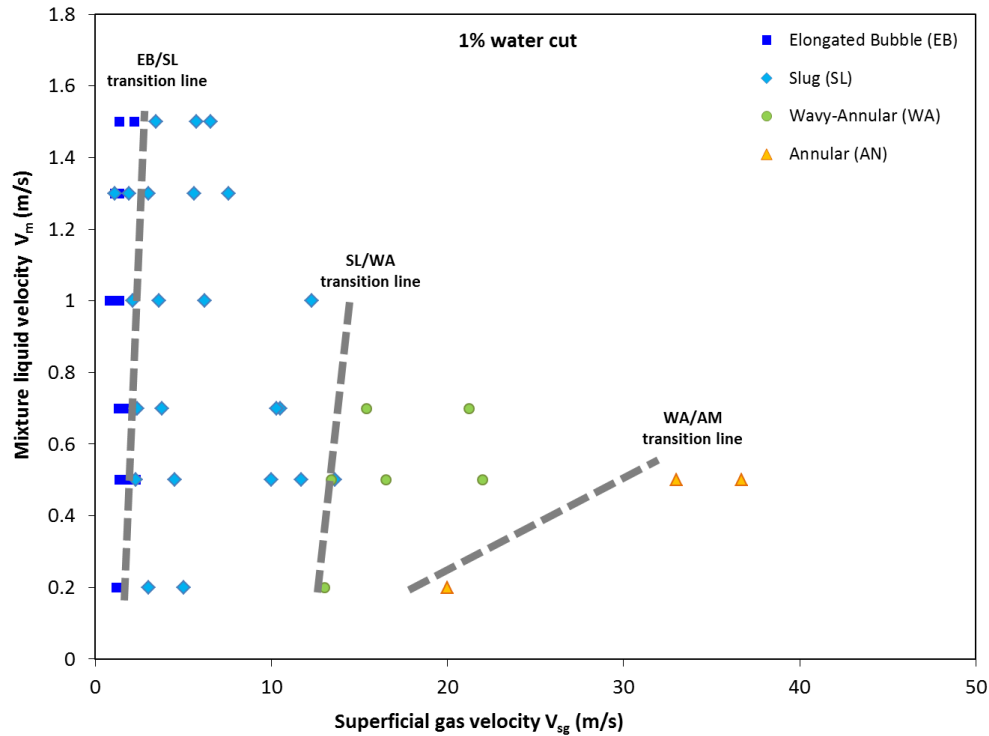
Figure 5-8: Flow pattern map for horizontal CO_2-LVT200-water system at 1% water cut.

5.3.2.2 5% water cut

The images for horizontal gas-oil-water flow conditions at 5% water cut were presented in Figure 5-9 and Figure 5-10. Given the tested liquid and gas velocities, four types of flow patterns namely *EB*, *SL*, *WA* and *AM* can be identified, each transitioning to the next one with increasing gas velocity. The flow data points are plotted on a flow pattern map at 5% water cut as shown in Figure 5-11 showing the transition of these flow patterns.

- Water distribution in *EB* flow

At 5% water cut, water can be seen in the forms of large droplets (approximate 6 mm) as well as thin water film in the pipe bottom. The water droplets became slightly perturbed in the liquid plug region but still mostly settled downward by gravity. At higher mixture liquid velocity

V_m = 1 m/s the water droplets (approximate 3 mm) were more dispersed and energetic, however most were still distributed in the lower pipe wall.

- Water distribution in *SL* flow

At low liquid velocity V_m = 0.2 m/s, water droplets were seen suspended and dispersed in the liquid slug, with increased concentration towards the bottom wall. Large water droplets (approximate 5 mm) were sheared and some eventually broken up in the slug body due to the circulatory action of vortex shedding in the liquid slug. After the slug passed, the liquid slowed down in the liquid film zone, leading to water accumulation at the pipe bottom. By increasing the mixture liquid velocity V_m = 1 m/s, the entrained water droplets were smaller (approximately 2.5 mm) and more energetic under the action of turbulence, resulting in an almost uniform dispersion across the pipe section.

- Water distribution in *WA* and *AM* flows

Because of the opaqueness of the fluid mixture caused by the gas entrainment, water cannot be distinguished clearly in the visualization. In a wall-bounded turbulent flow, the fast-flowing gas tends to displace the entrained particles sidewards to the wall due to the turbophoresis force (Varaksin, 2007), hence elevating the risk of water droplets wetting the wall. The liquid distribution was mostly circumferential, with the lower pipe section is water wetted more frequently than the upper section, corresponding to the dynamic nature of the flow.
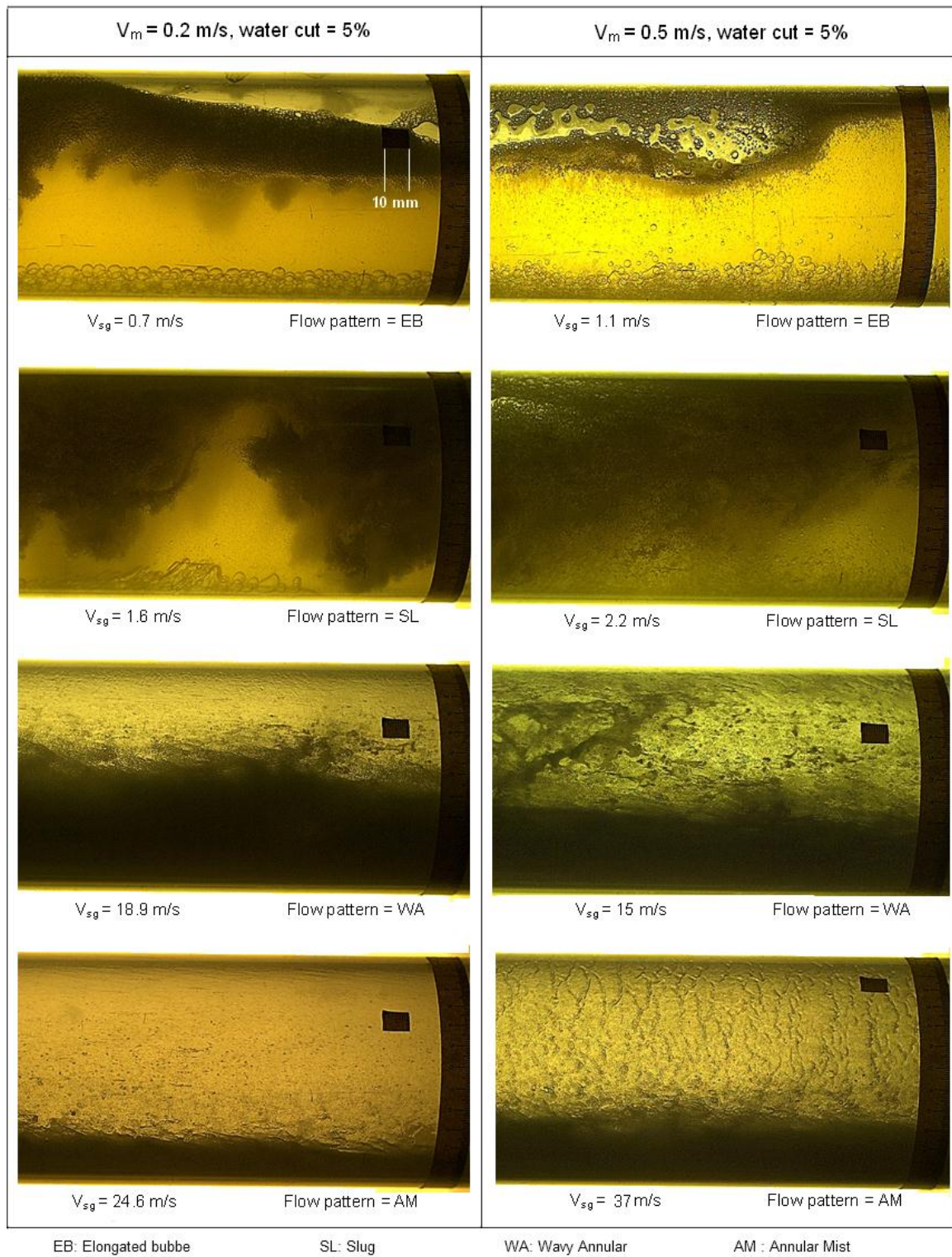
Figure 5-9: Images of various flow patterns at V_m = 0.2 m/s to 0.5 m/s, 5% water cut for CO_2-LVT200-water system.
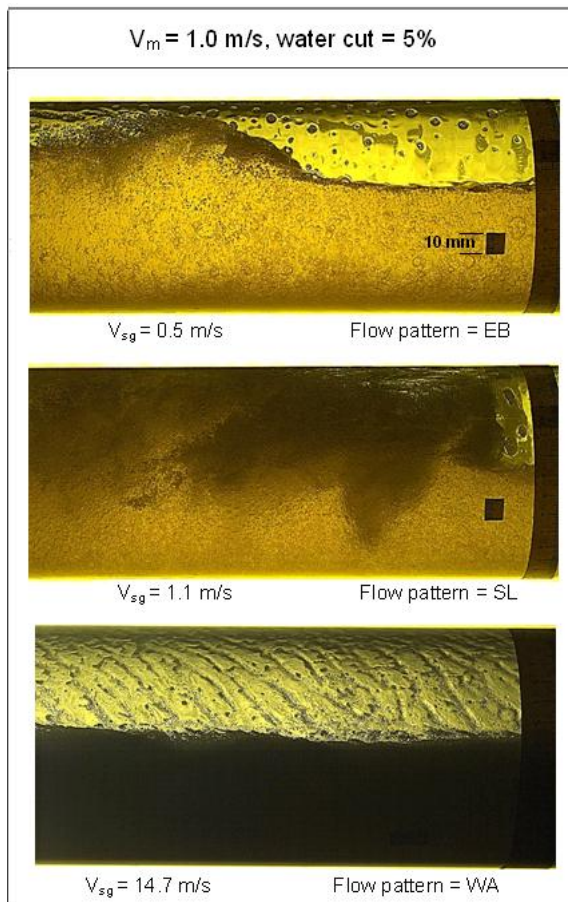
Figure 5-10: Images of various flow patterns at V_m = 1 m/s, 5% water cut for CO_2-LVT200-water system.
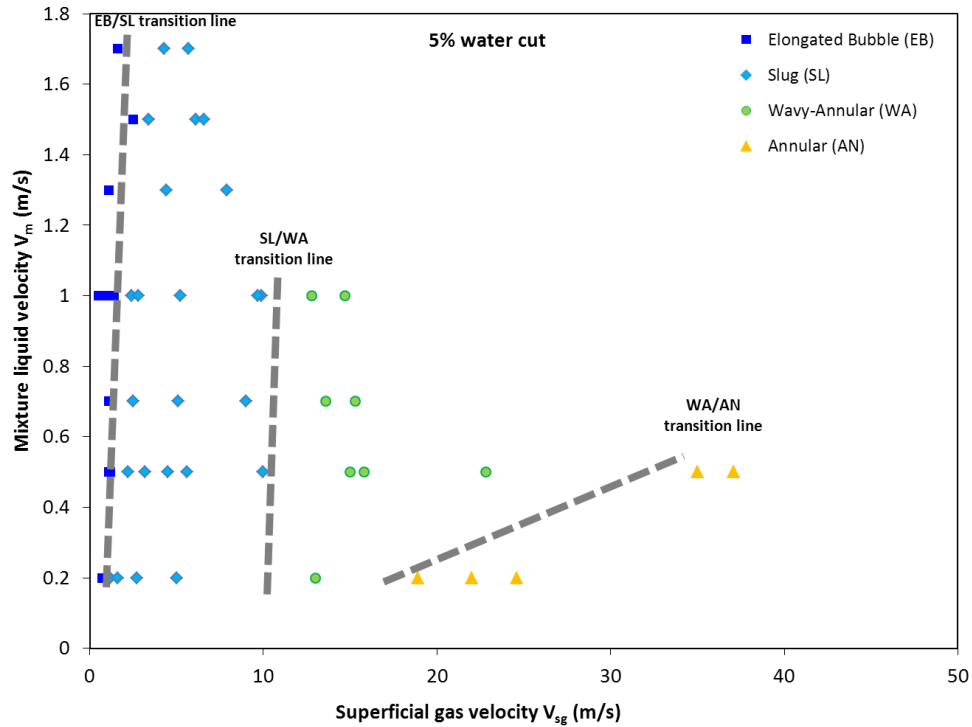
Figure 5-11: Flow pattern map for horizontal CO_2-LVT200-water flow at 5% water cut.

5.3.2.3 20% water cut

The visualization results at 20% water cut are given in Figure 5-12 and Figure 5-13. Similar to previous test series, four types of flow patterns: *EB*, *SL*, *WA* and *AM* flows were observable in the order of increasing gas velocity. The flow pattern map at 20% water cut is shown in Figure 5-14 complete with the transition lines between these flow patterns.

- Water distribution in *EB* flow

At 20% water cut, accumulation of a thick water layer and closely packed water droplets occur at the pipe bottom. As the liquid plug passed, the top portion of the water layer was slightly sheared by the faster moving oil phase. At higher mixture liquid velocity V_m = 1 m/s, the water droplets were more perturbed and energetic, but slower flowing stream of water was still distributed in the lower wall section.

- Water distribution in *SL* flow

By moderately increasing the gas velocity, the slug flow exerted more turbulent energy to mix and disperse the water phase. At lower mixture liquid velocity $V_m = 0.2$ m/s, the water droplets appeared larger (approximately 5.5 mm) but mostly stayed at the bottom wall. At the slug front, the droplets in the upper part of the water layer were more dispersed and suspended, whilst the bottom water layer was still unperturbed. As the slug passed, the suspended droplets settled back down. At higher mixture liquid velocity $V_m = 1$ m/s, the water droplets were smaller (~ 2.5 mm) and energetic, but still concentrated in the lower pipe section, particularly in the stratified gas bubble-liquid film region. Because of the high water cut, water is mostly distributed in the lower half circumferential of the pipe.

- Water distribution in *WA* and *AM* flows

The fluid mass appeared as an opaque mixture of liquid and gas phases. For a wall-bounded turbulent flow with high gas velocity, the fluid particles were dynamically distributed closer to the wall, with thicker film at the base than at the top of the pipe.

The general distribution and location of water for these three-phase flow patterns can be summarized in Table 5-3. It is noted the interplay of water cut and gas velocity strongly influence the whereabouts of water in the pipe flow.

Table 5-3: Water distribution and location

No.	Flow patterns	Water distribution, location
1	Stratified (ST)	separated, bottom
2	Elongated bubble (EB)	separated, bottom
3	Slug (SL)	dispersed/separated, mostly bottom
4	Wavy annular (WA)	dispersed, mostly circumferential
5	Annular-mist (AM)	dispersed, circumferential
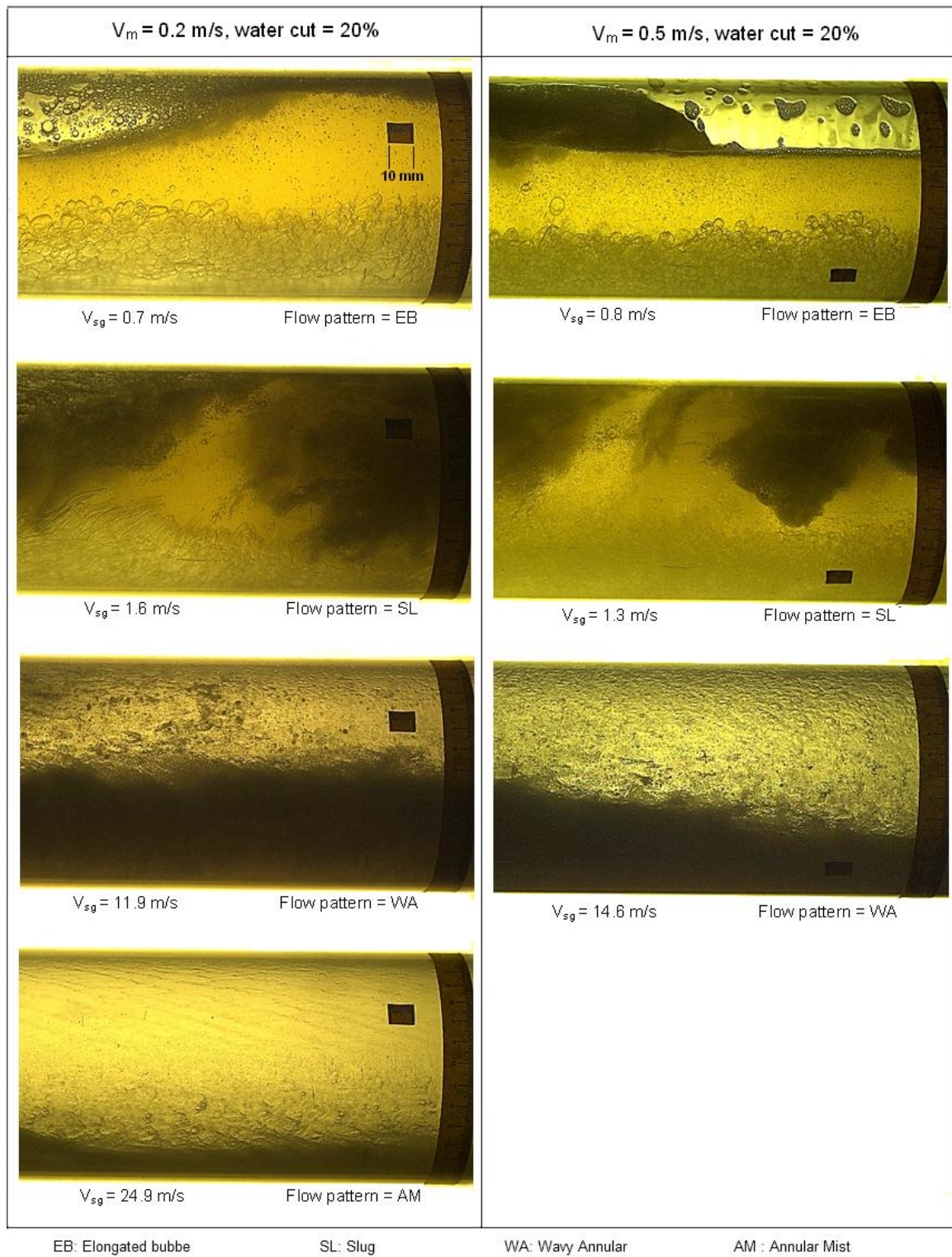
Figure 5-12: Images of various flow patterns at V_m = 0.2 m/s to 0.5 m/s, 20% water cut for CO_2-LVT200-water system.
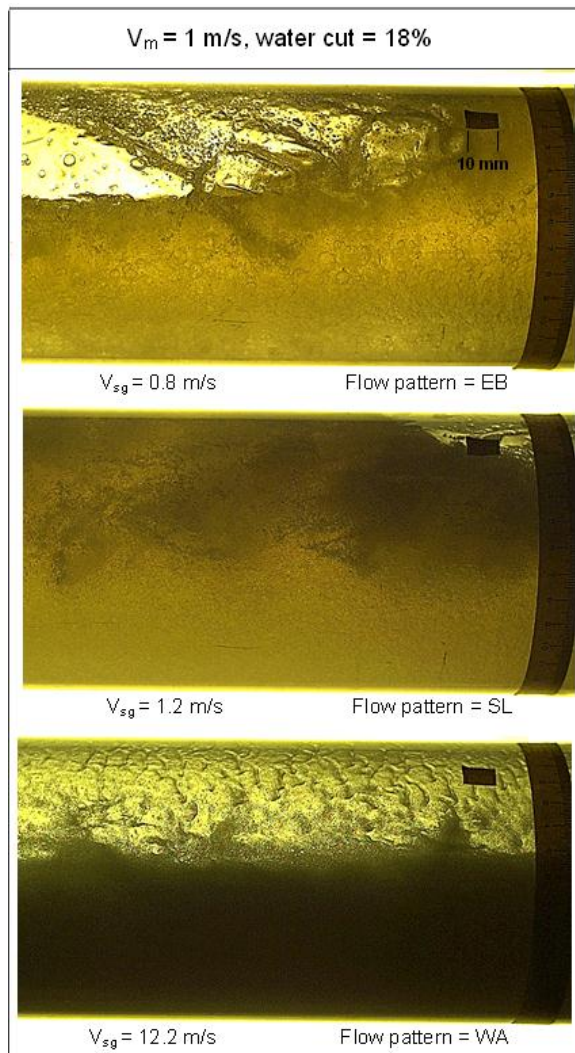
Figure 5-13: Images of various flow patterns at V_m = 0.2 m/s to 0.5 m/s, 18% water cut for CO_2-LVT200-water system.
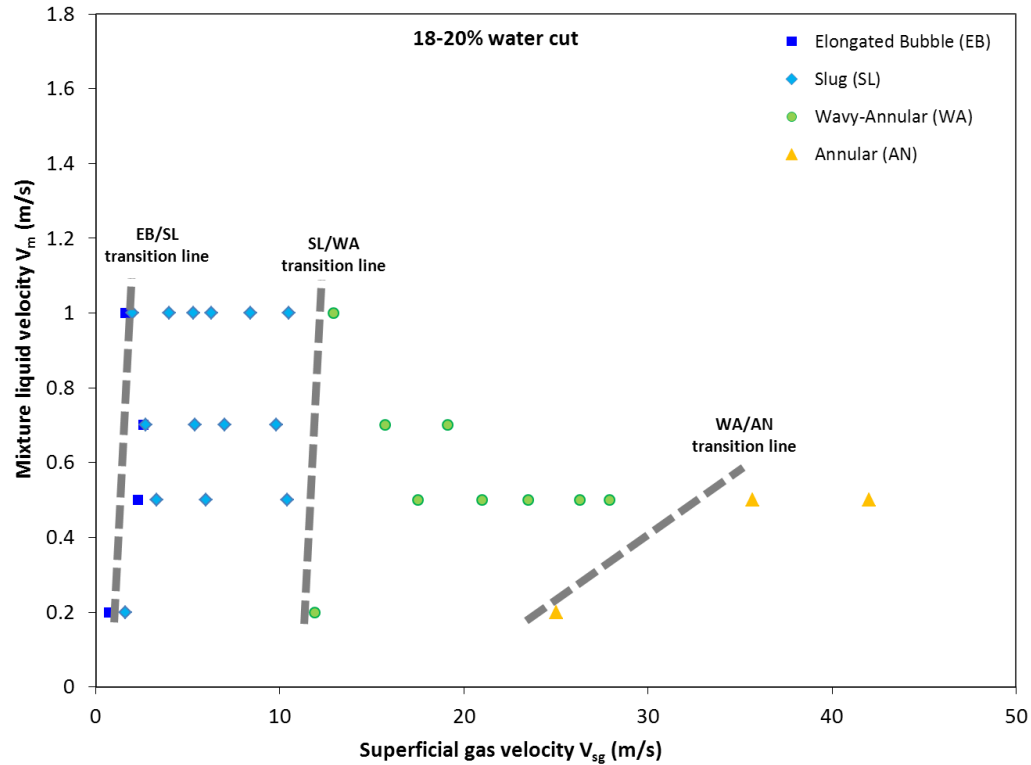
Figure 5-14: Flow pattern map for horizontal CO_2-LVT200-water system at 18%-20% water cuts.

5.3.3   Surface wetting

The surface wetting study was performed in the horizontal flow loop using a steel test section mounted with conductivity pins. Similar to the case in two-phase oil-water flow, the surface wetting results were obtained using model oil LVT200 as the oil phase (without additives), and tested on a clean steel surface condition. The surface wetting data were analyzed according to four categories of surface wetting regimes as described in Table 4-3. The wetting test series were performed such that the oil-water flow was first established at a specified mixture liquid velocity in the flow loop before the CO_2 gas stream was introduced and gradually increased in its velocity. By analyzing the wetting snapshots produced from the conductivity pin system, the surface wetting behavior at each given flow condition was represented as a data point in a surface wetting

map. Similar to the flow pattern map, the wetting map is produced by plotting the wetting data as a function of the superficial gas velocity V_{sg} on the *x*-axis and total mixture liquid velocity V_m on the *y*-axis. A broken line is drawn on the map to delineate the empirical transition between the *water wetting* and *oil wetting* conditions. The distinction can be viewed from the corrosion standpoint. The *water wetting* condition includes the stable water wet and unstable water wet behaviors that are likely for corrosion to occur, while the *oil wetting* condition includes the stable oil wet and unstable oil wet behaviors that are unlikely to incur corrosion or the corrosion is minimal.

5.3.3.1 1% water cut

Figure 5-15 shows the surface wetting map for 1% water cut in horizontal gas-oil-water flow. A wetting transition line is drawn on the map to represent the observed wetting behavior change from *water wetting* to *oil wetting*. The results showed that the water wetting prevailed when the mixture liquid velocity $V_m \leq 1$ m/s and the gas velocity was at the lowest ($V_{sg} \leq 1$ m/s), with the flow patterns identified as *EB* flow. As evidenced from the flow visualization results in Section 5.3.2, the water wetting was caused by the water droplets that dropped out and agglomerated in the bottom wall around the 4 to 8 o'clock pipe position.

For gas velocity $V_{sg} > 1$ m/s in which the flow patterns began to transition to *SL*, *WA*, *AM* flows, the *water wetting* behavior diminished and was replaced by *oil wetting* at the pipe bottom. Few instances of intermittent wetting showed up at the bottom and the side (3 o'clock) of the pipe wall, resulting in unstable oil wet and stable oil wet conditions. This behavior was in accordance with the vigorous mixing actions of the flow that can fragment and suspend the 1% water fraction in the system, as observed from the flow pattern visualization results. The wetting results revealed that *oil wetting* conditions prevailed with increasing gas velocity in *WA* and *AM* flows. As an

example, the changes of surface wetting results with increasing superficial gas velocity at $V_m = 0.5$ m/s, 1% water cut are displayed in Figure 5-16.

In summary, the *water wetting* condition prevails at low gas velocity which generally coincides with the transition from *EB* flow to *SL* flow. Above the transition, the *oil wetting* condition can be achieved at 1% water cut by increasing the gas velocity and/or increasing the mixture liquid velocity beyond $V_m = 1$ m/s. Figure 5-17 shows the effect of increasing gas velocity on surface wetting at $V_m = 1$ m/s, water cut = 1%. With higher V_m input, the *oil wetting* condition can be easily achieved. The small fraction of 1% water can be entrained and suspended by the turbulent flow, a more likely occurrence as velocity increases.
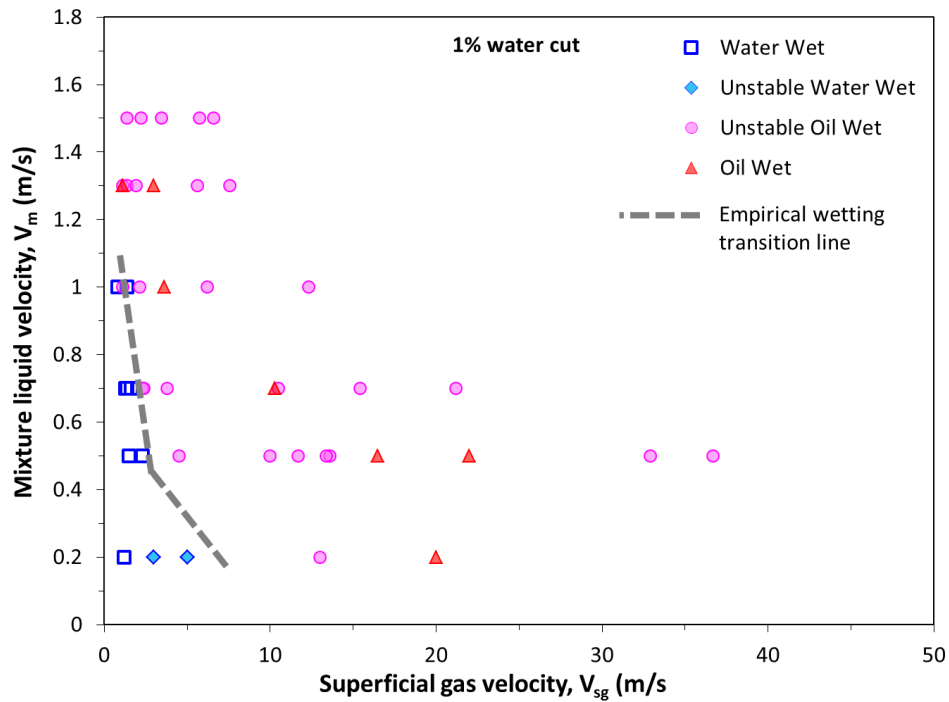
Figure 5-15: Surface wetting map for horizontal CO_2-LVT200-water system at 1% water cut.
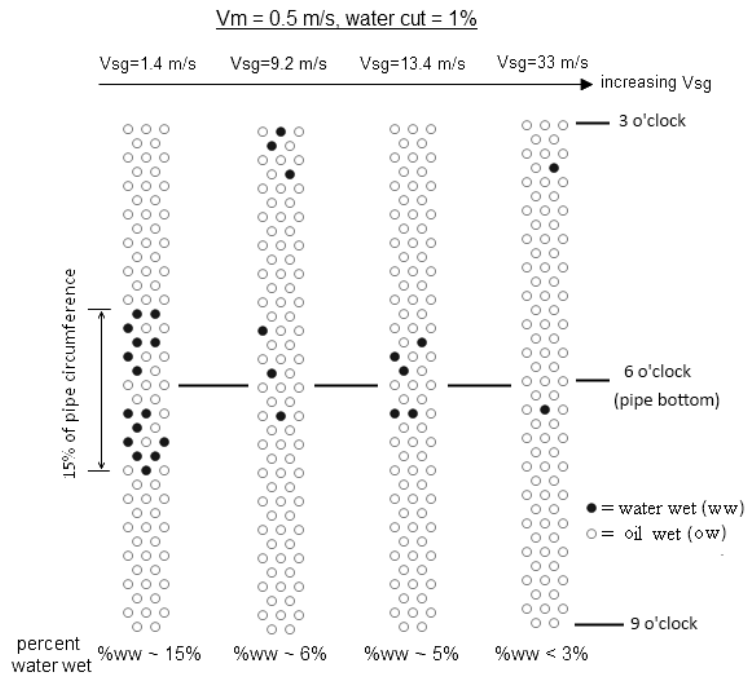
Figure 5-16: Wetting snapshots at varying gas velocities. Flow conditions: V_m = 0.5 m/s, 1% water cut, V_{sg} = 1.4 m/s – 33 m/s.
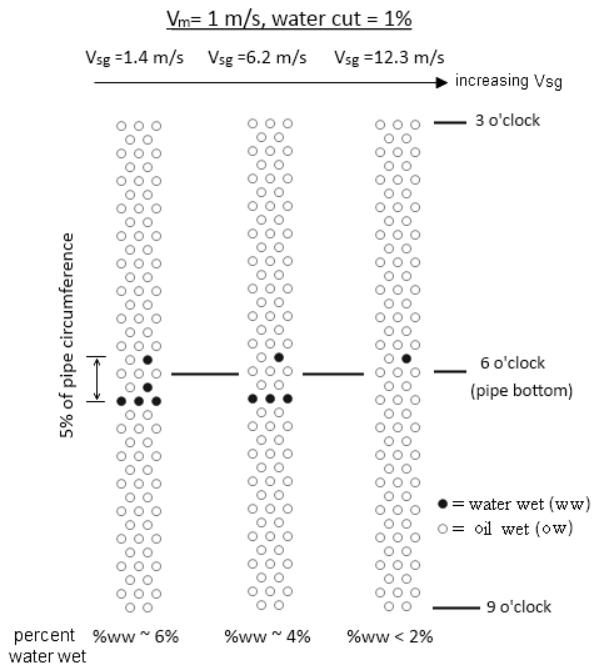
Figure 5-17: Wetting snapshots at varying gas velocities. Flow conditions: V_m = 1 m/s, 1% water cut, V_{sg} = 1.4 m/s – 33 m/s

5.3.3.2 5% water cut

Figure 5-18 shows the surface wetting map for horizontal gas-oil-water flow at 5% water cut. The results shared similar wetting behavior with the previous wetting map at 1% water cut, where the *water wetting* condition dominated in *EB* flow pattern with low gas velocity $V_{sg} \leq 1$ m/s, and *oil wetting* condition prevailed at higher liquid and gas velocities. In the former case, free water was observed to concentrate in the bottom pipe wall in *EB* flow, resulting in water wet behavior. For the latter case in the tested V_m range of 0.5 m/s to 1.7 m/s, the flow patterns transitioned to *SL*, *WA* and *AM* flows with rising gas velocity. In those flow patterns, stable water wet diminished at the pipe bottom, and instances of intermittent wetting between oil wet/water wet became more apparent, resulting in unstable oil wet. The intermittent wetting locations were not limited to the bottom wall but also spread up to the side of the pipe wall. The behavior was in accordance with the water distribution in the observed flow patterns, where the water droplets were mostly dispersed and suspended in the lower half of the pipe. The aperiodic upsurge nature of the liquid slugs/waves driven by the flowing gas led to the local distribution of water dynamically varied at different locations and instances of the flow structure. The effect of increasing superficial gas velocity at $V_m = 0.5$ m/s, 5% water cut on diminishing the intensity of water wetting is shown in Figure 5-19. The case at higher mixture liquid velocity $V_m = 1$ m/s, 5% water cut is depicted in Figure 5-20, which appears to be minimally different from the former case. For the case of smaller $V_m = 0.2$ m/s, the water wetting condition prevailed up to $V_{sg} = 13$ m/s, which corresponded to slug flow. As evidenced from the slug flow visualization results in Section 5.3.2, water droplets were not quite entrained and still visible at the bottom wall in the liquid film zone. It appeared that higher gas velocity was needed at low mixture liquid velocity to disperse the rather large water droplets, approximately 5 mm, in order to reduce the instances of water wetting.
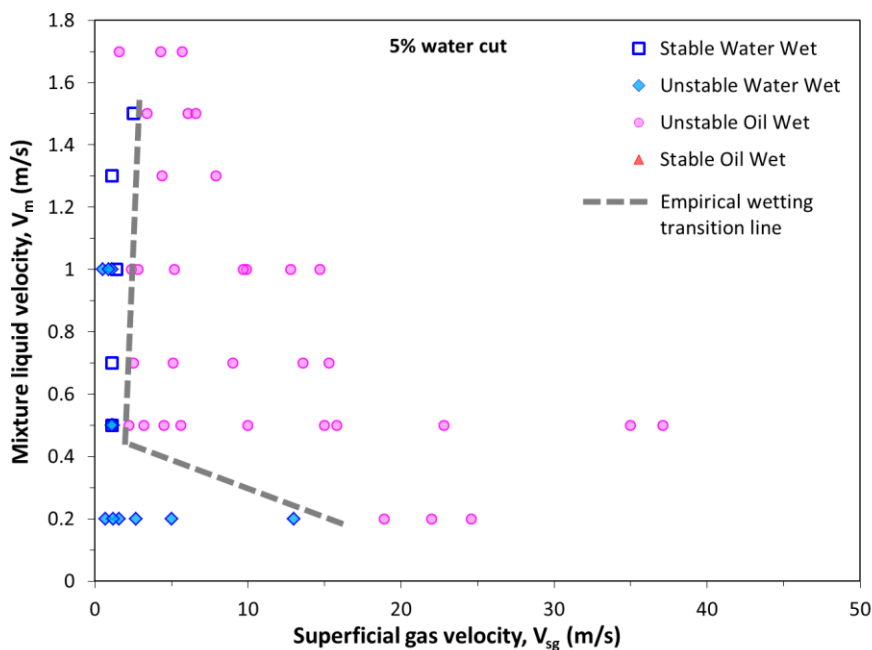
Figure 5-18: Surface wetting map for horizontal CO_2-LVT200 oil-water system at 5% water cut.
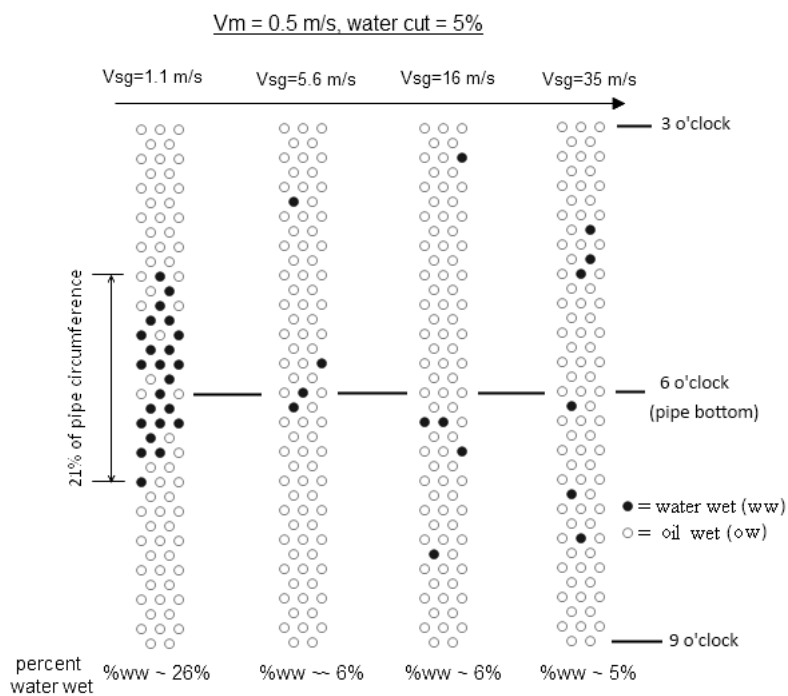
Figure 5-19: Wetting snapshots at varying gas velocities. Flow conditions: V_m = 0.5 m/s, 5% water cut, V_{sg} = 1.1 m/s – 35 m/s.
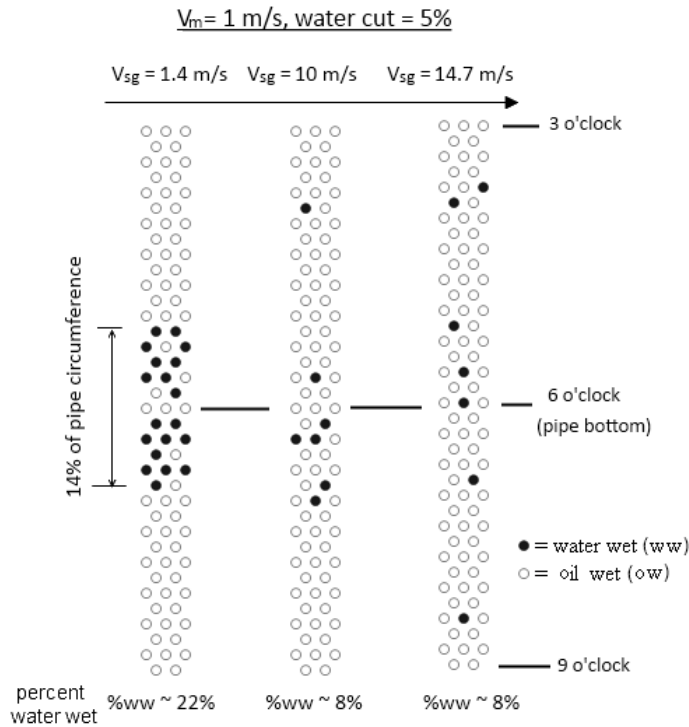
Figure 5-20: Wetting snapshots at varying gas velocities. Flow conditions: V_m = 1 m/s, 5% water cut, V_{sg} = 1.4 m/s – 14.7 m/s.

5.3.3.3 10% water cut

Figure 5-21 showed the surface wetting for horizontal gas-oil-water flow at 10% water cut. The results displayed predominantly *water wetting* condition across the tested liquid and gas velocities, which was different from the wetting results found in 1% and 5% water cut. For all tested liquid velocities, the test section demonstrated stable water wet condition at the bottom wall when the gas velocity ≤ 1 m/s was at the lowest in parallel to the *EB* flow pattern. As the gas velocity increased, the wetting behaviors at the bottom were affected, changing from stable water wet to unstable water wet conditions. In addition, instances of unstable water wet were observed to spread up to the upper circumferential wall rather than predominantly remain at the base. This was attributed to the dynamic nature of the intermittent flows having instances of unstable waves washing over the pipe periphery, leaving a liquid film behind. Apparently with 10% water content

in the pipe, the water wetting behavior could not be diminished by increasing the gas velocity. As shown in Figure 5-22 for flow condition at $V_m = 0.5$ m/s, 10% water cut, the mixing action driven by the gas in a wall-bounded turbulent flow is unable to fully entrain all the water, but appears to spread the water-wetted area further up the upper pipe wall. At the highest gas velocity $V_{sg} = 44$ m/s corresponding to annular-mist flow, unstable water wet condition can be detected by almost all the conductivity pins, which means the wall surface was wetted by water. Similar unstable water wet behaviors were also observed in all tested gas velocities for the case of higher $V_m = 1$ m/s, 10% water cut, as displayed in Figure 5-23.
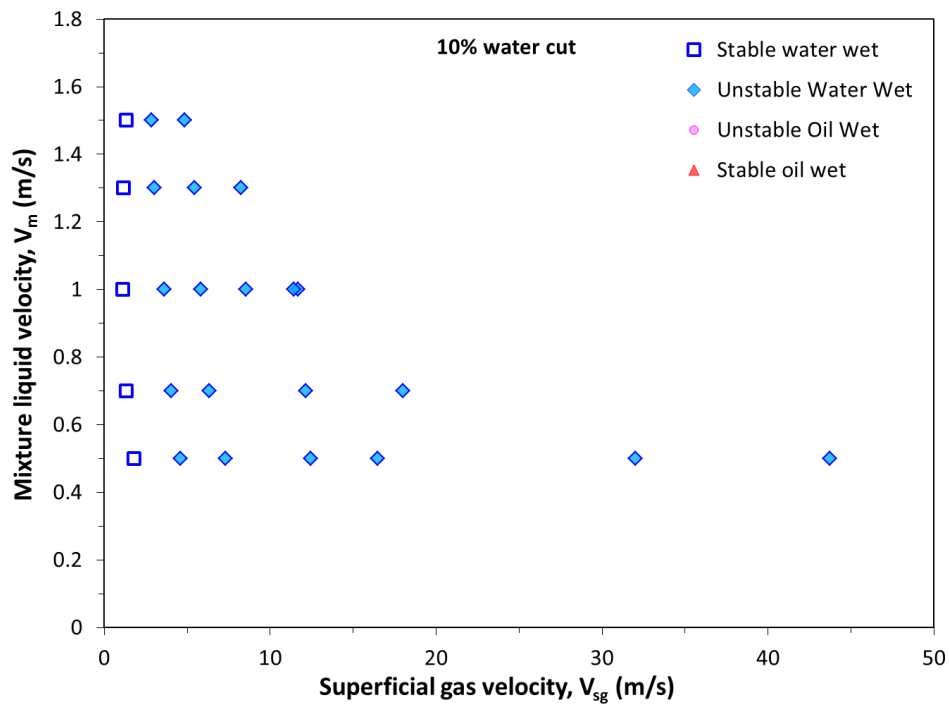
Figure 5-21: Surface wetting map for horizontal CO_2-LVT200-water system at 10% water cut.
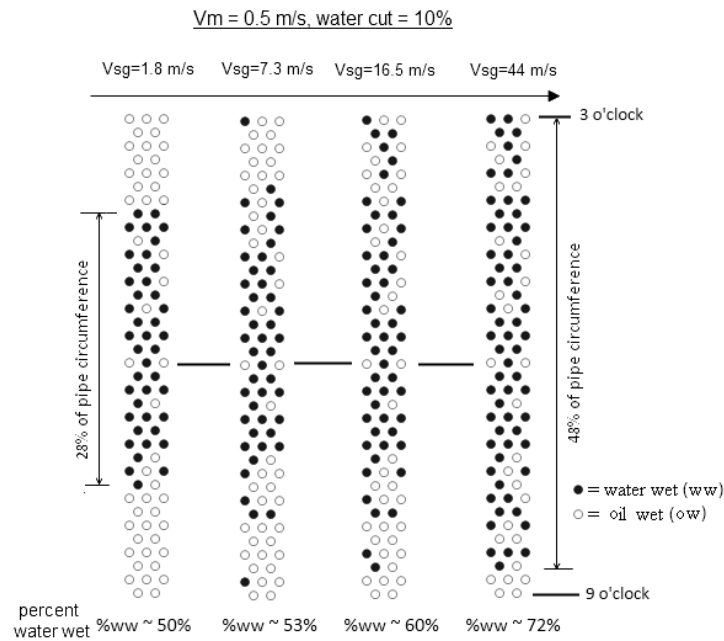
Figure 5-22: Wetting snapshots at varying gas velocities. Flow conditions: V_m = 0.5 m/s, 10% water cut, V_{sg} = 1.8 m/s – 44 m/s.
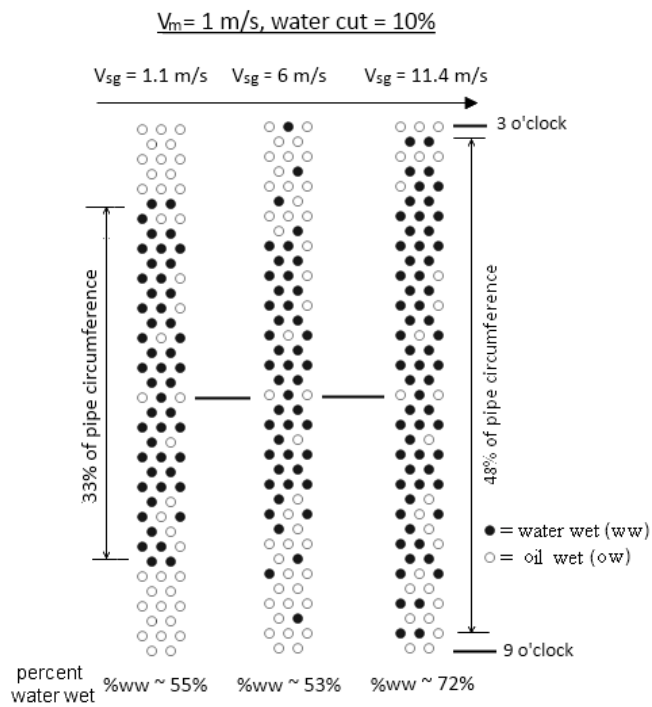
Figure 5-23: Wetting snapshots at varying gas velocities. Flow conditions: V_m = 1 m/s, 10% water cut, V_{sg} = 1.1 m/s – 11.4 m/s.

5.3.3.4 18% to 20% water cuts

The surface wetting for horizontal gas-oil-water flow performed at 18% to 20% water cut is presented in Figure 5-24. It was no surprise that the data shared similar wetting behaviors as the previous results at 10% water cut, with similar water wetting intensity across the tested range of liquid velocities V_m and gas velocities V_{sg}. The wetting results demonstrated stable water wet condition at pipe bottom when the gas velocity was low ($V_{sg} < 3$ m/s), and changed to unstable water wet condition with increasing gas velocities, accompanied by the transitions of flow patterns from *EB* to *SL* to *WA* and finally *AM* flows. At such high water cut, the surface wetting results at lower $V_m = 0.5$ m/s (Figure 5-25) showed similar wetting intensity as the case at higher $V_m = 1$ m/s (Figure 5-26). The water wetted area was observed to concentrate at the lower part of the pipe in moderate gas velocity as in *SL* flow pattern. At higher range of gas velocity parallel to *WA* and *AM* flows, the water wetted area was seen to spread up to both sides at 3 and 9 o'clock. Though water could not be distinguished from the flow visualization results, the effect of fast flowing gas pushing the fluids closer to the wall-bounded region, compounded by the presence of 20% water cut, greatly enhanced the risk of water wetting the wall surface.
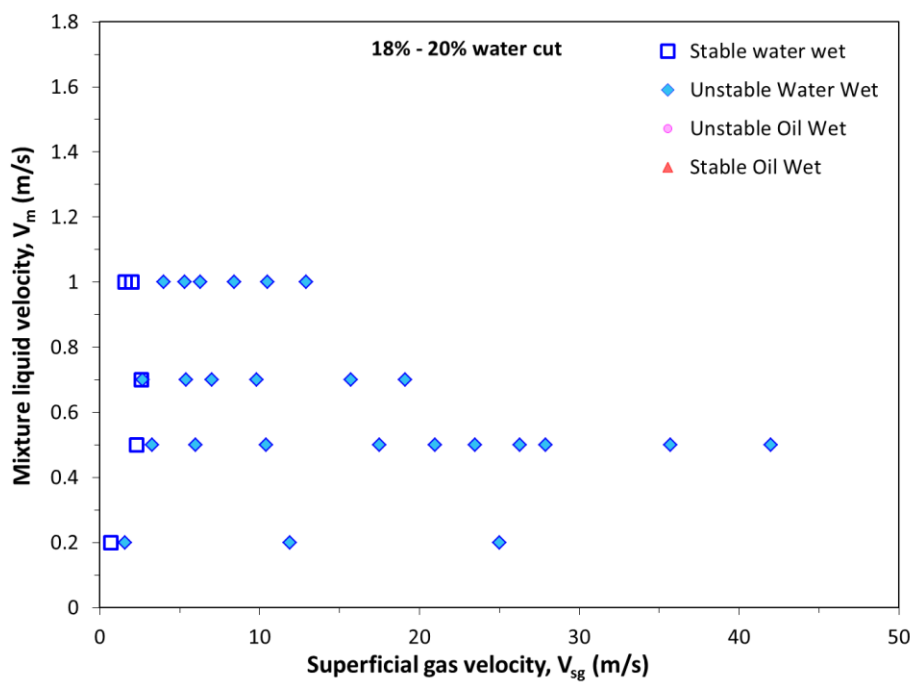
Figure 5-24: Surface wetting map for horizontal CO_2-LVT200-water system at 18-20% water cuts.
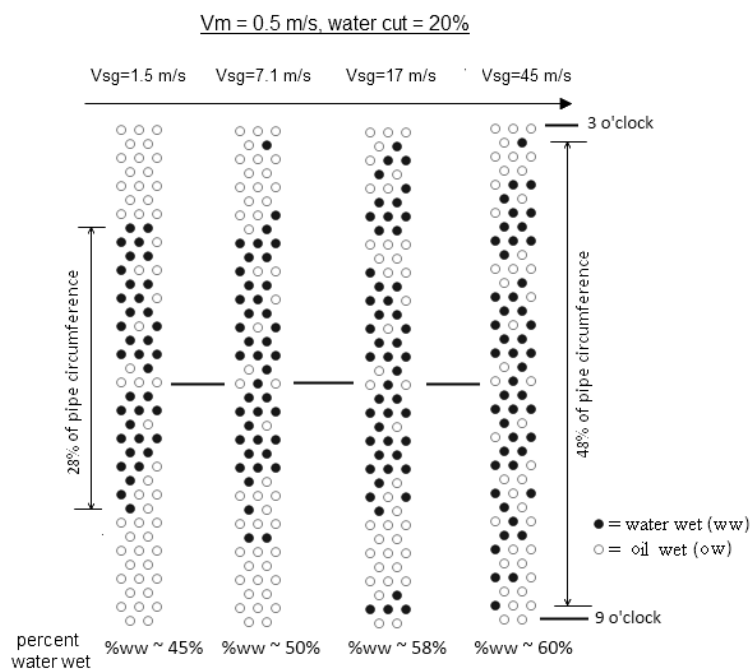
Figure 5-25: Wetting snapshots at varying gas velocities. Flow conditions: V_m = 0.5 m/s, water cut = 20%, V_{sg} = 1.5 m/s – 45 m/s.
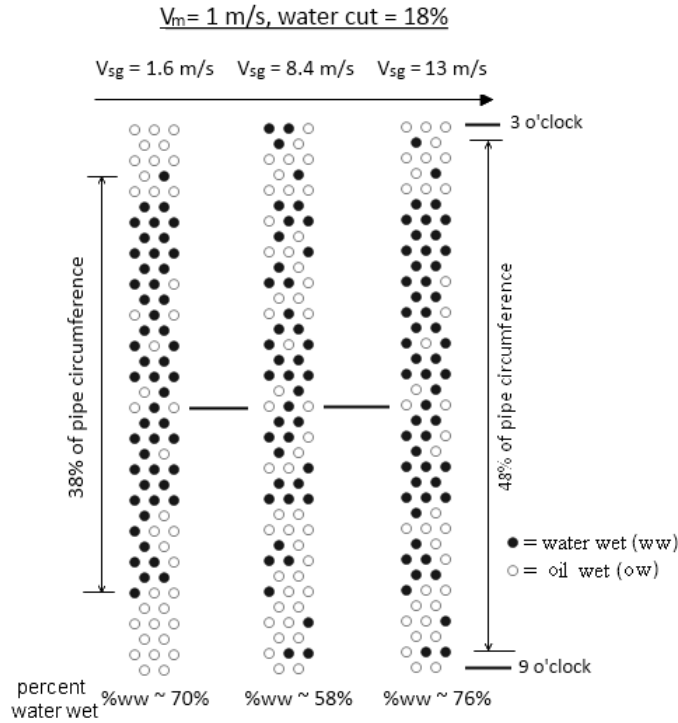
Figure 5-26: Wetting snapshots at varying gas velocities. Flow conditions: V_m = 1 m/s, 18% water cut, V_{sg} = 1.6 m/s – 13 m/s.

5.4 Vertical gas-oil-water flow

For the vertical upward flow experiments using LVT200-water-CO_2 gas system in a 0.1 m ID vertical pipe, the flow pattern results from the high speed video camera and the surface wetting results from the conductivity pins section are presented in the following section.

5.4.1 Flow patterns

There were two main types of vertical three-phase flow patterns identified from the visualization results, namely *churn* and *annular-mist* flows. They are collectively discussed in this section since the global structures and characteristics of the flow patterns do not vary significantly when tested at different phase velocities, but show important differences in terms of

local water distribution when varied from low to high water cuts. Other forms of flow patterns such as slug and dispersed bubbles were not attainable from the tests as they are out of operating range of the current flow loop system. The sequential evolution of the flow patterns and their characteristic features are qualitatively described below. The time series images of the vertical flow patterns are included as the pictorial description of the flow.

Churn flow is one form of intermittent flow condition between slug flow and annular-mist flow. The sequence of images taken at 75 ms interval is shown in Figure 5-27 for flow condition: mixture liquid velocity V_m = 0.5 m/s, 5% water cut and gas velocity V_{sg} = 20 m/s. The flow content appeared to be highly distorted, frequently broken into irregular chunks of liquid mass and gas pockets. The gas phase flows in the central core, usually entrained with an irregular mass of liquid such that neither phase is continuous. Traces of water cannot be discerned from the images, as the fluids had been vigorously churned and appeared as an opaque mixture. From t = 0 ms to 75 ms, a thick liquid mass of wave appearing as a darkish color is seen to flow upward. The liquid mass is distorted with isolated pockets of gas bubble. Images at t = 150 ms to 225 ms show the tailing region (light color feature) of the liquid phase, where the slug of gas flows in the pipe core and liquid film on the circumferential wall is observed to fall backwards. Images at t = 300 ms to 372 ms display that the liquid film pauses momentarily, accumulates on the circumferential wall as marked by the wavy ripple features on the wall, while the gas pressure continues to build up. At this point, the falling liquid film is counterbalanced by the drag of turbulent gas. At t = 450 ms onward, flooding phenomenon occurs in which large interfacial waves (dark mass feature) form and surge up the pipe, reversing the flow of the liquid film (Jayanti & Hewitt, 1992). This unstable oscillatory motion (up-down-pause) is largely attributed to the relative difference in interfacial shear force and gravitational force acting in the opposite direction to the liquid film.

Annular-mist flow typically occurs at very high gas velocity. Figure 5-28 shows the sequence of images taken at 50 ms interval for *AM* flow observed at mixture liquid velocity V_m = 0.5 m/s,

5% water cut and superficial gas velocity of $V_{sg} = 44$ m/s. All the images share a similar flow structure, where the gas (lighter feature) flows as a continuous phase at the pipe core while the liquid phase (darker feature) flows adjacent to the wall to form a thin annular film that flows upward on the wall. The liquid film is unstable, with ripples forming on the interface and some liquid droplets breaking out and becoming entrained in the gas core.
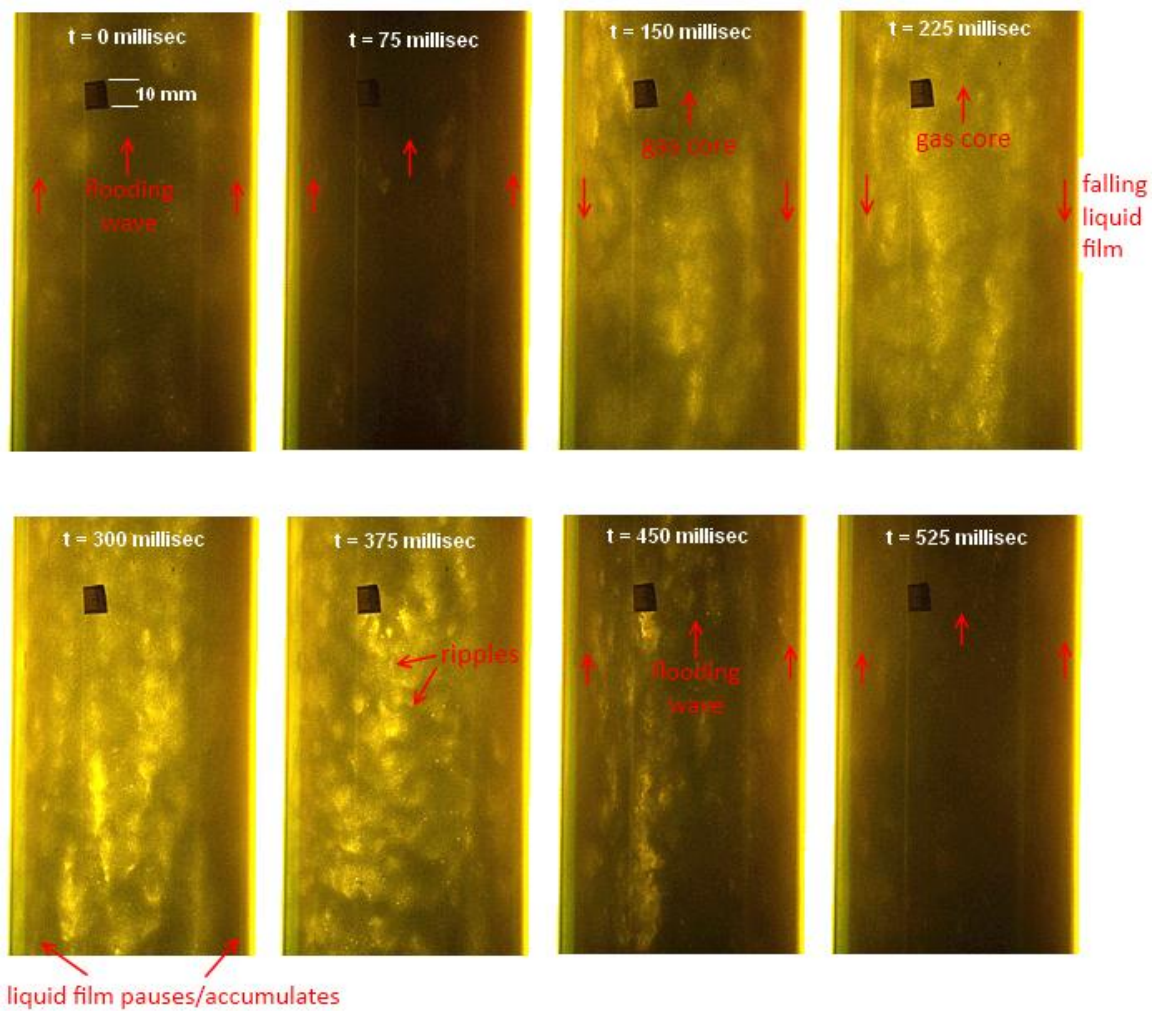
Figure 5-27: Sequential images at 75 ms interval, showing the evolution of churn flow. Flow condition: $V_m = 0.5$ m/s, 5% water cut, $V_{sg} = 20$ m/s.
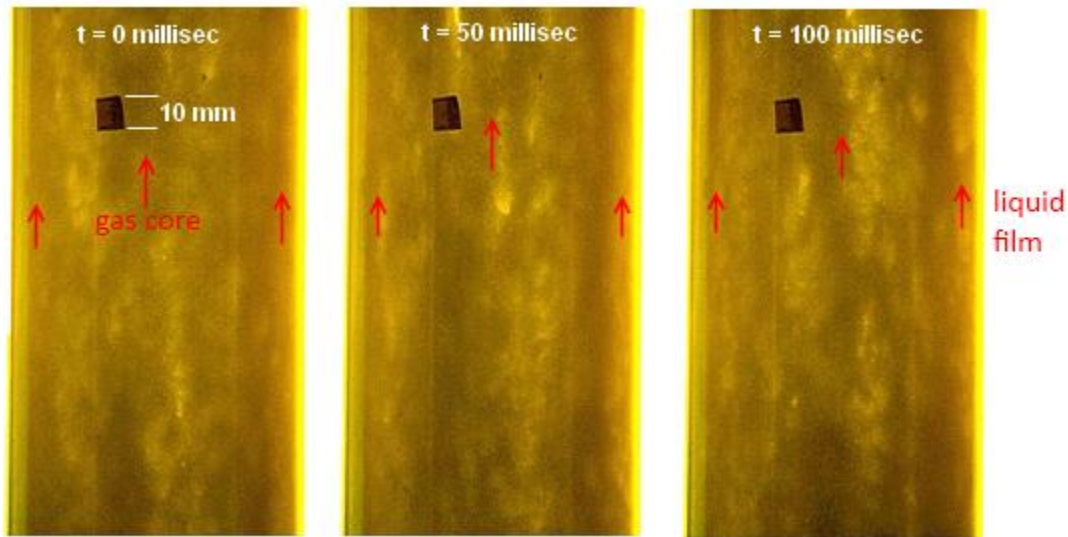
Figure 5-28: Sequential images at 50 ms interval, showing *annular-mist* flow. Flow condition: V_m = 0.5 m/s, 5% water cut, V_{sg} = 44 m/s.

The observed vertical flow pattern results were plotted in flow pattern maps for 1% to 10% water cuts as shown in Figure 5-29 to Figure 5-31. The flow data points showed that the *churn* flow, which is a form of intermittent flow, prevailed in the lower range of gas velocities between 6 m/s to 22 m/s. Ohnuki & Akimoto (2000) also observed similar behavior that the churn flow was dominant in the large diameter vertical pipe under the conditions where slug will occur in small diameter pipe. On increasing the gas velocities beyond 25 m/s, the flow show gradual transition to annular-mist flow. The increase of water cuts from 1% to 10% did not appear to alter the flow transitions. It should be stressed that the transition between the three-phase flow patterns was gradual without a hard flow transition boundary. The flow visualization also became somewhat limited, due to the increased opaqueness of the fluid mixtures with increased turbulence.
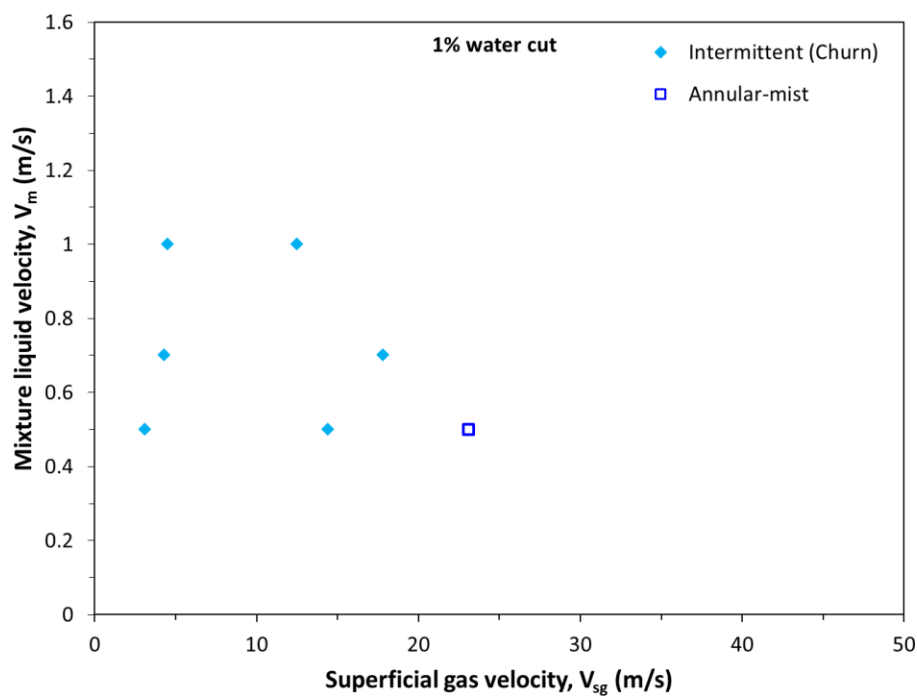
Figure 5-29: Flow pattern map for vertical CO_2-LVT200-water flow at 5% water cut.
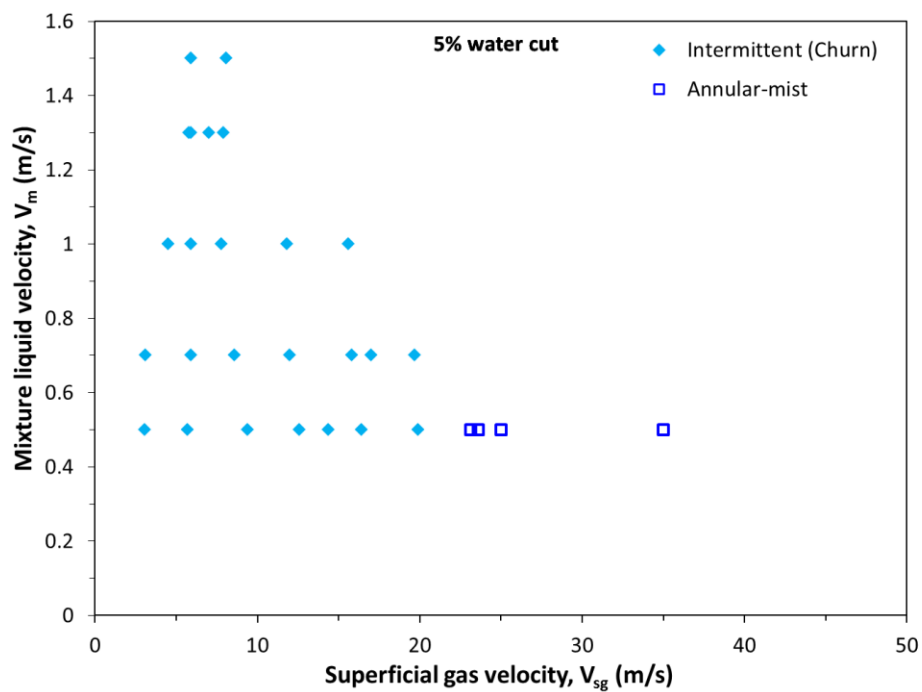
Figure 5-30: Flow pattern map for vertical CO_2-LVT200-water flow at 5% water cut.
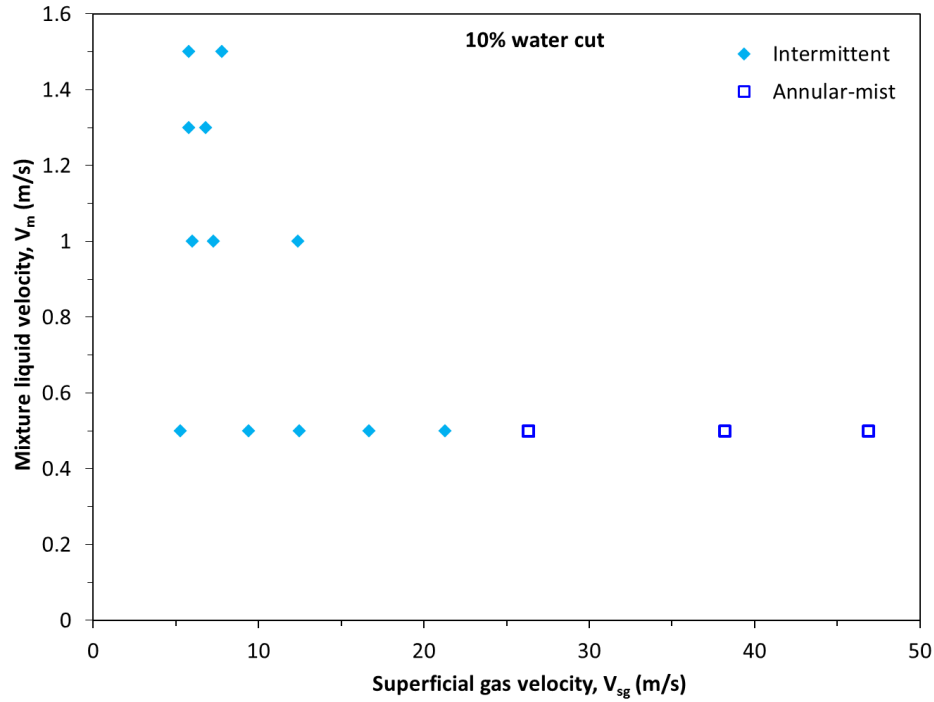
Figure 5-31: Flow pattern map for vertical CO_2-LVT200-water flow at 10% water cut.

5.4.2 Surface wetting

The surface wetting study was performed in the vertical flow loop using a steel test section mounted with conductivity pins. Similar to all previous experiments, the surface wetting tests were carried out using model oil LVT200 as the oil phase and tested on a clean steel surface condition. The wetting test series of experiments were performed by first establishing the vertical oil-water flow at the tested mixture liquid velocity. The CO_2 gas stream was then introduced and gradually increased in its superficial velocity.

The surface wetting results grouped by different water cuts will be presented, with each group tested at varying liquid and gas velocities. The wetting snapshot data were analyzed and plotted on a series of surface wetting maps at different water cuts. Each data point plotted in the wetting map represents one of the four types of wetting regimes as described in Table 4-3.

5.4.2.1 1% water cut

The surface wetting was unstable oil wet where majority of pin area appeared to be oil wet, with 2-4 pins switching between oil wet and water wet. The overall wetting results were plotted and shown in the surface wetting map in Figure 5-32. Unstable oil wet behavior was observed to prevail even when the liquid velocity and/or gas velocity was increased in the flow system. The unstable wetting pins were seen to randomly show up at any circumferential pin location.

The unstable oil wetting results implied that the low concentration of water can be entrained by the oil phase at 1% water cut, hence reducing the probability of water wetting the pipe wall. A continuous water layer was not observed from the flow visualization and the fluids appeared to be highly mixed with oil, water and gas. The liquid mixture was frequently churned and transversely displaced adjacent to the wall when the gas blew through the pipe core, more so at higher gas velocity. Figure 5-33 shows the effect of different liquid velocity V_m and gas velocity V_{sg} on surface wetting intensity at 1% water cut, with the observed flow pattern as churn flow. By increasing V_m and V_{sg} at fixed 1% water cut, the unstable oil wet condition still prevailed and complete oil wet condition was not achieved. Approximately 3% of the measurement area was still intermittently and randomly wetted by the water phase as detected by the conductivity pins.
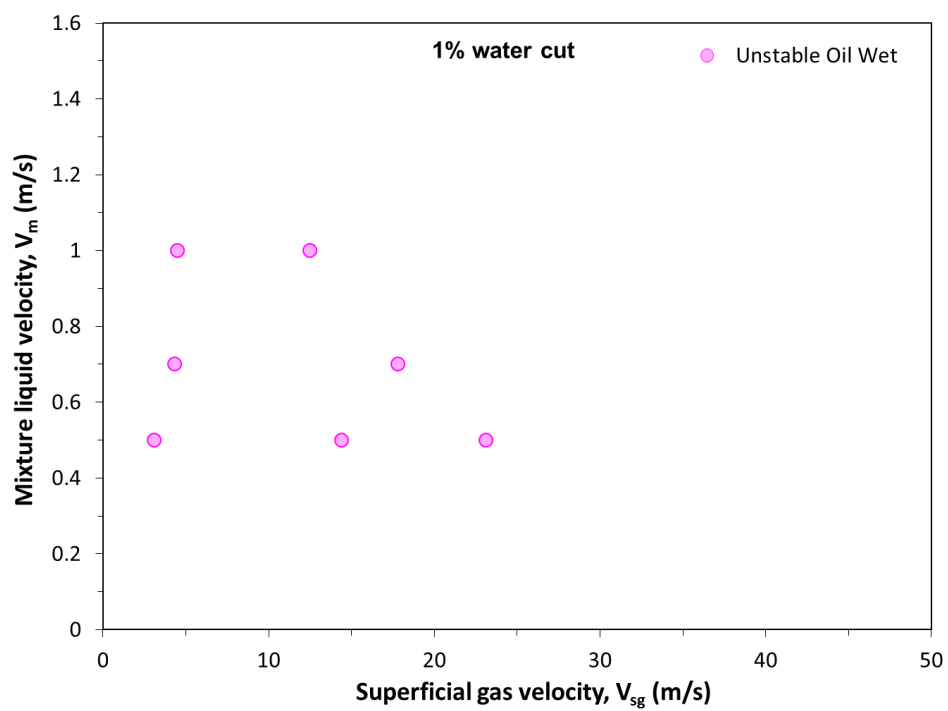
Figure 5-32: Surface wetting results for vertical CO_2-LVT200-water flow at 1% water cut.
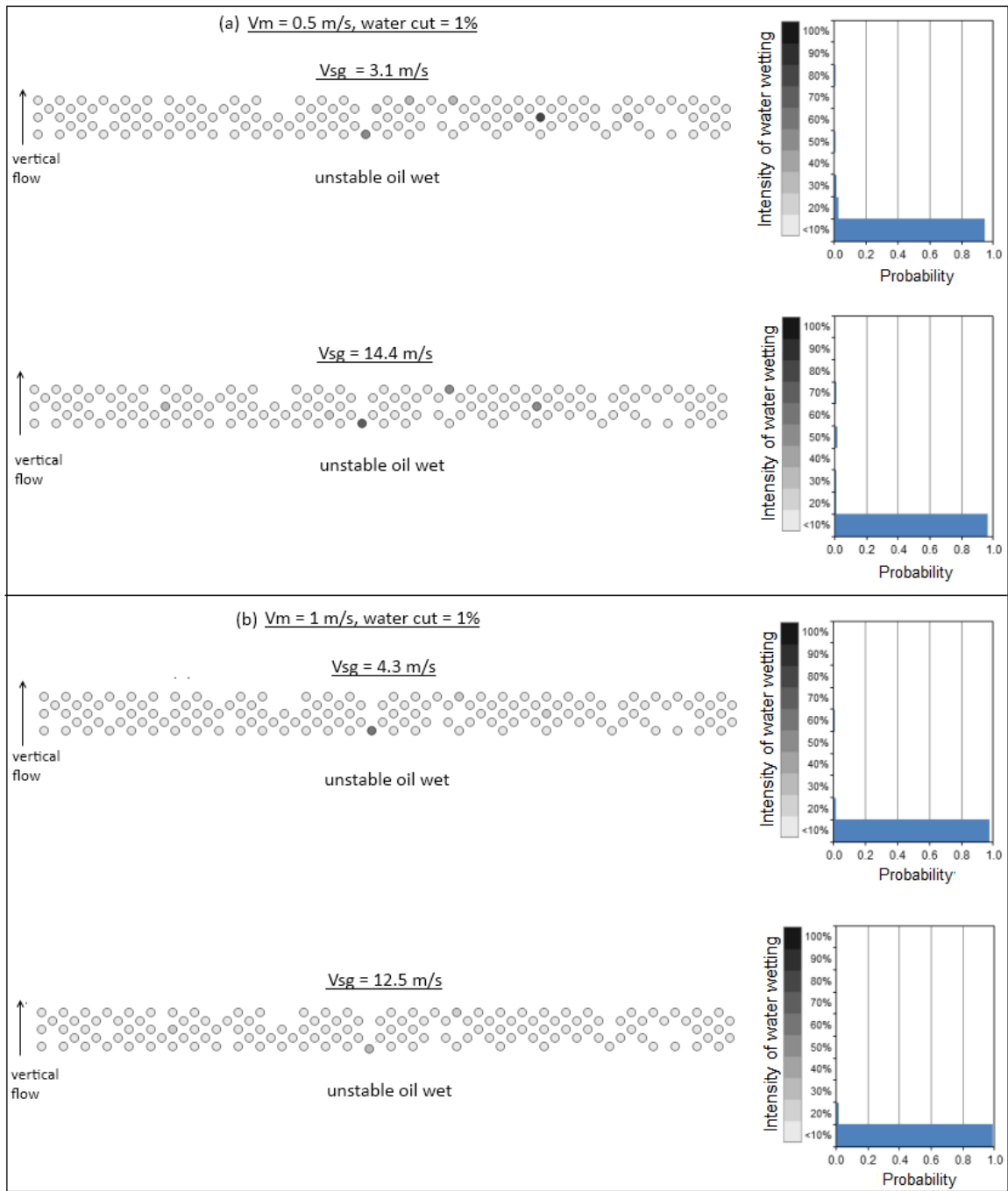
Figure 5-33: Wetting intensity analysis of vertical three-phase churn flow at 1% water cut for different superficial liquid V_m and gas V_{sg} velocities, (a) V_m = 0.5 m/s, (b) V_m = 1 m/s.

5.4.2.2 5% water cut

By increasing the water cut to 5%, the surface wetting at the pipe wall became unstable water wet, where more than 80% of pin area was mostly water wetted, with some measurement locations alternately wetted by oil and water. By increasing the gas velocity, the magnitude of water wetting was not lessened. Figure 5-35 shows the wetting intensity analysis at 5% water cut for $V_m = 0.5$ m/s and $V_m = 1$ m/s. The results show that unstable water wet prevailed for all tested flow conditions. Almost the entire circumference of the wall area was wetted by the water. The distribution of the water on the wall was unstable and appeared random in time and space. It could be attributed to the deposition of the water droplets adjacent to the wall driven by the turbulent gas stream in a wall-bounded tube. In churn flow, the liquid was frequently churned, displaced sideways to the wall and accumulated in the liquid film in response to the chaotic flow dynamics. All this could result in a high probability of water wetting the wall, particularly if the water cut is high enough and/or the oil is not viscous enough. Valle (2000) reported that viscous oil was able to retain more water dispersion and harder to separate out from the emulsion. As the gas velocity was further increased, the flow pattern changed to annular flow. In this condition, the gas flowed in the pipe core while the liquid was pushed to the wall and moved as a layer of liquid film along the pipe, enhancing the likelihood of water wetting the wall surface. The wetting intensity result as shown in Figure 5-36 still indicates unstable water wetting prevailed at annular flow condition. The turbophoresis forces could also contribute to the enhanced deposition and accumulation of fluid particles in the near wall region for a wall-bounded turbulent gas flow (Varaksin, 2007).

.
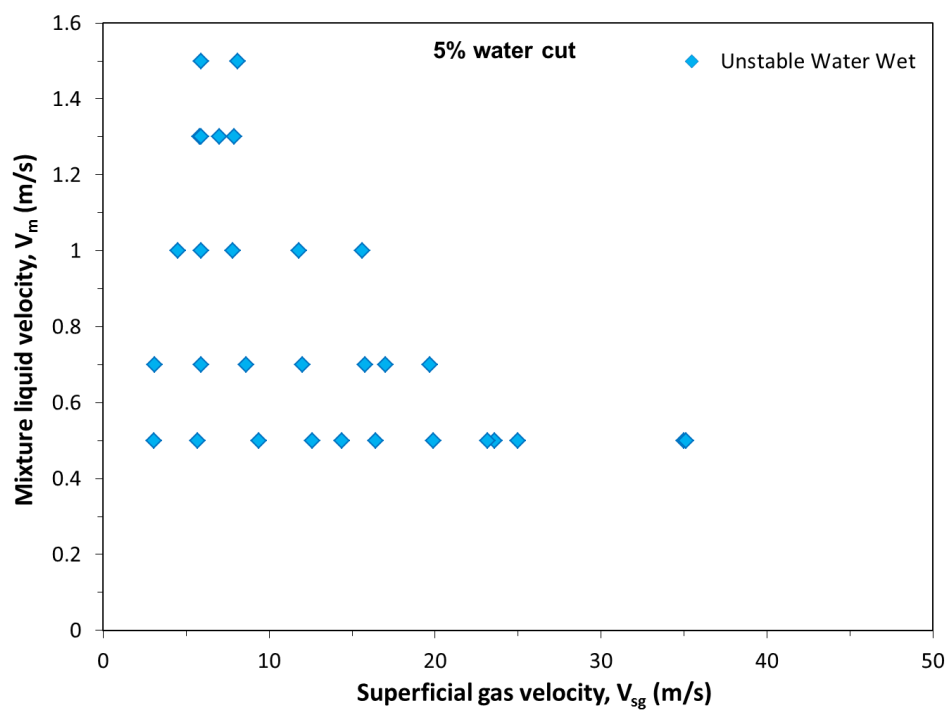
Figure 5-34: Surface wetting results for vertical CO_2-LVT200-water flow at 5% water cut.
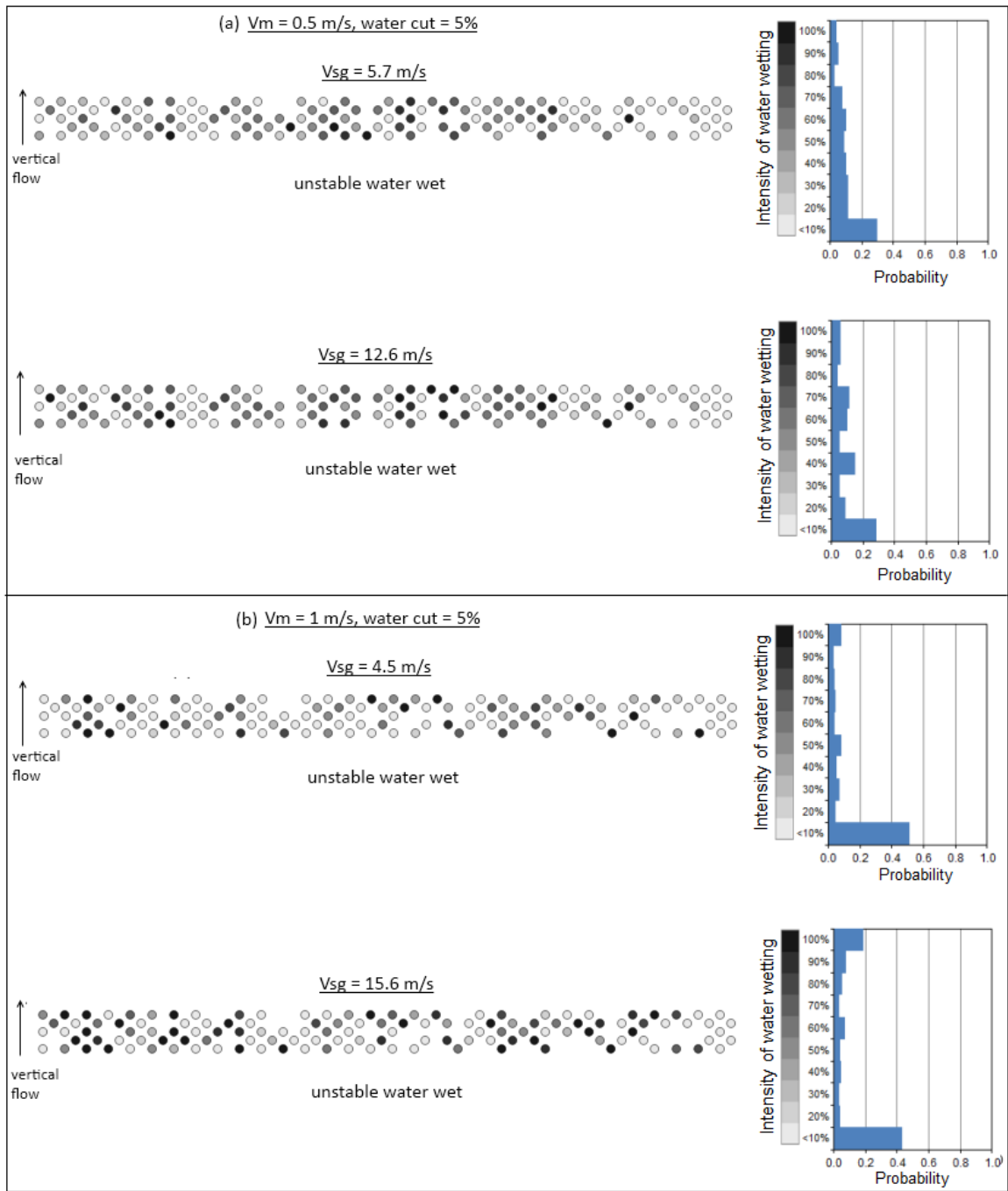
Figure 5-35: Wetting intensity analysis of vertical three-phase churn flow at 5% water cut for different superficial liquid V_m and gas V_{sg} velocities, (a) V_m = 0.5 m/s, (b) V_m = 1 m/s.
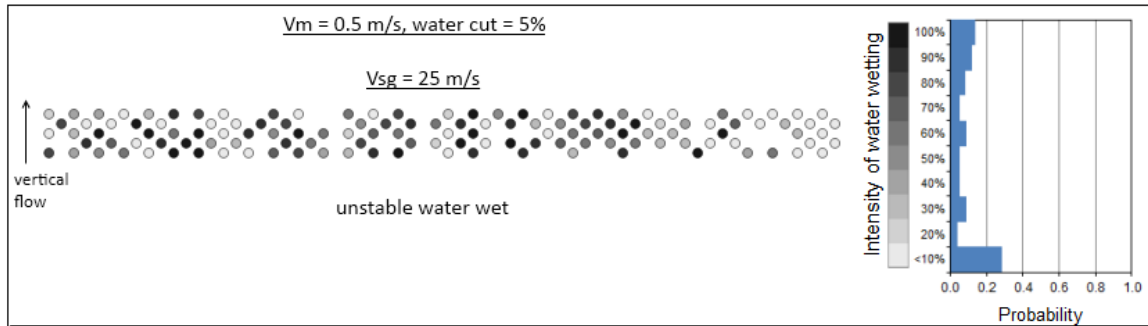
Figure 5-36: Wetting intensity analysis of vertical three-phase annular flow at 5% water cut, superficial liquid velocity V_m = 0.5 m/s and superficial gas velocity V_{sg} = 25 m/s.

5.4.2.3 10% water cut

Figure 5-37 shows the surface wetting map for the vertical gas-oil-water flow at 10% water cut. The wetting results were similar to the former case at 5% water cut, where unstable water wetting prevailed for all tested flow conditions. Upon examining the wetting data, the pin area wetted by water was seen to span more than 80% of the circumferential area. Figure 5-38 shows the wetting intensity analysis for churn flow conditions at 10% water cut. The distribution of water on the wall was highly unstable and seemed to appear randomly across the circumferential wall. Neither increasing the liquid velocity nor gas velocity could lessen the effect of unstable water wetting. With 10% water cut, the near-wall deposition and accumulation of water droplets enhanced the probability of water wetting the wall.
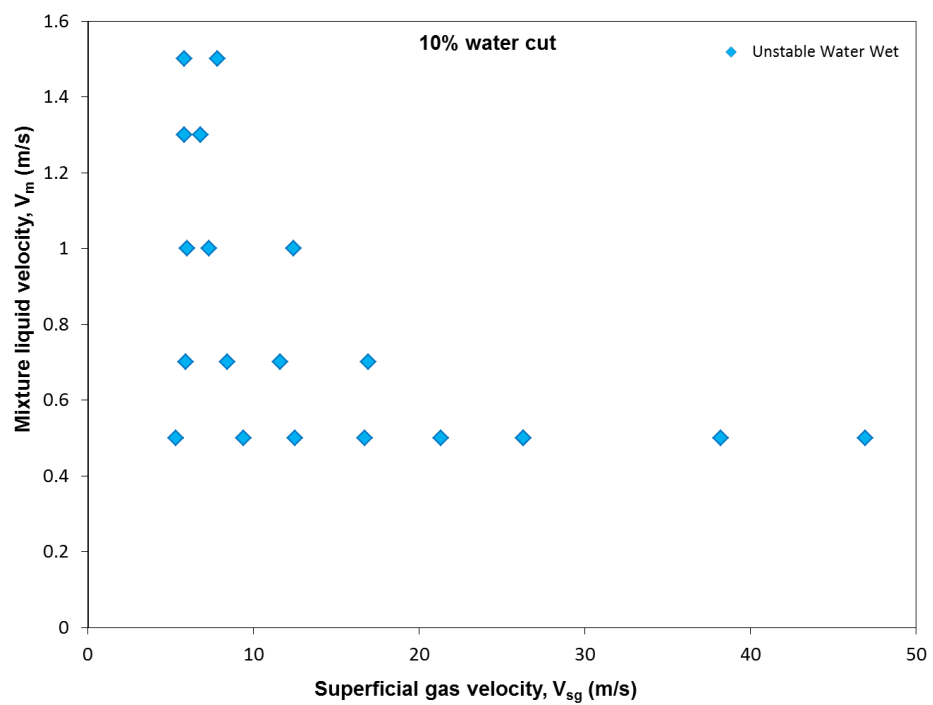
Figure 5-37: Surface wetting results for vertical CO_2-LVT200-water flow at 10% water cut.
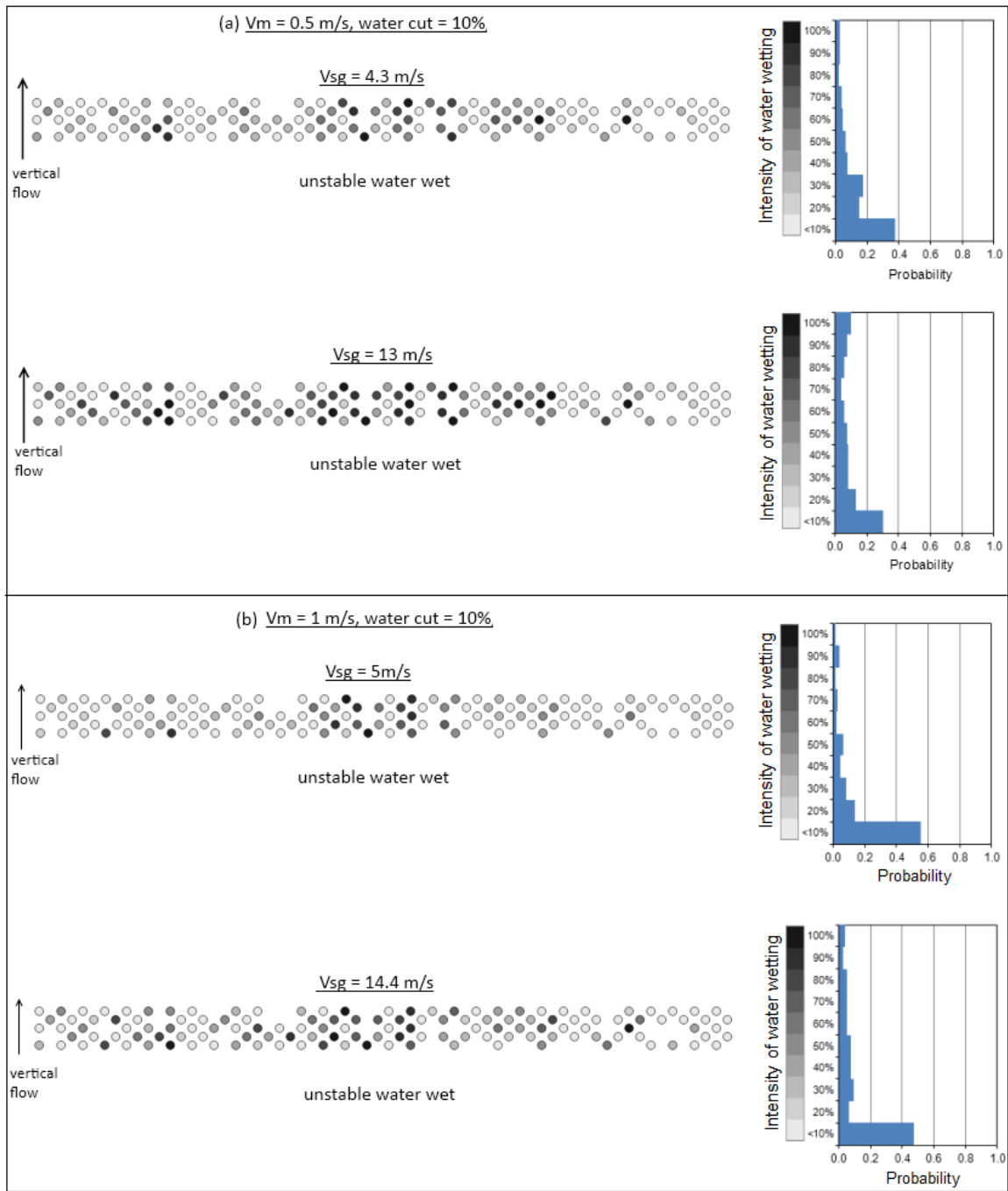
Figure 5-38: Wetting intensity analysis of vertical three-phase churn flow at 10% water cut for different superficial liquid V_m and gas V_{sg} velocities, (a) $V_m = 0.5$ m/s, (b) $V_m = 1$ m/s.

5.5 Summary

- The three-phase flow patterns can be categorized according to the global flow structure of gas-liquid flows. Elongated bubble, slug, wavy annular and annular-mist flow patterns were observed in horizontal flow. Churn and annular flow patterns were observed in vertical upward flow.

- The oil-water distribution in the flow structure can be analyzed for each flow pattern with the high speed camera and conductivity pins. The local water distribution was found to dynamically vary according to different locations and instances of the flow structures.

- With increase of gas and liquid velocities, the fluid mixture became more opaque and the whereabouts of water can only depend on the conductivity pins.

- In horizontal flow with water cuts of 1% to 5%, water separated out at low gas velocity, leading to water wetting at the pipe bottom. At higher gas velocity, water was mostly dispersed, reducing the extent of water wetting and showing unstable oil wetting. Water wetting behavior prevailed when the water cut was increased beyond 5%. The increase in gas velocity did not reduce the extent of water wetting. The water wetted area was seen to spread up to both sides of the pipe.

- In vertical flow, unstable oil wetting was observed at 1% water cut in churn and annular flows. The behavior changed to predominantly water wetting at higher water cut. The increase in gas velocity greatly enhanced the likelihood of water wetting, by pushing the liquid film closer to the wall. The water wetted area was extended to the entire pipe circumference.

CHAPTER 6: IMAGING RESULTS USING ELECTRICAL TOMOGRAPHY

Tomography is a non-intrusive imaging technique designed to visualize the internal structure of an object, generally by emitting waves or radiation. A tomographic image is presented as a two-dimensional view, or slice, conforming to a sensing plane across the object. The tomographic technique was first introduced as computed tomography (CT) 40 years ago and has been widely used as an imaging tool for clinical diagnostics (Garvey, 2002). While CT is generally based on a X-ray source, different imaging modalities based on other physical phenomena such as to microwaves, γ-rays, laser radiation, and ultrasound, electrical impedance have been developed (Grangeat, 2009). Each imaging modality measures a specific physical parameter. Some of these tomographic techniques have been adapted as an investigative tool for industrial processes, commonly called process tomography. Process tomography has found widespread use in mineral extraction, oil and gas, household products, food processing, and pharmaceutical industries. In this thesis, the use of electrical-based tomography is of particular interest, and the principle is briefly described below.

6.1 Principles and system structure

Electrical tomography is based on the measurement of the electrical property of the matter, such as resistivity, capacitance and impedance. The technique is used to visualize multi-component fluids moving in a process pipeline. The electrical-based tomography system typically comprises three functional systems: sensor system, data acquisition system (DAS) and image reconstruction system (Dickin & Wang, 1996). There are two core sensor systems developed for electrically based tomography: Electrical Resistance Tomography (ERT) for the resistivity measurement and Electrical Capacitance Tomography (ECT) for the capacitance measurement

Figure 3-25 shows a 0.1 m ID stainless steel test section mounted with two types of in-line, spool type ECT and ERT sensor systems (model m3000 by Industrial Tomography System, Plc). Both systems are non-intrusive to the flowing media in the pipeline, capable of rapid sensing and providing dynamic real-time imaging of the process. The dimensions of the test section and positions of the sensors are shown in Figure 2-3. The system information for ERT and ECT is listed in Table 6-1 and Table 6-2. Further details on the sensor system are described in the following section.
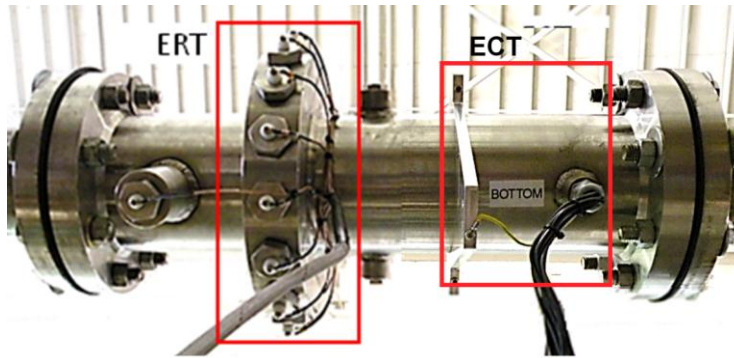
Figure 6-1: Tomography system with ERT and ECT probes in a 0.1 m ID test section.
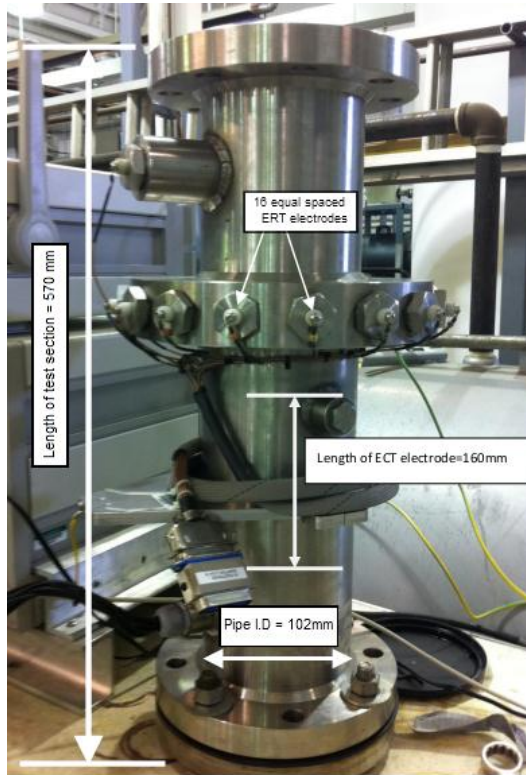
Figure 6-2: m3000 ERT/ECT tomography system showing dimensions and sensors position.

Table 6-1: m3000-ERT system specification (Qiu *et al.*, 2007)

M3000-ERT	
Max. no. electrodes:	16 electrodes
Current injection:	Adjacent
Algorithm:	Linear back projection (LBP)
Property of interest:	Conductivity (σ)
Image spatial resolution:	5%
Microcontroller:	DSP microcomputer ADSP-2181
Injection frequency:	Programmable up to 15 kHz (normal in 10 kHz)
Injecting current:	Up to 40 mA (ad–ad)
Measurement range:	-10 to $+10$ V (pp)
Measurement accuracy:	$\pm 1\%$ (@10 kHz) with ITS standard test vessel with water conductivity of 0.1 ms/cm
Speed of acquisition:	70 ms/Frame (10 kH@16 electrodes)
Communication interface:	USB2.0 with 480 Mbits
Size of PCBs:	Euro-card
Power consumption:	DC 24 V 60 W (power adapter output into DAS, $+5$ V, $+15$ V, -15 V)

Table 6-2: m3000-ECT system specification (Qiu *et al.*, 2007)

M3000-ECT	
Max. no. electrodes:	12 electrodes;
Voltage injection:	Adjacent
Algorithm:	Linear back projection (LBP).
Property of interest:	Permittivity (ε)
Image spatial resolution:	5%–10%
Microcontroller:	DSP microcomputer ADSP-2181
Injection frequency:	Fixed at 1 MHz
Injecting voltage:	Fixed at 18 V (peak–peak)
Measurement range:	$0.001 + 10$ V (pp) with 80 mV increment
Signal-to-noise ratio:	56 db
Measurement stability:	$+/-0.6$ mV
Speed of acquisition:	35 ms/Frame (demodulation @ 500 kH @ 12 electrodes)
Communication interface:	USB2.0 with 480 Mb/S
Size of PCBs:	Euro-card
Power consumption:	DC 24 V 70 W (output into DAS, $+5$ V, $+15$ V, -15 V)

6.1.1 Electrical Resistance Tomography (ERT)

For a multiphase pipeline containing a flowing mixture of gas, oil and water, each of the phases has a different conductivity (unit: S/cm). Conductivity is a measure of the ability of a material to conduct electrical current. Water is a better electrical conductor; hence, it has higher conductivity value compared to a non-conductive medium such as oil or gas. The conductivity of water increases with the introduction of soluble salts, as well as with temperature. By measuring the changes in media conductivity, ERT can be used to differentiate the conductive and non-conductive components of a flowing mixture, such as an oil-water mixture.

The ERT apparatus consists of 16 sensors arranged at equal distance and flush mounted to the inner wall of the circular section. The sensors are in contact with the fluids but not obstructing the flow; hence it is a non-intrusive technique. The 16-electrodes work in pairs, which consist of a pair of excitation electrodes and adjacent pairs as sensing electrodes. In operation, the ERT

system repeatedly injects current between an electrode pair and measures the resultant voltage signals at the remaining electrode pairs according to the adjacent measurement protocol (Giguère *et al.*, 2008). The acquired voltage data are processed *via* an image reconstruction algorithm to display a two-dimensional ERT tomogram of conductivity, as shown in Figure 6-3. The spatial distributions of media containing different conductivities in the pipe cross section are indicated by a color-coded temperature map, with a blue color area as a low conductivity region and red color area as a high conductivity region. The ERT system used in this work has a frame acquisition speed of approximately 14 fps.
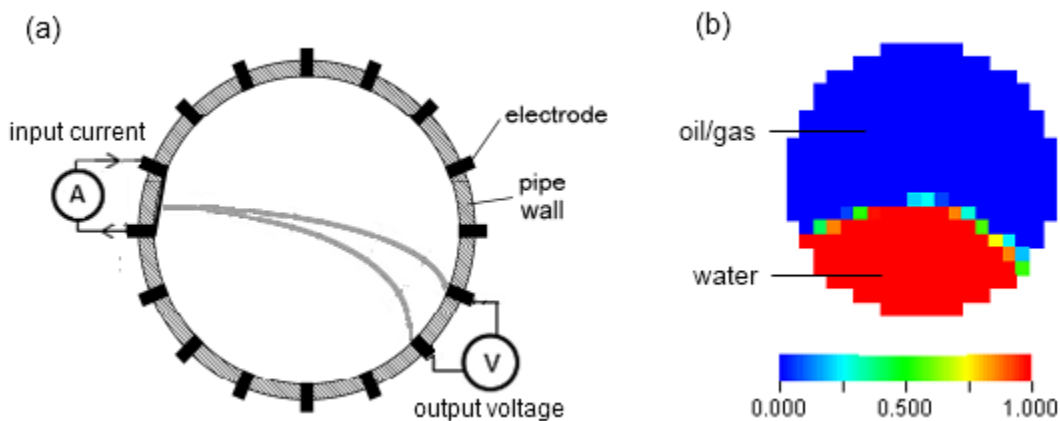
Figure 6-3: a) 16-ERT-electrodes mounted flushed inside the pipe, b) a typical ERT tomogram.

6.1.2 Electrical Capacitance Tomography (ECT)

Electrical capacitance tomography (ECT) can be used for imaging the content of a flowing mixture of dielectric materials having different values of capacitance or permittivity. The capacitance (unit: farad) is a measure of the ability of a dielectric material to store energy in an electric field. For a fixed measurement geometry, the system capacitance is linearly dependent on the permittivity ε (unit: farad/m) of the medium. Consequently, the system capacitance can be

increased by increasing the permittivity of the dielectric medium. The permittivity of a medium or dielectric material is often expressed in relative permittivity, symbolized as ε_r with respect to the vacuum ε_0. Typically, vacuum or air has a relative permittivity value of 1, oil is 3, and water has a much higher value at 80 (Perry *et al.*, 1997). Since the gas, oil and water display different values of permittivity, ECT can distinguish the distribution of different components in the pipeline, particularly between the components with low permittivity (gas) and high permittivity (liquid).

In ECT, capacitance measurements are taken from an in-line spool-type probe consisting of 12 equally spaced electrodes mounted radially around a pipe periphery as shown in Figure 6-4(a). The array of sensors is embedded within the pipe wall, separated from the internal flow medium by an insulating plastic layer and surrounded by an outer earthed screen to minimize noise interference (Isaksen, 1996). Hence, the ECT system is non-invasive and non-intrusive to the flowing process as the sensors do not directly contact the flowing fluid. In operation, $n(n-1)/2$ independent measurements can be obtained from the electrodes combination, where n is the number of electrodes (Bolton *et al.*, 1998). By injecting voltage to an electrode one at a time, and measuring the resultant voltage difference at the remaining electrodes simultaneously, a spatial distribution of media containing different permittivity can be determined across the sensing plane (Isaksen, 1996). The raw data are then converted by an image reconstruction algorithm to a two-dimensional ECT tomogram of permittivity as shown in Figure 6-4(b). The permittivity concentrations are designated by a color-coded temperature map showing blue color as high permittivity region and red color as low permittivity region. In this work, the ECT has a frame acquisition speed of 29 fps.
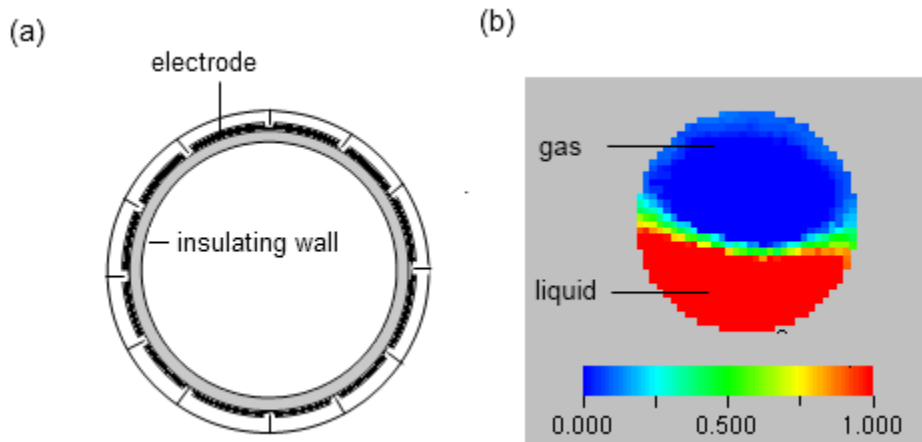
Figure 6-4: a) 12-ECT-electrodes mounted around the pipe periphery, b) a typical ECT permittivity tomogram.

6.1.3 Data acquisition system

The data acquisition system (DAS) consists of the following components: power supply, direct digital synthesizer for signal generation and digital conversion, multiplexer for routing stimulus, digital signal process card for control protocols (Qiu *et al.*, 2007). Figure 6-5 shows the front view of the DAS: a model m3000 which consists of an ERT module in the upper panel and ECT module in the lower panel. The sensor system first converts the electrical impedance (resistivity for ERT, capacitance for ECT) into waveform electrical signals. The signals are sent to the data acquisition unit for conversion into digital values. For ERT measurements, a coaxial cable with a male rectangular connector (IEEE 488 type 36-way cable mount plug) is used to connect the 16 ERT electrodes and one ground terminal. A serial resistor adapter (2.2k/4.7 kΩ) is added to the connector before feeding to the data acquisition unit. This is to regulate a useful range for the passing current signals to the electronic circuitry, and particularly useful for not so conductive media. For ECT system, 12 individual electrodes attached with color-coded cables are connected to the matching plug connectors on the lower panel of the data acquisition unit.

The processed digital signals are then sent *via* two high speed USB cables, one for each module, to a host computer installed with m3000 software (version 3.0) for on-line data acquisition settings and ITS Toolsuite software (version 7.0) for further data manipulation and image reconstruction. With this setup, the process data can be logged continuously to the host computer.

The m3000 ERT module generally performs well for media with slight conductivity such as municipal tap water (conductivity ~ 0.8 mS/cm). However, it was not well suited for measuring media with high conductivities such as 1 wt.% aqueous NaCl (conductivity 18.5 mS/cm) used as the water phase in the flow experiments. The output showed that the signal-to-noise ratio of voltage measurement was poor and can be attributed to the double layer effect formed at the electrode-solution surface (Bolton et al., 2007). Another dedicated DAS for the ERT system, namely ERT-p2+, was used to circumvent the problem. By using a high injection current of 75 mA as opposed to default 15 mA, the instrument was capable of detecting water phase with high salinity and acquiring voltage measurements with better signal-to-noise (SNR) ratio.

6.1.4   Image reconstruction system

The image reconstruction algorithm is a numerical procedure to recreate a cross-sectional image or tomogram from the measurements. It converts the acquired raw data and maps into an image of the spatial distribution of the electrical data across the sensing plane (Da Silva, 2008). The procedure involves two steps: the first step is the forward problem that calculates the electrical potential field profile generated by the injected current. A sensitivity matrix is constructed to describe the change in raw data relative to the reference data. A finite element method is applied to solve the problem by dividing the domain into rectangular grids. The next step formulates the inverse problem by converting the forward problem into a spatial distribution

of conductivity or permittivity across the domain (Dickin & Wang, 1996). The inverse problem can be solved by using a direct or iterative algorithm to reconstruct a cross-sectional image mapped by the spatial distribution of the acquired parameters. Some of the reconstruction techniques include linear back projection (LBP), high-dielectric reconstruction (HDR), Landweber iteration, parametric reconstruction, sensitivity conjugate gradient iteration and iterative algebraic reconstruction algorithms (Isaksen, 1996). In the current ECT equipment set-up, the system used the direct LBP algorithm to solve the inverse problem and reconstruct the image. LBP is a fast but crude one-step method that uses linear interpolation to map the changes in the raw data relative to the reference measurement. The final output can be either a processed parameter or a cross-sectional tomogram showing the spatial distribution of the parameter. It should be noted that the optimal application of image reconstruction technique remains a challenge as the usefulness of certain algorithms is often flow-pattern-dependent (Isaksen, 1996). This is because the ECT sensors are soft field sensors in which the sensitivity to the permittivity is non-uniform and largely depends on the distribution and position in the measurement domain (Johansen *et al*., 1995). The sensors are more sensitive to permittivity changes in the near wall region than to the pipe core.
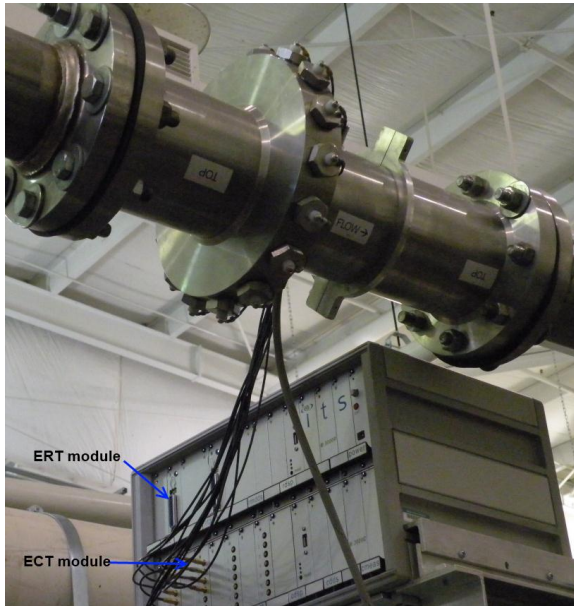
Figure 6-5: Front view of data acquisition unit: ITS m3000, showing ERT/ECT sensor connections.

6.1.5   Comparisons of ERT and ECT systems

ERT and ECT are the two major core sensor systems developed in the electrical tomography. Each has its own merits and disadvantages depending upon the types of application. There is no harmful radiation emitted from the system, as they are electrically based. They have relatively fast sensing speed and can display dynamic real-time images. Generally, ECT is used when bulk flowing media are not conductive. Therefore, it is useful to differentiate between the gas and liquid phases where the gas is the low dielectric material and liquid is the high dielectric material. It was reported that imaging problems can occur when conductive media such as water is present in the pipe (Jaworski & Bolton, 2000). The ECT system is not optimally designed to respond to overly conductive media that have a much higher relative permittivity compared to oil or gas due to signal saturation of the system (Corlett, 2001). The system behaves like an ERT rather than ECT system. For a flow system containing conductive media such as water, ERT is more suitable

as it distinguishes the distribution of electrical conductivity across the sensing plane. However, ERT does not work well if exclusively non-conductive media flow in the pipe, such as in a gas-oil system. It was also reported that ERT does not work well if the bulk medium is overly conductive such as for concentrated brine because of the signal saturation and the limitations of image reconstruction algorithms (Bolton et al., 2007). The images obtained from electrical tomography have rather moderate image spatial resolution of 5-10% (Grangeat, 2009). The spatial resolution refers to the ability to discriminate between adjacent objects. It is primarily affected by the size, quantity of electrodes and sensing distance between the circular electrodes (Isaksen, 1996). High spatial resolution means that relatively fine detail of an object can be distinguished. Comparisons of ERT and ECT are summarized in Table 6-3.

Table 6-3: Comparisons of ERT and ECT systems

ERT	ECT
• based on conductivity measurement	• based on permittivity measurement
• differentiate between conductive and non-conductive media	• differentiate between gas and liquid phases
• electrodes are invasive but not intrusive	• electrodes are non-invasive and non-intrusive
• temporal resolution of 14 fps	• temporal resolution of 29 fps
• image spatial resolution ~ 5%	• image spatial resolution ~ 5%-10%

6.1.6   *Limitation of ERT and ECT systems*

Before utilizing ERT and ECT systems as imaging tools for identifying the flow patterns, it is necessary to consider instrumental limitations. This includes the time resolution, spatial resolution and image reconstruction scheme. For example, if one examines the ECT system with an acquisition rate of 29 frames per second, it will take approximately a time resolution of 35 ms

to capture a frame. For a hypothetical fluid velocity of 1 m/s, any flow features larger than 35 mm will be theoretically captured. If the characteristic length of the flow feature is smaller or moves much faster than the time resolution, only the average gross feature will be captured (Jeanmeure *et al.*, 2002). The ERT/ECT systems used in this work have a spatial resolution of 5-10%; equivalently, they can distinguish an object detail larger than 10 mm in a 0.1 m ID pipe. Electrically-based tomographic systems have an inherent problem caused by the non-linear distribution of spatial sensitivity across the sensing domain. The sensitivity is high near the wall and deteriorates at the pipe center. This results in an ill-conditioned inverse problem which can easily inflate any measurement error or noise in the reconstructed image (Wang *et al.*, 2002). Linear back projection (LBP) is typically used as the reconstruction algorithm to reconstruct an image. While LBP is a fast and simple technique, it tends to smear out sharp transitions across the interface between different media, rendering poor contrast features with softened edges (Isaksen, 1996). In addition, both ERT and ECT systems do not respond well to overly conductive media that have large contrast in conductivity or permittivity values, as it could lead to signal saturation and highly ill-conditioned inverse problems in the image reconstruction process (Bolton et al., 2007). Because of the aforementioned limitations, the applicability of the ERT/ECT technique is often flow pattern dependent. Stratified flow with a distinctive interface can be visualized more successfully than the highly dynamic intermittent flow patterns such as slug flow.

6.2 Experimental Details

6.2.1 Calibration of tomographic system

The performance of ECT and ERT systems largely depend on the instrument calibration. When experimenting with multi-component fluid systems, the measuring electrodes have to be carefully calibrated beforehand in order to accurately depict the media distribution within the pipe.

6.2.1.1 ERT system

In the ERT system the electrodes were connected to the ERT-p2plus, which is a dedicated DAS for measuring media with high conductivities. The calibration was performed by completely filling the test section with 1 wt.% NaCl aqueous solution in quiescent condition (conductivity 18.5 mS/cm). The distribution of electrical conductivity across the sensing plane measured by ERT was taken as a reference point representing a 100% high conductivity phase. Figure 6-6 is the calibration measurements showing the wave-like voltage signals acquired by 16-electrodes from the calibration procedure using a high injection current of 75 mA at frequency 9.6 kHz. Since water is more conductive, the level of electrical voltage produced by the water phase will be much lower than the same volume of oil or gas flowing in the pipe. Based on the differential voltages produced by the two phases, the system can differentiate conductivities from the non-conductive phases.
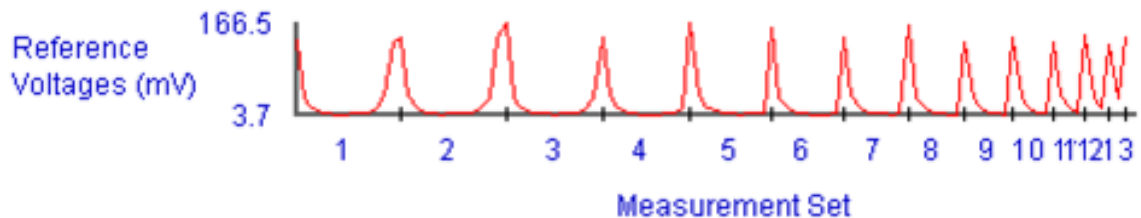
Figure 6-6: Profile of ERT reference voltages in LVT200-water system.

6.2.1.2 ECT system

In the ECT system, the electrodes were connected to the m3000 DAS for data measurement. The calibration was performed in two steps. In the first step, the test section was fully occupied with a low permittivity medium (gas). The measured value was referenced as 0, representing a 100% low permittivity phase. In the next step, the test section was fully filled with high permittivity medium (oil) and that measured value was referenced as 1, representing 100% high

permittivity phase. Any subsequent ECT measurements will fall between 0 and 1, normalized to the low and high calibration points. The normalized capacitance C_n fall is expressed in Eq. (6.1):

$$C_n = \frac{C_{meas} - C_{low}}{C_{high} - C_{low}} \tag{6.1}$$

where C_{low} and C_{high} are the low and high reference capacitances (or permittivities), respectively; C_{meas} is the measured capacitance. Figure 6-7 is the calibration measurements showing wave-like voltage signals acquired by the ECT electrodes during the standard calibration routine for the air-LVT200 oil system.
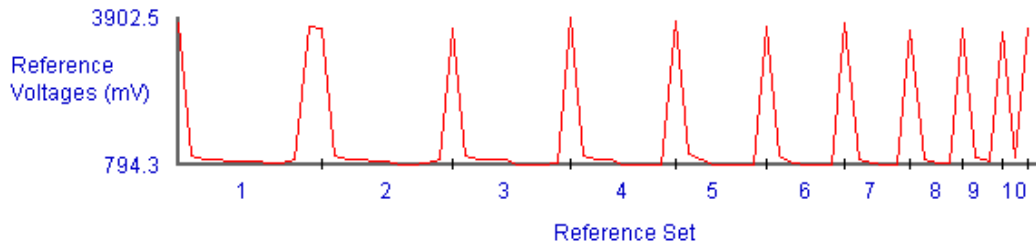
Figure 6-7: Profile of ECT reference voltages in air-LVT200 system.

It is noted that ECT measurement does not always work for all types of flow conditions using the default image reconstruction algorithm, namely linear back projection (LBP), particularly for mixtures containing large contrast in permittivity such as concentrated brine (Bolton et al., 1998; Jaworski & Bolton, 2000). Because of this issue, another image reconstruction algorithm, namely high dielectric reconstruction (HDR), was considered in this work. HDR is able to suppress most of the reconstruction artifacts associated with processes having high dielectric media.

6.2.2   Experimental set-up

The general layout of the large-scale flow loop is given in Figure 4-4. The upstream leg of the

0.1 m ID main loop is mounted with a tomographic test section located approximately at L = 7.5

m (L/D = 75), as shown schematically in Figure 6-8. A visualization section made of transparent

PVC pipe is located further downstream at L = 12.5 m (L/D = 125) to provide visual observation

of the flow patterns. The test liquids used were light model oil LVT200 and 1 wt.% aqueous NaCl

solution. The gas phase was air circulated by a gas blower in the closed loop at ambient

temperature and pressure. The fluid properties are given in Table 3-1.
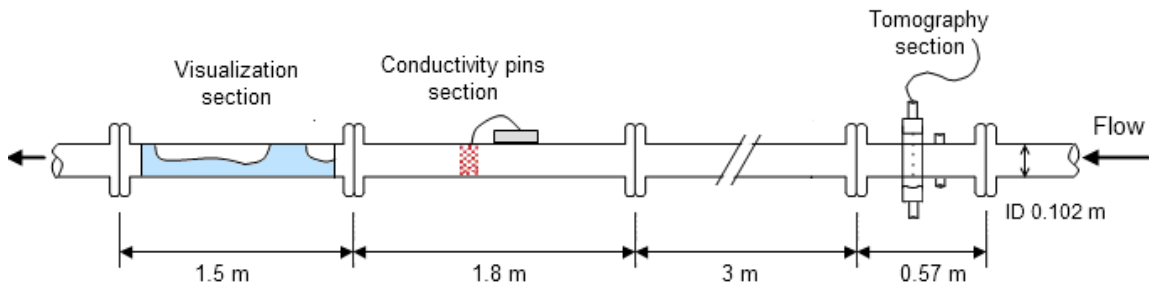
Figure 6-8: Schematics of test sections installed in the upstream leg of the main line.

In this work, the aim of using the ECT and ERT systems was to identify the multiphase flow

patterns and the relative phase distribution in multiphase flow conditions. Two major groups of

flow experiments were conducted based on the specific applicability of the ECT and ERT

techniques, respectively, as follows:

- ERT experiments – horizontal oil-water flow.

- ECT experiments – horizontal gas-oil flow, horizontal gas-oil-water flow and vertical

  gas-oil-water flow.

6.3 ERT experiments

6.3.1 Test matrix

In order to demonstrate the applicability of ERT instrument for the detection of water in oil-water flow, an ERT experimental series for horizontal oil-water flow is presented in this section. The primary oil-water flow pattern studied here is the stratified flow at different mixture liquid velocities (0.2 m/s to 1 m/s) and water cuts (5% to 50%). The flow experiments were carried out in a 0.1 m ID flow loop. The test fluids used were model oil LVT200 and 1 wt.% aqueous NaCl. The test matrix is shown in Table 6-4.

Table 6-4: ERT test matrix for horizontal oil-water flow

Parameter	Value
Tomographic technique	ERT
Pipe ID (m)	0.1
Pipe Inclination	0°
Oil phase	LVT200
Water phase	1 wt.% NaCl (aq.)
Conductivity (mS/cm)	18.5
Mixture liquid velocity (m/s)	0.2 – 1.0
Water cut (%)	5 - 50

The ERT sensor system was connected to a data acquisition system ERT-p2plus that was configured with an injection current of 75 mA and an excitation frequency of 9.6 kHz. At the beginning of the experiments, a standard ERT calibration procedure was carried out to take the reference measurement with the static water phase fully filling the test section. A frame burst mode of 200 was configured for fast data collection. The frame burst mode controls how many frames in an acquisition block are collected, stored in its internal buffer and downloaded to the host PC in one go. For fast data capture, the sampling time interval was set to zero so that the data will be captured at the maximum possible rate based on PC hardware. The flow-pattern

identification was carried out by analyzing the ERT imaging results and the time series mean concentration data.

6.3.2   Horizontal oil-water flow

6.3.2.1 Mixture liquid velocity V_m of 0.2 m/s

Figure 6-9 shows the ERT results for oil-water flow at liquid mixture velocity of 0.2 m/s with water cuts varied from 5% to 50%. Photographs of the flow patterns taken from the transparent pipe section are also included in Figure 6-9. At that low mixture velocity, the oil and water phases flowed separately with a dispersion layer at the oil-water interface. Increasing water separation can be seen at the lower section of the pipe as the water cut increased. At 5% water cut, the flow pattern was observed as stratified with globules in which a small water stream (approximately 2cm width) was seen moving at the pipe bottom along with swarms of dispersed globules/droplets. Above 5% water cut, a stratified flow pattern with mixing layer at the interface was observed. In comparison, ERT barely detected water at 5% water cut when the water was mostly in the form of globules. The tomogram showed a tiny area of water which flickered unstably during the flow, indicated by the 2-3 red pixels at the pipe bottom. As the water cut increased at fixed mixture velocity, the water phase as indicated by the red pixels grew larger to form a convex interface. At the interface, green pixels can be seen which represent the dispersion layer.

The time series mean concentration fractions estimated by ERT are shown in Figure 6-10. The concentration values were simulated by ERT from the computation of mean normalized conductivity values across the sensing plane. In this work, the mean concentration is treated as the area fraction or holdup of the water phase. In Figure 6-10, the simulated water holdup values increased with water cuts but was somewhat under estimated compared to the actual water holdup. At 50% water cut, the actual water holdup measured from the flowing pipe was around 40% but

the simulated water holdup by ERT was approximately 20%. It seemed that the simulated water holdup by the ERT images did not quite match up to the actual water holdup observed visually.

Another measurement was done by comparing the estimated height of the continuous water layer obtained from the pipe with the highest point of the red color region from the ERT tomogram, as indicated in Figure 6-9. Results showed that the values compared quite well between these two parameters. The largest percent difference was 36% at 10% water cut, and decreased as water cuts increased. However, the convex-shaped interface produced by the ERT was found to be more pronounced than the rather flat interface observed in the flow. This might explain why ERT predicted lower water holdup than the actual flow. It was also noted that the dispersion layer at the interface was detectable but not pronounced in the ERT measurement.

6.3.2.2 Mixture liquid velocity V_m of 0.4 m/s

The effect of mixture liquid velocity was studied by repeating the ERT experiments at higher mixture velocity. Figure 6-11 displays the flow patterns and ERT results at mixture velocity of 0.4 m/s with water cuts varied from 5% to 50%. Similar to previous results, stratified flow with globules was observed at 5% water cut, and stratified flow with mixing layer at the interface was observed at water cut > 5%. In comparison, ERT did not detect water at 5% water cut as the tomogram image showed 100% oil flow. Apparently, ERT was not able to detect if the water existed as segmented rivulets (approximately 2 cm in width) flowing along with clusters of dispersed droplets or globules at the pipe bottom. At 10% water cut, a continuous water layer was seen to flow at the pipe bottom. The tomogram images showed some small area of water flickered unstably at the pipe bottom, as indicated by the red pixels. As the water cut further increased, the area of water grew larger to form a convex interface, with a few green pixels representing the dispersion layer at the interface.

The time series mean concentration fractions simulated by ERT are shown in Figure 6-12. Similarly to previous results at mixture velocity of 0.2 m/s, the simulated water holdups increased with water cuts but was under predicted compared to the actual water holdup, probably due to the appearance of the convex interface. As for the data comparison between the heights of the water layer obtained from the pipe *versus* the height from the ERT tomogram, the results agreed quite well. The largest percent difference was 27% at 10% water cut and the height difference narrowed as the water cut increased.

6.3.2.3 Mixture liquid velocity V_m of 0.5 m/s

Figure 6-13 presents the ERT results and the flow pattern photos for 0.5 m/s mixture velocity at 5% to 20% water cuts. Similar to previous results, stratified flow with globules was observed at 5% water cut, and stratified flow with mixing layer at the interface was observed at water cut > 5%. The water layer was seen to thicken with increased water cuts. Similar to previous results, ERT was not sensitive enough to detect water at 5% water cut corresponding to the stratified flow pattern with globules. At 10% to 20% water cuts, water can be detected at the pipe bottom. In Figure 6-14, the results show the simulated mean concentrations were on the low side at 1% and 8% respectively, probably due to the appearance of the convex interface. The water height data comparison between the pipe and the tomogram were in good agreement.

6.3.2.4 Mixture liquid velocity V_m of 1 m/s

Figure 6-15 shows the ERT results and the flow pattern photos for 1 m/s mixture velocity at 5% to 20% water cuts. At the high mixture velocity of 1 m/s, water was more dispersed as smaller droplets rather than large globules. Stratified flow with globules was observed up to 10% water cut, and stratified flow with mixing layer at the interface was seen at 20% water cut. Similar to previous results, the tomogram showed 100% full oil pipe flow at 5% and 10% water

cuts as ERT was insufficiently sensitive to detect dispersed water droplets in the flow. At 20% water cuts, water can be detected by ERT corresponding to a continuous water layer flowing at the pipe bottom. In Figure 6-16, the simulated mean concentrations by ERT were on the low side at approximately 5%. The water height data compared well between the pipe and the tomogram.

The findings showed ERT can be used to identify the presence of water in stratified flow condition but it often under predicted the water holdup, more apparently at higher water cut. The constructed ERT images showed a rather convex shaped interface for the water phase, which probably resulted in an under estimation in water holdup. The holdup measurement is based on the ERT sensitivity field which is nonlinear in nature, hence the mapping relation between the actual and measured area fraction cannot be represented in simple linear formulations (Heikkinen *et al.*, 2001). Factors such as the type of flow patterns and the distribution of the water phase could influence the accuracy of the holdup prediction (Dong *et al.*, 2003). This resulted in large spatial variance in the measured holdup data. On the other hand, ERT seemed to predict well if linear measurement data were compared between the measured and actual height of the observed water layer. Moderate differences were found at low water cut of 10% and the difference decreased as the water cut increased.

With the current setup, ERT was not sensitive enough to detect a stratified with globules flow pattern. The ERT uses an adjacent sensing strategy for each electrode pair (Williams & Beck, 1995). In order to detect the presence of water, the water film will need to cover at least a pair of electrodes, each with a size of 7 mm and approximately 30 mm apart from each other. This could lead to sub-optimum detection at low water cut, more apparently at higher mixture liquid velocity when the water was more dispersed as droplets or as a discontinuous water layer.
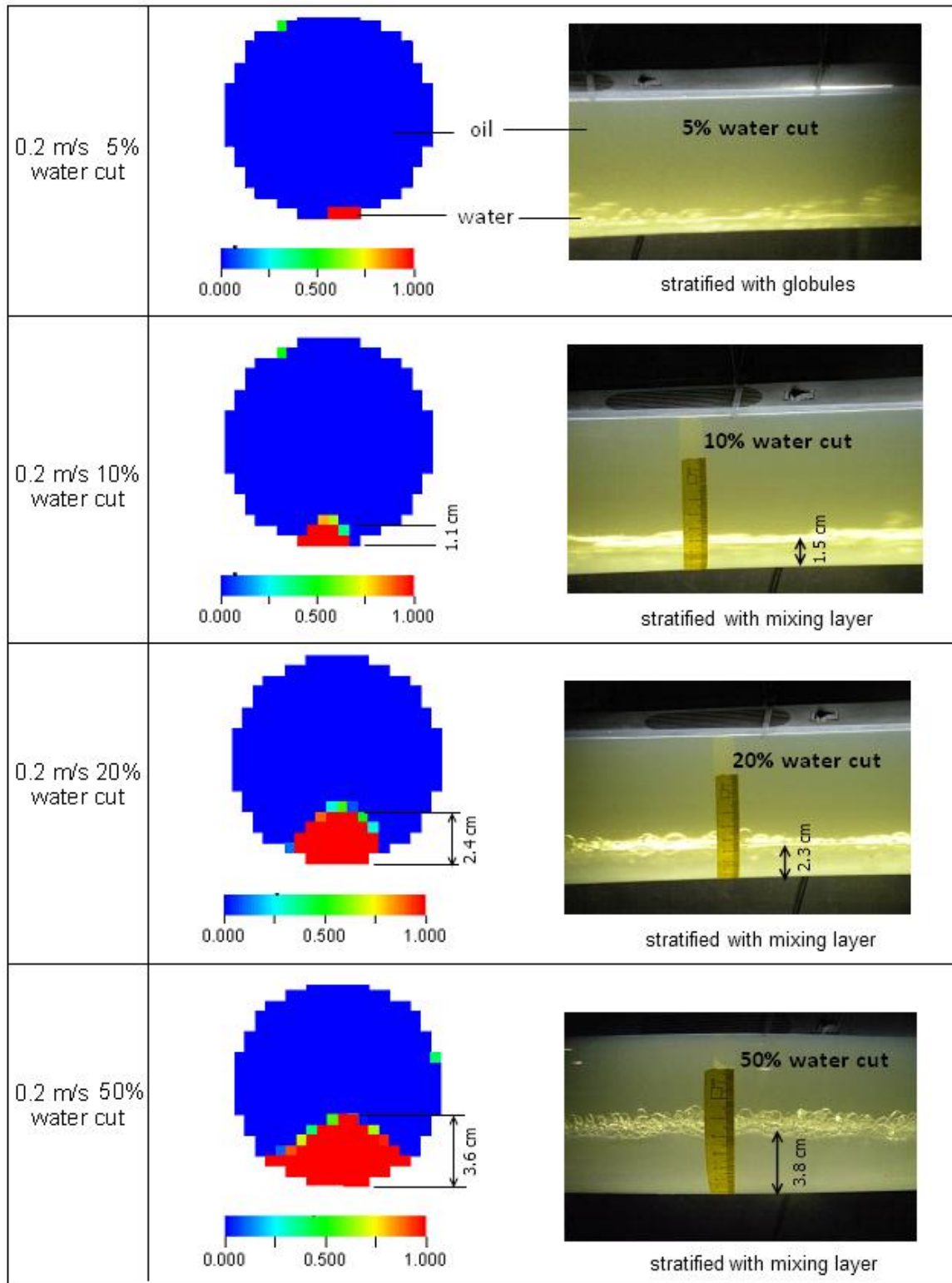
Figure 6-9: ERT images and flow pattern photos at V_m = 0.2 m/s from 5% to 50% water cuts.
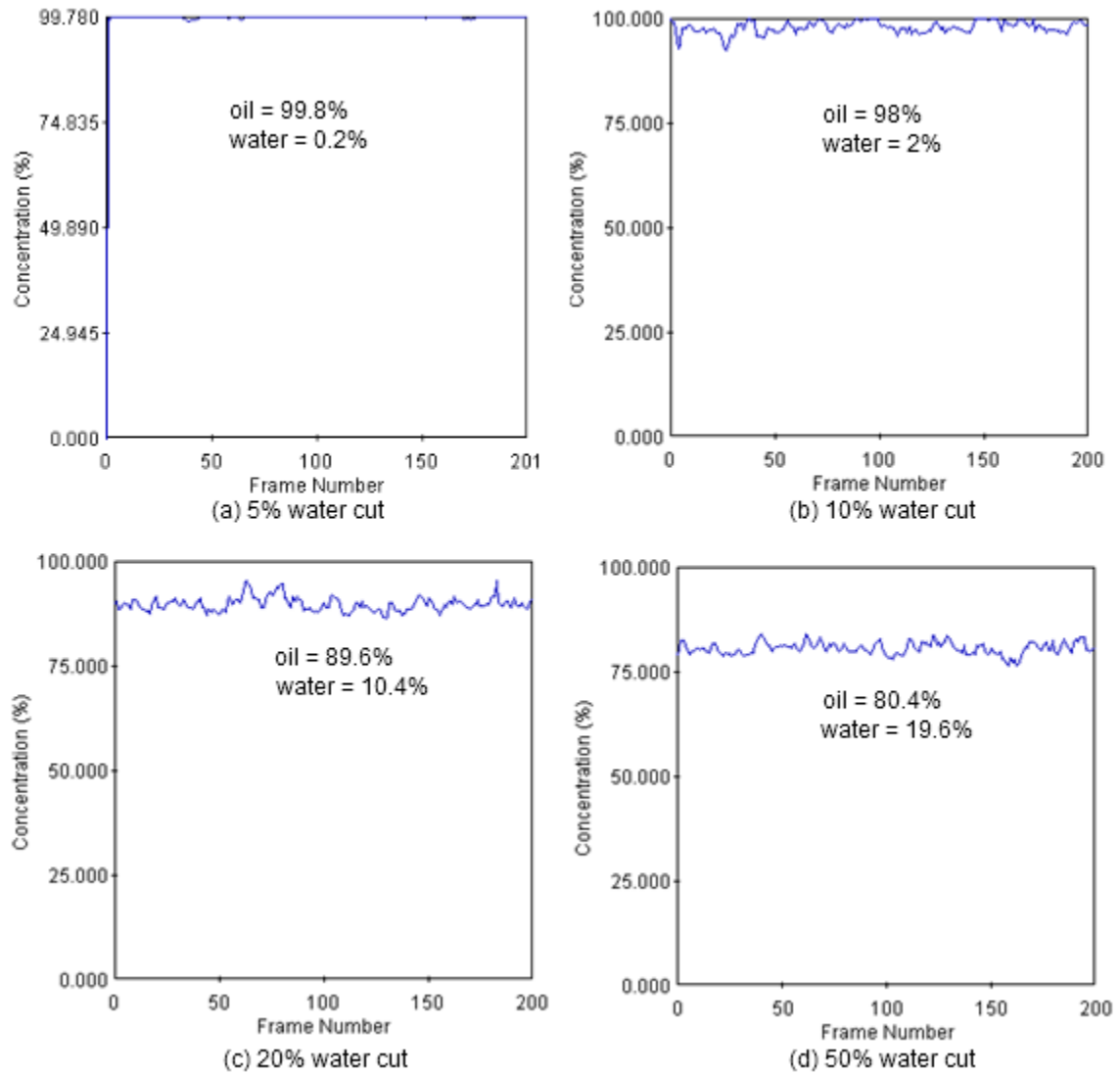
Figure 6-10: ERT simulated mean concentrations at V_m = 0.2 m/s from 5% to 50% water cuts.
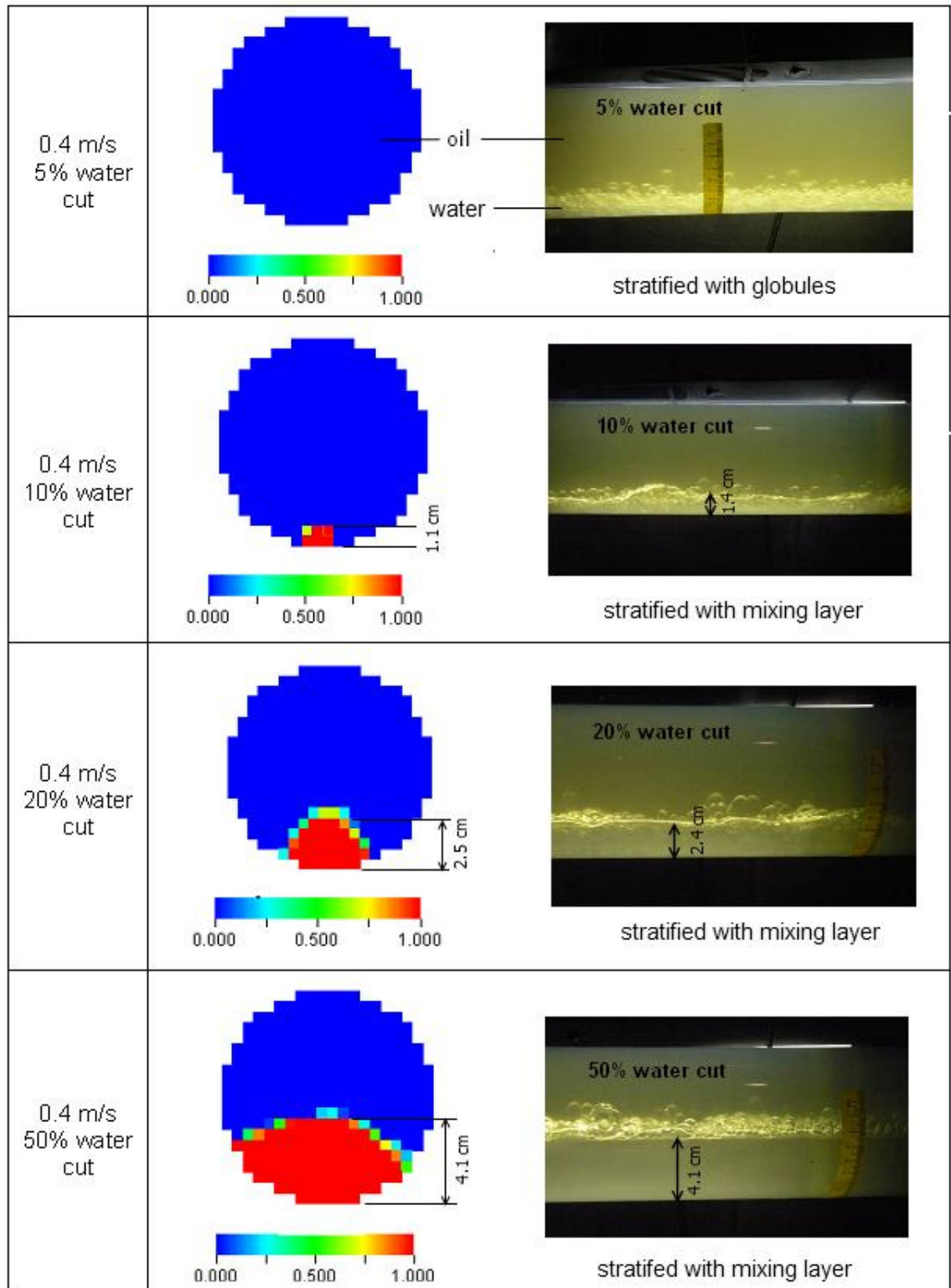
Figure 6-11: ERT images and flow pattern photos at V_m = 0.4 m/s from 5% to 50% water cuts.
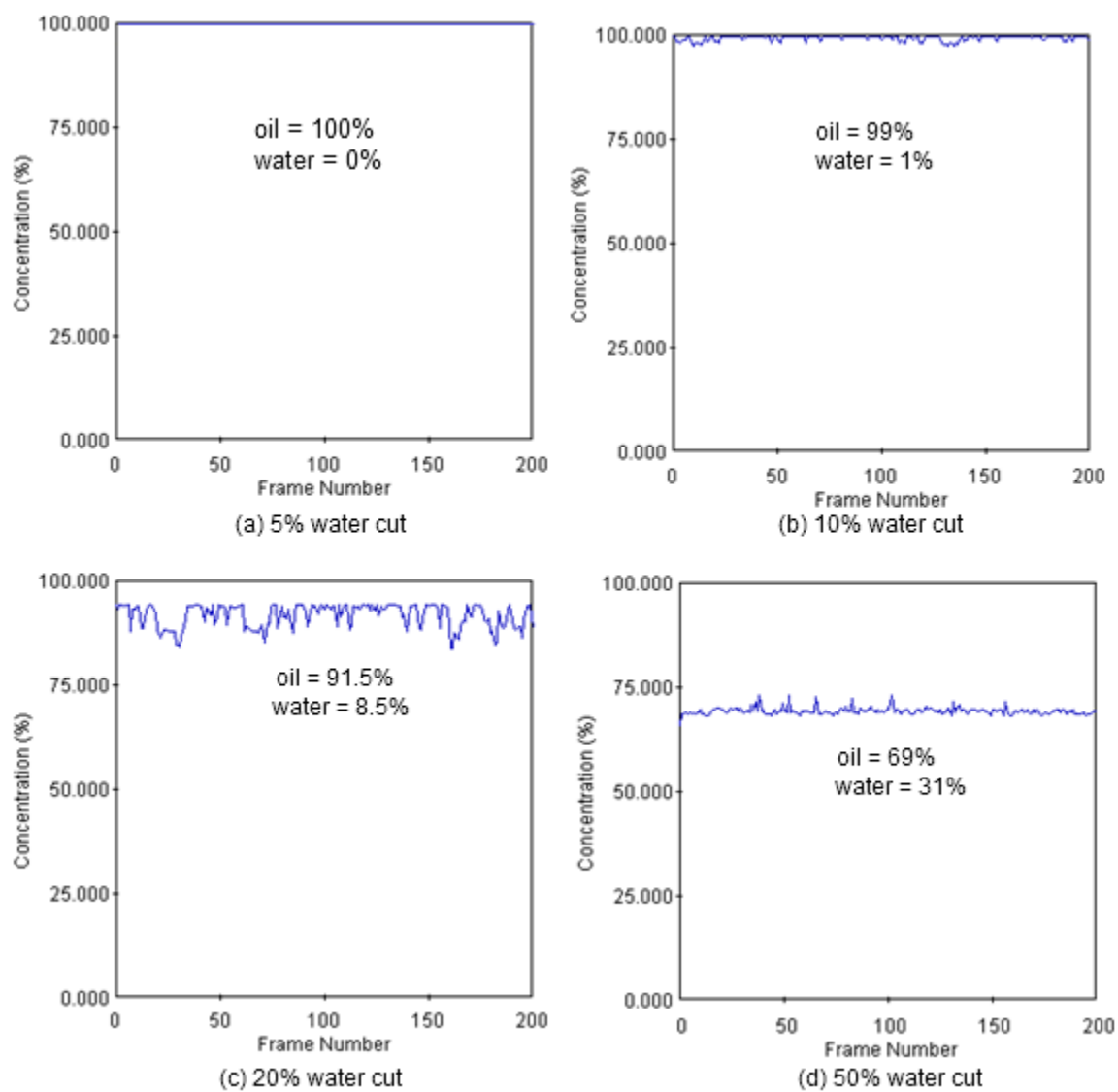
Figure 6-12: ERT simulated mean concentration (%) at V_m = 0.4 m/s from 5% to 50% water cuts.
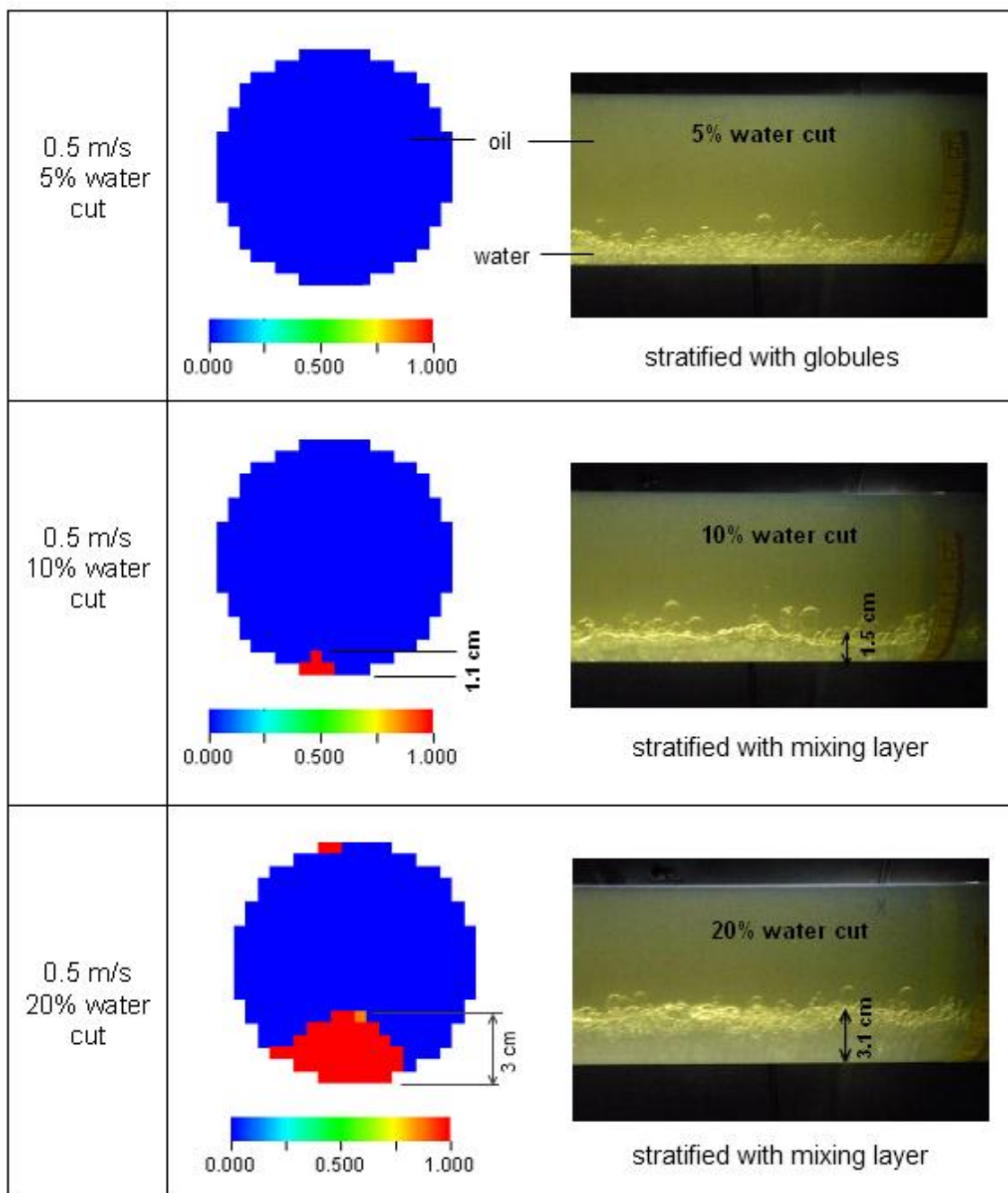
Figure 6-13: ERT image and flow pattern photos at V_m = 0.5 m/s from 5% to 20% water cuts.

(a) 5% water cut

oil = 100%
water ~ 0%

(b) 10% water cut

oil = 99.1%
water = ~1%

(c) 20% water cut

oil = 92.2%
water = 7.8%
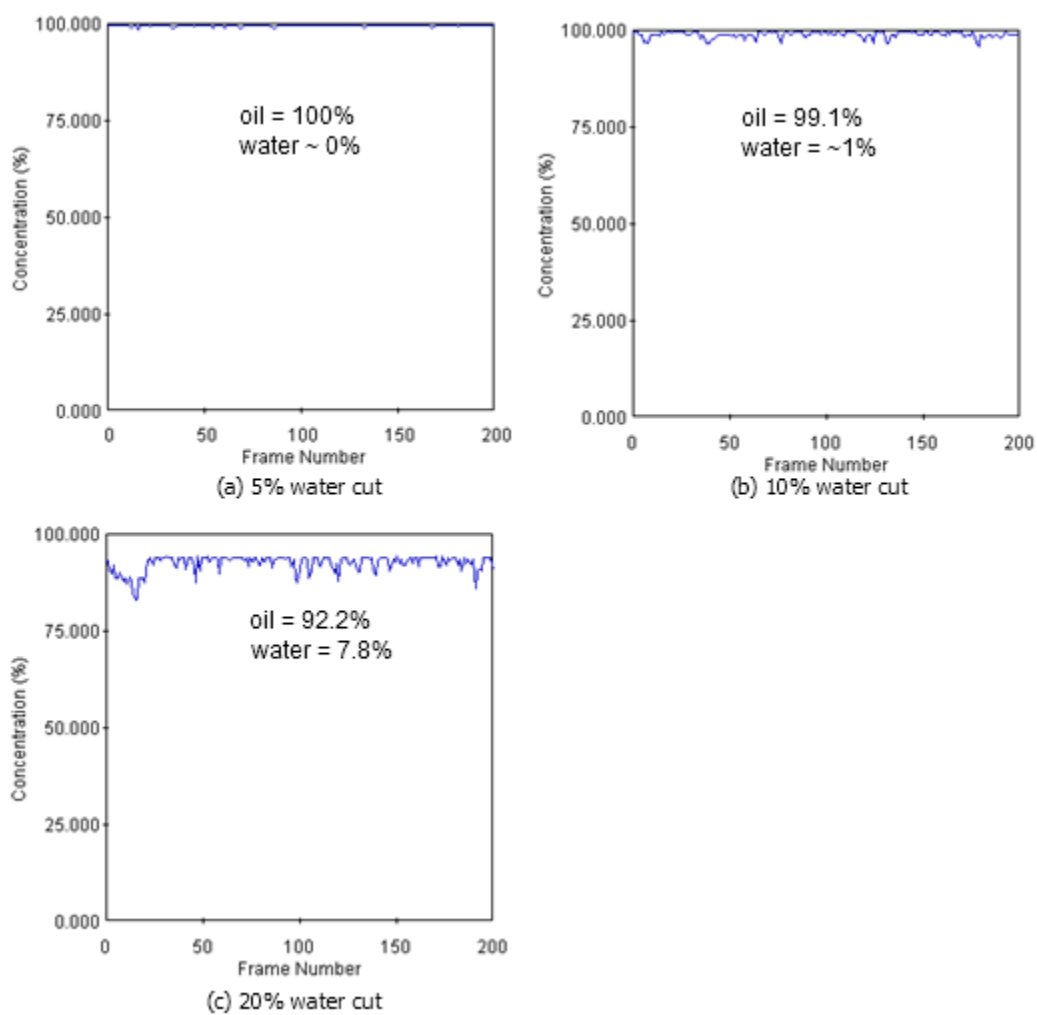
Figure 6-14: ERT simulated mean concentrations (%) at V_m = 0.5 m/s from 5% to 20% water cuts.
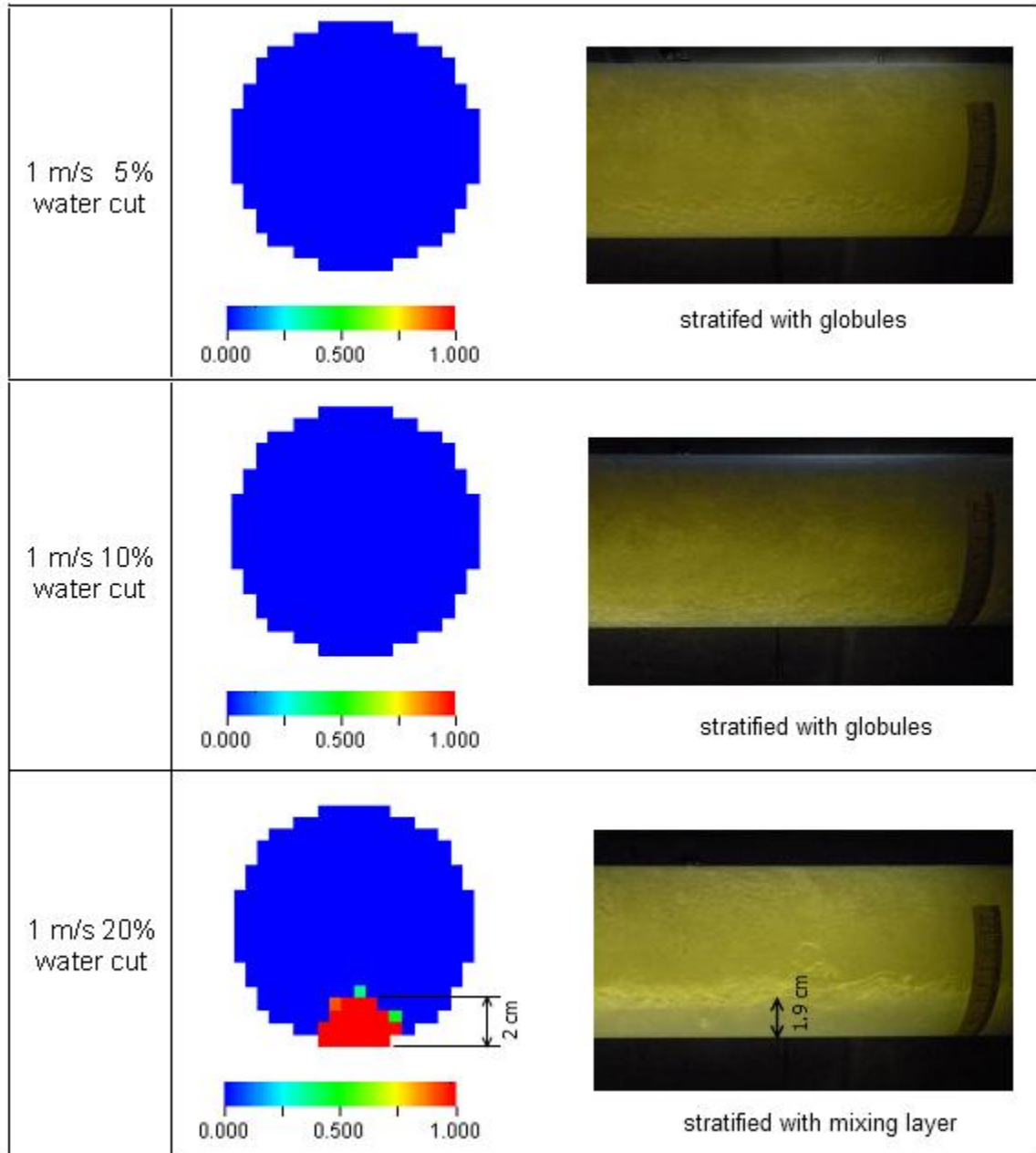
Figure 6-15: ERT images and flow pattern photos at V_m = 1 m/s from 5% and 20% water cuts.
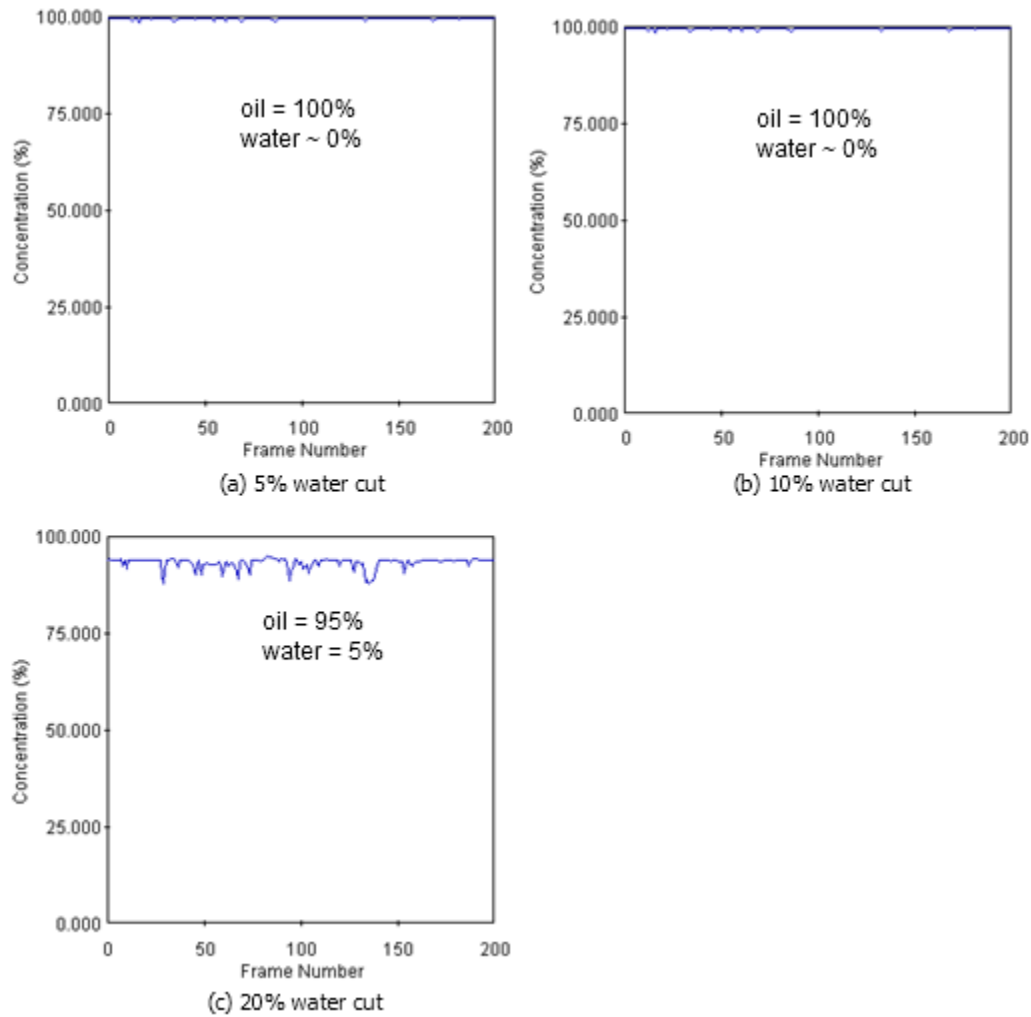
Figure 6-16: ERT simulated mean concentrations (%) at $V_m = 1$ m/s from 5% and 20% water cuts.

6.4 ECT experiments

6.4.1   Test matrix

In this work, ECT was used to identify the flow patterns by differentiating the gas phase from the liquid phase (oil-water mixture). It should be noted ECT is not designed to detect the water phase alone. Three different sets of ECT experiment series covering the horizontal gas-oil flow, horizontal gas-oil-water flow and vertical gas-oil-water flow were carried out to investigate the

flow patterns, as listed in Table 6-5 and Table 6-6. The test fluids used were LVT200 as the oil phase, 1 wt.% aqueous NaCl as the water phase and air as the gas phase. The flow experiments were conducted in a 0.1 m ID flow loop (see Figure 4-5) with the tomography test section mounted on the first leg of the loop, located approximately $L/D = 75$ from the entrance nozzle. Before the start of the experiments, a standard ECT calibration routine was performed in which the air filled pipe was referenced as the low permittivity phase and the oil filled pipe as the high permittivity phase. The flow pattern identification was carried out by analyzing the ECT imaging results and the time series concentration data.

Table 6-5: ECT test matrix for horizontal gas-oil flow

Parameter	Value
Tomographic technique	ECT
Oil phase	LVT200
Gas phase	Air
Pipe ID	0.1 m
Pipe Inclination	0°
System temperature, pressure	25°C, 1 atm.
Flow patterns:	**Superficial oil and gas velocities:**
a. Stratified (ST) flow	$V_{oil} = 0.05$ m/s, $V_{gas} = 0.1$ m/s
b. Elongated bubble (EB) flow	$V_{oil} = 0.5$ m/s, $V_{gas} = 0.6$ m/s
c. Slug (SL) flow	$V_{oil} = 0.5$ m/s, $V_{gas} = 1.6$ m/s
d. Wavy annular (WA) flow	$V_{oil} = 0.5$ m/s, $V_{gas} = 15.2$ m/s
e. Annular-mist (AM) flow	$V_{oil} = 0.5$ m/s, $V_{gas} = 31$ m/s

Table 6-6: ECT test matrix for horizontal gas-oil-water flow

Parameter	Value
Tomographic technique	ECT
Oil phase	LVT200
Gas phase	Air
Water phase	1wt.% NaCl (aq.)
Pipe ID	0.1 m
Pipe Inclination	0°
System temperature, pressure	25°C, 1 atm.
Flow patterns	**Superficial liquid and gas velocities at 5% water cut**
a. Stratified (ST)	V_{liquid} = 0.05 m/s, V_{gas} = 0.1 m/s
b. Elongated bubble (EB)	V_{liquid} = 0.5 m/s, V_{gas} = 1.1 m/s
c. Elongated bubble (EB)	V_{liquid} = 1 m/s, V_{gas} = 1 m/s
d. Slug (SL)	V_{liquid} = 1 m/s, V_{gas} = 2 m/s
e. Wavy annular (WA)	V_{liquid} = 1 m/s, V_{gas} = 14.7 m/s
f. Annular-mist (AM)	V_{liquid} = 1 m/s, V_{gas} = 30 m/s

Table 6-7: ECT test matrix for vertical gas-oil-water flow

Parameter	Value
Tomographic technique	ECT
Oil phase	LVT200
Gas phase	Air
Water phase	1wt.% NaCl (aq.)
Pipe ID	0.1 m
Pipe Inclination	90°
System temperature, pressure	25°C, 1 atm.
Flow patterns	**Superficial liquid and gas velocities at 5% water cut**
a. Churn	V_{liquid} = 0.5 m/s, V_{gas} = 5 m/s
b. Churn	V_{liquid} = 0.5 m/s, V_{gas} = 15 m/s
c. Annular-mist	V_{liquid} = 1 m/s, V_{gas} = 25 m/s

6.4.2   Horizontal gas-liquid flow

6.4.2.1 Stratified flow

In stratified (ST) flow, the heavier liquid stream flows at the base and the lighter gas stream flows at the top of the tube as shown in Figure 6-17. The gas-liquid interface can be smooth or wavy with small amplitude waves.
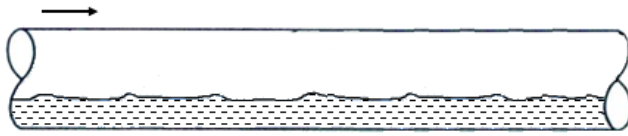
Figure 6-17: Schematics of stratified (ST) flow.

Figure 6-18 shows the ECT cross-sectional image as well as the vertical and horizontal slicing images for the stratified flow at superficial oil velocity V_{oil} = 0.05 m/s and superficial gas velocity V_{gas} = 0.1 m/s. The high oil concentration layer, shown in red, is located at the lower part of the pipe while the high gas concentration layer, shown as the blue region, is in the upper part of the pipe. The oil/gas interface at the intermediate layer is indicated by the green region which shows rather flat interface. The reconstructed interface is rather blurred and not as sharp as it was seen in the actual flow due to the reconstruction limitation of LBP (Isaksen, 1996). The vertical and horizontal slicing images represent the side and top view of the pipe sectioned in the vertical and horizontal plane, respectively. They are constructed by stacking up the consecutive slices of multiple images. Figure 6-19 shows the time series liquid concentration plot produced by ECT based on the computation of mean normalized permittivity value across the sensing plane at each frame for 500 consecutive frames. The result shows that the liquid concentration is rather constant (mean = 0.39) that varies little with time. Figure 6-20 is the sequence of ECT cross-

sectional images at 1 sec apart, which shows minimal change to the flat interface. The ECT results agreed well with the visual examination from the transparent pipe section.

Figure 6-18: ECT images showing cross-sectional, vertical slice and horizontal slice views for gas-LVT200 stratified flow at $V_{oil}= 0.05$ m/s and $V_{gas}= 0.1$ m/s.

Figure 6-19: ECT time series of liquid concentration fraction, showing stratified flow at $V_{oil} = 0.05$ m/s and $V_{gas} = 0.1$ m/s.

Figure 6-20: Sequence of ECT tomograms at 0.5 s interval for stratified flow at V_{oil} = 0.05 m/s and V_{gas} = 0.1 m/s.

6.4.2.2 Elongated bubble flow

Elongated bubble flow, also known as plug flow, is one type of intermittent flow. It can be observed at low gas velocity with the gas pockets moving along the pipe top and separated intermittently by sections of continuous liquid, as shown schematically in Figure 6-21.
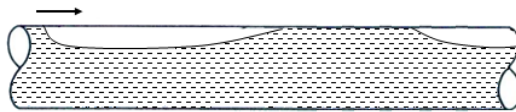
Figure 6-21: Schematics of elongated bubble (EB) flow.

For flow conditions corresponding to V_{oil} = 0.5 m/s and V_{gas} = 0.6 m/s, the ECT tomogram cross-sectional image as well as vertical and horizontal slicing images are shown in Figure 6-22. The oil layer (red) can be seen flowing at the bottom of the pipe with the gas pocket (blue) in the upper section. The gas/liquid interface (green) is seen at the boundary of the gas pockets, which expand and collapse in a concave profile alternately between segments where the pipe is oil-filled. This compared well with the visualization from the transparent pipe section. In Figure 6-23, the

liquid fraction results show periodic fluctuations from 0.55 to 1, corresponding to the alternate evolution of gas bubbles and continuous liquid section filling the pipe. Figure 6-24 shows the evolution of cross-sectional ECT images obtained at 0.1 ms interval for the elongated bubble flow pattern. The sequential image frames are evaluated as the elongated bubble flow because of the relatively high liquid fraction (mean 0.67), with gas bubbles trapped alternately at the upper part of the pipe.
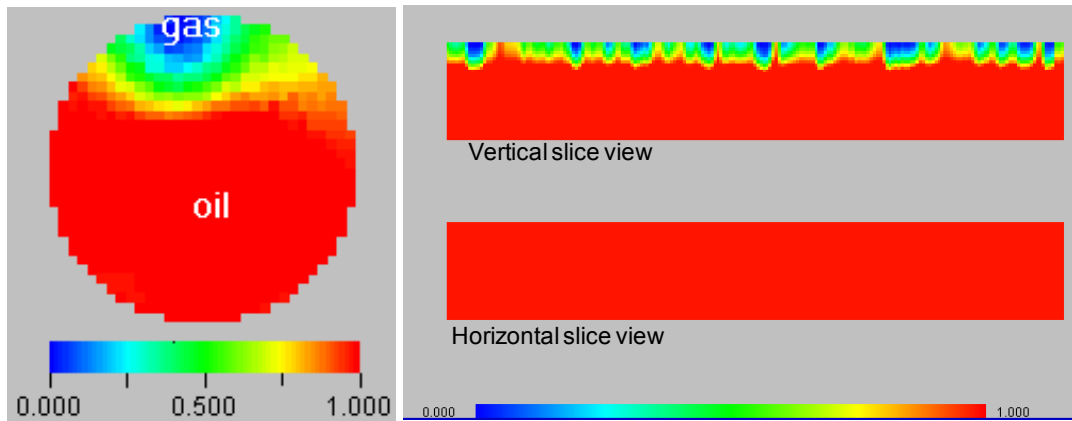
Figure 6-22: ECT images showing cross-sectional, vertical slice and horizontal slice views for gas-LVT200 elongated bubble flow at V_{oil} = 0.5 m/s and V_{gas} = 0.6 m/s.
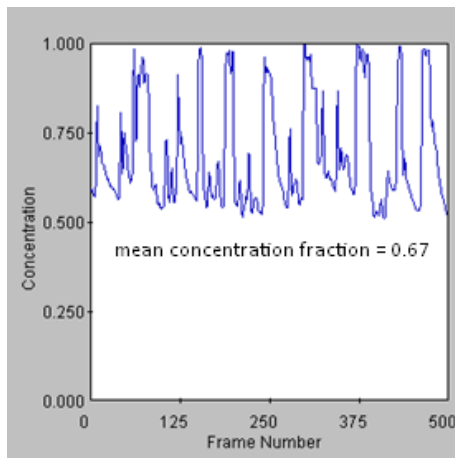
Figure 6-23: ECT Time series of liquid concentration fraction for elongated bubble flow at V_{oil} = 0.5 m/s, V_{gas} = 0.6 m/s.
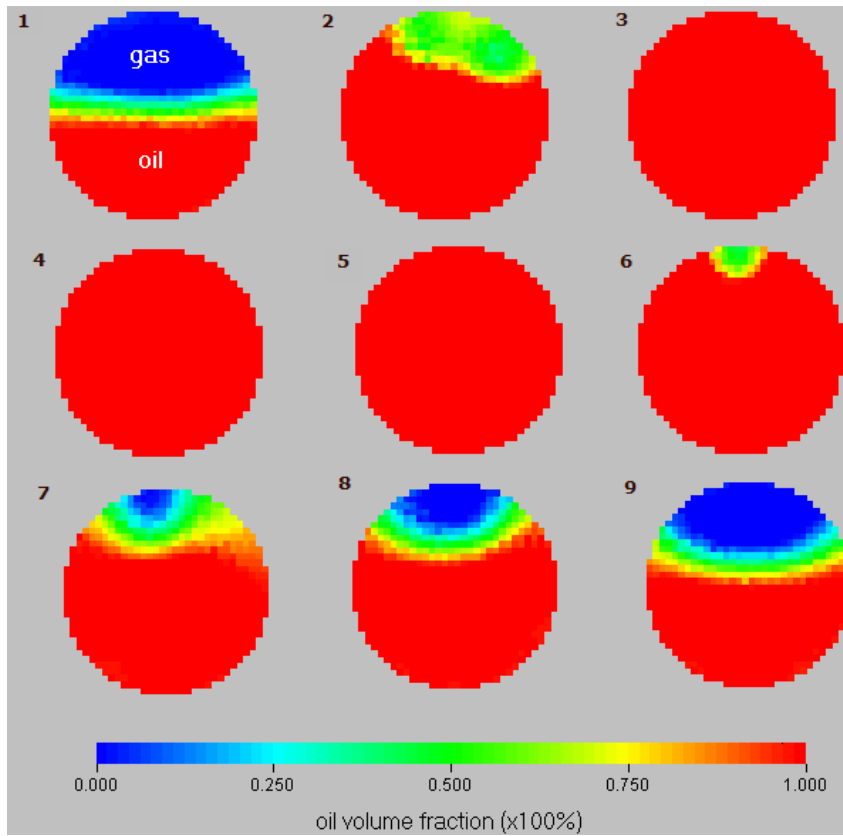
Figure 6-24: Sequence of ECT tomograms at 100 ms interval, showing the evolution of elongated bubble flow at V_{oil} = 0.5 m/s and V_{gas} = 0.6 m/s.

6.4.2.3 Slug flow

Slug flow is another form of intermittent flow. It is observed when the gas velocity is further increased, creating liquid waves (slugs) that wash over the entire pipe section periodically, followed by a gas bubble-liquid film zone in between the slugs, as shown in Figure 6-25.
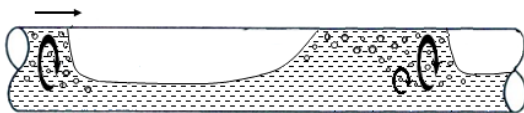
Figure 6-25: Schematics for slug (SL) flow.

The cross-sectional, vertical and horizontal slicing images of the ECT tomogram for flow conditions with V_{oil} = 0.5 m/s and V_{gas} = 1.6 m/s are shown in Figure 6-26. As the liquid slug approaches, the level of the liquid rises until the entire pipe section is filled. After the slug passes, the liquid level subsides as the gas and liquid separate into stratified flow before the next train of liquid slug. The ECT time series mean liquid concentration plot, as shown in Figure 6-27, displays periodic fluctuations from 0.3 to 1 corresponding to the intermittency of the slug flow. The magnitude of the fluctuation is larger than that of elongated bubble flow. Figure 6-28 shows the hydrodynamic evolution of the slug flow at a 35 ms interval. Frames 3 and 4 show that the liquid level rises and completely envelopes the pipe area, before it collapses and separates into a stratified region in the following frames. In frame 5, the concave interface appears as if a gas bubble is trapped within a slug. This observation was in line with the notion that the slug formation is a three-dimensional phenomenon, as discussed by Jeanmeure *et al*. (2002). This intermittent flow pattern shows a characteristic concave interface that curves up and down on both sides of the pipe wall during the slug evolution.
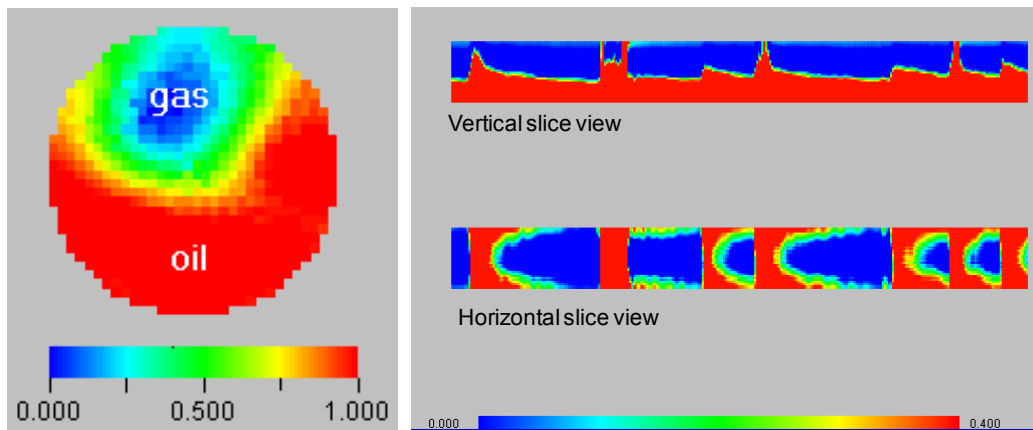
Figure 6-26: ECT images showing cross-sectional, vertical slice and horizontal slice views for gas-LVT200 slug flow at V_{oil} = 0.5 m/s and V_{gas} = 1.6 m/s.
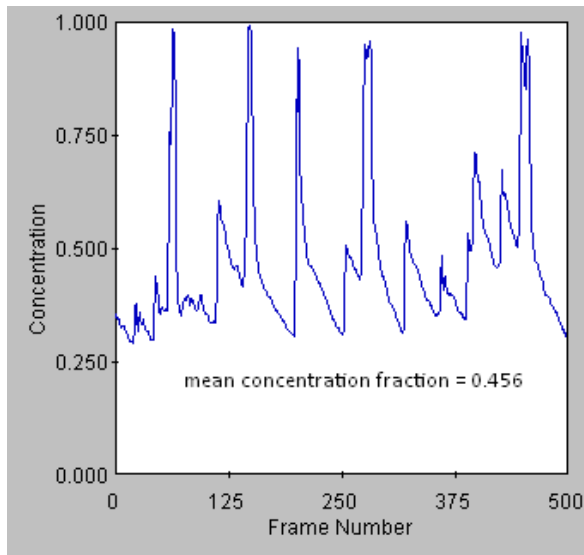
Figure 6-27: ECT time series of liquid concentration fraction for slug flow at $V_{oil} = 0.5$ m/s, $V_{gas} = 1.6$ m/s.
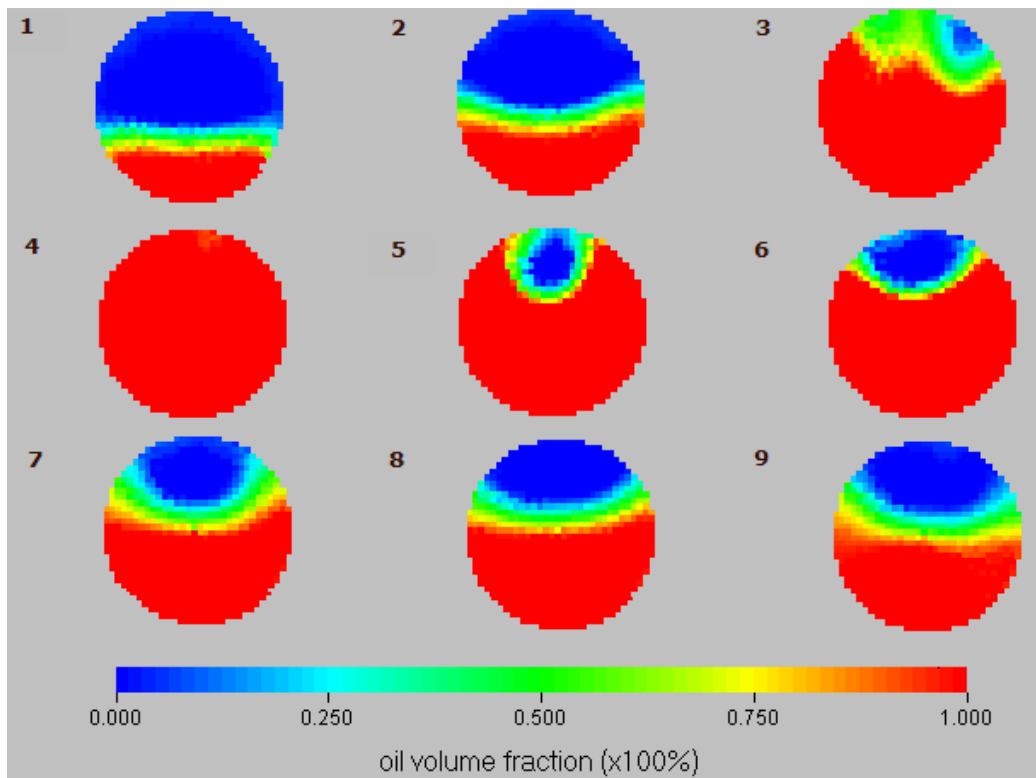
Figure 6-28: Sequence of ECT tomograms at 35 ms interval, showing the evolution of slug flow at $V_{oil} = 0.5$ m/s and $V_{gas} = 1.6$ m/s.

6.4.2.4 Wavy annular flow

Transitioning from slug flow, the wavy annular flow can be observed at relatively high gas velocity. It is a transitional flow between slug and annular flow. Unstable liquid waves are seen to briefly sweep up to the top of the pipe, but the waves do not quite occupy the entire pipe, as illustrated in Figure 6-29. There is an unstable liquid film covering the upper pipe wall which keeps running diagonally downward between waves.
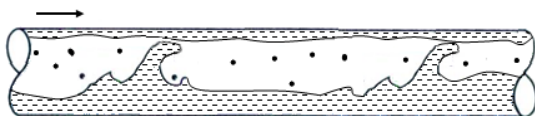
Figure 6-29: Schematics of wavy annular (WA) flow.

For flow conditions of V_{oil} = 0.5 m/s and V_{gas} = 15.2 m/s, the ECT tomogram cross-sectional image as well as vertical and horizontal slicing images are shown in Figure 6-30. As can be seen, there is an unstable liquid film (green) enveloping the top half of pipe, and spikes of waves wash over the pipe. Due to the limits of spatial resolution, the thin liquid layer on the wall was not displayed as a film with a sharp interface in the ECT tomogram, but was represented as a rather thick interface having intermediate liquid concentration (greenish color). Figure 6-31 is the ECT time series mean liquid concentration plot showing that the liquid fluctuates in a much narrow range from 0.15 to 0.25, as opposed to the characteristic fluctuations found in the elongated bubble and slug flows. The spikes in the graph correspond to the intermittent generation of the unstable waves, which do not quite bridge the upper pipe wall. The evolution of the wavy annular flow in Figure 6-32 shows that the liquid interface assumes a characteristic concave shape. In frame 3 and 4, the liquid never quite occupies the entire pipe area; instead it leaves an empty gas void at the pipe core as if a gas bubble has been trapped within. This can be explained by the generation of unstable wave, which is essentially a three-dimensional flow structure.
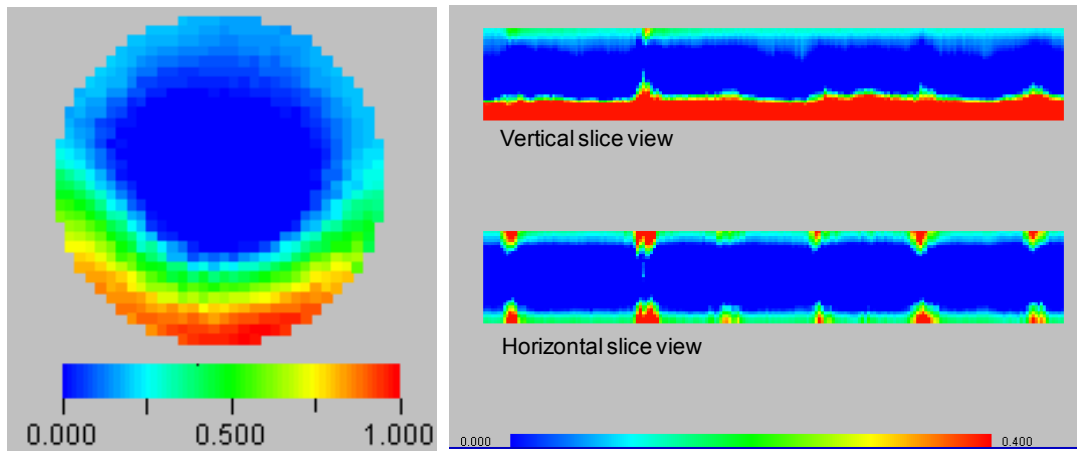
Figure 6-30: ECT images showing cross-sectional, vertical slice and horizontal slice views for gas-LVT200 wavy annular flow at V_{oil} = 0.5 m/s and V_{gas} = 15.2 m/s.
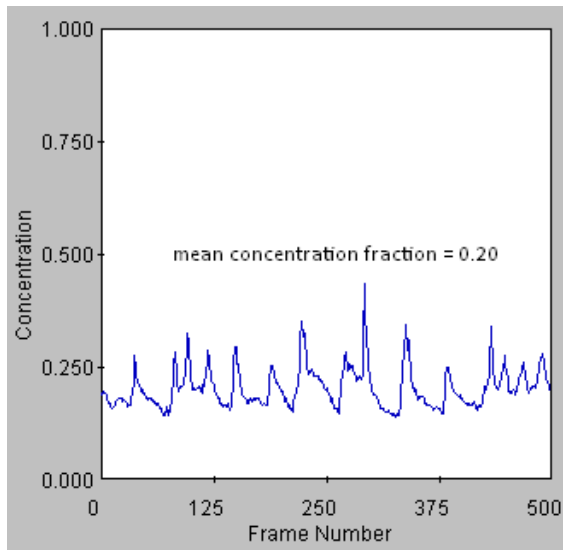
Figure 6-31: ECT time series of liquid concentration fraction for wavy annular flow at $V_{oi} = 0.5$ m/s and $V_{gas} = 15.2$ m/s.
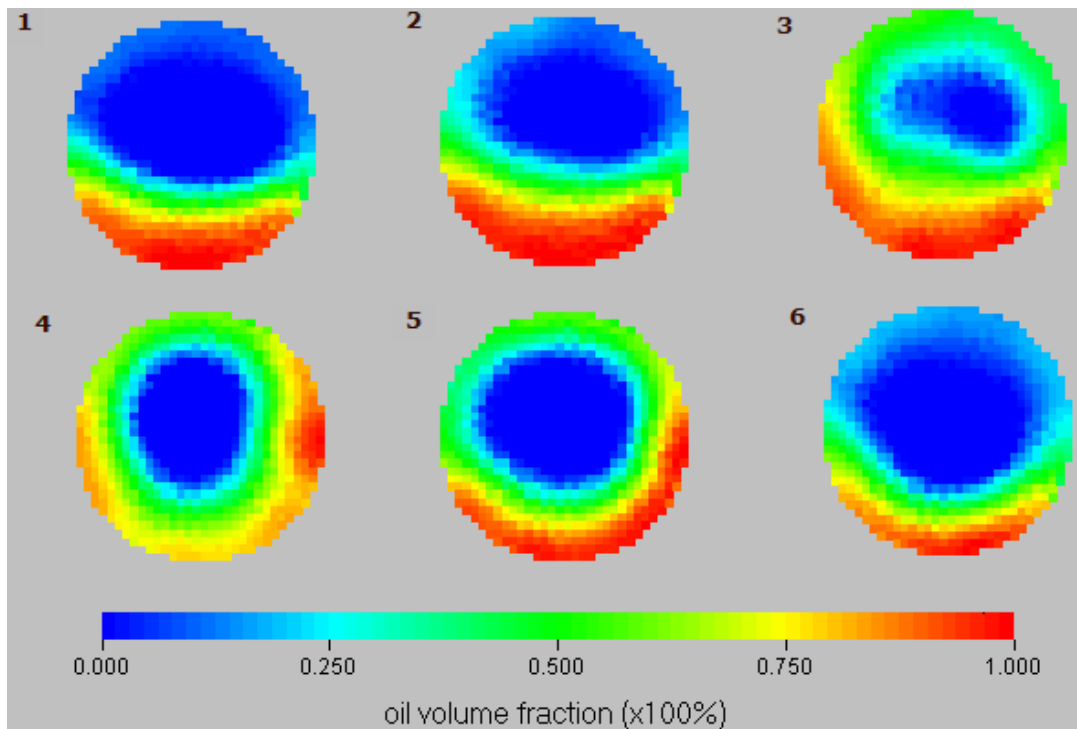
Figure 6-32: Sequence of ECT tomograms at 100 ms interval, showing the evolution of wavy annular flow at $V_{oil} = 0.5$ m/s and $V_{gas} = 15.2$ m/s.

6.4.2.5 Annular-mist flow

Annular-mist flow is observed at very high gas flow rate. The gas phase flows as a core in the pipe center while a symmetric annular liquid film flows along the pipe wall as shown in Figure 6-33. Because of gravity, the bulk of the liquid flows at the lower half of the pipe. Some of the liquid droplets are entrained as mist and carried by the gas in the pipe core.
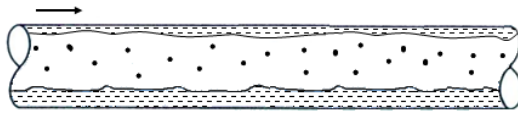
Figure 6-33: Schematics of annular-mist (AM) flow.

Figure 6-34 depicts the cross-sectional image as well as vertical and horizontal slicing images of the ECT tomogram for annular-mist flow conditions of V_{oil} = 0.5 m/s and V_{gas} = 31 m/s. The ECT images show that the liquid layer (red) is being pushed by the gas to curve up the wall, simultaneously falling due to gravity. This results in a concave interface and thin liquid film (green) forming around the tube periphery. Due to limits of spatial and time resolutions, very fine details like the entrained droplets in the pipe core cannot be reliably distinguished. In addition, the measurement sensitivity is at the lowest in the pipe core and cannot capture the entrained droplets. Figure 6-35 shows that the time series mean concentration plot for the flow has a relatively low mean liquid fraction of 0.18 with minimal fluctuation. The evolution of the annular flow is shown in Figure 6-36, showing a concave interface unstably creeping up and down on both sides of the wall. The imaging results concurred with the work of Jeanmeure, *et al.*, (2002) that also showed similar flow imaging behavior.
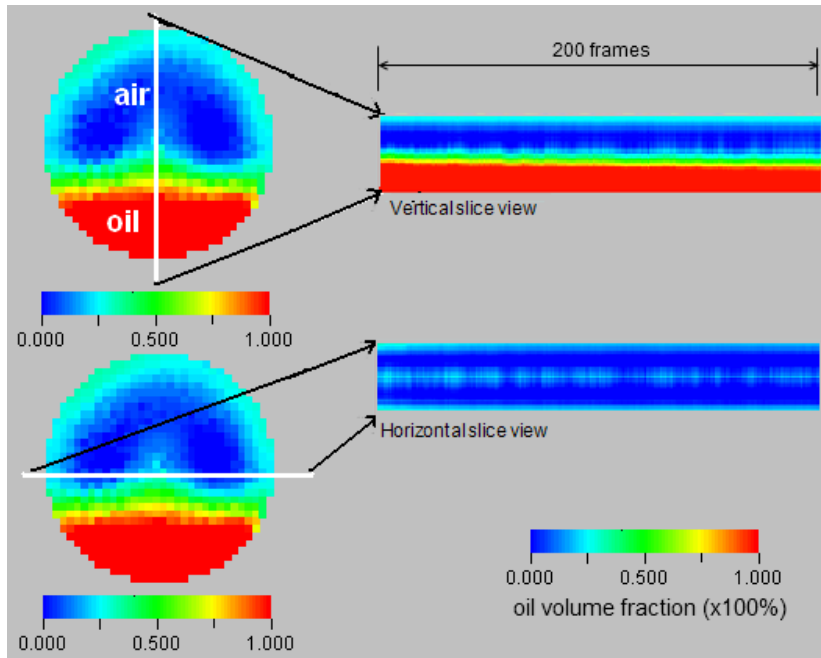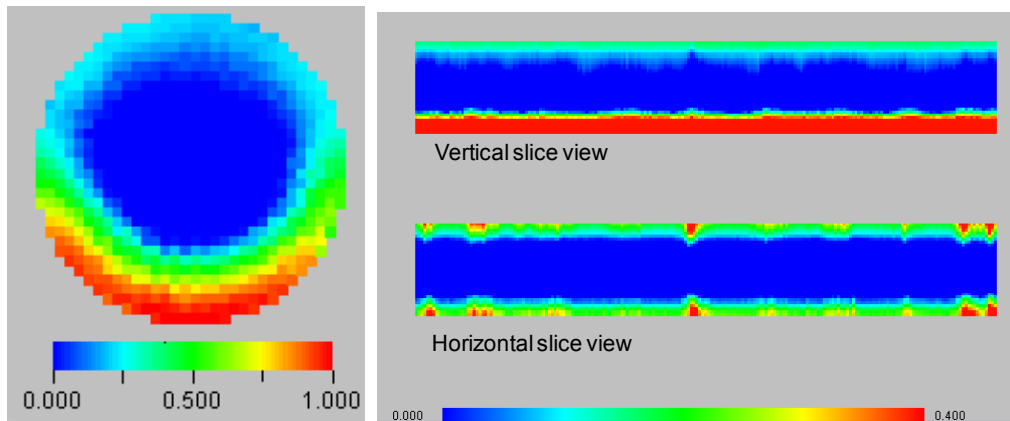
Figure 6-34: ECT images showing cross-sectional, vertical slice and horizontal slice views for gas-LVT200 annular-mist flow at V_{oil} = 0.5 m/s and V_{gas} = 31 m/s.
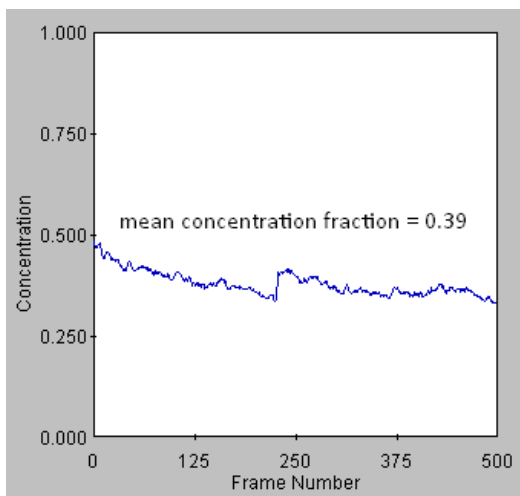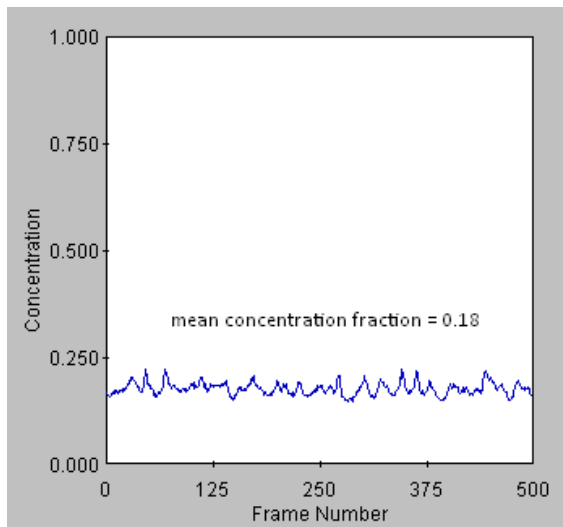

Figure 6-35: ECT time series of liquid concentration fraction for annular-mist flow at V_{oil} = 0.5 m/s and V_{gas} = 31 m/s.
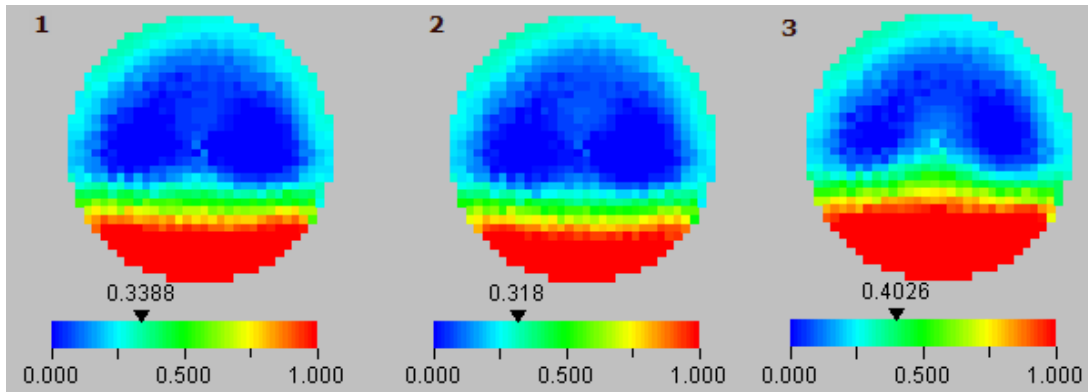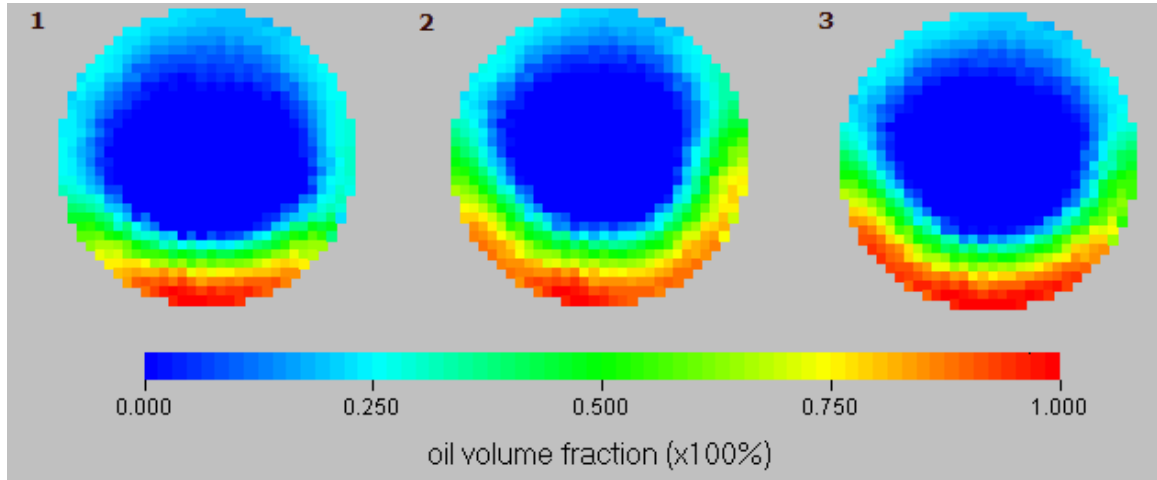
Figure 6-36: Sequence of ECT images at 0.5 s interval, showing the evolution of annular-mist flow at V_{oil} = 0.5 m/s and V_{gas} = 31 m/s.

Table 6-8 summarizes the results of mean liquid concentration data measured by ECT for five types of flow patterns. The results showed that the ECT can be used to qualitatively detect various characteristic flow patterns in horizontal gas-oil flow. By analyzing a sequence of ECT slice images rather than a single slice image and the liquid concentration data, it was possible to identify the characteristic features associated with each type of flow pattern. The time series concentration data also gives important information about the phase fraction variations and the intermittency of the flow pattern.

Table 6-8: Summary of ECT mean liquid concentration fractions in horizontal gas-oil flow

Flow patterns	Superficial velocities	ECT mean liquid concentration (fraction)
a. Stratified (ST)	V_{oil} = 0.05 m/s, V_{gas} = 0.1 m/s	0.39
b. Elongated bubble (EB)	V_{oil} = 0.5 m/s, V_{gas} = 0.6 m/s	0.67
c. Slug (SL)	V_{oil} = 0.5 m/s, V_{gas} = 1.6 m/s	0.46
d. Wavy annular (WA)	V_{oil} = 0.5 m/s, V_{gas} = 15.2 m/s	0.20
e. Annular-mist (AM)	V_{oil} = 0.5 m/s, V_{gas} = 31 m/s	0.18

6.4.3   Horizontal gas-oil-water flow

6.4.3.1 Image reconstruction related problems

The ECT tomograms are reconstructed by a linear back projection (LBP) scheme which delivers fast computations and moderate spatial resolution. LBP generally work well for gas-oil systems. However it was found that LBP image reconstruction scheme was inadequate in producing accurate images for three-phase gas-oil-water flow experiments. Considering a flow condition at superficial velocities of V_{liquid} = 0.05 m/s, V_{gas} = 0.1 m/s at 5% water cut, the observed flow pattern was stratified flow with separation of gas at the top, oil in the middle and water in the bottom layer. Figure 6-37(a) is the ECT image showing the high gas concentration region (blue) at both the top and bottom layers, whereas the high oil concentration layer (red) is the middle layer. The water layer was represented as the low permittivity phase '0' instead of high permittivity phase '1'. In fact, water has a much higher permittivity than the other two phases. It has a high relative permittivity of 80, compared to oil with a relative permittivity of around 3. In ECT, all the measured permittivity data are normalized within the bounds of 0 to 1. A linear relationship is applied during the data conversion for the LBP image reconstruction scheme. For normal application in the case of the oil/gas system, the permittivity difference is low and linear approximation is valid. The ECT sensors measure predominantly the capacitive component of the dielectric media. In the presence of conductive water, the ECT sensors also respond to the conductive component if the system contains water of finite conductivity (Jaworski & Bolton, 2000). When the media conductivity is further increased, the reduced media resistance causes more current to flow and saturate the sensor electronic circuitry. The ECT system will start to behave like an ERT system rather than a strictly capacitance measurement. If the permittivity contrast is too large for the case of the water/oil/gas system, the computations become an ill-conditioned mathematical problem and the linear approximation for the LBP image reconstruction algorithm is no longer valid. This leads to capacitance inversion phenomena as

described by Corlett (2001), where the permittivity data saturated by water are flipped during LBP image reconstruction and shown as an artifact at the 6 o'clock position in the ECT images. Because of this issue, another image reconstruction algorithm, high dielectric reconstruction (HDR), was applied in this work. HDR is able to suppress the reconstruction artifact associated with processes containing high dielectric media such as water. Figure 6-37 shows the tomogram comparisons between (a) LBP and (b) HDR algorithms for a test case of stratified flow. The LBP method is unable to suppress the artifact caused by the stratified water layer at the base, while the HDR method suppresses most of the artifacts but does not completely lead to their suppression. There were still residual artefacts at the pipe bottom with this alternative reconstruction method. In addition, the constructed interface appeared convex at the gas-liquid interface; as opposed to what observed in the experiments; most probably form the overcompensation of the reconstruction method.
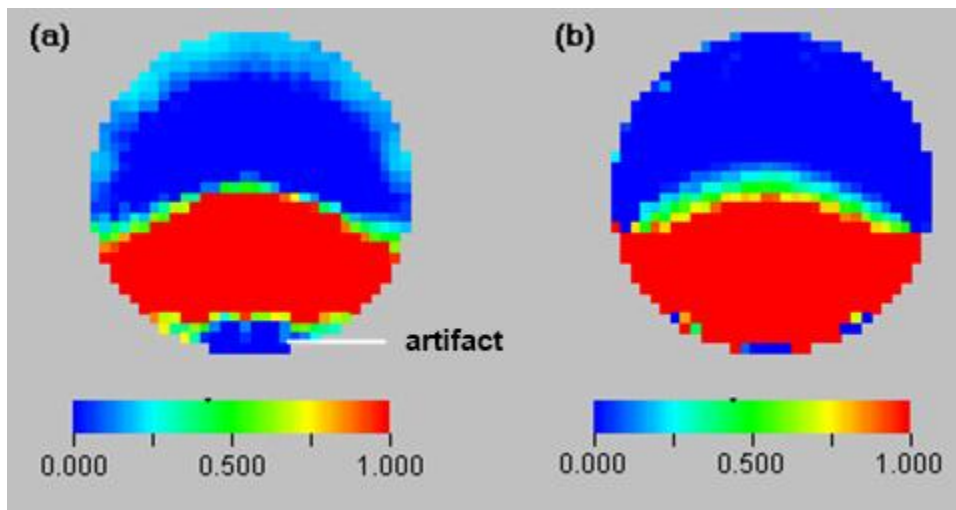
Figure 6-37: ERT image reconstruction for three-phase stratified flow using (a) linear back projection (LBP), (b) high dielectric reconstruction (HDR) scheme.

6.4.3.2 Flow pattern results

Figure 6-38 and Figure 6-39 present the ECT tomogram results showing stacked section and cross-section views for three-phase stratified, elongated bubble, slug, wavy annular and annular-mist flow patterns. HDR has been applied in reconstructing the images in order to minimize the artefacts due to the presence of conductive water. The stacked section is a sequential vertical slice of 200 images assembled together in time series at an acquisition rate of 29 fps. The cross-section images depict the selected frames showing the evolution of the flow pattern. The ECT results for three-phase flow system showed there were variations between flow patterns. The ECT constructed flow structure for three-phase flow patterns appeared to be qualitatively similar to that of gas-liquid flow patterns. At the lowest superficial gas velocity V_{gas} = 0.1 m/s, the separation of gas (blue area) and liquid (red area) phases can be seen. Though HDR image reconstruction algorithm has been applied, residual artifacts due to the capacitance inversion can still be seen at the pipe bottom. At a slightly higher superficial gas velocity of 1 m/s, the first form of intermittent flow, namely an elongated bubble, can be observed. The flow pattern has a high liquid to gas fraction ratio. In the ECT images, the intermittency is characterized by the alternate flow of sections with high liquid fraction (red) followed by low gas fraction (blue). At moderate superficial gas velocity, the next form of intermittent flow, slug, can be seen. The gas and liquid phases showed large fluctuations in their fractions during the slug propagation. As the gas velocity was further increased, the fluids are more mixed and agitated by the turbulence as the flow pattern transitioned to wavy annular and annular flows. The flow patterns have a relatively high gas to liquid fraction ratio. The ECT images show that the fluid (green) at the lower part of the pipe is a mixture of liquid and gas phases.

Figure 6-40 shows the time series liquid concentration data produced by ECT for the whole set of experiments. The liquid concentration data were collected for 500 frames, equivalent to 16.7 s at an acquisition rate of 29 fps. By studying the phase fraction variations and the manner of

flow intermittency, the plots can be used as a flow pattern identification tool to identify the characteristic features associated with each type of flow pattern.
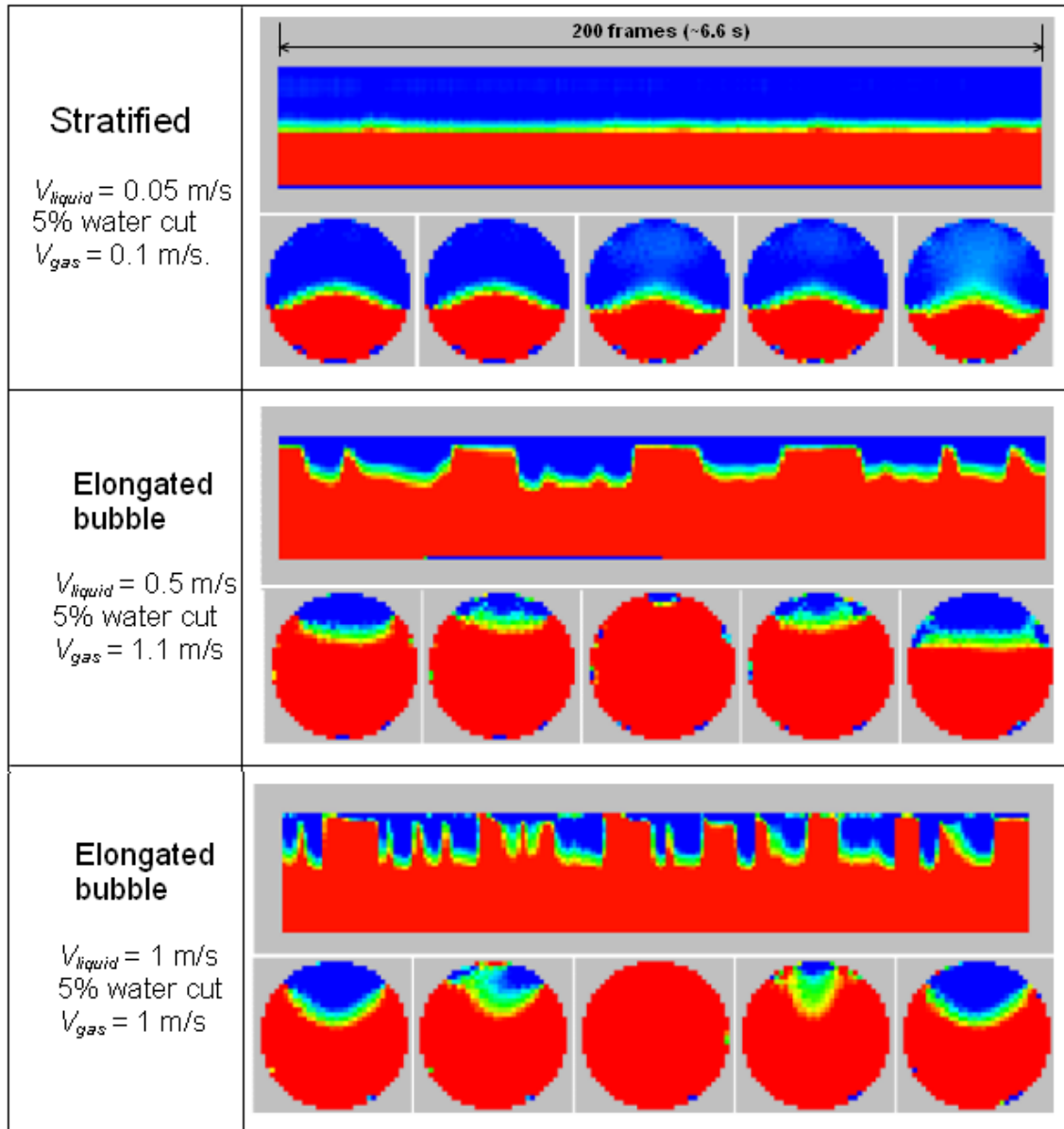
Figure 6-38: Cross-sectional ECT images, vertical and horizontal slice views for three-phase stratified and elongated bubble flows in air-LVT200-water systems.
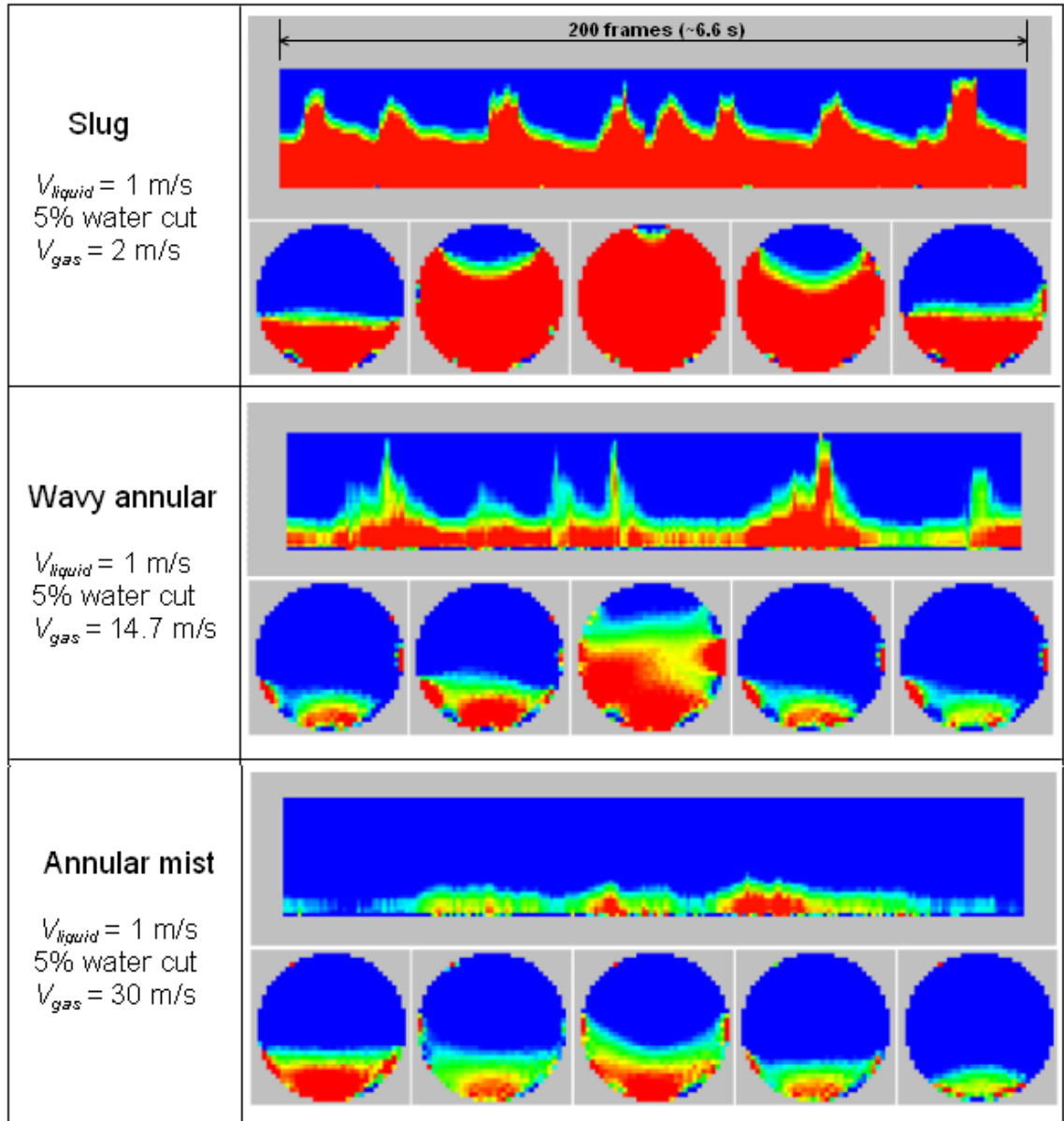
Figure 6-39: Cross-sectional ECT images, vertical and horizontal slice views for three-phase slug, wavy annular and annular-mist flows in air-LVT200-water systems.
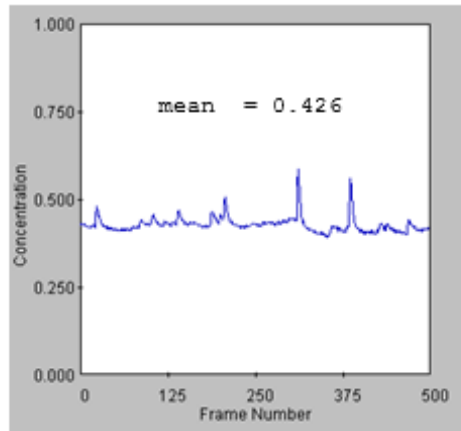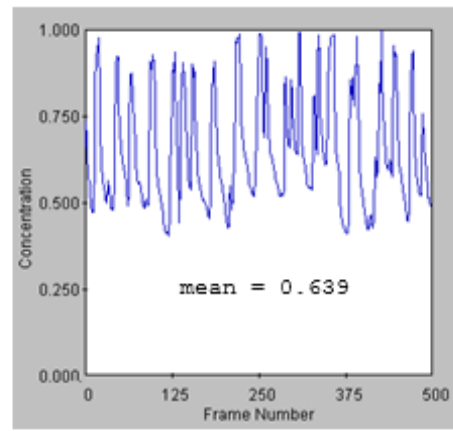
259
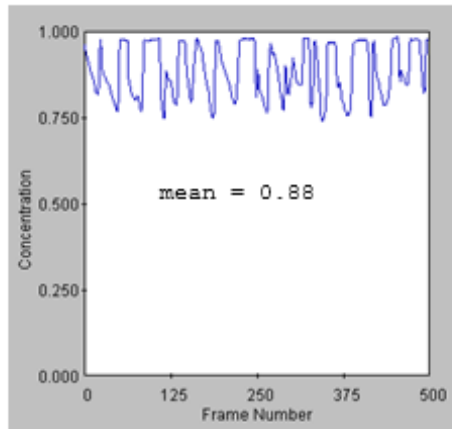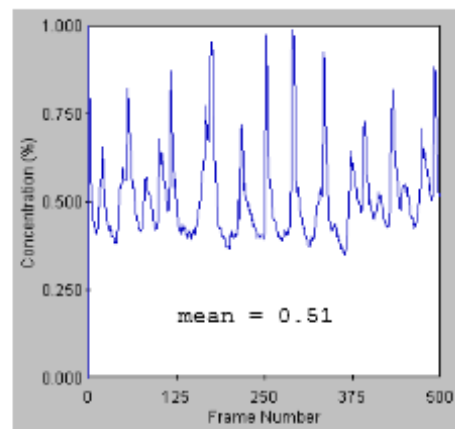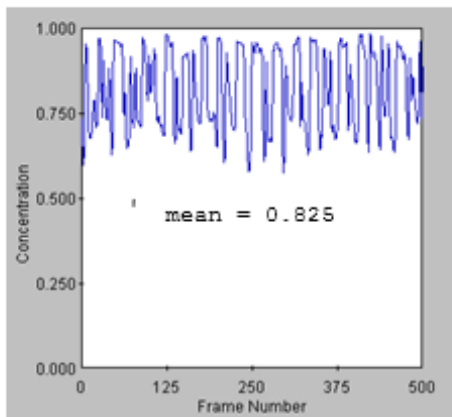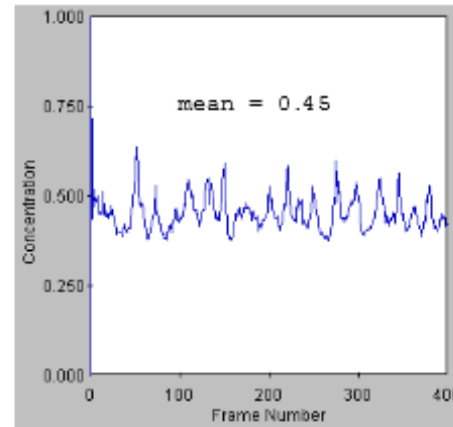
Figure 6-40: ECT time series of liquid concentration fraction for horizontal three-phase (a) stratified, (b) elongated bubble, (c) elongated bubble, (d) slug, (e) wavy annular and (f) annular-mist.

6.4.4   Vertical gas-oil-water flow

In vertical upward three-phase gas-oil-water flow, ECT was used to visualize the cross-sectional distribution of gas and liquid phases. Due to the operational limits of the current flow loop setup, only two types of flow pattern can be observed in this work, namely churn and annular-mist flow. As explained in Section 5.1.2, churn flow is an intermittent flow that exists between slug and annular flow. It is characterized by an oscillatory up and down fluid motion in the pipe, in which the liquid mixture is highly distorted by the high gas flow. This results in an accumulation of the falling liquid film which is subsequently lifted by the interfacial waves that surge periodically up the pipe (Chen & Brill, 1997). The annular-mist flow exists at very high gas flow rates, in which a thin annular liquid film flows upward adjacent to the wall; whilst the gas flows at the pipe core. Some liquid may detach from the wavy gas-liquid interface and entrain as mist in the core (Taitel, *et al*., 1980). The schematics for these two upward flow patterns are shown in Figure 5-2.
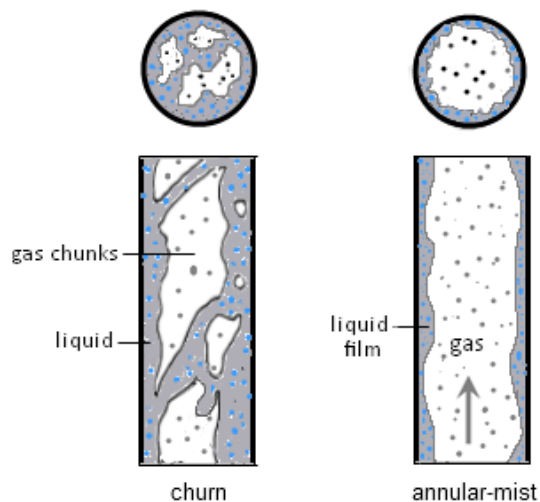
Figure 6-41: Schematics of three-phase churn and annular-mist flow patterns.

The ECT tomogram results in Figure 6-42 illustrate the vertical stacked section and cross-section views for churn and annular-mist flows for liquid velocities of 0.5 m/s, water cut of 5% and gas velocities of 5 m/s to 25 m/s. The stacked section is a sequential vertical slice of 200 images assembled together in time series at an acquisition rate of 29 fps. HDR has been used to reconstruct the ECT images in order to minimize the artefacts. The ECT tomograms for the churn flow in Figure 6-42(a) show instances of chunks of highly mixed gas-liquid phases (shown in green) that flicker unstably with time and space as they move upwards. Figure 6-42(c) is annular-mist flow at the highest superficial gas velocity V_{gas} = 25 m/s, showing mostly high gas concentration area (blue) and few gas-liquid mixture areas (green) flickering in the pipe circumference. At a gas velocity of 15 m/s, the flow condition was visually observed as churn flow. The ECT images in Figure 6-42(b) show that the flow is a transitional from churn to annular, showing increased gas concentration and diminished gas-liquid mixture concentration as the velocity rises. The time series liquid concentration plots for each flow conditions are shown in Figure 6-43. The results in Figure 6-43 (a) indicated that the liquid fraction in churn flow displayed larger amplitude of fluctuations from 0.25 to 0.6 compared to a narrower range of 0.25 to 0.3 for annular flow in Figure 6-43(c). This corresponded to the alternate evolution of large interfacial waves in churn flow that intermittently 'flood' up the pipe in a chaotic manner. In annular-mist flow, the high gas flow rate resulted in high void fraction and low liquid fraction in the pipe. The results showed that the produced ECT images were somewhat qualitative due to the unstable nature of highly mixed fluids at high velocities. There were intermittent instances that moving chunks of gas-liquid mixtures were captured by the ECT in churn flow. This became increasing rare when the flow pattern changed to annular flow where the liquid was pushed to the wall. Unlike the ECT results in the horizontal case, the flow structures lack distinctive interfaces in the constructed tomograms to distinguish the flow patterns.
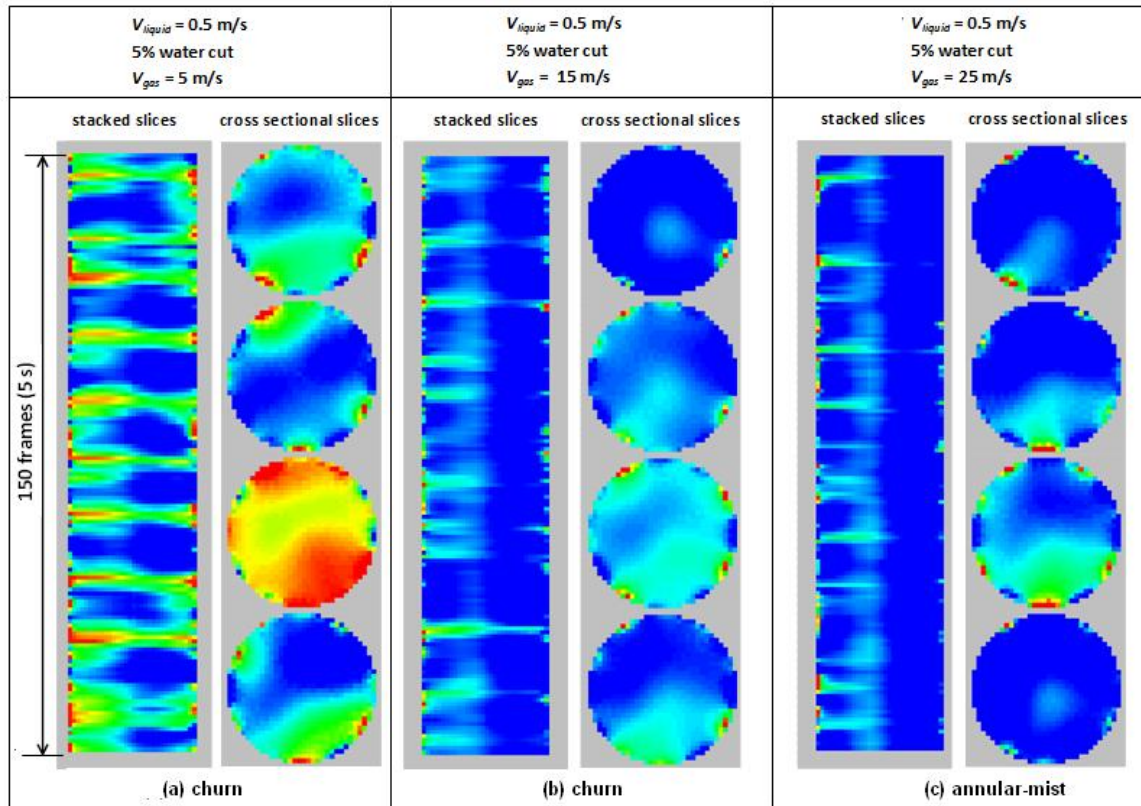
Figure 6-42: ECT tomograms for vertical three-phase flow at V_{liquid} = 0.5 m/s and water cut 5%, showing stacked section and cross section views for (a) churn at V_{gas} = 5 m/s, (b) churn at V_{gas} = 15 m/s, and (c) annular-mist at V_{gas} = 25 m/s.

(a) Churn: V_{liquid} = 0.5 m/s, 5% w.cut, V_{gas} = 5 m/s

(b) Churn: V_{liquid} = 0.5 m/s, 5% w.cut, V_{gas} = 15 m/s

(c) Annular-mist: V_{liquid} = 0.5 m/s, 5% w.cut, V_{gas} = 25 m/s
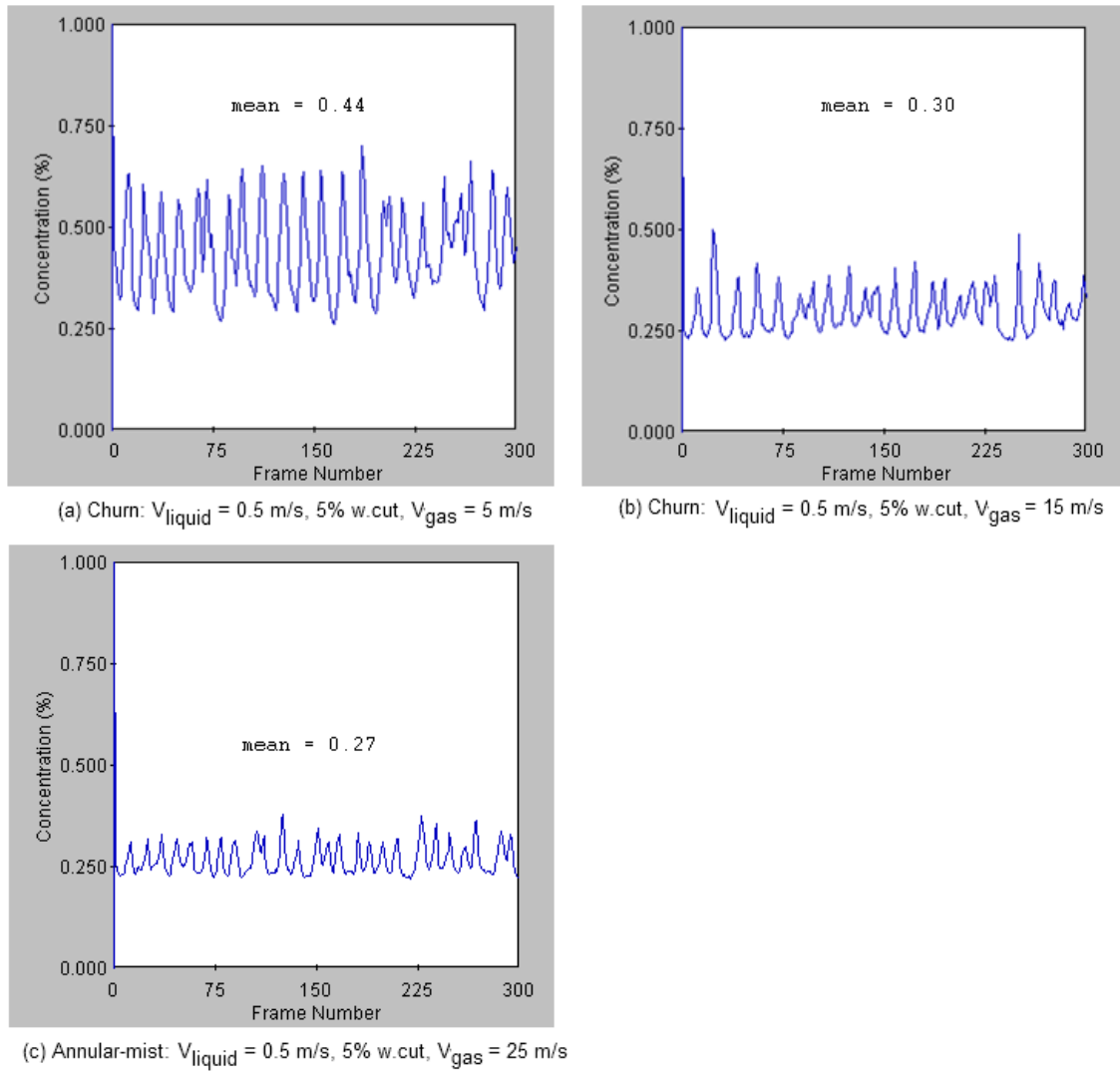
Figure 6-43: ECT time series of liquid concentration fraction for vertical three-phase (a) churn at V_{gas} = 5 m/s, (b) churn at V_{gas} = 15 m/s, (c) annular-mist at V_{gas} = 25 m/s.

6.5 Summary

- ERT can be used to detect the presence of water in the oil-water system. However the present ERT set-up does not have the resolution to detect low water cut <10% corresponding to stratified with globules flow.

- For water cut > 10%, the constructed ERT results showed a rather convex shaped interface for the water phase, resulting in an underestimation of water holdup.

- ECT can be used to differentiate the gas and liquid phases in the horizontal gas-liquid system. By analyzing a sequence of slice images, the characteristic features associated with each flow pattern can be identified.

- The time series ECT concentration data can provide information regarding the phase fraction variations and the phase intermittency associated with each flow pattern.

- The ECT constructed flow structure for horizontal three-phase flow patterns appeared to be qualitatively similar to that of horizontal gas-liquid flow patterns. In three-phase flow system, the HDR reconstruction scheme was applied to minimize the artifacts caused by the issue of capacitance inversion.

- In vertical three-phase flow, ECT images did not show distinctive interfaces because of the nature of highly mixed gas-liquid phases in churn and annular flows.

CHAPTER 7: WATER WETTING MODEL

7.1 Wetting model for oil-water flow

Two versions of water wetting models (WW models) have been developed by researchers at Ohio University and will be described in the following section. Both WW models are based on mechanistic formulations rooted in droplet breakup theory by Hinze (1955) and later by Brauner (2001). The WW models are primary applicable to oil-water flow systems. By considering the input parameters such as pipe diameter, pipe inclination, phase velocity, water cut and fluid properties, the models produce output for the wetting state (oil or water wet) and the critical entrainment velocity required to entrain the water into water-in-oil dispersion flow under given flow conditions. The first model, WW model I developed by Cai *et al.* (2004) was used in predicting the wetting transition for model oil-water system free from additives. The second model, WW model II developed by Tang (2010) considered the effect of liquid/solid surface wettability caused by the additive or crude oil compounds that can influence the wetting transition. The model descriptions are given in the following sections.

7.1.1   Water wetting model

In the first version of the water wetting model (WW model I), the wetting criterion is essentially based on the flow pattern transition from the stratified to water-in-oil dispersed flow. Following the model, the criterion for transition is determined by evaluating the maximum droplet size d_{max} and critical droplet size d_{crit}. The transition from water wetting to oil wetting takes place when the turbulence of the bulk oil phase is intense enough to break up the dispersed phase (water) into droplets such that the resulting droplet size $d_{max} \leq d_{crit}$. More explanation about

this model can be referred in prior published work by Cai and co-workers (Cai *et al.*, 2004; Cai *et al.*, 2012).

- Maximum droplet size

In a turbulent flow field, the largest stable droplet size d_{max} that can be sustained in the flow without further breakup can be determined from the Kolmogorov-Hinze droplet breakup model (Kolmogorov, 1949; Hinze 1955). They independently discovered that the maximal droplet size from single droplet breakup can be found from the force balance between the surface tension force and the dynamic pressure force of the turbulent eddies surrounding the droplet. According to Hinze (1955):

$$d_{\max} = 0.725 \left(\frac{\rho_c}{\sigma} \right)^{-0.6} \left(\frac{2 f_c U_c^3}{D} \right)^{-0.4} ; \qquad \ell_k \le d_{\max} \le 0.1D \qquad (7.1)$$

where ℓ_k is the Kolmogorov microscale and $0.1D$ is the inertial subrange which is the energy-containing eddies.

Brauner (2001) later extended the Hinze droplet breakup model for dense dispersion system, where the droplet coalescence process and the interaction of swarms of droplets become important, leading to an increase of the droplet size. The model was based on the energy balance as follows:

$$\left(\begin{array}{c} \text{Rate of turbulent kinetic} \\ \text{energy from the continous phase} \end{array} \right) = \left(\begin{array}{c} \text{Rate of surface energy} \\ \text{formed in dense dispersion} \end{array} \right) \qquad (7.2)$$

The final expression for d_{max} in dense dispersion is given as (Brauner, 2001): .

$$d_{\max} = 2.93 C_H^{-0.6} \left(\frac{\rho_c}{\sigma} \right)^{-0.6} \left(\frac{1 - \varepsilon_d}{\varepsilon_d} \right)^{-0.6} \bar{e}^{-0.4} \qquad (7.3)$$

where ρ_c is the density of the continuous phase, σ is the interfacial tension, ε_d is the input water cut, $\bar{e}$ is the mean energy dissipation rate related to the frictional pressure gradient as follows:

$$\bar{e} = \left(\frac{dP}{dL}\right)\frac{U_c}{\rho_c \varepsilon_c} \tag{7.4}$$

- Critical droplet size

The droplets resulting from the breakup process in turbulent pipe flow can exhibit different behavior depending on their size. If the resulting droplet size is larger than the critical droplet size d_{crit}, the dispersed phase (water) starts to drop out from the dispersion and wet the wall. The d_{crit} parameter can be calculated from Eqs.(7.6) and (7.7) as the minimum of two values as suggested by Barnea (1987):

$$d_{crit} = MIN(d_{CB}, d_{CD}) \tag{7.5}$$

d_{CB} is the critical droplet size due to the buoyancy/gravitational forces, which acts predominantly in horizontal oil-water flow. d_{CB} is expressed as:

$$d_{CB} = \frac{3}{8}\frac{\rho_c}{|\Delta\rho|}\frac{fU_c^2}{g\ \cos\theta} \qquad \text{where } |\Delta\rho| = |\rho_c - \rho_d| \tag{7.6}$$

d_{CD} is the critical droplet size caused by the deformation of non-spherical droplets. Based on dimensional analysis, Brodkey (1967) expressed d_{CD} as a function of surface tension and gravity forces. Barnea *et al.* (1982) proposed that if the resulting droplet is larger than d_{CD}, it loses its sphericity and is subjected to deformation and coalescence. Because of the non-spherical shape, the distorted droplet also tends to swerve sideways (Cai *et al.*, 2012). Brauner (2001) included the effect of pipeline inclination such that the parameter is important in vertical or near-vertical flow where the gravity force is not dominant. d_{CD} is expressed as:

$$d_{CD} = \sqrt{\frac{0.4\sigma}{|\Delta\rho|g\ \cos\beta'}} \tag{7.7}$$

$$\text{where} \quad \begin{aligned} \beta' &= |\beta| & \text{if } |\beta| \le 45° \\ \beta' &= 90° - |\beta| & \text{if } |\beta| > 45° \end{aligned}$$

Since d_{CD} is derived purely from the argument of dimensional reasoning between the surface tension and gravity, it is not a function of flow rate and water cut.

- Transition criterion

The water wetting model assumes oil wetting occurs if the dispersed phase (water) is entrained by the bulk oil flow, hence preventing water from wetting the wall. On the other hand, water wetting prevails if the water droplets drop out from the oil phase and wet the pipe wall. In this case, the flow pattern transition is assumed to coincide with the wetting transition. The transition from water wetting to oil wetting takes place when the turbulence of the oil phase is intense enough to break up the water phase into droplets not larger than d_{max} and smaller than d_{crit} (Cai *et al*., 2004). The critical velocity required to entrain the water phase can be calculated by solving the following criterion:

$$d_{\max} \leq d_{crit} \tag{7.8}$$

The model predicts that the critical entrainment velocity is a function of several parameters including water cut, oil density, oil viscosity, oil-water interfacial tension, pipe diameter and inclination. For light crude oil with low density and viscosity ratios, higher critical velocity is required for water entrainment as compared to heavy viscous oil. If the parameters for pipe diameter and water cut are increased, the critical velocity required for water entrainment is also increased accordingly. A change in interfacial tension has a slight effect in the critical velocity. If the water cut is further increased until the system reaches the phase inversion point (typically 30-50% water cut), a phenomenon in which the water-in-oil dispersion inverts to oil-in-water dispersion, the resulting flow pattern will be considered as water continuous flow and water wetting is predicted to occur. A logic flow chart for the model is presented in Figure 7-1.
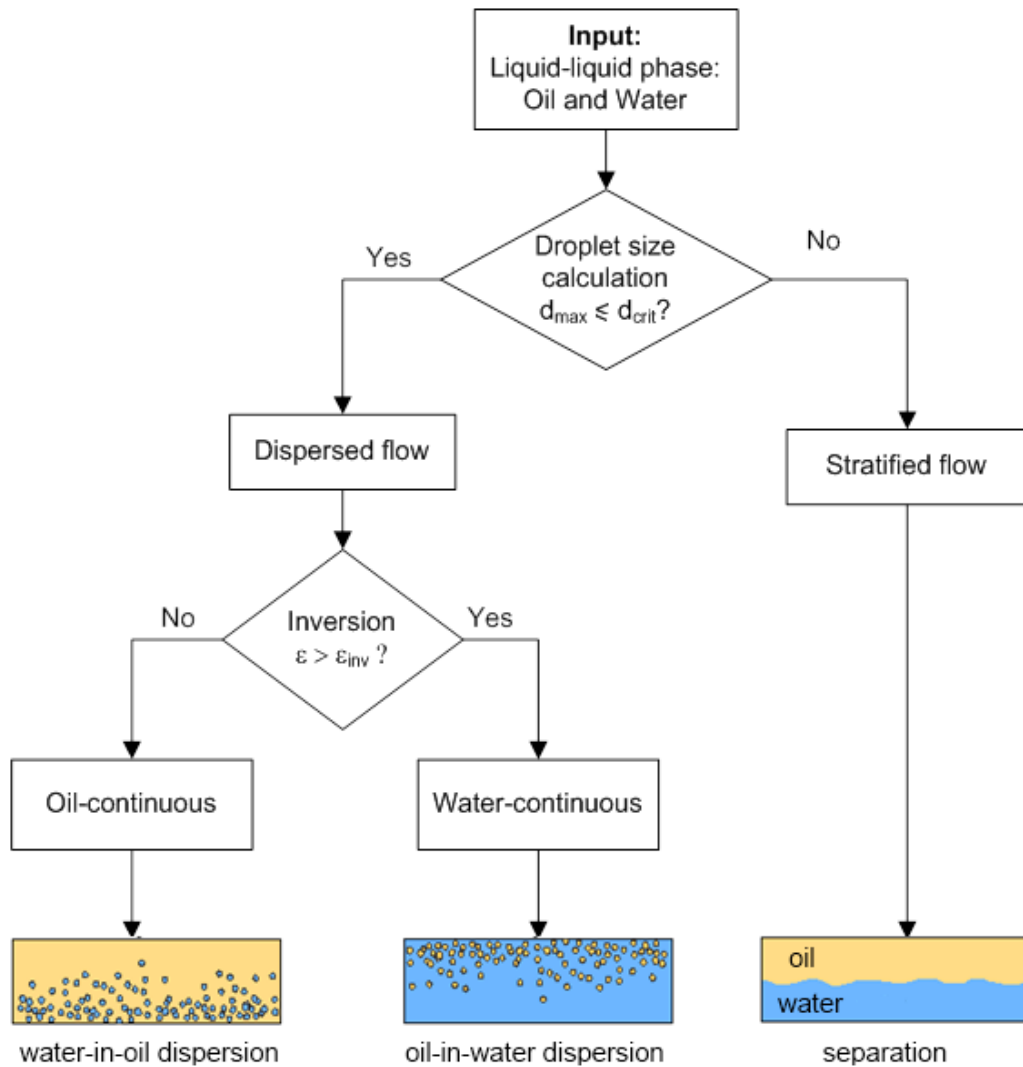
Figure 7-1: Logic flow chart of oil-water flow model.

7.1.2 *Water wetting model with surface wettability effect*

The model is a modified version of the previous water wetting model by considering the effect of steel surface wettability. It is noted that the presence of surface active substances such as corrosion inhibitors or other naturally occurring compounds in crude oil can influence the wettability of the steel surface. The adsorption of surface active substances at the steel surface can form an oil-based microfilm that can repel water and inhibit corrosion (Hackerman & Roebuck,

1954; Hernandez *et al.*, 2003; Ayello *et al*., 2011). The inhibitory role of surface active substances in oil-water pipe flow is complicated, as they can act in the oil-water interface as well as in the oil-steel and water-steel interface. The accumulation of surface active compounds on the oil-water interface may decrease the oil-water interfacial tension, leading an increased tendency of emulsion formation and stability. The adsorption of surface active compounds on the steel surface may alter the wetting behavior of steel/water and steel/oil interface, leading to a change in water-in-oil contact angle that precludes water droplet from spreading on the steel surface (Ayello *et al*., 2011).

In WW model I, it assumed that all of the available turbulent kinetic energy from the oil phase was used to overcome the oil-water surface energy and fragment the water phase into discrete droplets. The inherent assumption here was that the water phase has already been entrained in the dispersion and the turbulent kinetic energy was solely expended to sustain the water-in-oil dispersion. By considering the surface wettability altering effect, Tang *et al*. (2013) argued that additional interactions between the water-steel and oil-steel surfaces in the presence of surface active components can influence the droplet breakup process and the level of turbulent kinetic energy required to maintain the dispersion. They proposed an updated model, namely WW model II, that included an additional turbulent kinetic energy to create new surfaces resulting from the solid/fluid surface interactions. Following the similar approach from the previous model, the model calculates the maximum droplet size d_{max} and critical droplets size d_{crit} in the oil-water flow system. The essence of the model is summarized below. Further detailed explanation on this model can be found in prior publication by Tang *et al*., (2013).

- Maximum droplet size

The determination of maximum droplet size d_{max} follows the same energy balance route as the previous model except for the calculation of surface energy. The model assumes 4 parts of surface related (oil-water, oil-steel, water-steel) energies as listed below (Tang *et al.*, 2013):

i. E_{S1} = rate of surface energy gained from the newly formed oil-water interface

ii. E_{S2} = rate of surface energy lost from the disappeared oil-water interface

iii. E_{S3} = rate of surface energy gained from the newly formed oil-steel interface

iv. E_{S4} = rate of surface energy lost from the disappeared water-steel interface

The total rate of surface energies E_{ST} (Joule/s) can be written as:

$$\text{Total surface energies, } E_{ST} = \left\{ \underbrace{\frac{6\sigma_{ow}}{d_{max}}Q_w}_{E_{S1}} - \underbrace{\frac{L_1\sigma_{ow}}{\varepsilon_w(\pi D^2/4)}Q_w}_{E_{S2}} + \underbrace{\frac{L_2\sigma_{os}}{\varepsilon_w(\pi D^2/4)}Q_w}_{E_{S3}} - \underbrace{\frac{L_2\sigma_{ws}}{\varepsilon_w(\pi D^2/4)}Q_w}_{E_{S4}} \right\} \tag{7.9}$$

where Q_w is the water flow rate (m^3/s), $\sigma_{ow}, \sigma_{os}, \sigma_{ws}$ are the oil-water, oil-steel, water-steel interfacial tensions (N/m), respectively. L_1, L_2, α are the geometrical parameters as depicted in Figure 7-2. L_1, L_2 are the chord length and arc length, 2α is the angle (radians) subtended by the chord length L_1 from the pipe center. The geometrical parameters can be calculated as follows:

$$L_1 = D\sin\alpha \qquad L_2 = D\alpha \tag{7.10}$$

$$\varepsilon_w = \frac{2\alpha - \sin 2\alpha}{2\pi} \tag{7.11}$$
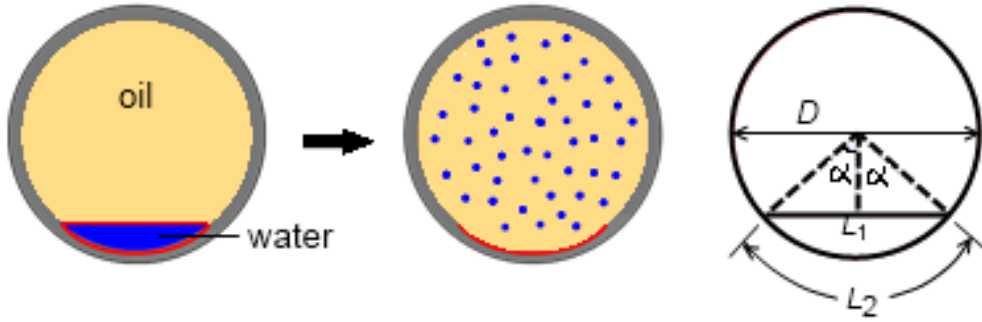
Figure 7-2: Schematics of flow transition from stratified to water-in-oil dispersed flow and the geometrical parameters (reproduced with permission from Tang *et al.*, 2013).

The relationship of different interfacial tensions and contact angle β can be expressed by Young's equation (Young, 1805) as follow:

$$\cos\beta = \frac{\sigma_{os} - \sigma_{ws}}{\sigma_{ow}} \tag{7.12}$$

The maximum droplet diameter can be found from the energy balance between the turbulence kinetic energy and the total surface tension energies. The proportional relation between these two energies is given as:

$$\frac{\rho_c u'^2}{2} Q_o \propto \left\{ \frac{6\sigma_{ow}}{d_{max}} Q_w - \frac{L_1\sigma_{ow}}{\varepsilon_w(\pi D^2/4)} Q_w + \frac{L_2\sigma_{os}}{\varepsilon_w(\pi D^2/4)} Q_w - \frac{L_2\sigma_{ws}}{\varepsilon_w(\pi D^2/4)} Q_w \right\} \tag{7.13}$$

By introducing proportionality constants C_H, C_W and using relations in Eq.(7.10) to (7.12), the final expression becomes:

$$\left[\frac{d_{max}}{D} \cdot 2U_o{}^3 f \frac{\rho_m}{\rho_o(1-\varepsilon_w)} \right]^{2/3} = \frac{\sigma_{ow}}{\rho_o}\left(\frac{\varepsilon_w}{1-\varepsilon_w}\right)\left[C_H\left(\frac{6}{d_{max}} - \frac{4\sin\alpha}{\varepsilon_w\pi D}\right) + C_W\frac{4\alpha\cos\beta}{\varepsilon_w\pi D} \right] \tag{7.14}$$

In the wetting model as expressed in Eq.(7.14), the proportionality constant C_H is set as 1 while the new proportionality constant C_W is set as 30, as estimated from the laboratory test data

for different types of crude oils (Tang *et al*., 2013). It is noted that Eq.(7.14) is an implicit nonlinear equation for which the maximum diameter d_{max} can be solved numerically using a root-seeking algorithm.

- Critical droplet size

The determination of critical droplet size follows the same procedure as the previous model. The d_{crit} parameter can be calculated as the minimum of two values: d_{CB} and d_{CD}. d_{CB} is the critical droplet size due to the gravity, and can be calculated using Eq.(7.6). d_{CD} is the critical droplet size caused by the deformation of non-spherical droplets. Based on the experimental droplet data from Bond & Newton (1928), Tang *et al*., (2013) argued that the constant 4 should be used instead of 0.4 in Eq.(7.7) for the d_{CD} parameter. The expression for d_{crit} is rewritten as:

$$d_{crit} = MIN\left(\frac{3}{8}\frac{\rho_c}{|\Delta\rho|}\frac{fU_c^2}{g\,\cos\theta} \,,\, \sqrt{\frac{4\sigma}{|\rho_c\text{-}\rho_d|g\,\cos\beta'}}\right) \tag{7.15}$$

$$\text{where} \quad \begin{array}{ll} \beta' = |\beta| & \text{if}\,|\beta| \leq 45° \\ \beta' = 90° - |\beta| & \text{if}\,|\beta| > 45° \end{array}$$

- Transition criterion

The water wetting model assumes oil wetting occurs if the water phase is entrained by the bulk oil flow, whereas water wetting occurs if the water wets the pipe wall. The wetting transition criterion is evaluated by comparing the maximum droplet size d_{max} with the critical droplet size d_{crit}. If $d_{max} \leq d_{crit}$, the water phase is entrained by the bulk oil flow and the wall is 'wetted' by the oil phase. On the other hand, if $d_{max} > d_{crit}$, water drops out from the oil and the wall is wetted by the wall phase. The critical entrainment velocity required to sustain the dispersion can be calculated by solving the criterion: $d_{max} \leq d_{crit}$. By considering the surface wettability effect, the current model is sensitive to the change in contact angle.

7.1.3   Model comparisons

The predictions from the WW models were compared with the experimental wetting results in horizontal oil-water flow system. The baseline experiments were conducted at ambient pressure and temperature (25 °C) in a 0.1 m ID large-scale flow loop. The test fluids used were light model oil LVT200 (ρ_o = 823 kg/m^3, μ_o = 2.7 cP) as the oil phase, and 1 wt.% NaCl aqueous solution (ρ_w = 1000 kg/m^3, μ_w = 1 cP) as the water phase. The model oil was clear, colorless and free of surface active compounds. The oil-water surface tension and water-in-oil contact angle were measured as σ_{ow} = 40 mN/m and θ = 70°, respectively. Further details on the oil-water flow and wetting experiments can be found in Chapter 4.

As presented in Figure 7-3, the surface wetting map was plotted for model oil-water flow with the mixture liquid velocity as abscissa and the water cut as the ordinate. Each data point on the map corresponds to the wetting state on the wall surface, which includes stable water wet, unstable water wet, unstable oil wet and stable oil wet. For model comparison purposes, two types of wetting conditions: oil wetting or water wetting, are adopted since the models cannot distinguish the unstable wetting. From the corrosion standpoint, the water wetting condition refers to both stable and unstable water wet, which means water can access to the wall surface, leading to corrosion. *Vice versa* for the oil wetting condition, it refers to both stable and unstable oil wet, which means water is kept off from the wall surface, reducing the corrosion risk. A transition line can be drawn in the wetting map to delineate between the water wetting (leftward of the line) and oil wetting (rightward of the line). As shown in Figure 7-3, both transition lines generated from the models have the same trend. The WW model I can predict well for the wetting transition at lower ranges of water cut but becomes less conservative at higher ranges of water cut (>5%). The WW model II transition line shows a rightward shift caused by the water-in-oil contact angle of

θ=70°. The model predicts well for cases at high water cut (>4%) but becomes slight more conservative at lower ranges of water cut (<5%).
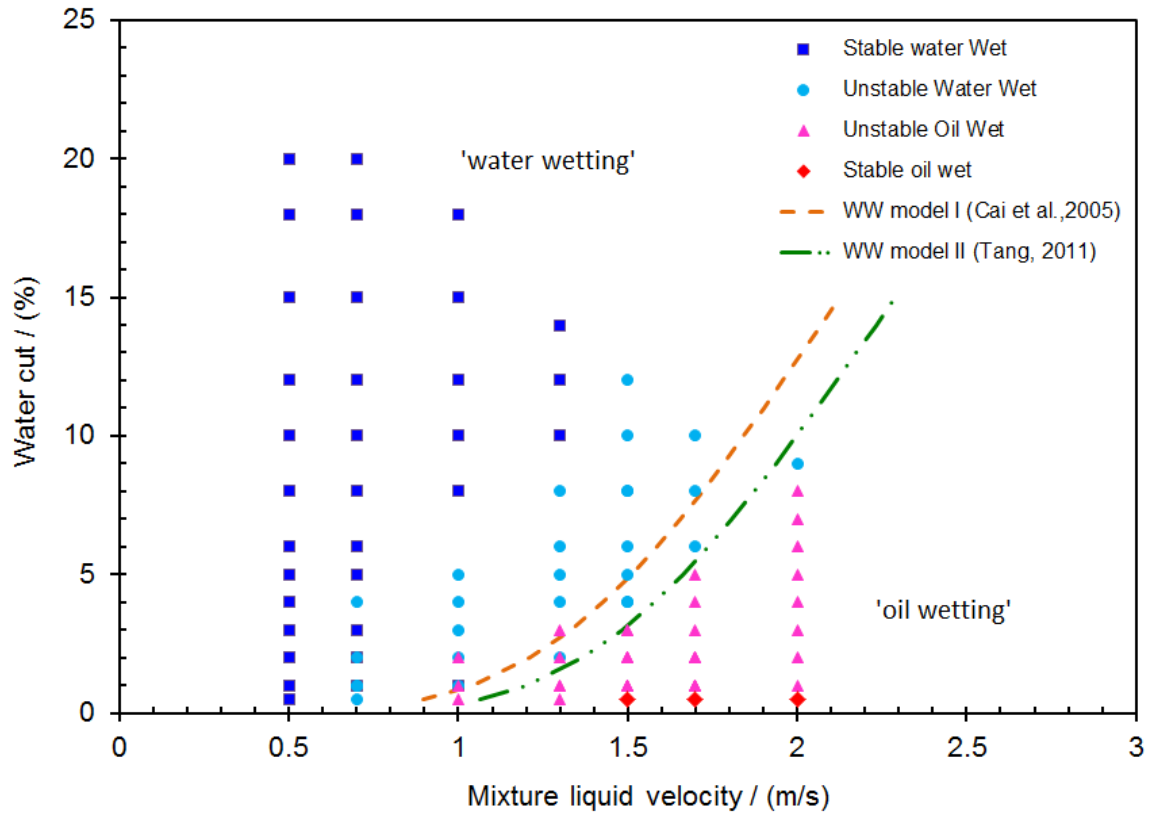
Figure 7-3: Comparison of model prediction results with the experimental result for model oil-water system.

7.2 Wetting model for gas-oil-water flow

Based on the experimental and visualization results presented previously, in addition to the understanding of the water wetting model used in the oil-water flow, a new three-phase gas-oil-water wetting model has been developed with the integration of both gas-liquid and oil-water model.

7.2.1 Model configuration

For the concurrent flow of three different phases of immiscible fluids, varying degree of spatial distributions of the fluids can result in a broad variety of complicated flow patterns (Hewitt, 2005). Therefore, the modeling for three-phase flow is not as straightforward as its two-phase flow counterparts. The foremost difficulties lie in assessing the local distribution of oil-water phases within the flows as well as predicting the flow patterns arising from the interaction of the gas, oil and water phases. In most cases, the global flow pattern configuration is dictated dominantly by the spatial distribution of the gas-liquid phases rather than the distribution of the oil-water phases. This is because of the large contrast in physical properties between the gas/liquid phases and the gas phase, leading to a highly deformable interfacial structure.

The development of the three-phase water wetting model involves the simplification of the flow pattern determination based on the framework of a gas-liquid flow model, in which the liquid phase is assumed to be a homogenous oil-water mixture flowing at the same velocity. The local distribution of oil-water (dispersion or separation) in the liquid phase within the flow can be predicted by the water wetting model using the flow parameters and closure relations specific to the flow pattern. Based on the proposed modeling strategy, a three-step solution approach has been formulated as shown in a flow chart in Figure 7-4:

Step 1: Configure the mixture liquid properties (apparent density and viscosity) by assuming the liquid phase is an effective homogenous mixture of oil and water phases. The liquid flow rate is the sum of the individual oil and water flow rates.

Step 2: Predict the global gas-liquid flow pattern and the relevant hydrodynamic parameters using the two-phase gas-liquid model. The input fluids properties data are the gas properties and the configured mixture liquid properties.

Step 3: Based on the predicted global flow pattern and the flow characteristics data, the oil-water flow model is configured to an equivalent pipe diameter having a similar rate of dissipation

of energy. The local oil-water distribution in the liquid phase (see Figure 7-5) is further distinguished as to whether it is in dispersion or separated by applying the water wetting model. The liquid phase occupying the wetted pipe area is approximated to be full pipe flow using the hydraulic diameter concept. The model assumes that:

- the flow is fully developed, steady state and isothermal flow without mass transfer or chemical reactions between the immiscible fluids.

- in the global gas-liquid model, the liquid phase is a homogeneous oil-water mixture described by the mixture properties.

- in local oil-water model, the liquid phase is in turbulent dispersion and the wetting model is used to determine whether water will drop out from the oil.

- the slug flow model is considered for the intermittent flow pattern.
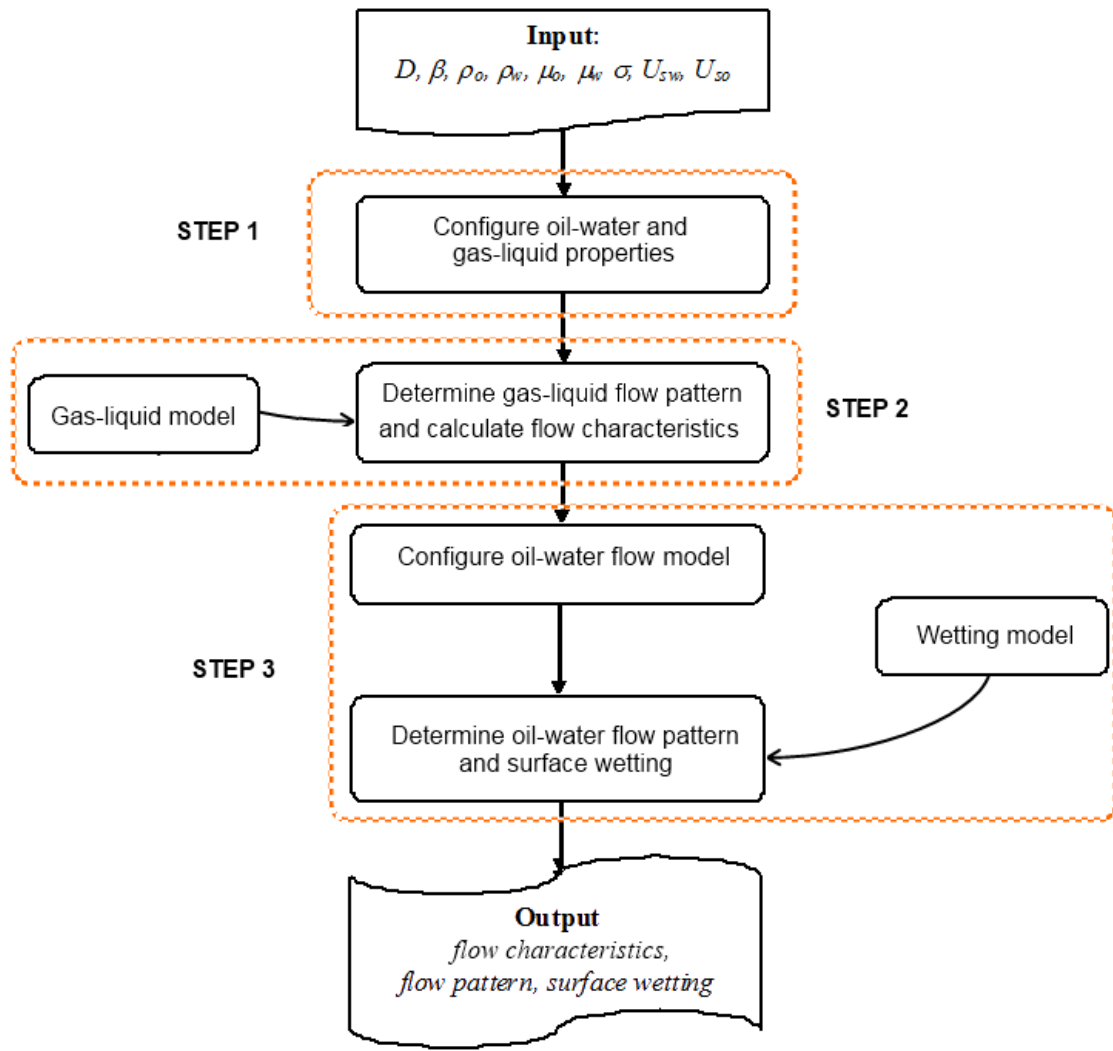
Figure 7-4: Solution logic flow chart in three-phase flow and wetting models.
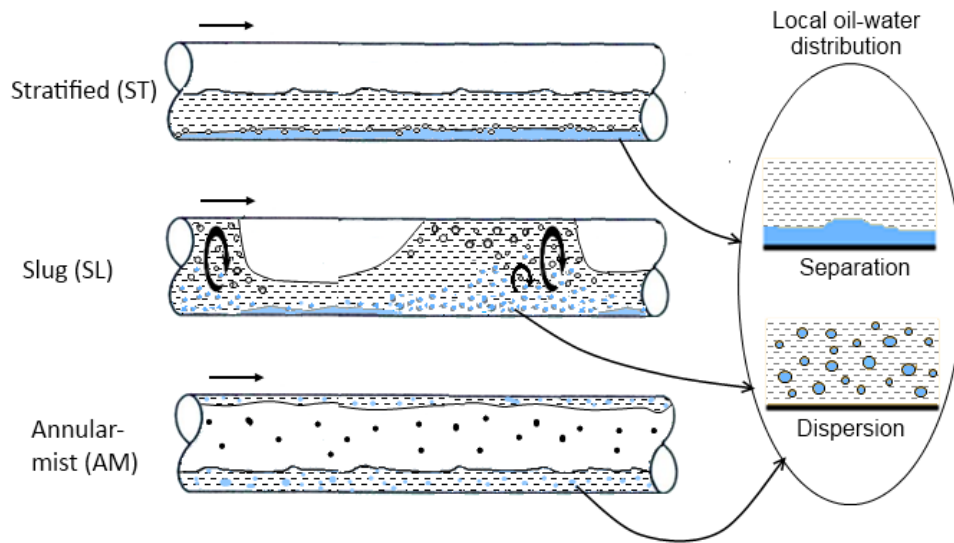
Figure 7-5: Possible scenarios of local oil-water distribution (separation or dispersion) in the liquid phase of the three-phase flow pattern.

The development of the three-phase water wetting model depends on the determination of flow pattern by gas-liquid flow as well as the approximation of oil-water phases as a homogeneous no-slip mixture flow with equivalent pipe diameter and effective physical properties. They are described next, focusing on a configuration with respect to the fluid properties, pipe geometry, flow pattern, and related characteristics:

7.2.2 Configuration in gas-liquid flow model

The two-phase gas-liquid flow model, developed by Jauseau (2012) is implemented in Microsoft Visual Basic 2010 using object-oriented programming. The flow model is mechanistic in nature as all the gas-liquid flow phenomena are described by simplified physical mechanisms, expressed in mathematical equations. Literature or experimental data are used to refine the closure laws and to check the validity of the model. Therefore, the model is an intermediate method between the exact and the experimental approach. The physics of this flow model is

closely aligned with the school of thought of Taitel, Dukler, Barnea and their co-workers (see papers by Dukler & Hubbard, 1975; Taitel & Dukler, 1976; Shoham & Taitel, 1984; Barnea, 1986, 1987, Shoham, 2006). More details can be referred to the work of Jauseau (2012) on the flow model.

The global logic flow chart of the gas-liquid flow model is shown in Figure 7-6. Based on the input fluid properties, flow and piping data, the model predicts the possible flow patterns occurring in the pipe which include bubble, stratified, annular and intermittent flows. The determination of the flow pattern is done by first assuming a flow pattern and examining the flow-pattern-specific mechanism that is responsible for the transition to that specific flow pattern. If it satisfies the flow transition criterion, then the flow pattern can exist under the given conditions. If not, the next flow pattern is investigated. If none of the first three flow patterns is valid (see Figure 7-6), then the intermittent (slug) flow is assumed to prevail. Note that the intermittent flow covers the elongated bubble, slug and churn flows. For practical purposes, the intermittent flow in this flow model specifically refers to the slug flow, as the flow occurs predominantly over a broad range of intermediate flow rates. Once the flow pattern is predicted, the associated flow characteristics such as the liquid holdup, pressure gradient, wall shear stress and *in situ* velocity can be computed as output. Figure 7-7 presents a typical flow pattern map for horizontal gas-liquid flow.

In gas-liquid flow model, the liquid phase is treated as a homogenous oil-water mixture flowing with no slippage. In this case, the oil-water mixture is assumed to be a single phase mixture described by the effective mixture properties. The mixture liquid velocity is the sum of superficial velocity of oil and water phase: $U_L = U_O + U_W$. The mixture liquid density is simply calculated as the arithmetic weighted average density of oil and water phases:

$$\rho_L = \rho_o(1 - \varepsilon_w) + \rho_w \varepsilon_w \tag{7.16}$$

Several water-in-oil dispersion pipe flow experiments (Nädler & Mewes, 1997; Angeli & Hewitt, 1998; Elseth, 2001) have shown that the frictional pressure gradient increases monotonically until reaching a maximum value close to the phase inversion point. Pal (1993) suggested that the apparent viscosity of the oil-water mixture can be considerably larger than the viscosity of the respective phases alone. To account for this behavior, the apparent viscosity of the mixture is modeled using Brinkman's relation (Brinkman, 1952), which describes a rise in viscosity as a function of the water cut until it reaches the phase inversion point where the water-in-oil dispersion inverts to oil-in-water dispersion:

$$\mu_L = \mu_o(1 - \varepsilon_w)^{-2.5} \tag{7.17}$$

At the phase inversion, the transition from water-in-oil to oil-in-water dispersion is calculated by an empirical correlation given by Arirachakaran *et al.* (1989):

$$\varepsilon_{inv} = 0.5 - 0.1088 \log_{10}(\mu_o / \mu_w) \tag{7.18}$$

Once the physical properties of the liquid phase have been configured, the gas-liquid flow model can be executed to determine the flow patterns and the flow pattern-specific parameters. As given in Figure 7-6, four main types of flow patterns can be predicted from the model. The local oil-water distribution in the liquid phase of the flow patterns will be evaluated by the three-phase water wetting model in the next step, except for the dispersed-bubble flow pattern which oil wetting is assumed to prevail due to the high liquid velocity.
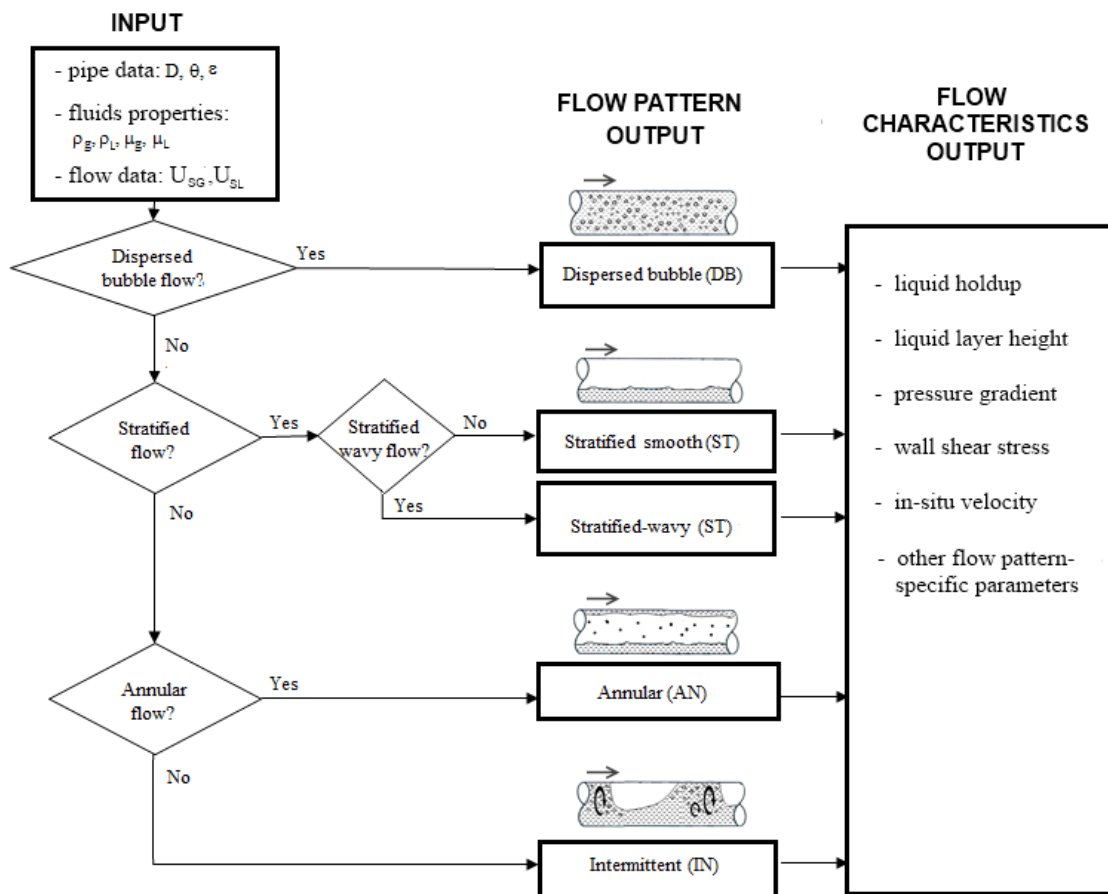
Figure 7-6: Logic flow chart of gas-liquid flow model.
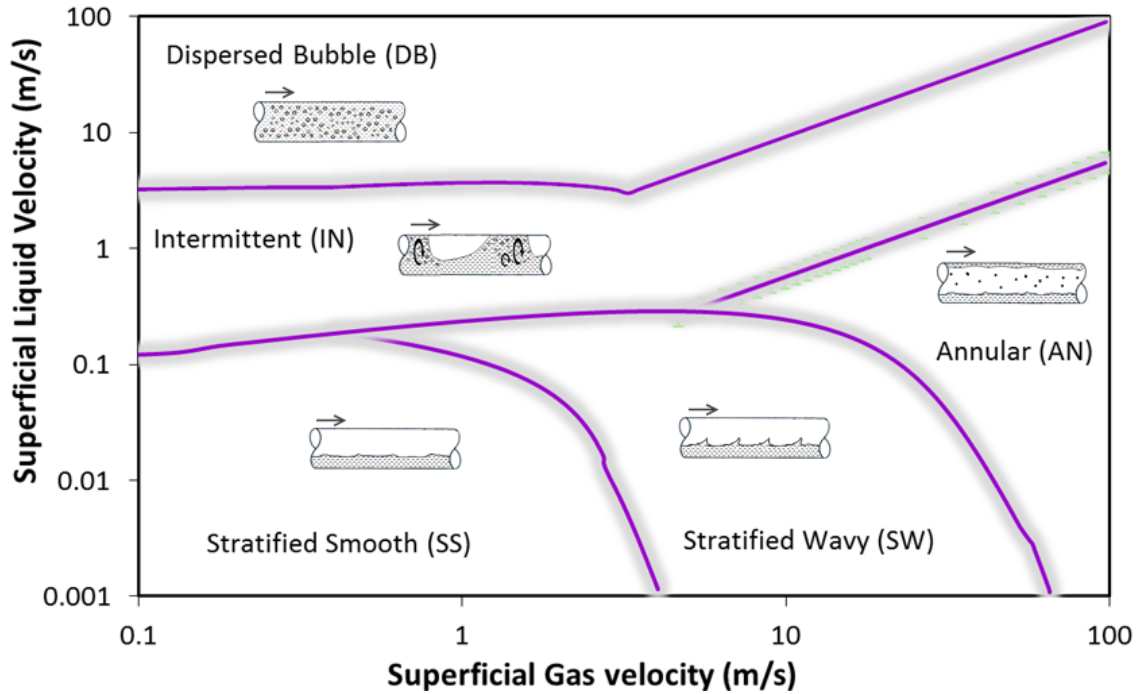
Figure 7-7: Typical air-water flow pattern map in horizontal flow generated by MULTICORP 5.

- Hydraulic Diameter

The concept of hydraulic diameter is customarily used to describe the characteristic length scale for non-circular geometries such as channels. Based on dynamic similarity, the length scale can be used to obtain the friction factor which connects the pressure loss to sinks such as wall, elbows, reducer, and fittings. The generic equation for hydraulic diameter is given as:

$$d_{hyd} = 4 \times \frac{\text{wetted area}, A}{\text{wetted perimeter}, P} \tag{7.19}$$

The concept is applied to the gas-liquid flow which comprises two different immiscible fluids occupying separate areas such as stratified flow (see Figure 7-8). Taitel & Dukler (1976) proposed that the gas phase can be modeled as closed channel flow, whereas the liquid phase as the open channel flow since the gas often moves faster than the liquid phase. The hydraulic diameter for the respective phase has the following form:

$$\text{Gas: } d_G = \frac{4A_G}{S_G + S_i} \qquad \text{Liquid: } d_L = \frac{4A_L}{S_L} \tag{7.20}$$

The above relationship simply means that the interface acts as a sink of energy in the gas phase and as a source of energy in the liquid phase.
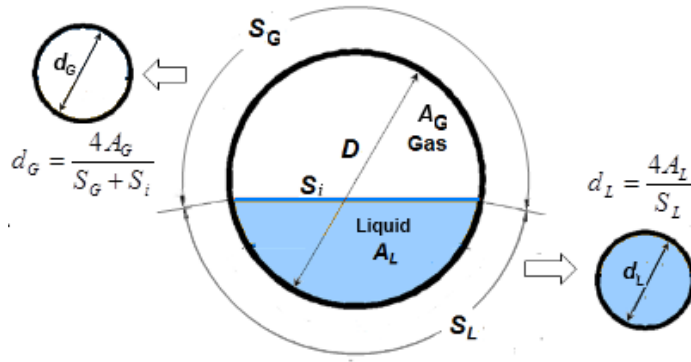
Figure 7-8: Hydraulic diameter for each phase in stratified flow.

In this case, the non-circular wetted area has been transformed to a fully circular pipe with a diameter equivalent to the hydraulic diameter. Then the calculations for wall shear stress in relation to each phase and the interfacial wall shear stress proceed as usual:

$$\tau_G = \frac{f_G \rho_G U_G^2}{2} \qquad \tau_L = \frac{f_L \rho_L U_L^2}{2} \qquad \tau_i = \frac{f_i \rho_G (U_G - U_L)|U_G - U_L|}{2} \tag{7.21}$$

The Fanning friction factor f is given by the Blasius-type correlation as follows:

$$f = C \operatorname{Re}^{-n} \qquad \begin{cases} C = 16, \ n = 1 & \operatorname{Re} \le 2300 \ (\text{Laminar}) \\ C = 0.046, \ n = 0.2 & \operatorname{Re} > 2300 \ (\text{Turbulent}) \end{cases} \tag{7.22}$$

The Reynolds numbers for each phase are calculated using the hydraulic diameter:

$$\operatorname{Re}_G = \frac{\rho_G U_G d_G}{\mu_G} \qquad \operatorname{Re}_L = \frac{\rho_L U_L d_L}{\mu_L} \tag{7.23}$$

Because of the straightforward transformation from physical to characteristic length scale, the choice of using the hydraulic diameter with a non-circular passage has been debated (Obot, 1988; Yilmaz, 1990). The hydraulic diameter concept is much more accurate if the flow is turbulent (Schlichting, 1979). One drawback is that the 'hydraulic' area computed from the hydraulic diameter is numerically smaller than the true wetted area (Muzychka & Yovanovich, 1998). Obot (1988) argued that the mismatch in areas was the cause of the critical Reynolds number (*Re*) discrepancy between the circular and non-circular ducts. It appeared that the critical *Re* increases with increasing aspect ratio of the rectangular duct and diameter ratio of the annular passage.

7.2.3   Configuration in water wetting model

In a pressure-driven turbulent pipe flow containing two immiscible fluids, the frictional pressure gradient is connected to the mean rate of energy dissipation (unit: m^2/s^3) supplied by the turbulent eddies, responsible for the breakup of droplets. As a heuristic approach, the rate of energy dissipation calculated from the gas-liquid model in the previous step is assumed to remain the same in an equivalent pipe, given as a function of the following hydrodynamic parameters:

$$\bar{e} = \left| \frac{dP}{dl} \right|_{fric} \frac{U_c}{\rho_c \varepsilon_c} = \frac{2 f_c \rho_L U_c^3}{d_{fict}} \frac{\rho_L}{\rho_c \varepsilon_c} \tag{7.24}$$

A trial and error scheme is formulated numerically to compute the equivalent fictitious diameter, denoted as d_{fict} with a full pipe flow that retains an identical rate of energy dissipation and pressure gradient. The trial values of d_{fict} are iteratively computed until the equality of Eq. (7.24) is achieved that satisfies the given rate of energy dissipation. The d_{fict} is calibrated such that the droplet breakup process occurring in the wall-bounded full pipe flow is at the same level of turbulence intensity as in the local liquid phase occupied in the gas-liquid flow. This heuristic

approach is implemented before the calculations proceed to the water wetting model as described in Section 7.1.1.

It should be noted that the contribution from the gas-liquid interface is difficult to characterize because of the complex nature of the interface S_i (not always flat) that could influence the energy source/sink terms. For concurrent gas-liquid flow, the momentum is typically transferred from the faster moving gas phase to the slower moving liquid phase through the interface, and then to the wetted wall (energy sink). A more involved method requires the empirical determination of the interfacial geometry that can vary from one to another flow pattern (e.g. stratified or annular flow as S_i changes with liquid holdup).

Once the local liquid phase has been transformed to an equivalent fictitious full pipe, the wetting transition is evaluated by the water wetting model. The idea is that the maximal droplet size resulting from the breakup process can be evaluated based on a local energy balance, equating the rate of turbulent kinetic energy provided by the continuous phase with the rate of surface energy required for forming the droplets in dispersion.

Depending on the type of flow patterns predicted from the gas-liquid flow model, the flow pattern is configured accordingly to the solution framework of the water wetting model in order to determine the local oil-water distribution in the liquid phase. Three types of configuration for flow patterns are described the following sections:

7.2.3.1 Stratified flow

In stratified flow, the two-fluid model (Wallis, 1969; Taitel & Dukler, 1976) is commonly used to calculate the holdup and pressure gradient with reasonable accuracy. One would account for the equations of conservation of mass, momentum and energy for the two-fluid pipe flow model. Here the stratified flow problem is simplified to one-dimensional momentum equations by assuming a simple case of steady state, isothermal flow without mass transfer or chemical

reactions between the immiscible fluids. In the three-phase flow model, the liquid phase is initially assumed as a homogenous oil-water mixture flowing at the same velocity.

The schematic of a stratified flow is given in Figure 7-9. Using the two-fluid model approach, the momentum equations for the respective gas and liquid phase are:

$$\text{Gas:} \qquad -\left(\frac{dP}{dl}\right)_G - \frac{\tau_G S_G}{A_G} - \frac{\tau_i S_i}{A_G} - \rho_G g \sin\theta = 0 \tag{7.25}$$

$$\text{Liquid:} \qquad -\left(\frac{dP}{dl}\right)_L - \frac{\tau_L S_L}{A_L} + \frac{\tau_i S_i}{A_L} - \rho_L g \sin\theta = 0 \tag{7.26}$$

By assuming an equal pressure drop, the combined momentum equations are obtained as:

$$\tau_G \frac{S_G}{A_G} - \tau_L \frac{S_L}{A_L} + \tau_i S_i \left(\frac{1}{A_G} + \frac{1}{A_L}\right) + (\rho_G - \rho_L)g \sin\theta = 0 \tag{7.27}$$

where the subscripts 'G', 'L', 'i' denote gas, liquid and interface respectively, A is the wetted area, S is the wetted perimeter, τ is the wall shear stress, ρ is the density, θ is the angle of inclination from horizontal axis. The relevant geometric parameters are depicted in Figure 7-9. Eq.(7.27) is an implicit nonlinear equation that can be solved numerically for liquid layer height h_L in the pipe, provided that the input superficial velocity, geometrical parameters and closure relations are given. A complete description of the calculation for other parameters can be found from the texts of Shoham & Taitel, (1984); Xiao et al., (1990); Shoham, (2006).

$$X = 1 - \frac{2h_L}{D}$$

$$S_G = D\left(\pi - \cos^{-1} X\right)$$

$$S_L = D\cos^{-1} X \qquad A_G = \frac{D^2}{4}\left(\pi - \cos^{-1} X + X\sqrt{1-X^2}\right)$$

$$S_i = D\sqrt{1-X^2} \qquad A_L = \frac{D^2}{4}\left(\cos^{-1} X - X\sqrt{1-X^2}\right)$$
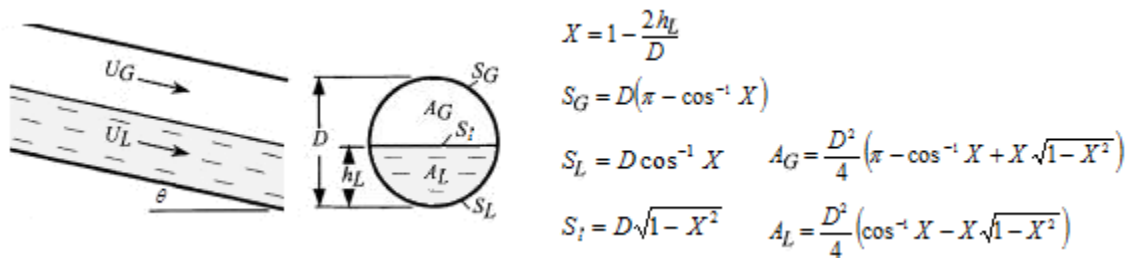
Figure 7-9: Schematics of idealized stratified flow.

For the water wetting model calculation, the frictional pressure gradient term in the stratified liquid phase is sought for the calculation of dissipation energy rate. The frictional term can be determined from Eq.(7.26) as follows:

$$\left(\frac{dP}{dl}\right)_{fric} = -\frac{\tau_L S_L}{A_L} + \frac{\tau_i S_i}{A_L} \tag{7.28}$$

The dissipation energy rate in the stratified liquid layer then follows as:

$$\bar{e} = \left(-\frac{\tau_L S_L}{A_L} + \frac{\tau_i S_i}{A_L}\right)\frac{U_L}{\rho_L} \tag{7.29}$$

7.2.3.2 Annular flow

The schematic of the annular flow is given in Figure 7-10. The annular flow can be solved using the two-fluid model approach in a similar way as the previous case of stratified flow because both flows pattern have phases that are segregated. The liquid phase is assumed to be an oil-water mixture and the annular film has uniform thickness around the pipe periphery.

The momentum balance equations for the gas core and liquid film are written as:

Gas core:
$$-\left(\frac{dP}{dl}\right)_C - \frac{\tau_i S_i}{A_C} - \rho_C g \sin\theta = 0 \tag{7.30}$$

Liquid film:
$$-\left(\frac{dP}{dl}\right)_L - \frac{\tau_L S_L}{A_L} + \frac{\tau_i S_i}{A_L} - \rho_L g \sin\theta = 0 \tag{7.31}$$

The combined momentum equation can be obtained by equating the pressure gradients term in gas core to the one in liquid film, yielding:

$$-\tau_L \frac{S_L}{A_L} + \tau_i S_i\left(\frac{1}{A_C} + \frac{1}{A_L}\right) + (\rho_C - \rho_L)g \sin\theta = 0 \tag{7.32}$$

Eq.(7.32) is the governing equation that can be solved numerically for the liquid film thickness h_L, provided that the input superficial velocity, geometrical parameters and closure relations are provided. A more detailed description of the calculation of the hydrodynamic parameters and closure laws used can be found in the work of Xiao *et al.*, (1990); Alves *et al.* (1991); Gomez *et al.*, (2000).

$$Y = 1 - \frac{2\delta_L}{D}$$

$$S_L = \pi D$$

$$S_i = \pi D Y$$

$$A_c = \frac{\pi D^2}{4} Y^2$$

$$A_L = \frac{\pi D^2}{4}(1 - Y^2)$$
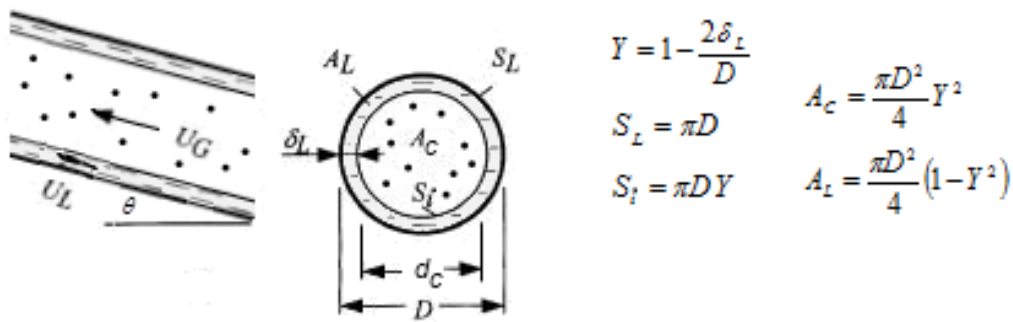
Figure 7-10: Schematics of idealized annular-mist flow.

The frictional pressure gradient term in the liquid film phase can be expressed as:

$$\left(\frac{dP}{dl}\right)_{fric} = -\frac{\tau_L S_L}{A_L} + \frac{\tau_i S_i}{A_L} \tag{7.33}$$

The dissipation energy rate in the stratified liquid layer then follows as:

$$\bar{e} = \left(-\frac{\tau_L S_L}{A_L} + \frac{\tau_i S_i}{A_L}\right)\frac{U_L}{\rho_L} \tag{7.34}$$

In the case of annular flow, the liquid phase flows as a continuous annular film adjacent to pipe wall and also flows as entrained droplets in the gas core. Because the film is typically thin especially on the top and sides of the horizontal tube, it is not a crude approximation to assume that the mixture liquid flows in a small diameter duct. Brauner *et al.*, (1998) proposed that the occurrence of core-annular flow pattern in oil-water systems can be characterized by a

dimensionless parameter: Eotvös number $Eo_D = \Delta\rho g D_{pipe}^2/8\sigma$. For large $Eo_D \gg 1$, the system

corresponds to a gravity dominated flow in a sufficiently large diameter pipe. For small

$Eo_D \ll 1$, the system becomes a surface tension dominated flow where the surface wettability

effect, surface tension σ can start to influence the flow pattern. The annular film can be

considered as a small Eo_D system because of the locally thin film. In the water wetting model, the

transition criterion is obtained by comparing the maximal droplet size d_{max} defined in Eq. (7.3)

with the critical droplet size d_{crit} defined in Eq.(7.5). For flow system with $0.2 < Eo_D < 5$,

Brauner, (2001) suggested when the critical droplet size caused by deformation, d_{CD} exceeds the

pipe diameter, then the only relevant scale for d_{CD} is the pipe diameter and the criterion is

rescaled as $d_{CD} < 0.5 D_{pipe}$. By drawing the same analogy, the d_{CD} is set as half of the film

thickness in annular flow as follows:

$$d_{crit} = MIN\left(\frac{3}{8}\frac{\rho_c}{|\Delta\rho|}\frac{fU_c^2}{g\,\cos\theta}\ ,\ 0.5h_L\right) \tag{7.35}$$

7.2.3.3 Slug flow

Slug flow is a complex intermittent flow due to its unsteady nature and multi-dimensional

flow hydrodynamics. As suggested by Taitel & Barnea (1990), the slug flow structure can be

approximated as a slug unit consisting of two elementary zones: liquid slug body and gas bubble-

liquid film zone as depicted schematically in Figure 7-11. The liquid slug of length L_s is a fast

moving continuous body of liquid that bridges the pipe. The slug front has a turbulent mixing

region that is highly aerated with gas bubbles as it continues to pick up the slower moving liquid

in the film ahead. The gas bubble-liquid film zone of length L_f is a stratified region with a large

gas pocket (Taylor bubble) flowing above a slow moving liquid film similar to the stratified flow

(Dukler & Hubbard, 1975; Taitel & Barnea, 1990).
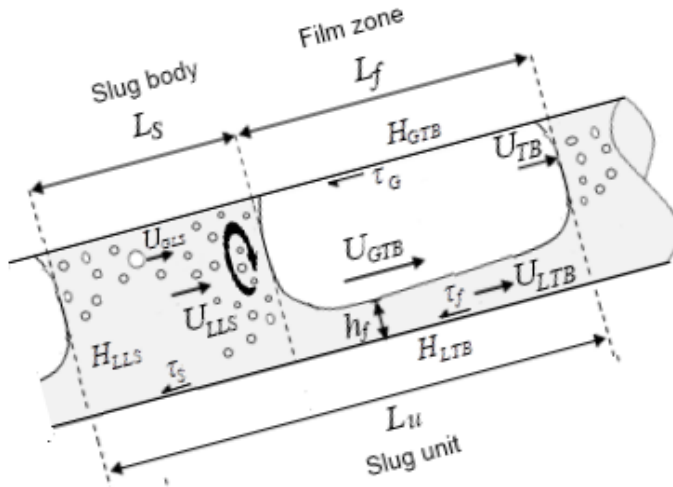
Figure 7-11: Schematics of idealized slug flow with parameters for velocity (U), holdup (H) and wall shear stress (τ).

Based on the experimental slug flow observation, the liquid film zone appears to be the slower moving part from which the water is most likely to drop out and accumulate at the base, leading to water wetting. Therefore the hydrodynamic of the liquid film is considered the worst case scenario for the water wetting calculation.

Following the methodology of Shoham (2006), the force balance over the liquid film zone can be derived from the combined momentum equations by assuming the pressure in the liquid film zone is constant. The final form is formulated as:

$$\rho_L H_{LTB} g \sin\theta = \frac{f_i \rho_G}{2}\left(U_{GTB} + U_{LTB}\right)^2 \frac{S_i}{A} - \frac{f_L \rho_L}{2} U_{LTB}^2 \frac{S_f}{A} \tag{7.36}$$

where interfacial friction faction $f_i = 0.0142$. The geometrical, velocity and holdup parameters can be referred in Figure 7-11.

Eq.(7.36) is an implicit nonlinear equation that can be solved numerically for the film height h_f, provided the geometric parameters and closure relationships are known. More detailed descriptions on the calculation of the hydrodynamic parameters and closure relations can be found in publications by Taitel & Barnea, (1990); Gomez *et al*., (2000); Kaya *et al*., (2001); Shoham, (2006).

Due to the inhomogeneous structure and characteristic intermittency of the slug flow, the axial pressure gradient across the pipe section may vary periodically. Findings suggested that the pressure drop in the liquid film zone is usually much smaller than the liquid slug (Dukler & Hubbard, 1975; Nicholson *et al*., 1978) . A simplified approach for pressure drop calculation is to consider the total pressure gradient for a control volume of a slug unit. Assuming the liquid film flow backward to balances the shear and the pressure remains constant in the bubble region (Taitel & Barnea, 1990), the pressure gradient along the slug unit is formulated as:

$$-\left(\frac{dP}{dl}\right) = \frac{L_f}{L_u}\frac{\left(\tau_f S_f + \tau_G S_G\right)}{A} + \frac{L_S}{L_u}\frac{4\tau_S}{D} + \frac{g\sin\theta}{L_u}\left(L_S\rho_S + L_f\rho_f\right) \tag{7.37}$$

where ρ_f is the average density over the gas bubble-liquid film zone given as:

$$\rho_f = H_{LTB}\rho_L + (1 - H_{LTB})\rho_G \tag{7.38}$$

Similarly, the frictional pressure gradient of the liquid film is taken across the gas bubble/film zone. The term can be written as:

$$\left(\frac{dP}{dl}\right)_{fric} = \frac{L_f}{L_u}\frac{\left(\tau_f S_f + \tau_G S_G\right)}{A} \tag{7.39}$$

The dissipation energy rate in the film zone then follows as:

$$\bar{e} = \frac{L_f}{L_u}\frac{\left(\tau_f S_f + \tau_G S_G\right)}{A}\frac{U_L}{\rho_L} \tag{7.40}$$

7.2.4   Model verifications

A comparison between the experimental results and model prediction will be presented in this section. All the flow pattern and wetting experimental results were obtained from the multiphase flow loop facility at the Institute for Corrosion and Multiphase Technology (ICMT), Ohio University. The horizontal three-phase flow experiments were performed at ambient pressure and temperature (25 °C) in a 0.1 m ID large-scale inclinable multiphase flow loop. The test fluids phase used were model oil LVT200 as the oil phase, 1 wt.% NaCl aqueous solution as the water phase and CO_2 as the gas phase. The properties of test fluids are given Table 3-1. The flow pattern and wetting measurements were performed by fixing the water cut, and changing the liquid and gas velocities for each test series. The tested range of mixture liquid velocity was from 0.2 m/s to 1.5 m/s at fixed water cut of 1%, 5%, 10% and 20%. The tested range of superficial gas velocity was 0.5–40 m/s. Further details on the three-phase flow and wetting experiments can be found in Chapter 4.

7.2.4.1 Flow patterns

Figure 7-12 to Figure 7-15 show the flow pattern maps generated by MULTICORP 5 for 1% three-phase flow data at 1%, 5%, 10% and 20% water cuts. The three-phase data were converted into equivalent gas-liquid data by assuming the liquid phase to be a homogenous oil-water mixture. The maps were produced for three-phase flow data by plotting the superficial gas velocity in x-axis and the mixture liquid velocity in y-axis. The flow transition boundaries (purple lines) were drawn in the map to define the flow patterns that could physically exist which include dispersed bubble (DB), intermittent (IN), stratified (ST) and annular (AN) flows. It should be noted the transition boundary is not a hard line, as the flow often transitions progressively from one pattern to another.

The flow pattern data plotted in the flow maps (Figure 7-12 to Figure 7-15) show that most data are in the intermittent flow region while some data points fall in the annular and stratified flows. The elongated bubble and slug flows were considered as the intermittent flow, while the wavy annular was considered as an unstable annular flow. Upon comparisons, the results matched well the model predictions considering the simplification of the model. Some disagreements were found for data close to the transition lines, and can be explained by the uncertainties of the predicted transition lines. The overall flow pattern prediction performance is given in Table 7-1.

Table 7-1: Flow pattern prediction by MULTICORP 5

Flow pattern	Total cases	Good prediction (%)
Intermittent	102	86%
Annular	41	95%
Total	143	91%
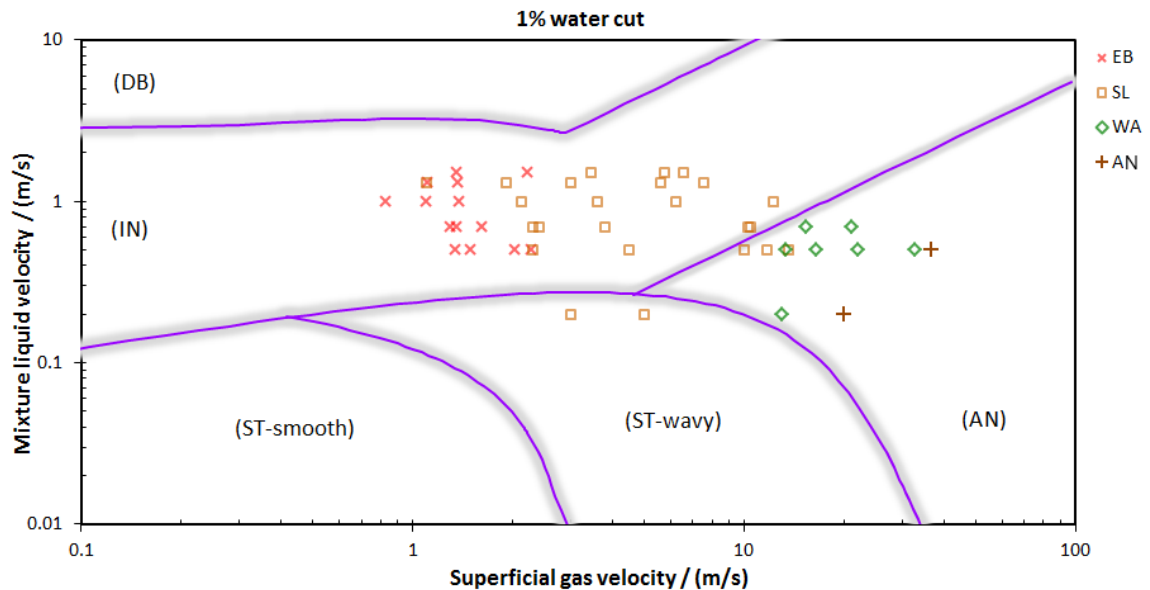
Figure 7-12: Comparison of horizontal three-phase flow pattern results with WW model at 1% water cut for CO_2-LVT200-water system.
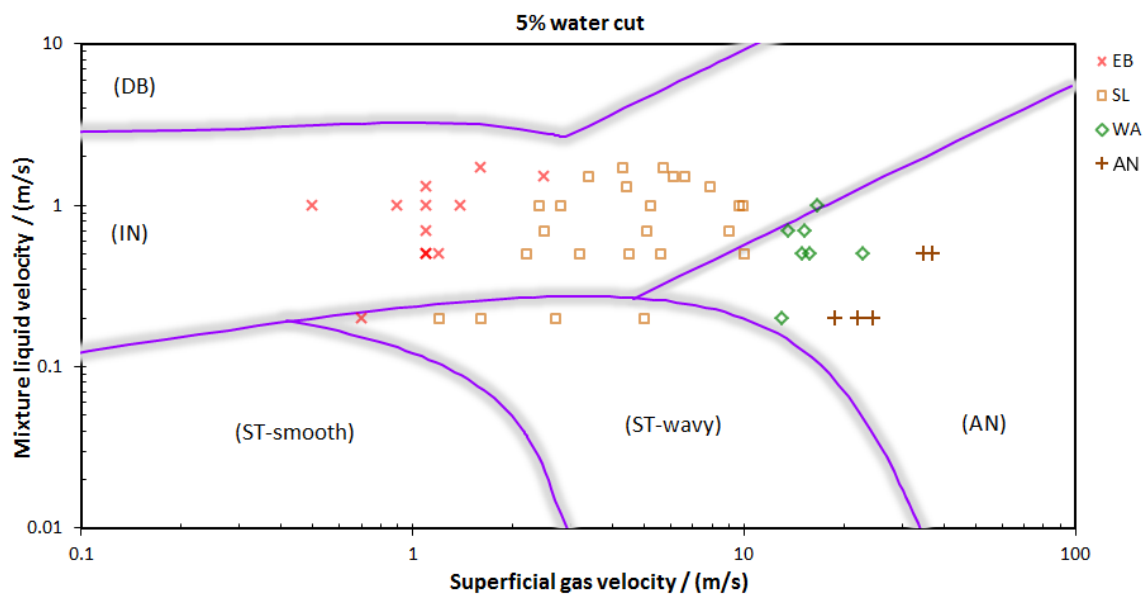
Figure 7-13: Comparison of horizontal three-phase flow pattern results with WW model at 5% water cut for CO_2-LVT200-water system.
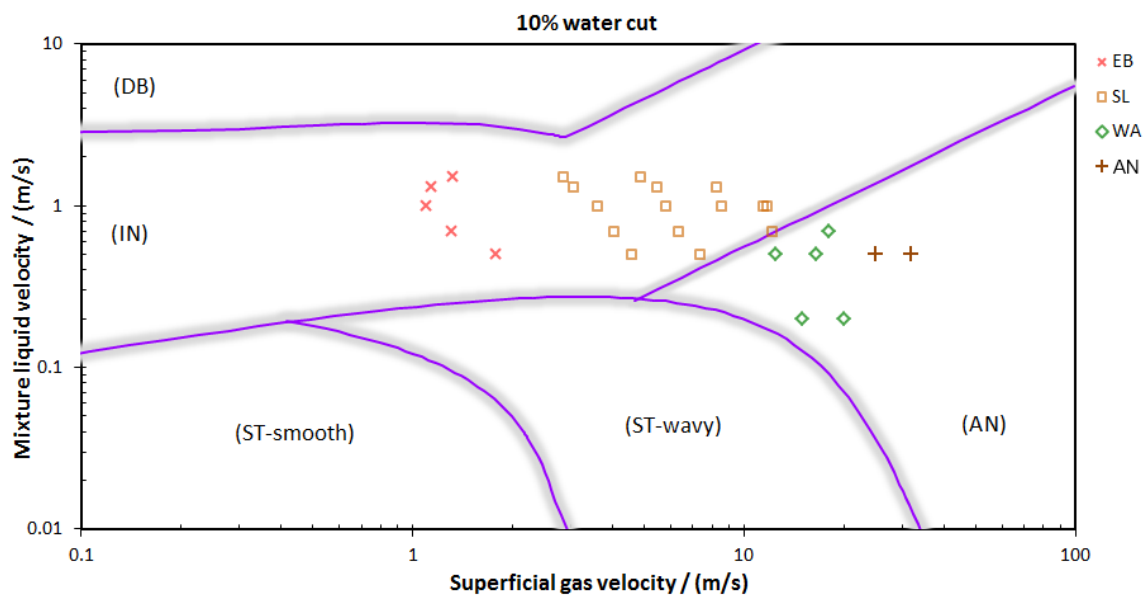
Figure 7-14: Comparison of horizontal three-phase flow pattern results with WW model at 10% water cut for CO_2-LVT200-water system.
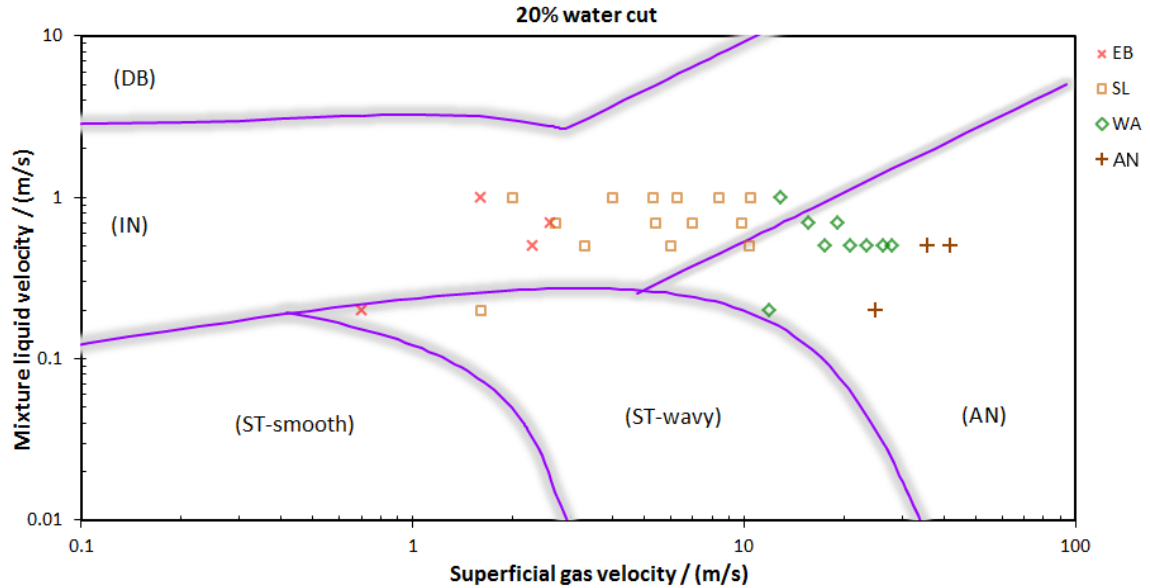
Figure 7-15: Comparison of horizontal three-phase flow pattern results with WW model at 20% water cut for CO_2-LVT200-water system.

7.2.4.2 Surface wetting

The surface wetting data measured from the flow experiments were plotted in the wetting map to indicate two types of surface wetting conditions: oil wetting or water wetting. The oil wetting condition includes stable oil wet and unstable oil wet, while the water wetting condition includes stable water wet and unstable water wet. As the wetting data were water cut and flow pattern specific, they were analyzed and presented according to the water cut (1% to 20%) as well as the type of flow patterns that they came to resemble. The flow patterns were stratified, annular and intermittent flows. In this way, the effects of water cut and flow patterns on surface wetting conditions can be analyzed and compared accordingly.

The three-phase water wetting model was programmed and executed to make comparisons with the experimental wetting results. By simulating the flow pattern test data according to the given water cut and fluid velocities, a wetting transition line can be produced for each case of intermittent and annular flow patterns and drawn on the flow map to indicate the delineation

between the water wetting (left or bottom side of the line) and oil wetting (right or top side of the line) under the given conditions.

Figure 7-16 shows the comparison for three-phase stratified flow at 1% to 5% water cut. The model predicts water wetting (indicated as blue shaded region) which was in agreement with the measured wetting data. Figure 7-17 to Figure 7-20 present the wetting result comparisons for three-phase slug flow from 1% to 20% water cuts. The wetting region is demarcated by a wetting transition line, showing water wetting (blue shaded region) to the left and oil wetting (red shaded region) to the right of the wetting transition line. From the graphs, the wetting transition lines are seen to shift rightward to higher gas velocity ranges with increasing water cuts which means the propensity for water wetting increases. For 1% and 5% water cuts, the predicted results by the model in slug flow were rather conservative, as it predicted water wetting prevailing up to higher gas velocity ($V_{SG} \sim$ 10 m/s for 1% water cut and $V_{SG} \sim$ 14 m/s for 5% water cut). The discrepancy can be attributed to the conservative assumption made in the model, by configuring the gas bubble/liquid film zone as the calculation basis for local oil-water distribution. For higher water cuts of 10% to 20%, the transition line was at higher gas velocity ($V_{SG}=$ 17 m/s for 10% water cut, $V_{SG}=$ 22 m/s for 20% water cut). The model prediction was in agreement with the measured data.

Figure 7-21 to Figure 7-24 present the wetting results comparisons for the three-phase annular flow. Similarly, the wetting region is demarcated by a wetting transition line, showing water wetting (blue shaded region) above and oil wetting (red shaded region) below the wetting transition line. From the graphs, the wetting transition lines are seen to shift upward as the water cut is increased. For 1% and 5% water cuts, the model predicts oil wetting condition is dominant if the mixture liquid velocities $V_m \leq$ 0.1 m/s for 1% water cut and $V_m \leq$ 0.15 m/s for 5% water cut, respectively. The predicted data show good agreement to the measured wetting data. For higher water cuts at 10% to 20%, oil wetting is predicted to prevail when the mixture liquid velocity $V_m \leq$ 0.3 m/s for 10% water cut, and $V_m \leq$ 0.5 m/s for 20% water cut, respectively. Upon

comparison with the wetting results, the model behaves rather less conservatively for the data close to the wetting transition, as it tends to predict oil wet at higher mixture liquid velocity.
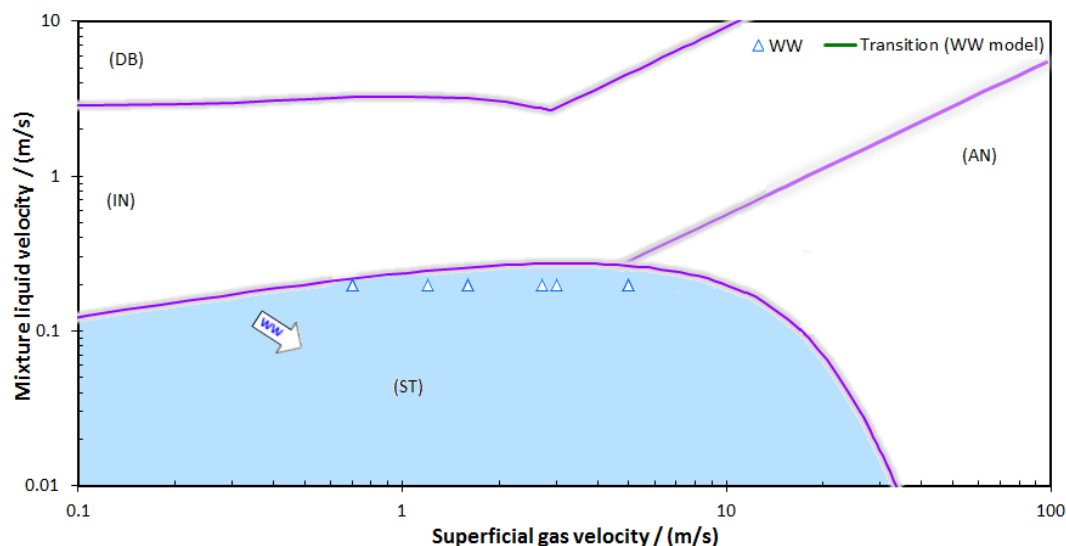
Figure 7-16: Comparison of surface wetting results with WW model in three-phase stratified flow at 1%-5% water cuts.
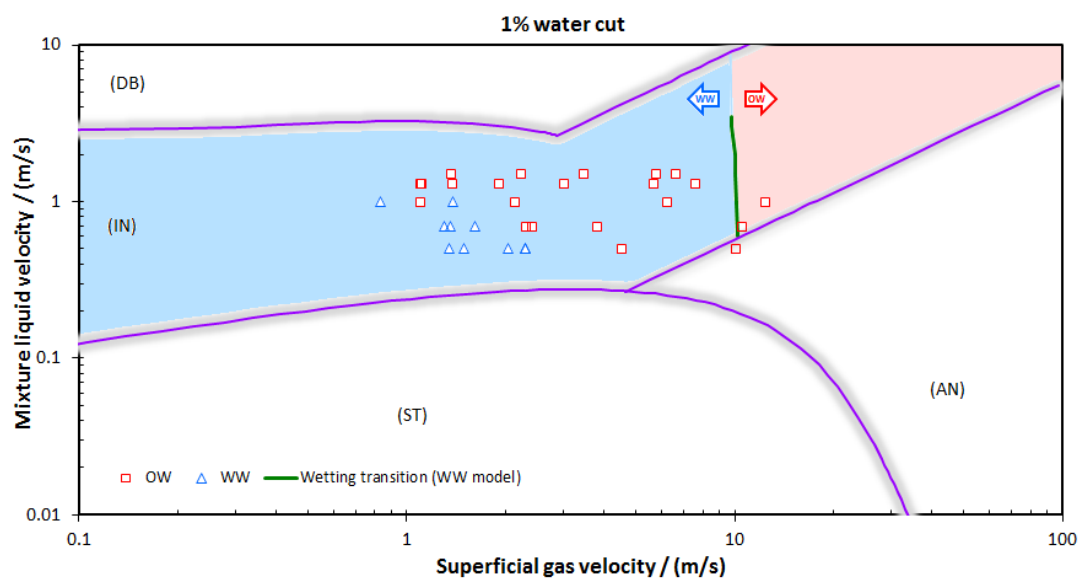
Figure 7-17: Comparison of surface wetting results with WW model in three-phase slug flow at 1% water cut.
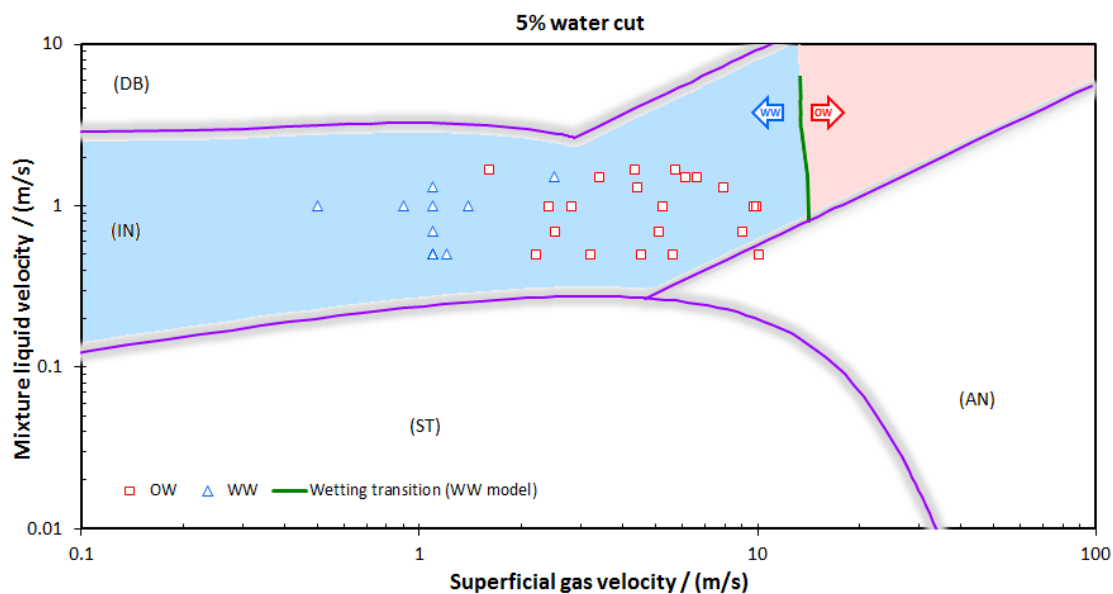
Figure 7-18: Comparison of surface wetting results with WW model in three-phase slug flow at 5% water cut.
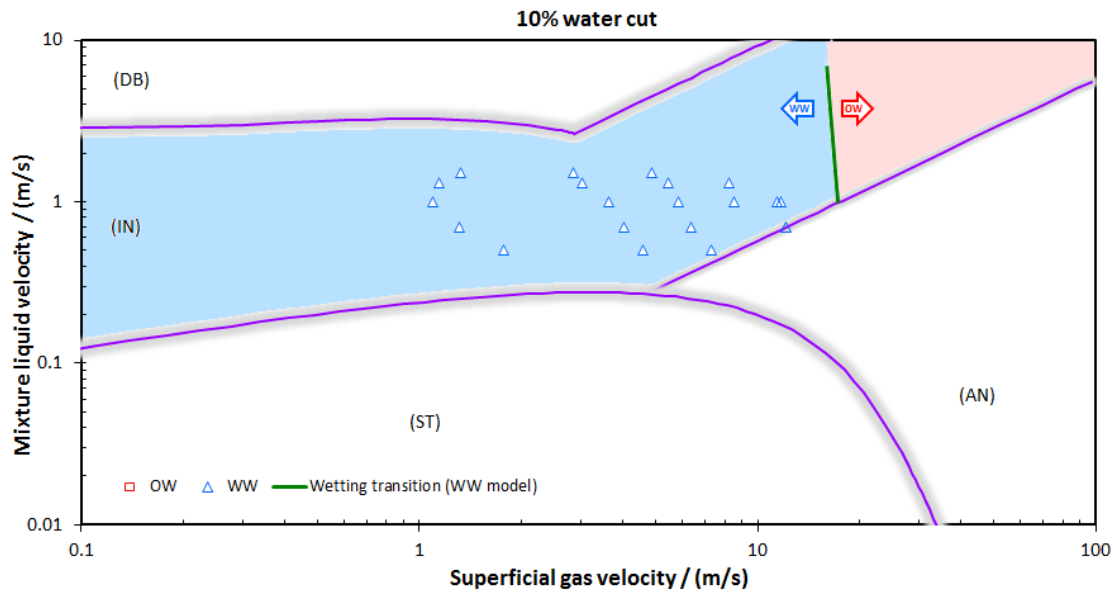
Figure 7-19: Comparison of surface wetting results with WW model in three-phase slug flow at 10% water cut.
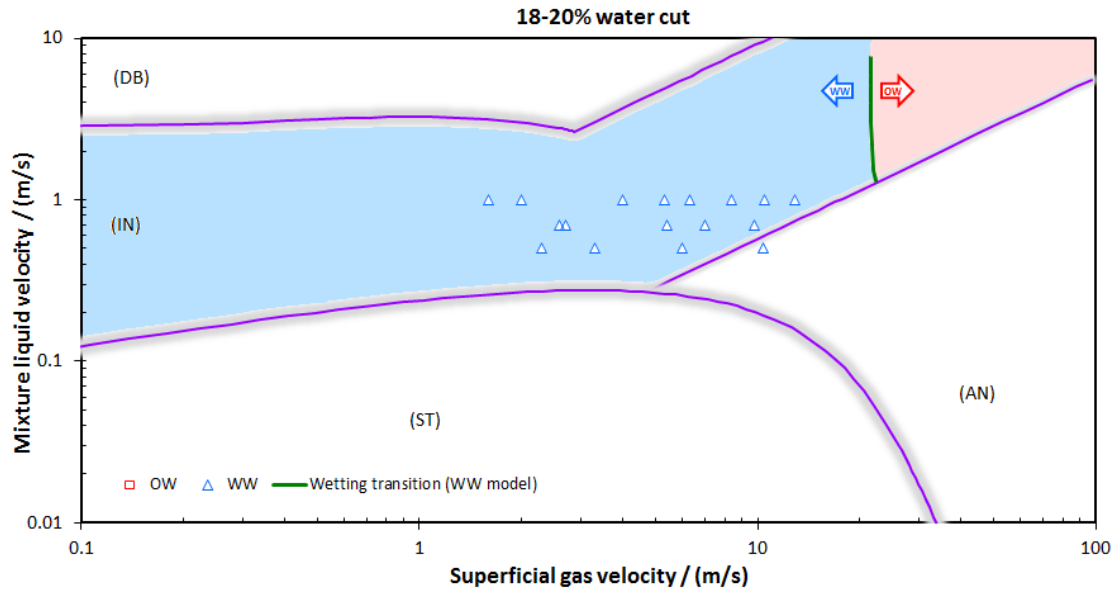
Figure 7-20: Comparison of surface wetting results with WW model in three-phase slug flow at 18% - 20% water cut.
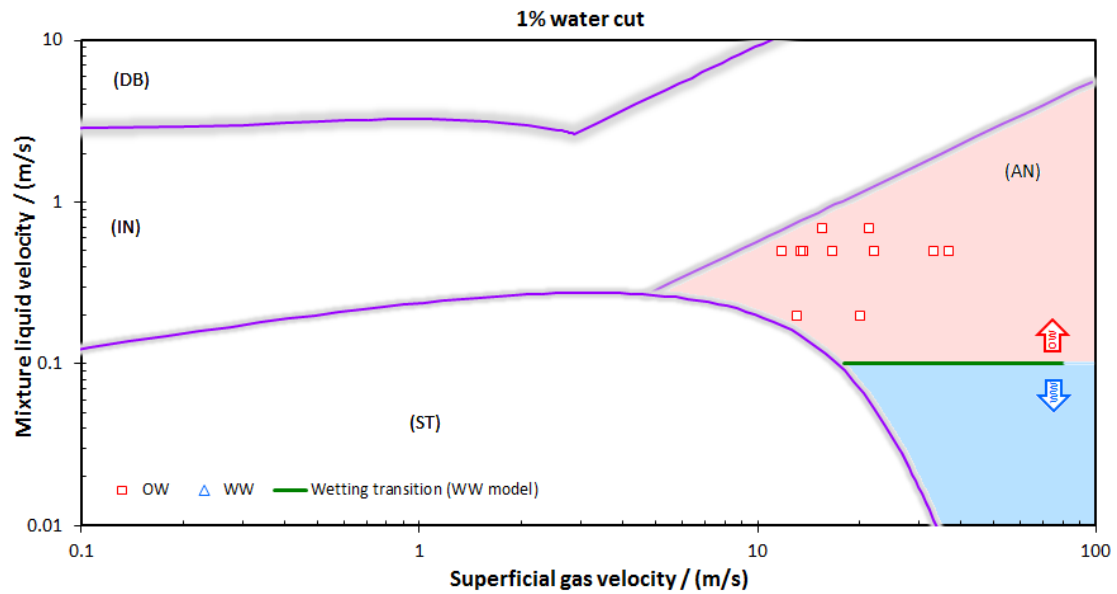
Figure 7-21: Comparison of surface wetting results with WW model in three-phase annular flow at 1% water cut.
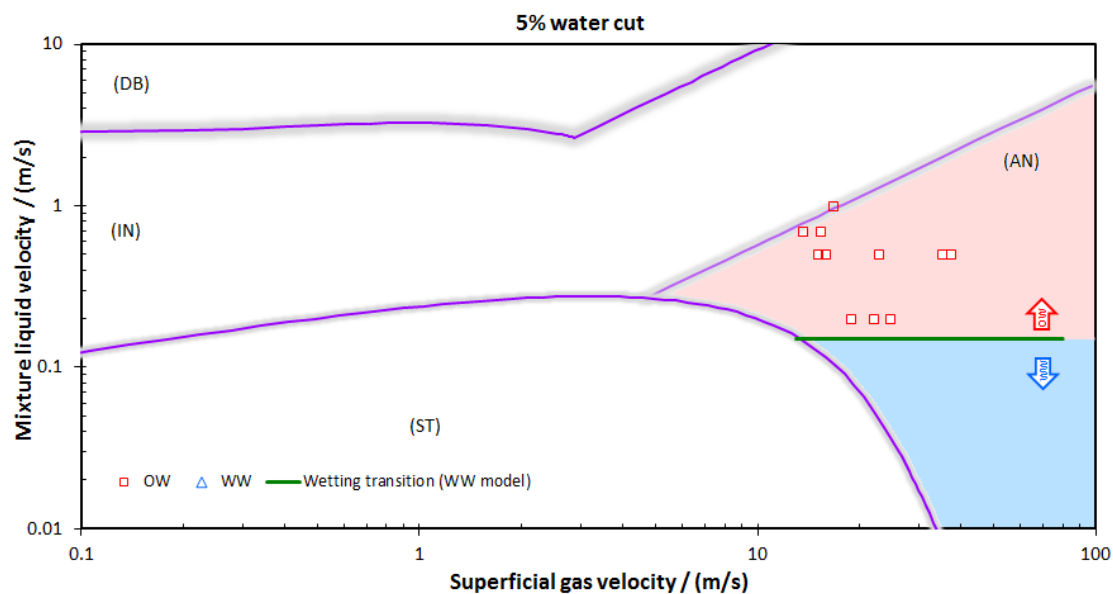
Figure 7-22: Comparison of surface wetting results with WW model in three-phase annular flow at 5% water cut.
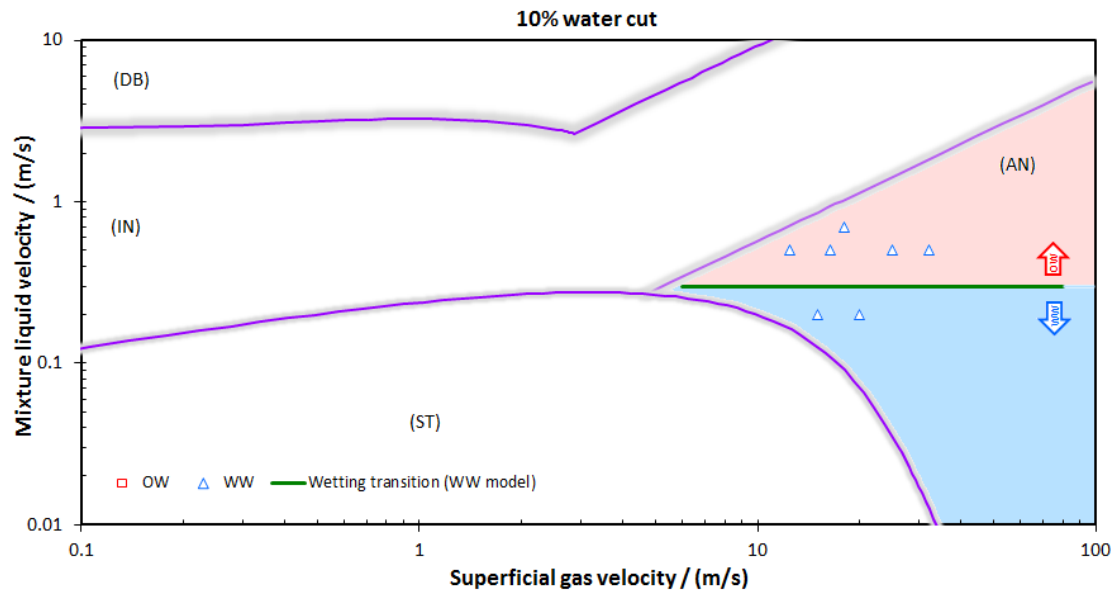
Figure 7-23: Comparison of surface wetting results with WW model in three-phase annular flow at 10% water cut.
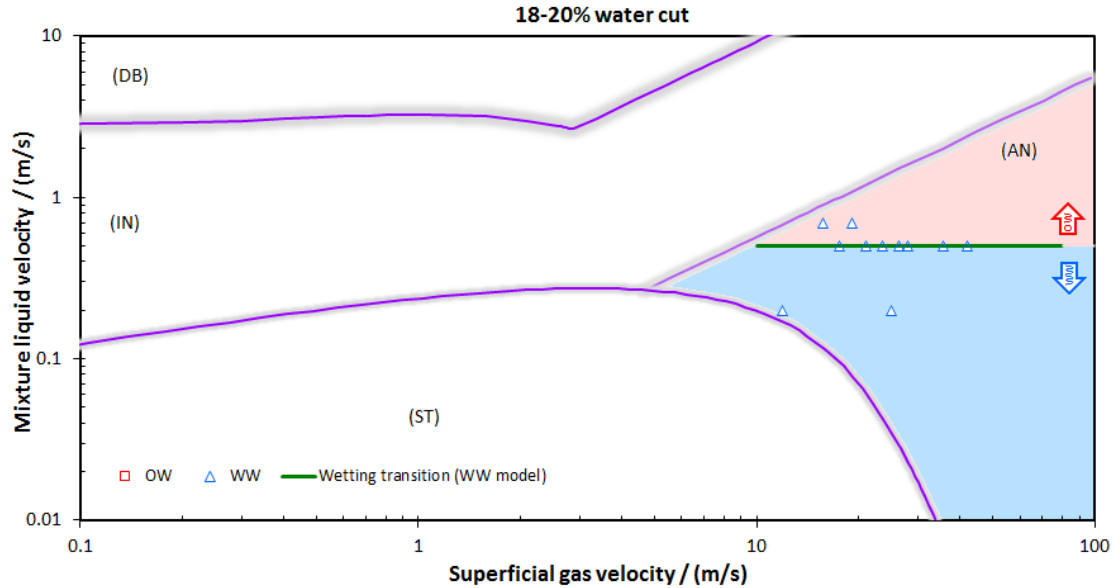
Figure 7-24: Comparison of surface wetting results with WW model in three-phase annular flow at 18%-20% water cuts.

7.2.5 Sensitivity analyses

Sensitivity analyses were performed for four different parameters: oil viscosity, oil density, oil-water interfacial tension and pipe diameter in order to study the effect of these parameters on the overall three-phase wetting behavior. These simulated parameters were compared with the 'baseline' condition, which was the experimental condition used in the present flow loop work as follows: horizontal pipe ID = 0.1 m, oil viscosity μ_o = 2.7 cP, oil density ρ_o = 823 kg/m^3, oil-water interfacial tension σ = 0.04 N/m. By varying the test parameters one at a time, while maintaining the other parameters constant, the wetting transition lines for the simulated and baseline cases can be plotted and shown in Figure 7-25 to Figure 7-28.

The effects of changing the oil viscosity from the baseline value of μ_o = 2.7 cP to 30 cP at varying water cuts are represented by the change of wetting transition lines plotted in flow pattern maps in Figure 7-25(a) for 1% water cut and (b) for 20% water cut. With higher oil viscosity, the

intermittent and annular flow regions appear to enlarge at the expense of the stratified flow region as indicated by the flow transition boundary lines (solid purple lines). The wetting transition lines at baseline and simulated viscosity of 30 cP are plotted for intermittent and annular flow regions in the graph. The left or bottom side of the transition line indicates water wetting (blue color region), while the right or top side of the transition line indicates oil wetting (red color region). In intermittent flow, the wetting transition lines are not sensitive to the change of oil viscosity. In annular flow, the transition lines appear to shift down as the oil viscosity is increased. As reported by Cai *et al.* (2012) in oil-water flow, viscous oil tends to entrain water more effectively than the less viscous oil. As depicted in Figure 7-25(a) and (b), an increase in water cut has an effect of shifting the transition lines rightward and upward, leading to an enlarged region of water wetting and a reduced region of oil wetting. This is in accordance to the fact that higher mixture liquid and gas velocities are required to fully disperse the water.

Figure 7-26(a) and (b) shows the effects of increasing the oil density from the baseline $\rho_o = 823$ kg/m^3 to 950 kg/m^3 on the wetting transition lines at 1% and 20% water cuts. The flow transition boundary lines are not affected by the change in oil density. In intermittent flow, the wetting transition lines at 1% and 20% water cuts shift leftward as the oil density increases, making it easier to entrain the water since the density difference between oil and water phases is small. In annular flow, the wetting transition lines do not appear to be significantly affected by the change in oil density. With an increase of water cut, the wetting transition lines move rightward and upward to envelop a smaller region of oil wetting.

Figure 7-27(a) and (b) shows the effect of decreasing the oil-water interfacial tension from the baseline $\sigma = 0.04$ N/m to 0.01 N/m on the wetting transitions lines at 1% and 20% water cuts. The model simulation shows that the flow transition is not influenced by the change in interfacial tension. For both intermittent and annular flows, the wetting transition lines simulated at 1% and 20% water cuts shift leftward (in intermittent flow) and downward (in annular flow) as the

interfacial tension is reduced, making it easier for the occurrence of oil wetting since the surface energy barrier between the oil and water phases diminishes. By increasing the water cut, the wetting transition lines move to higher liquid and gas velocities.

Figure 7-28(a) and (b) show the effect of increasing the pipe diameter from the baseline ID = 0.1 m to 0.3 m. With higher pipe diameter, the stratified flow region appears to expand at the expense of the intermittent and annular flow regions as the oil and water phases separate more easily. In intermittent flow, the simulated wetting transition lines moves to the right, resulting in an increased likelihood of water wetting as the pipe diameter increases. In annular flow, the predicted wetting transition lines do not vary much but higher range of gas velocity is required to entrain the water. Similar to previous cases, an increase of water cut causes the region of water wetting to expand as bounded by the wetting transition lines.
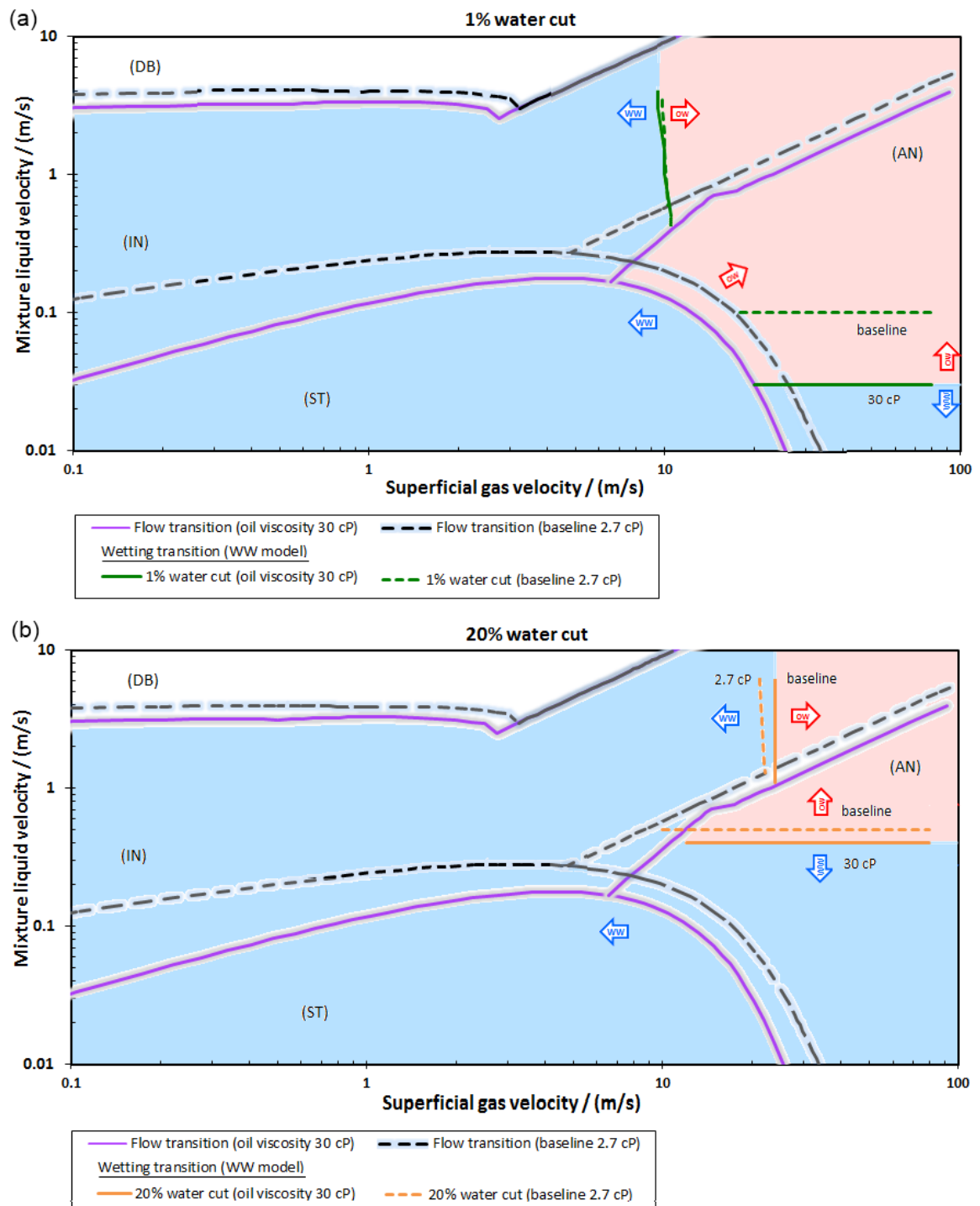
Figure 7-25: Sensitivity analysis of predicted wetting transitions for oil viscosity μ_o = 30 cP deviated from the baseline oil viscosity of 2.7 cP at (a) 1% water cut and (b) 20% water cut.
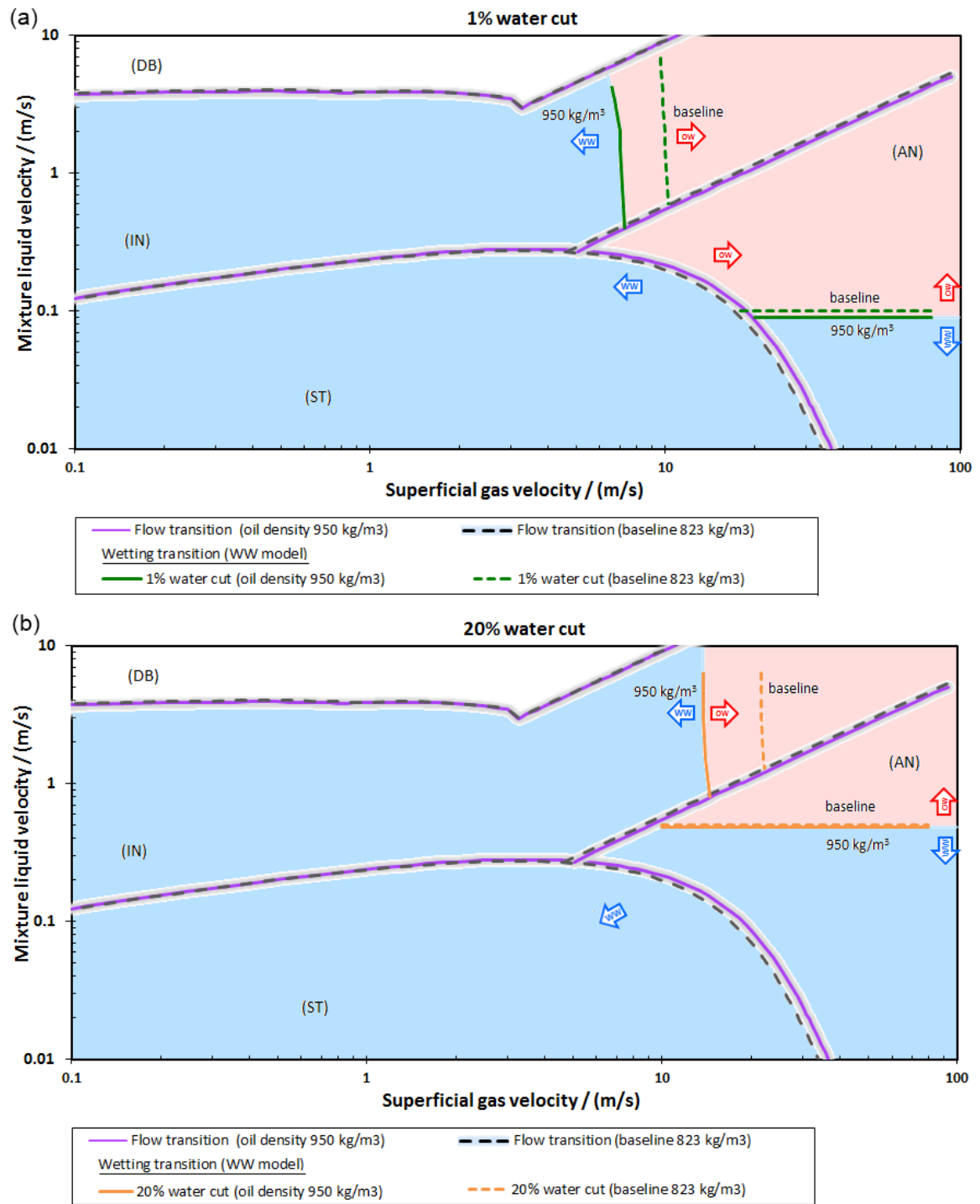
Figure 7-26: Sensitivity analysis of predicted wetting transitions for oil density $\rho_o = 950$ kg/m³ deviated from the baseline density of 823 kg/m³ at (a) 1% water cut and (b) 20% water cut.
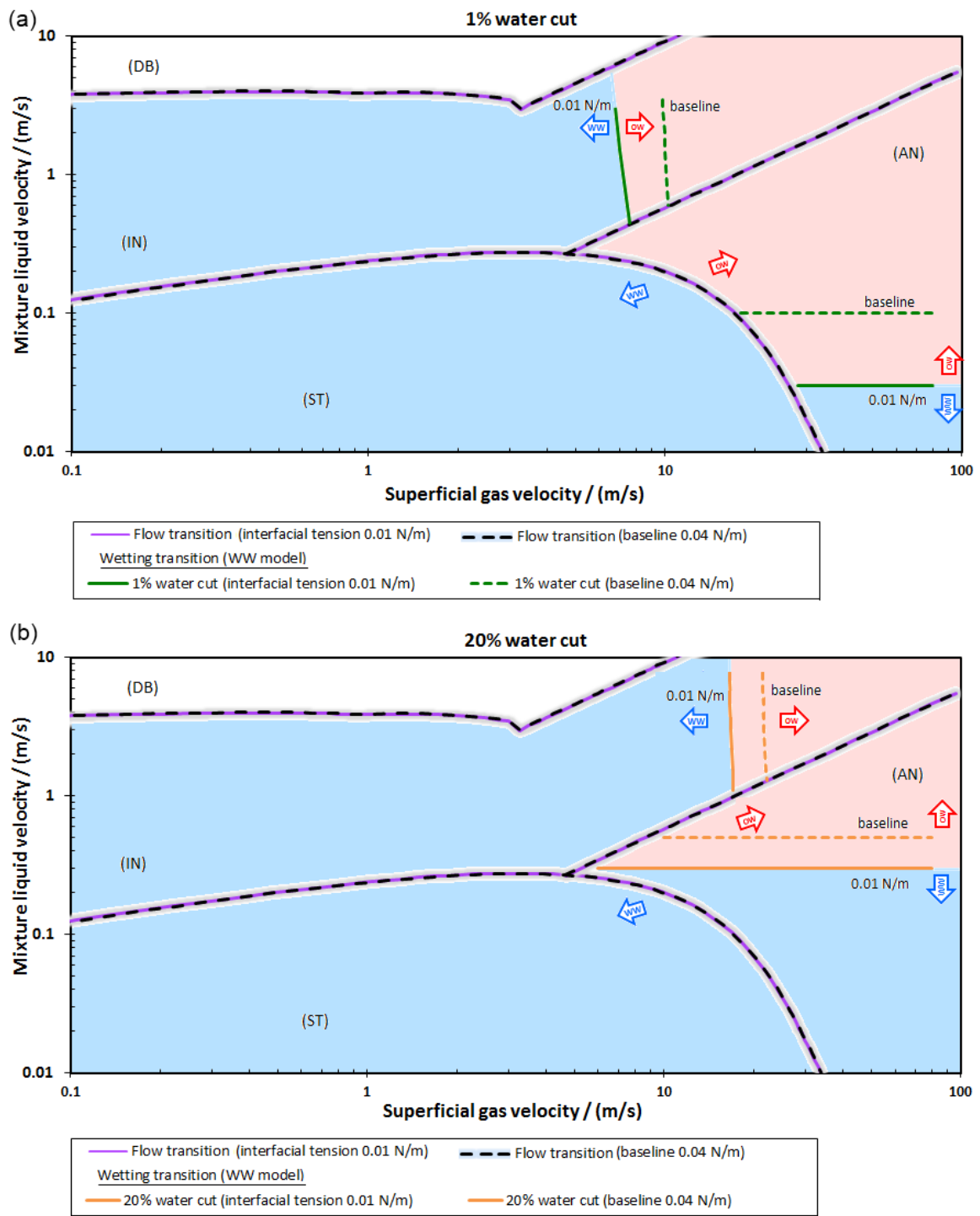
Figure 7-27: Sensitivity analysis of predicted wetting transitions for interfacial tension σ = 0.01 N/m deviated from the baseline interfacial tension of 0.04 N/m at (a) 1% water cut and (b) 20% water cut.
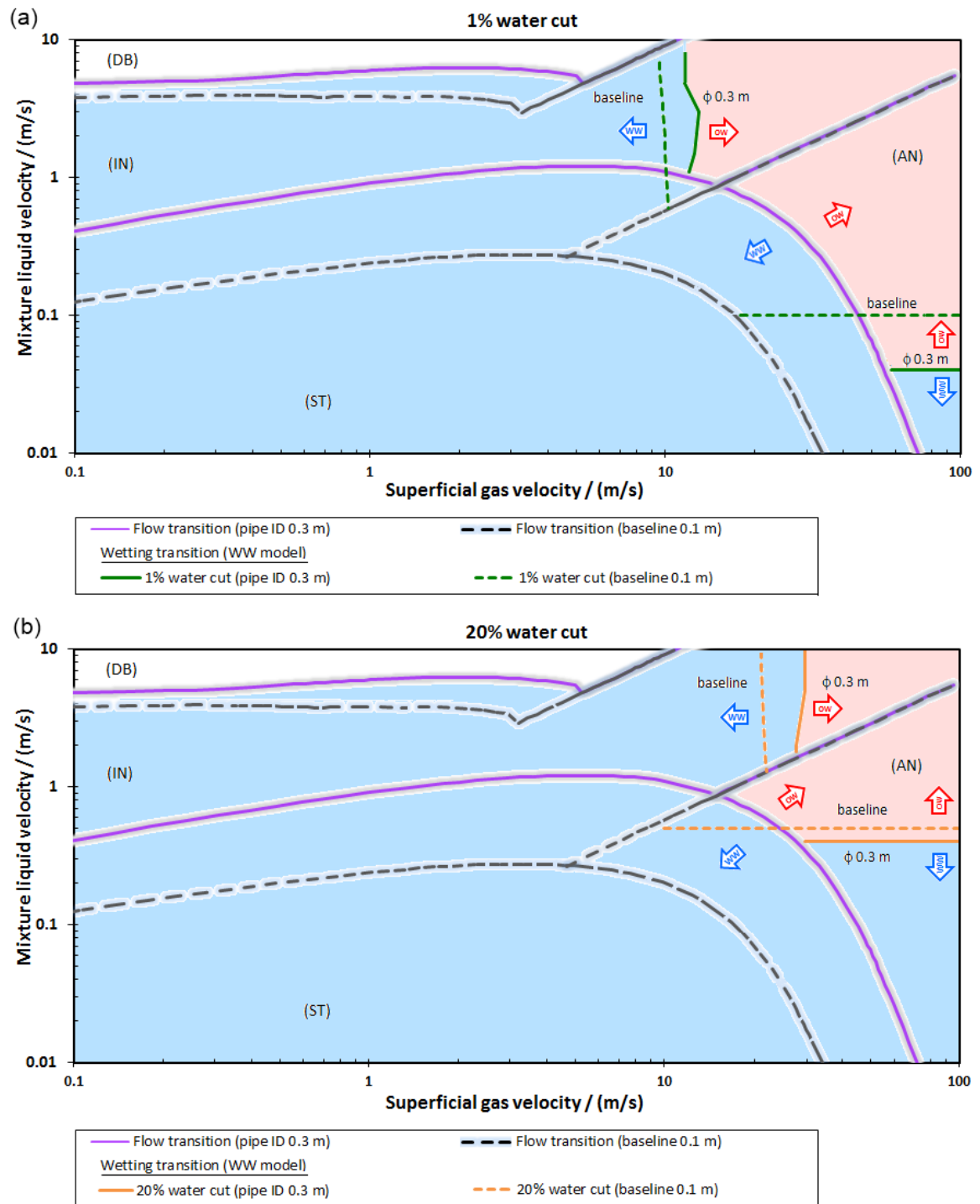
Figure 7-28: Sensitivity analysis of predicted wetting transitions for pipe ID = 0.3 m deviated from the baseline ID of 0.1 m at (a) 1% water cut and (b) 20% water cut.

7.2.6   Model context and limitations

The present model was built from the framework of gas-liquid hydrodynamic model and oil-water model. By comparing the model predictions with the experimental wetting data, the model showed a reasonably good agreement for annular flow at low water cuts (1% and 5%) and for intermittent flow at high water cuts (10% and 20%). However less-than-optimal agreements were reported for the annular flow at high water cut (10% and 20%) and the intermittent flow at low water cut (1% and 5%). While correction factor can be calibrated for the model to improve the predictions for the less-than-optimum cases, questions still remain over the actual mechanisms that dictate the wetting behavior in three-phase flow environment. By analyzing the performance of the present model, the following limitations have been identified:

- The main premise of the wetting model is that the turbulent kinetic energy generated in the oil phase is expended to overcome the surface energy and break out the water droplets. For the case of oil-water flow, an average value of turbulent energy can be assumed for oil-water flow in steady state. However, the same may not hold true for three-phase flow environment where the flow can be chaotic and intermittent. The detailed accounting of the turbulent energy in the local liquid phase requires modeling of complex interaction between the gas and liquid phases, which can be time and space dependent. The calculation of the turbulent energy is connected to the pressure gradient and rate of energy dissipation.

- Hydrodynamic equations used in the gas-liquid flow model are developed for turbulent transport in each fluid phase. Closure relation is then used to predict the shear at the interface. Finally, the results of the hydrodynamics parameters are input to the oil-water model to predict the wetting behavior in the local liquid phase. Hence, the prediction of the wetting model is highly dependent upon the accuracy of the closure relations used in the gas-liquid flow model as the estimation of the pressure gradient is related to the shear stress. .

- In the present model, the oil and water phases are assumed as a homogenous liquid mixture flowing without slippage in an equivalent full pipe diameter, retaining a similar level of energy dissipation rate. It is yet to prove experimentally the concept of equivalent diameter, considering the complex nature of the deformable gas-liquid interface. This warrants further investigation to test out the assumption.

- The model is valid for oil-continuous flow up to 20% water cut. As water cut increases, the liquid mixture properties may behave differently and other mechanisms may become dominant when approaching the phase inversion point.

- In slug flow, the flow structure is assumed as a slug unit consisting of a liquid slug and a gas bubble/liquid film zone. The wetting predictions for slug flow tend to be more conservative as the oil-water model calculation is applied to the liquid film zone, in which the oil and water phase are likely in separation.

- The liquid phases are hypothetically assumed as a homogenous oil-water mixture with mixture density and viscosity. However the liquids might mix inhomogenously when the flow is highly intermittent as in slug flow where the flow mixes more intensely at the slug front and slow down at the liquid film zone.

- In horizontal annular flow, a uniform liquid film is assumed in the model which in reality the liquid film is distributed asymmetrically. The geometry mismatch may impact the correct prediction of the pressure gradient and energy dissipation rate.

- The present model does not take into consideration the steel surface wettability which can be important when the liquid layer moves adjacent to the wall as in annular flow. The model also does not consider droplet coalescence which can be dominant when the droplet population is crowded at high water cut. As reported by Coulaloglou & Tavlarides (1977), the crowding of

droplets may lead to a "dampening" effect on the local turbulent intensities at high fraction of the dispersed phase.

It is desirable to acquire more wetting data using different fluids to check the validity of the model, but there are no other published data available at present. While there is no other workable model for predicting the wetting behavior in three-phase flow, the present model can be used as a preliminary predictive tool which can be further enhanced as new analytical insight uncovered.

7.3 Summary

- A three-phase water wetting model integrated with the multiphase flow model and two-phase water wetting has been developed and implemented

- The model can predict the wetting state at a given flow condition and the critical entrainment velocity required to entrain the water phase by the flowing bulk oil phase.

- The model has been compared with the experimental wetting data on three types of flow pattern. In stratified flow, the model predictions matched with the experimental data. In slug flow, the predicted results agreed with the wetting data at water cut > 10%, but rather conservative in low water cut <10%. In annular flow, the predicted results agreed well with the wetting data at low water cut <10%. Discrepancies were found when compared with wetting data at high water cut >10%.

CHAPTER 8: CONCLUSIONS AND RECOMMENDATIONS

8.1 Conclusions

A comprehensive experimental study has been carried out to investigate the flow patterns and water wetting phenomena in oil-water flow and gas-oil-water flow systems. The experimental work was carried in a large-diameter 0.1 m ID inclinable flow loop. Horizontal and vertical flow experiments were tested using light model oil LVT200 as the oil phase, 1% aqueous NaCl as the water phase and CO_2 as the gas phase. The main findings are summarized as follows:

- The present study focuses on oil-dominated flow with water cuts up to 20%. Five types of horizontal oil-water flow patterns and two types of vertical oil-water flow patterns were observed in the experiments.

- The use of conductivity pins was instrumental in detecting the surface wetting on the pipe wall. The surface wetting behavior can be categorized into four types of wetting regimes depending on the intermittency or persistency of the wetting behavior as measured by the conductivity pins. The visualization of droplet interactions in the flow field by a high speed camera confirms the surface wetting behavior.

- In horizontal oil-water flow, the increase of liquid mixture velocity provides more turbulence breaking forces that split and disperse the water droplets, whereas the increase of water cuts promotes the coalescence of water droplets that drop onto the pipe bottom.

- The degree of dispersion depends on the interplay of liquid mixture velocity and water cuts. Unstable wetting is largely caused by the water droplets that momentarily settle and touch the pipe wall.

- By using model oil LVT200, a light oil (API °40), with no surface active substance, the wetting results was predominantly water wet. This is largely due to the high density and low

viscosity differences between the oil and water phases, leading to a separation of phases. In addition, steel pipe is hydrophilic by nature, such that water preferentially adheres to it.

- For vertical oil-water flow, the wetting is predominantly oil wet, as evidenced by the flow of dispersed droplet in a relatively straight path. Changes in liquid velocities do not appear to greatly affect the surface wetting. Unstable water wetting was observed to be caused by the crowding of water droplets near the wall at high water cuts.

- The Sauter mean diameter (SMD) of the water droplet reduces with liquid velocity due to higher turbulent breakage forces. The SMD at 1% water cut is smaller than that at 5% water cut. The size difference diminishes as the liquid velocity increases.

- In horizontal gas-oil-water flow, surface wetting was investigated for three major types of flow patterns: stratified, slug and annular-mist flows. For water cut ≤ 5%, the wetting results showed that adding the gas phase provides adequate turbulence for the oil phase to entrain water, leading to oil wetting. For water cut ≥10%, the water wetting prevailed and adding gas did not lessen the intensity of water wetting. The water wetted area was observed to spread up on both sides of the wall.

- In vertical gas-oil-water flow, unstable oil wetting was observed at 1% water cut both in churn and annular flows. The behavior changed to predominantly water wetting at higher water cut >1%. The increase in gas velocity greatly enhanced the intensity of water wetting, by pushing the liquid film closer to the wall, thus extending the water wetted area over the entire pipe circumference.

- ERT and ECT were used to study the cross sectional phase distribution within the pipeline. ERT can detect water at high water cut if there was water separation at pipe bottom. ERT lost sensitivity if the separated water level was too low or water droplets were flowing at the pipe bottom. ECT can be used to differentiate the flow patterns for two-phase and three-phase

flow systems containing gas, by identifying the characteristic features in phase fraction variations and intermittency associated with each flow pattern.

- A new three-phase water wetting model integrated with the gas-liquid flow model and two-phase water wetting model has been proposed. The model has been validated with the experimental data for three types of flow patterns.

8.2 Recommendations for future work

There are two important elements, namely hydrodynamics and wetting, in the development of three-phase wetting model. Future work should further explore these aspects in terms of experimental design and modeling approach. Some of the recommendations are:

- Possibility of making synchronous measurements of the surface wetting and flow structure observation. Such data would be useful to validate the role of water droplet dynamics in surface wetting.

- The pressure gradients, *in situ* phase velocities and liquid hold-ups are some of the pertinent hydrodynamic parameters that should be measured and compared with model predictions.

- Use of traversing conductance probes to assess the height of water layer in stratified, slug, and annular flows. It would be useful to determine if a phase is continuous or not if the fluids become opaque under intense mixing action.

- Vertical flow patterns and surface wetting data were limited in the present work. Current flow loop setups need to be modified to expand the testing range. Surface wetting measurement for inclined pipes should be considered.

- The mechanism of droplet breakup model needs to be examined further in the oil-water wetting model. There is only a limited physical model available for determining the maximum stable droplet size in dense dispersion in which the coalescence and interactions

between droplets may become significant. Other forces such as the upward potential force required for elevation difference and Saffman lift forces may be important.

- The validity of the three-phase wetting model depends on the predictive accuracies of both the gas-liquid hydrodynamic model and the oil-water wetting model. The three-phase flow model was built from the framework of gas-liquid flow model and oil-water wetting model. These assumptions should be tested with more extensive experimental data using fluids with different viscosity.

- The effects of gas bubble entrainment in the oil-water mixture in slug and annular flows need to be investigated in order to determine how they may influence the surface wetting.

- Most of the closure equations used in the flow models were obtained from well-tested correlations published in the literature. However, in most cases, they were mostly calibrated with small diameter pipes. Hence, more experimental effort is required to determine accurate interfacial friction factor and frictional forces occurring in multiphase flow.

- Surface wettability can be altered if different pipe materials or fluids with added surfactants are used. These are topics worth researching.

REFERENCES

Açikgöz, M., França, F., & Lahey, R. T. (1992). An experimental study of three-phase flow regimes. *Int. J. of Multiphase Flow*, *18*(3), 327–336.

Ajmera, P., Robbins, W. K., Richter, S., & Nešić, S. (2010). The role of asphaltenes in inhibiting CO2 corrosion and altering the wettability of the steel surface. In *CORROSION/2010, paper no. 10329*. Houston, TX: NACE, 2010.

Alves, I. M., Caetano, E. F., Minami, K., & Shoham, O. (1991). Modeling Annular Flow Behavior for Gas Wells. *SPE Production Engineering*, *6*(4), 435.

Amundsen, L. (2011). *An experimental study of oil-water flow in horizontal and inclined pipe*. Ph.D. dissertation, Norwegian University of Sc. & Tech., Norway.

Angeli, P., & Hewitt, G. F. (1998). Pressure gradient in horizontal liquid-liquid flows. *Int. J. of Multiphase Flow*, *24*(7), 1183–1203.

Angeli, P., & Hewitt, G. F. (2000a). Flow structure in horizontal oil-water flow. *Int. J. of Multiphase Flow*, *26*(7), 1117–1140.

Angeli, P., & Hewitt, G. F. (2000b). Drop size distributions in horizontal oil-water dispersed flows. *Chemical Eng. Sc.*, *55*(16), 3133–3143.

Arirachakaran, S. (1983). *An experimental study of two-phase oil-water flow in horizontal pipes*. M.S. thesis, The University of Tulsa, Tulsa, OK.

Arirachakaran, S., Oglesby, K. D., Malinowsky, M. S., Shoham, O., & Brill, J. P. (1989). An Analysis of Oil/Water Flow Phenomena in Horizontal Pipes. In *Proceedings of SPE Production Operations Symposium* (pp. 155–167).

ASTM Standard D445. (2006). *Standard Test Method for Kinematic Viscosity of Transparent and Opaque Liquids (and Calculation of Dynamic Viscosity)*. West Conshohocken, PA: ASTM International.

ASTM Standard D971. (2004). *Standard test method for interfacial tension of oil against water by the ring method*. West Conshohocken, PA: ASTM International.

Ayello, F., Li, C., Tang, X., Cai, J., Nešić, S., Cruz, C. I., & Al-Khamis, J. (2008). Determination of phase wetting in oil-water pipe flows. In *CORROSION/2008, paper no. 08566*. Houston, TX: NACE, 2008.

Ayello, F., Robbins, W. K., Richter, S., & Nesic, S. (2011). Crude oil chemistry effects on inhibition of corrosion and phase wetting. In *CORROSION/2011, paper no. 11060*. Houston, TX: NACE, 2011.

Barnea, D. (1986). Transition from annular flow and from dispersed bubble flow-unified models for the whole range of pipe inclinations. *Int. J. of Multiphase Flow*, *12*(5), 733–744.

Barnea, D. (1987). A unified model for predicting flow-pattern transitions for the whole range of pipe inclinations. *Int. J. of Multiphase Flow*, *13*(1), 1–12.

Barnea, D., Shoham, O., & Taitel, Y. (1982a). Flow pattern transition for downward inclined two phase flow; horizontal to vertical. *Chemical Eng. Sc.*, *18*(4), 735–740.

Barnea, D., Shoham, O., & Taitel, Y. (1982b). Flow pattern transition for vertical downward two phase flow. *Chemical Eng. Sc.*, *37*(5), 741–744.

Becher, P. (1966). *Emulsions: Theory and Practice* (2nd ed.). Washington, DC: American Chemical Society.

Ben Amar, M., Goriely, A., Müller, M. M., & Cugliandolo, L. (Eds.). (2011). *New Trends in the Physics and Mechanics of Biological Systems* (p. 27). Oxford University Press.

Bolton, G. T., Bennett, M., Wang, M., Qiu, C., Wright, M., & Primrose, M. (2007). Development of an electrical tomographic system for operation in a remote, acidic and radioactive environment. *Chemical Eng. J.*, *130*(2-3), 165–169.

Bolton, G. T., Korchinsky, W. J., & Waterfall, R. C. (1998). Calibration of capacitance tomography systems for liquid-liquid dispersions. *Meas. Sci. Technol.*, *9*(11), 1797–1800.

Bolton, G. T., Korchinsky, W. J., & Waterfall, R. C. (1999). Imaging Immiscible Liquid-Liquid Systems by Capacitance Tomography. *Chemical Eng. Research & Design*, *77*(8), 699–708.

Bond, W. N., & Newton, D. A. (1928). Bubbles and drops and Stokes' law. *Philosophical Magazine*, 794–800.

Bonizzi, M., & Issa, R. I. (2003). A model for simulating gas bubble entrainment in two-phase horizontal slug flow. *Int. J. of Multiphase Flow*, *29*(11), 1685–1717.

Boxall, J. A., Koh, C. A., Sloan, E. D., Sum, A. K., & Wu, D. T. (2010). Measurement and Calibration of Droplet Size Distributions in Water-in-Oil Emulsions by Particle Video Microscope and a Focused Beam Reflectance Method. *Industrial & Engineering Chemistry Research*, *49*(3), 1412–1418.

Brauner, N., Moalem Maron, D., & Rovinsky, J. (1998). A two-fluid model for stratified flows with curved interfaces. *Int. J. of Multiphase Flow*, *24*(6), 975–1004.

Brauner, Neima. (2001). The prediction of dispersed flows boundaries in liquid–liquid and gas–liquid systems. *Int. J. of Multiphase Flow*, *27*, 885–910.

Brinkman, H. C. (1952). The viscosity of concentrated suspensions and solutions. *The J. of Chemical Physics*, *20*(4), 571.

Brodkey, R. S. (1967). *The phenomena of fluid motions*. Reading, MA: Addison-Wesley.

Brown, R. A. S., & Govier, G. W. (1961). High-speed photography in the study of two-phase flow. *The Canadian J. of Chemical Eng.*, *39*(4), 159–164.

Buckley, J. S., Liu, Y., & Monsterleet, S. (1998). Mechanisms of wetting alteration by crude oils. *SPE Journal*, *3*(1), 54–61.

Cai, J., Li, C., Tang, X., Ayello, F., Richter, S., & Nesic, S. (2012). Experimental study of water wetting in oil-water two phase flow-Horizontal flow of model oil. *Chemical Eng. Sc.*, *73*, 334–344.

Cai, J., Nešić, S., & de Waard, C. (2004). Modeling of water wetting in oil-water pipe flow. In *CORROSION/2004, paper no. 04663*. Houston, TX: NACE, 2004.

Cai, J., Nesic, S., Li, C., Tang, X., Ayello, F., Ivan, C., … Al-Khamis, J. (2005). Experimental studies of water wetting in large-diameter horizontal oil/water -pipe flows. In *SPE Annual Technical Conference and Exhibition (ATCE)*. Dallas, TX: Society of Petroleum Engineers (SPE).

Cartellier, A., & Achard, J. L. (1991). Local phase detection probes in fluid/fluid two-phase flows. *Review of Scientific Instruments*, *62*(2), 279.

Chanson, H. (1996). *Air Bubble Entrainment in Free-Surface Turbulent Shear Flows*. Academic Press.

Chaouki, J., Larachi, F., & Duduković, M. P. (1997). Noninvasive Tomographic and Velocimetric Monitoring of Multiphase Flows. *Ind. & Eng. Chemistry Research*, *36*(11), 4476–4503.

Charles, M. E., Govier, G. W., & Hodgson, G. W. (1961). The horizontal pipeline flow of equal density oil-water mixtures. *The Canadian J. of Chemical Eng.*, *39*(1), 27–36.

Chau, T. T., Bruckard, W. J., Koh, P. T. L., & Nguyen, A. V. (2009). A review of factors that affect contact angle and implications for flotation practice. *Advances in Colloid and Interface Sc.*, *150*(2), 106–15.

Chen, X. T., & Brill, J. P. (1997). Slug to churn transition in upward vertical two-phase flow. *Chemical Eng. Sc.*, *52*(23), 4269–4272.

Clay, P. H. (1940). The mechanism of emulsion formation in turbulet flow. I: Experimental part. *Proc. K. Ned. Akad. Wet.*, *43*, 852–865.

Clift, R., Grace, J., & Weber, M. E. (2005). *Bubbles, drops and particles*. Mineola, New York: Dover Publications, Inc.

Cohen, L. S., & Hanratty, T. J. (1965). Generation of waves in the concurrent flow of air and a liquid. *AIChE Journal*, *11*(1), 138–144.

Corlett, A. E. (1999). Three-phase flow pattern recognition in horizontal pipelines using electrical capacitance tomography. *J. Visualization*, *2*(1), 31–36.

Corlett, A. E. (2001). Determination of flow patterns and liquid holdup of multiphase flows using electrical capacitance tomography. In *Int. Conf. of Flow Measurement* (pp. 1–12).

Coulaloglou, C. A., & Tavlarides, L. L. (1977). Description of interaction processes in agitated liquid-liquid dispersions. *Chemical Eng. Sc.*, *32*(11), 1289–1297.

Crowe, C. T., Schwarzkopf, J. D., Sommerfeld, M., & Tusji, Y. (1997). *Multiphase flows with droplets and particles* (1st ed.). New York: CRC Press.

Da Silva, M. J. (2008). *Impedance sensors for fast multiphase flow measurement and imaging*. Ph.D. dissertation,Technische Universitat Dresden, Dresden, Germany.

Daaou, M., & Bendedouch, D. (2012). Water pH and surfactant addition effects on the stability of an Algerian crude oil emulsion. *J. of Saudi Chemical Society*, *16*(3), 333–337.

De Waard, C., & Lotz, U. (1993). Prediction of CO2 corrosion of carbon steel. In *CORROSION/1993, paper no. 69*. Houston, TX: NACE, 1993.

De Waard, C., Smith, L., & Craig, B. D. (2003). The influence of crude oil on well tubing corrosion rates. In *CORROSION/2003, paper no.03629*. Houston, TX: NACE, 2003.

Dean, W. R. (1928). The stream-line motion of fluid in a curved pipe. *Phil. Mag.*, *5*, 671–695.

Dickin, F., & Wang, M. (1996). Electrical resistance tomography for process applications. *Measurement Sc. & Tech.*, *7*(3), 247–260.

Dittmann, I., & Maug, E. G. (2008). Biases and error measures: how to compare valuation methods.

Dong, F., Jiang, Z. X., Qiao, X. T., & Xu, L. A. (2003). Application of electrical resistance tomography to two-phase pipe flow parameters measurement. *Flow Meas. & Instrumentation*, *14*(4-5), 183–192.

Du, M., Jin, N., Gao, Z., Wang, Z., & Zhai, L. (2012). Flow pattern and water holdup measurements of vertical upward oil–water two-phase flow in small diameter pipes. *Int. J. of Multiphase Flow*, *41*, 91–105.

Dukler, A., & Hubbard, M. (1975). A model for gas-liquid slug flow in horizontal and near horizontal tubes. *Ind. & Eng. Chemistry Fundamentals*, *14*(4), 337–347.

Elseth, G. (2001). *An experimental study of oil/water flow in horizontal pipes*. Ph.D. dissertation, Norwegian University of Sc. & Tech., Norway.

Fabre, J., & Line, A. (1992). Modeling of two-phase slug flow. *Annual Review of Fluid Mechanics*, *24*(1), 21–46.

Flores, J. (1997). *Oil-water flow in vertical and deviated wells*. Ph.D. dissertation, The University of Tulsa, Tulsa, OK.

Flores, J., Chen, X., Sarica, C., & Brill, J. (1999). Characterization of oil–water flow patterns in vertical and deviated wells. *SPE Prod. & Facilities*, *14*(2), 102–109.

Fulford, G. D. (1964). The flow of liquids in thin films. *Adv. Chem. Eng.*, *5*, 151–236.

Gamio, J. C., Castro, J., Rivera, L., Alamilla, J., Garcia-Nocetti, F., & Aguilar, L. (2005). Visualisation of gas-oil two-phase flows in pressurised pipes using electrical capacitance tomography. *Flow Measurement & Instrumentation*, *16*(2-3), 129–134.

Gao, Z.-K., & Jin, N.-D. (2011). Nonlinear characterization of oil–gas–water three-phase flow in complex networks. *Chemical Eng. Sc.*, *66*(12), 2660–2671.

Garvey, C. J. (2002). Computed tomography in clinical practice. *BMJ*, *324*(7345), 1077–1080.

George, D. L., Ceccio, S. L., O'Hern, T. J. O., Shollenberger, K. A., & Torczynski, J. R. (1998). Advance material distribution measurement in multiphase flows: A case study. In *Conf. Int. Mech. Eng. Congress and Exposition*. Anaheim, CA.

Giguère, R., Fradette, L., Mignon, D., & Tanguy, P. A. (2008). ERT algorithms for quantitative concentration measurement of multiphase flows. *Chemical Eng. J.*, *141*(1-3), 305–317.

Gomez, L. E., Shoham, O., Schmidt, Z., Chokshi, R. N., & Northug, T. (2000). Unified Mechanistic Model for Steady-State Two-Phase Flow: Horizontal to Vertical Upward Flow. *SPE Journal*, *5*(3), 339–350.

Govier, G. W., Sullivan, G. A., & Wood, R. K. (1961). The upward vertical flow of oil-water mixtures. *The Canadian J. of Chemical Eng.*, *39*(2), 67–75.

Grangeat, P. (Ed.). (2009). *Tomography*. London, UK: ISTE Ltd.

Hackerman, N., & Roebuck, A. H. (1954). Adsorption of polar organic compounds on steel. *Ind. & Eng. Chemistry*, *46*(7), 1481–1485.

Hammer, E. A., & Johansen, G. A. (1997). Process tomography in the oil industry - state of the art and future possibilities. *Measurement and Control*, *30*, 212–216.

Hanratty, T. J., & Hershman, A. (1961). Initiation of roll waves. *AIChE J.*, *7*(3), 488–497.

Hasan, N. M., & Azzopardi, B. J. (2007). Imaging stratifying liquid–liquid flow by capacitance tomography. *Flow Meas. & Instrumentation*, *18*(5-6), 241–246.

Hasson, D., Mann, V., & Nir, A. (1970). Annular flow of two immiscible liquids I. Mechanisms. *The Canadian J. of Chemical Eng.*, *48*(5), 514–520.

Heikkinen, L. M., Vauhkonen, M., Savolainen, T., & Kaipio, J. P. (2001). Modelling of internal structures and electrodes in electrical process tomography. *Measurement Sc. & Tech.*, *12*(8), 1012–1019.

Hernandez, S., Bruzual, J., Lopez-Lineares, F., & Luzon, J. G. (2003). Isolation of potential corrosion inhibiting compounds in crude oils. In *CORROSION/2003, paper no. 03330* (pp. 1–24). Houston, TX: NACE, 2003.

Hesketh, R. P., Etchells, A. W., & Russell, T. W. F. (1991). Experimental observations of bubble breakage in turbulent flow. *Ind. Eng. Chem. Res.*, *30*(5), 835–841.

Hesketh, R. P., Fraser Russell, T. W., & Etchells, a. W. (1987). Bubble size in horizontal pipelines. *AIChE Journal*, *33*(4), 663–667.

Hewitt, G. F. (2005). Three-phase gas-liquid-liquid flows in the steady and transient states. *Nuclear Eng. & Design*, *235*(10-12), 1303–1316.

Hewitt, G. F., & Jayanti, S. (1993). To churn or not to churn. *Int. J. of Multiphase Flow*, *19*(3), 527–529.

Hinze, J. O. (1955). Fundamentals of hydrodynamic mechanism of splitting in dispersion processes. *AIChE Journal*, *1*(3), 289–295.

Hubbe, M. A., Chen, H., & Heitmann, J. A. (2009). Permeability reduction phenomena in packed beds, fiber mats, and wet webs of paper exposed to flow of liquids and suspensions: A review. *BioResources*, *4*(1), 405–451.

Isaksen, Ø. (1996). A review of reconstruction techniques for capacitance tomography. *Meas. Sci. and Technol.*, *7*(3), 325–337.

Ismail, I., Gamio, J. C., Bukhari, S. F. A., & Yang, W. (2005). Tomography for multi-phase flow measurement in the oil industry. *Flow Measurement and Instrumentation*, *16*(2-3), 145–155.

Jauseau, N. (2012). *Multiphase Flow Effects on Naphthenic Acid Corrosion of Carbon Steel*. Ph.D. dissertation, Ohio University, Athens, OH.

Jaworski, A. J., & Bolton, G. T. (2000). The design of an electrical capacitance tomography sensor for use with media of high dielectric permittivity. *Measurement Sc. & Tech.*, *11*(6), 743–757.

Jayanti, S., & Hewitt, G. F. (1992). Prediction of the slug-to-churn flow transition in vertical two-phase flow. *International Journal of Multiphase Flow*, *18*(6), 847–860.

Jeanmeure, L. F. ., Dyakowski, T., Zimmerman, W. B. ., & Clark, W. (2002). Direct flow-pattern identification using electrical capacitance tomography. *Experimental Thermal and Fluid Sc.*, *26*(6-7), 763–773.

Johansen, G. A., Frøystein, T., Hjertaker, B. T., Isaksen, Ø., Olsen, Ø., Strandos, S. K., … Hammer, E. A. (1995). The development of a dual mode tomography for three-component flow imaging. *The Chemical Eng. J.*, *56*(3), 175–182.

Karabelas, A. J. (1977). Vertical distribution of dilute suspensions in turbulent pipe flow. *AIChE J.*, *23*(4), 426–434.

Karabelas, A. J. (1978). Droplet size spectra generated in turbulent pipe flow of dilute liquid/liquid dispersions. *AIChE Journal*, *24*(2), 170–180.

Kaya, A. S., Sarica, C., & Brill, J. P. (2001). Mechanistic modeling of two-phase flow in deviated wells. *SPE Production and Facilities*, *16*(3), 156–165.

Kee, K. E., Richter, S., Babic, M., & Nešić, S. (2014). Flow patterns and water wetting in oil-water two-phase flow - A flow loop study. In *CORROSION/2014, paper no. 4068* (pp. 1–15). Houston, TX: NACE, 2014.

Keskin, C., Zhang, H., & Sarica, C. (2007). Identification and Classification of New Three-Phase Gas/Oil/Water Flow Patterns. In *Proc. of SPE Annual Tech. Conf. & Exh., paper no. SPE 110221* (pp. 1–13). Society of Petroleum Engineers.

Kokal, S. (2005). Crude oil emulsions: a state-of-the-art review. *SPE Prod. & Facilities*, *20*(1), 5–13.

Kolmogorov, A. N. (1949). On the breaking of drops in turbulent flow. *Doklady Akad. Nauk.*, *66*, 825–828.

Kubie, J., & Gardner, G. C. (1977). Drop sizes and drop dispersion in straight horizontal tubes and in helical coils. *Chemical Eng. Sc.*, *32*(2), 195–202.

Lee, A. H. (1993). *A study of flow regime transitions for oil-water-gas mixtures in large diameter horizontal pipelines*. M.S. thesis, Ohio University, Athens.

Levich, V. G. (1962). *Physicochemical hydrodynamics*. Englewood Cliffs, NJ: Prentice Hal.

Li, C. (2009). *Effect of Corrosion Inhibitor on Water Wetting and Carbon Dioxide Corrosion in Oil-Water Two-Phase Flow*. Ph.D. dissertation, Ohio University, Athens, OH.

Li, C., Tang, X., Ayello, F., Cai, J., Nesic, S., Cruz, C. I., & Al-Khamis, J. (2006). Experimental study on water wetting and CO2 corrosion in oil-water two-phase flow. In *CORROSION/2006, paper no. 06595* (pp. 1–26). Houston, TX: NACE, 2006.

Liao, Y., & Lucas, D. (2009). A literature review of theoretical models for drop and bubble breakup in turbulent dispersions. *Chemical Eng. Sc.*, *64*(15), 3389–3406.

Lucas, D., Krepper, E., & Prasser, H.-M. (2001). Prediction of radial gas profiles in vertical pipe flow on the basis of bubble size distribution. *Int. J. of Thermal Sc.*, *40*(3), 217–225.

Ma, Y., Zheng, Z., Liu, X., & Wu, Y. (2001). Application of electrical resistance tomography system to monitor gas/liquid two-phase flow in a horizontal pipe. *Flow Measurement and Instrumentation*, *12*(4), 259–265.

Malhotra, A. (1995). *Study of two and three-phase flows in large diameter horizontal pipelines*. M.S. thesis, Ohio University, Athens, OH.

Maxworthy, T. (1967). A note on the existence of wakes behind large, rising bubbles. *J. of Fluid Mechanics*, *27*(02), 367–368.

McLean, J. D., & Kilpatrick, P. K. (1997). Effects of Asphaltene Aggregation in Model Heptane–Toluene Mixtures on Stability of Water-in-Oil Emulsions. *J. of Colloid and Interface Sc.*, *196*(1), 23–34.

Mishima, K., & Hibiki, T. (1996). Some characteristics of air-water two-phase flow in small diameter vertical tubes. *Int. J. of Multiphase Flow*, *22*(4), 703–712.

Mols, B., & Oliemans, R. V. A. (1998). A turbulent diffusion model for particle dispersion and deposition in horizontal tube flow. *Int. J. of Multiphase Flow*, *24*(1), 55–75.

Muzychka, Y., & Yovanovich, M. (1998). Modeling friction factors in non-circular ducts for developing laminar flow. In *2nd AIAA, Theoretical Fluid Mechanics Meeting*. Reston, Virigina.

Nädler, M., & Mewes, D. (1997). Flow induced emulsification in the flow of two immiscible liquids in horizontal pipes. *Int. J. of Multiphase Flow*, *23*(1), 55–68.

Nesic, S., Cai, J., & Lee, J. K.-L. (2005). A multiphase flow and internal corrosion prediction model for mild steel pipelines. In *CORROSION/2005, paper no. 05556* (pp. 1–35). Houston, TX: NACE, 2005.

Nesic, S., & Postlethwaite, J. (1990). Relationship between the structure of disturbed flow and erosion-corrosion. *Corrosion*, *46*(11), 874–880.

Nicholson, M. K., Aziz, K., & Gregory, G. A. (1978). Intermittent two phase flow in horizontal pipes: Predictive models. *The Canadian J. of Chemical Eng.*, *56*(6), 653–663.

Obot, N. T. (1988). Determination of incompressible flow friction in smooth circular and noncircular passages: a generalized approach including validation of the nearly century old hydraulic diameter concept. *J. of Fluids Engineering*, *110*(4), 431.

Oglesby, K. D. (1979). *An experimental study on the effects of oil viscosity, mixture velocity, and water fraction on horizontal oil-water flow*. M.S. thesis, The University of Tulsa, Tulsa, OK.

Ohnuki, A., & Akimoto, H. (2000). Experimental study on transition of flow pattern and phase distribution in upward air–water two-phase flow along a large vertical pipe. *Int. J. of Multiphase Flow*, *26*(3), 367–386.

Pal, R. (1993). Pipeline flow of unstable and surfactant-stabilized emulsions. *AICHE Journal*, *39*(11), 1754–1764.

Pan, L. (1996). *High pressure three-phase (gas/liquid/liquid) flow*. Ph.D. dissertation, Imperial College, London.

Paras, S. V., & Karabelas, A. J. (1991). Droplet entrainment and deposition in horizontal annular flow. *Int. J. of Multiphase Flow*, *17*(4), 455–468.

Paul, H. I., & Sleicher, C. A. (1965). The maximum stable drop size in turbulent flow: effect of pipe diameter. *Chemical Eng. Sc.*, *20*(1), 57–59.

Perry, R. H., Green, D. W., & Maloney, J. O. (1997). *Perry's Chemical Engineers' Handbook* (7th Ed.). New York: McGraw-Hill.

Pleshko, A. R. (1990). *An experimental study of vertical three phase (oil-water-air) upwards flows*. M.S. thesis, University of Wyoming, USA.

Pots, B. F. M., Hollenberg, J. F., & Hendriksen, E. L. J. A. (2006). What are the real influences of flow on corrosion? In *CORROSION/2006, paper no. 06591*. Houston, TX: NACE, 2006.

Qiu, C., Hoyle, B. S., & Podd, F. J. W. (2007). Engineering and application of a dual-modality process tomography system. *Flow Measurement and Instrumentation*, *18*(5-6), 247–254.

Reyssat, É., Chevy, F., Biance, A.-L., Petitjean, L., & Quéré, D. (2007). Shape and instability of free-falling liquid globules. *Europhysics Letters (EPL)*, *80*(3), 34005.

Rodriguez, J. M. (2009). *Numerical simulation of two-phase annular flow*. Ph.D. dissertation, Rensselaer Polytechnic Institute, Troy, NY.

Rosen, M. J. (2004). *Surfactants and interfacial phenomena* (3rd ed.). Hoboken, NJ: John Wiley & Sons, Inc.

Russell, T. W. F., Hodgson, G. W., & Govier, G. W. (1959). Horizontal pipeline flow of mixtures of oil and water. *The Canadian J. of Chemical Eng.*, *37*(1), 9–17.

Russell, T. W. F., & Lamb, D. E. (1965). Flow mechanism of two-phase annular flow. *The Canadian J. of Chemical Eng.*, *43*(5), 237–245.

Saffman, P. G. (1965). The lift on a small sphere in a slow shear flow. *J. of Fluid Mechanics*, *22*(2), 385–400.

Schlichting, H. V. (1979). *Boundary layer theory*. New York: McGraw-Hill.

Segev, A. (1984). Mechanistic model for estimating water dispersion in crude oil flow. In *1984 annual AIChE meeting*. San Francisco, CA: AIChE, 1984.

Shanahan, M. E. R. (1995). Simple theory of "stick-slip" wetting hysteresis. *Langmuir*, *11*(3), 1041–1043.

Sharifi, M., & Young, B. (2013). Electrical resistance tomography (ERT) applications to chemical engineering. *Chemical Eng. Research & Design*, *91*(9), 1625–1645.

Sharma, A., Al Sarkhi, A., Sarica, C., & Zhang, H. (2011). Modeling of oil-water flow using energy minimization concept. *Int. J. of Multiphase Flow*, *37*(4), 326–335.

Shean, A. R. (1976). *Pressure drop and phase fraction in oil-water-air vertical pipe flow*. M.S. thesis, MIT, USA.

Shoham, O. (2006). *Mechanistic modeling of gas-liquid two-phase flow in pipes*. Richardson, TX: Society of Petroleum Engineers.

Shoham, O., & Taitel, Y. (1984). Stratified turbulent-turbulent gas-liquid flow in horizontal and inclined pipes. *AIChE J.*, *30*(3), 377–385.

Simmons, M., & Azzopardi, B. (2001). Drop size distributions in dispersed liquid–liquid pipe flow. *Int. J. of Multiphase Flow*, *27*, 843–859.

Sleicher, C. A. J. (1962). Stable drop size in turbulent flow. *A.I.Ch.E.Journal*, *8*(4), 471–477.

Sobocinski, D. P. (1955). *Horizontal co-current flow of water, gas-oil and air*. M.S. thesis, University of Oklahoma, Norman, OK.

Sotto Mayor, T. (2007). *Hydrodynamics of gas-liquid flows in slug flow regime*. Ph.D. dissertation, Universidade do Porto, Porto, Portugal.

Taitel, Y., & Dukler, A. E. (1976). Model for predicting flow regime transitions in horizontal and near horizontal gas-liquid flow. *AICHE Journal*, *22*(1), 47–55.

Taitel, Yehuda, & Barnea, D. (1990). A consistent approach for calculating pressure drop in inclined slug flow. *Chemical Eng. Sc.*, *45*(5), 1199–1206.

Taitel, Yehuda, Bornea, D., & Dukler, A. E. (1980). Modelling flow pattern transitions for steady upward gas-liquid flow in vertical tubes. *AIChE J.*, *26*(3), 345–354.

Taitel, Yehudah, Lee, N., & Dukler, A. E. (1978). Transient gas-liquid flow in horizontal pipes: Modeling the flow pattern transitions. *AIChE Journal*, *24*(5), 920–934.

Tang, X. (2010). *Effect of Surface State on Water Wetting and Carbon Dioxide Corrosion in Oil-water Two-phase Flow*. Ph.D. dissertation, Ohio University, Athens, OH.

Tang, X., Richter, S., & Nešić, S. (2013). An improved model for water wetting prediction in oil-water two-phase flow. In *CORROSION/2013, paper no.2393* (pp. 1–15). Houston, TX: NACE, 2013.

Trallero, J. L. (1995). *Oil-Water Flow Patterns in Horizontal Pipes*. Ph.D. dissertation, The University of Tulsa, Tulsa, OK.

Trallero, J. L., Sarica, C., & Brill, J. (1997). A study of oil-water flow patterns in horizontal pipes. *SPE Production & Facilities*, *12*(3), 165–172.

Tsouris, C., & Tavlarides, L. (2004). Breakage and coalescence models for drops in turbulent dispersions. *AIChE Journal*, *40*(3), 395–406.

Utvik, O. H., Rinde, T., & Valle, A. (2001). An experimental comparison between a recombined hydrocarbon-water fluid and a model fluid system in three-phase pipe flow. *J. of Energy Resources Technology*, *123*(4), 253–259.

Valle, A. (2000a). CO2-corrosion and water distribution in two phase flow of hydrocarbon liquids and water. In *CORROSION/2000, paper no. 00047* (pp. 1–11). Houston, TX: NACE, 2000.

Valle, A. (2000b). *Three phase gas-oil-water pipe flow*. Ph.D. dissertation, Imperial College, London.

Van der Zande, M. J., van Heuven, K. R., Muntinga, J. H., & van den Broek, M. . (1999). Effect of flow through a choke valve on emulsion stability. In *Proc. of the 1999 SPE Annual Tech. Conf. & Exh., paper SPE 56640* (pp. 1–8). Houston, TX: SPE, 1999.

Varaksin, A. Y. (Ed.). (2007). *Turbulent Particle-Laden Gas Flows* (Vol. 41). Berlin, Heidelberg: Springer Berlin Heidelberg.

Vedapuri, D., Bessette, D., & Jepson, W. P. (1997). A segregated flow model to predict water layer thickness in oil-water flows in horizontal and slightly inclined pipe lines. *Multiphase BHRA*, 75–105.

Vera, J. R., & Hernandez, S. (2006). Oil characteristics, water/oil wetting and flow influence on the metal loss corrosion. Part 1: effct of oil and flow on CO2/H2S corrosion. In *CORROSION/2006, paper no. 06113* (pp. 1–29). Houston, TX: NACE, 2006.

Vielma, M., Atmaca, S., Sarica, C., & Zhang, H. (2008). Characterization of Oil/Water Flows in Horizontal Pipes. *SPE Projects, Facilities & Construction*, *3*(4), 3133–3143.

Vigolo, D., Griffiths, I. M., Radl, S., & Stone, H. A. (2013). An experimental and theoretical investigation of particle–wall impacts in a T-junction. *J. of Fluid Mechanics*, *727*, 236–255.

Wallis, G. B. (1969). *One-dimensional two-phase flow*. New York: McGraw-Hill.

Wang, M., Yin, W., & Holliday, N. (2002). A highly adaptive electrical impedance sensing system for flow measurement. *Meas. Sci. and Technol.*, *13*(12), 1884–1889.

Wenzel, R. N. (1936). Resistance of solid surfaces to wetting by water. *Ind. & Eng. Chemistry*, *28*, 988.

Wicks, M., & Fraser, J. P. (1975). Entrainment of water by flowing oil. *Materials Performance*, *14*(5), 9–12.

Williams, R. A., & Beck, M. S. (1995). *Process tomography - principles, techniques and applications*. Oxford: Butterworth-Heinemann.

Woelflin, W. (1942). The viscosity of crude-oil emulsions. *API Drilling and Production Practice*, *1*, 148–153.

Woods, G. S., Speddeng, P. L., Watterson, J. K., & Raghunathan, R. S. (1998). Three-phase oil/water/air vertical flow. *Chemical Engineering Research and Design*, *76*, 571–584.

Xiao, J. J., Shoham, O., & Brill, J. P. (1990). A comprehensive mechanistic model for two-phase flow in pipelines. In *Proc. of SPE Annual Technical Conf. & Exh., paper SPE 20631* (pp. 167–180). SPE, 1990.

Yang, S. S., Richter, S., Robbins, W., & Nešić, S. (2012). Evaluation of the protectiveness of a paraffin layer in CO2 corrosion of mild steel. In *CORROSION/2012, paper no.1323* (pp. 1–15). Houston, TX: NACE, 2012.

Yang, W., Stott, A., Beck, M., & Xie, C. (1995). Development of capacitance tomographic imaging systems for oil pipeline measurements. *Review of Scientific Instruments*, *66*(8), 4326–4332.

Yilmaz, T. (1990). General equations for pressure drop for laminar flow in ducts of arbitrary cross sections. *J.of Energy Resources Technology*, *112*(4), 220.

You, D. (2013). *Re-engineering of the legacy software systems by using object-oriented technologies*. M.S. thesis, Ohio University, Athens, OH.

Young, T. (1805). An essay on the cohesion of fluids. *Philosophical Trans. of the Royal Soc. of London*, *95*, 65–87.

Zavareh, F., Hill, A. D., & Podio, A. (1988). Flow regimes in vertical and inclined oil/water flow in pipes. In *Proc. of SPE Annual Tech. Conf. & Exh., paper SPE 18215*. Houston, TX: SPE, 1988.

Zenit, R., Koch, D. L., & Sangani, A. S. (2001). Measurements of the average properties of a suspension of bubbles rising in a vertical channel. *J. of Fluid Mechanics*, *429*, 307–342.

Zuidema, H., & Waters, G. (1941). Ring Method for Determination of Intrfacial Tension. *Ind. & Eng. Chem. Anal. Ed.*, *13*(5), 312–313.